DTNSRDC-SME-CR-19-83

Contract No. N00024-80-C-5337

Acoustic Emission Determination of Deformation Mechanisms Leading to Failure of Naval Alloys

J. T. Glass, S. Majerowicz, R. E. Green, Jr.
Materials Science and Engineering Department
The Johns Hopkins University
Baltimore, MD 21218

May 1983

FINAL REPORT

(VOLUME II)

Prepared for:

David Taylor Naval Ship R&D Center (Code 2820)

and

Naval Sea Systems Command (SEA 05R25)

Approved for public release; distribution unlimited

UNCLASSIFIED

SECURITY CLASSIFICATION OF THIS PAGE (When Data Entered)

REPORT DOCUMENTATION PAGE	READ INSTRUCTIONS BEFORE COMPLETING FORM
1. REPORT NUMBER: DTNSRDC SME-CR-19-83	2. GOVT ACCESSION NO.: A130 385
	3. RECIPIENT'S CATALOG NUMBER:
4. TITLE (and Subtitle): Acoustic Emission Determination of Deformation Mechanisms Leading to Failure of Naval Alloys (Volume II)	5. TYPE OF REPORT & PERIOD COVERED: Final 12/27/79 - 12/27/82
	6. PERFORMING ORG. REPORT NUMBER:
7. AUTHOR(s): J. T. Glass, S. Majerowicz, R. E. Green, Jr.	8. CONTRACT OR GRANT NUMBER(s): N00024-80-C-5337
9. PERFORMING ORGANIZATION NAME AND ADDRESS: The Johns Hopkins University, Materials Science and Engineering Dept., Baltimore, MD 21218	10. PROGRAM ELEMENT, PROJECT, TASK AREA & WORK UNIT NUMBERS:
11. CONTROLLING OFFICE NAME AND ADDRESS: Naval Sea Systems Command, Washington, D.C. 20362, SEA05R25, Dr. H. H. J. Vanderveldt	12. REPORT DATE: May 1983
	13. NUMBER OF PAGES: 250
14. MONITORING AGENCY NAME & ADDRESS(if different from Controlling Office): David Taylor Naval Ship R&D Center, Ship Materials Engineering Department, Annapolis, MD 21402, Code 2820, Mr. Charles A. Zanis	15. SECURITY CLASS. (of this report): Unclassified
	15a. DECLASSIFICATION/DOWNGRADING SCHEDULE:

16. DISTRIBUTION STATEMENT (of this Report)

Approved for public release, distribution unlimited.

17. DISTRIBUTION STATEMENT (of the abstract entered in Block 20, if different from Report)

18. SUPPLEMENTARY NOTES

19. KEY WORDS (Continue on reverse side if necessary and identify by block number)

Acoustic Emission
Laser Beam Interferometer
HY80, 100, 130 Steels
Mechanical Deformation
Nondestructive Evaluation

20. ABSTRACT (Continue on reverse side if necessary and identify by block number)

An experimental investigation was conducted in order to determine the degree of acoustic emission signal modification due to propagation through specimens of different geometries. Initial efforts were directed at comparison of a number of acoustic emission probes in order to determine their sensitivity and their ability to detect an unmodified reproducible theoretically predicted waveform. The results of these tests showed that an optical interferometric probe possessed the largest frequency

DD FORM 1 JAN 73 1473 EDITION OF 1 NOV 65 IS OBSOLETE
S/N 0102-014-6601

UNCLASSIFIED
SECURITY CLASSIFICATION OF THIS PAGE (When Data Entered)

20. (Continued)

bandwidth and a National Bureau of Standards conical piezoelectric transducer possessed the best waveform detection sensitivity. These two probes were therefore selected to make measurements of the surface displacements due to a reproducible acoustic emission source as a function of distance from the source for several different geometrically shaped objects. Long test specimens in the form of a right circular cylinder, a rectangular cross-section bar, a moderately thin-walled pipe, and an I-beam were used for these propagation measurements. Results of the propagation tests showed that the acoustic emission waveforms propagated further distances without significant modification in the solid cylinder and bar than in the pipe and I-beam. In all cases the higher frequency components of the waveform attenuated faster than the lower frequency components. In addition the thin sections of the pipe and I-beam caused rapid distortion of the initial waveform because of multiple reflections and associated mode conversions at their interfaces.

The results of this work clearly show that the ability to detect acoustic emission waveforms, which still retain features characteristic of the source, may be physically impossible at locations remote from the source in real structural members. This will be particularly difficult when the structure possesses dimensions of the same order or smaller than the wavelengths of the acoustic signals.

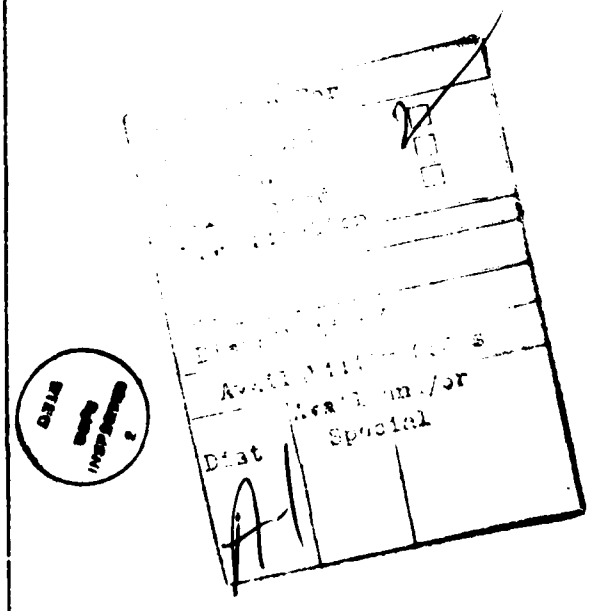

EXECUTIVE SUMMARY

This is the final technical report (two volumes) summarizing research activities performed for the David Taylor Naval Ship Research and Development Center (Code 2820) and the Naval Sea Systems Command (SEA 05R15). The authors wish to thank Mr. Charles A. Zanis (DTNSRDC) and Dr. H. H. J. Vanderveldt (NAVSEA) for their continued encouragement and support during the course of this research. The purpose of this research was to use innovative optical techniques and superior signal capture and processing systems to determine the waveforms, frequency spectra, and propagational behavior of the acoustic emission signals generated by the various mechanical deformation mechanisms leading to failure of metal alloys of prime importance to naval structures. Experiments were performed using a laser interferometer detector and a new piezoelectric transducer, both of which permitted recording of the first arriving acoustic emission signal unmodified by transducer construction artifacts as experienced with conventional commercially available piezoelectric acoustic emission transducers.

Acoustic emission events were either generated by pulling microtensile specimens in an extremely quiet microtensile machine (Volume I) or by the brittle, step unloading fracture of glass capillary tubes on the surface of test specimens possessing different geometries (Volume II). All acoustic emission event waveforms were recorded by a high speed transient

recorder and stored on magnetic mini-diskettes for analysis on a high speed digital omputer and for future propagational behavior and waveform analysis. Specimens which were pulled in the microtensile machine were examined using optical and scanning electron microscopes to determine correlation between acoustic emission events and microstructural changes.

ABSTRACT

An experimental investigation was conducted in order to determine the degree of acoustic emission signal modification due to propagation through specimens of different geometries. Initial efforts were directed at comparison of a number of acoustic emission probes in order to determine their sensitivity and their ability to detect an unmodified reproducible theoretically predicted waveform. The results of these tests showed that an optical interferometric probe possessed the largest frequency bandwidth and a National Bureau of Standards conical piezoelectric transducer possessed the best waveform detection sensitivity. These two probes were therefore selected to make measurements of the surface displacements due to a reproducible acoustic emission souce as a function of distance from the source for several different geometrically shaped objects. Long test specimens in the form of a right circular cylinder, a rectangular cross-section bar, a moderately thin-walled pipe, and an I-beam were used for these propagation measurements. Results of the propagation tests showed that the acoustic emission waveforms propagated further distances without significant

modification in the solid cylinder and bar than in the pipe and I-beam. In all cases the higher frequency components of the waveform attenuated faster than the lower frequency components. In addition the thin sections of the pipe and I-beam caused rapid distortion of the initial waveform because of multiple reflections and associated mode conversions at their interfaces.

The results of this work clearly show that the ability to detect acoustic emission waveforms, which still retain features characteristic of the source, may be physically impossible at locations remote from the source in real structural members. This will be particularly difficult when the structure possesses dimensions of the same order or smaller than the wavelengths of the acoustic signals.

I. INTRODUCTION

When a solid material undergoes sufficient mechanical deformation, the elastic strain energy stored within can be rapidly released due to structural alterations. As a result, transient elastic waves propagate through the material. This phenomena is known as stress wave emission or more commonly as acoustic emission. Sources for acoustic emission include, [1]:

a. Twinning
b. Grain boundary sliding and rotation
c. Slip band formation
d. Dislocation unpinning and motion
e. Plastic deformation at a stress concentration
f. Void initiation and growth
g. Crack initiation and propagation
h. Fracture of inclusions and second phase particles

Signals resulting from acoustic emission events may range in frequency from a minimum of a few hertz to a maximum of tens of megahertz. Acoustic emissions are characteristic of the source from which the event originated. It is this source which must ultimately be identified such that there is no doubt as to the mechanism causing the acoustic emission event. However, before one can begin to accurately identify a mechanism of acoustic

emission, one must be able to detect and record an acoustic emission event without mechanically or electronically altering the signal. Conventional probes used to record acoustic emission signals have been traditionally made from piezoelectric materials. The inherent problem plaguing users of these probes is whether or not the recorded signal is truly representative of the source, rather than an artifact of the recording probe itself. Standard piezoelectric transducers must be attached directly to the surface of the specimen via an acoustic impedance matching couplant. Acoustic couplants act as attenuators of certain waveforms, particularly shear and surface waves. Yet, even without the acoustic couplant present, there is some modification of the waveform detected due to the contact between the transducer and the specimen surface. The modifications generally seen at the interface of two solids are in the form of mode conversions [2].

In order for a signal to be representative of the source and not the transducer, one must assume that the stress acting on the sensitive face of the transducer is uniform. If the stress acting over the

sensitive face of the transducer is non-uniform, a more complicated stress mode will result, [3]. Often it is assumed that the transducer is excited in a one-dimensional stress mode.

Along with the direct contact problem, standard piezoelectric transducers exhibit a non-uniform frequency response due to the resonant nature of the transducer. The main problem with detection of true acoustic emission waveforms using conventional piezoelectric transducers is that the various elements making up the transducer (wear plate, piezoelectric element, backing material, mounting case, etc.) all "ring" at their resonant frequencies creating artifacts which mar and severely distort the true waveform and associated frequency spectra. Analysis and subsequent identification of the source of an acoustic emission using the conventional piezoelectric transducer is extremely difficult under these conditions, [4].

In recent years the use of flat frequency response probes has played an important part in the isolation of acoustic emission information. Air gap capacitance transducers, optical interferometers, as well as a new generation of piezoelectric

transducers and path stabilized interferometers, have been developed which allow a higher order of certainty in the detection and subsequent identification of acoustic emission events.

The air gap capacitance transducer is a non-contact type transducer in the sensitive region of the probe, Fig. 1a. There are, however, support shims which must come into contact with the specimens to keep the air gap constant. These shims contribute to waveform modifications because of their contact with the specimen surface. The air gap capacitance transducer exhibits a flat frequency response, [5], but compared to conventional piezoelectric probes, Fig. 1b, it is not as sensitive. Use of the air gap capacitance transducer has been restricted to the recording of more energetic acoustic emisssion events. While the air gap capacitance transducer has a flat frequency response, it also acts as a filter to eliminate certain waveforms. Because it is necessary to have all waveforms represented for the proper characterization of an event, signal to source matching is often impossible when the air gap capacitance transducer is used, [1].

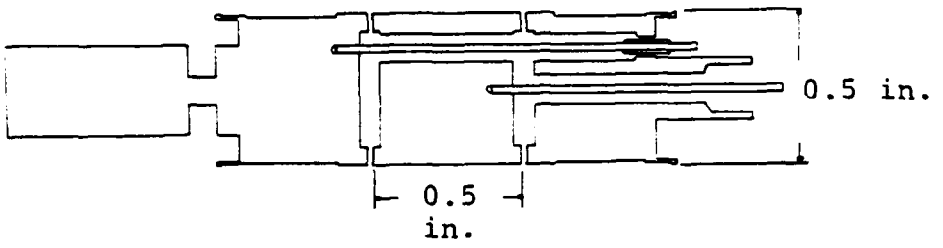

a)

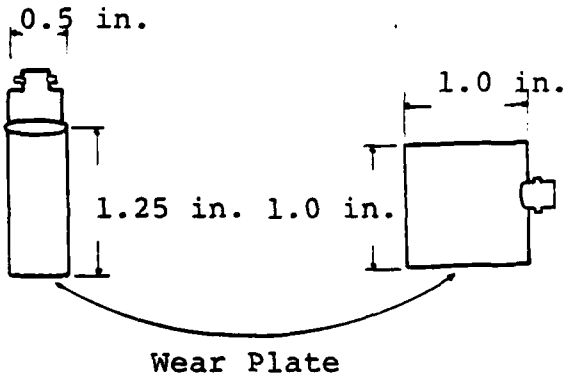

b)

Figure 1. Schematic drawings of a) air gap capacitance transducer and b) standard commercial acoustic emission transducers.

Optical interferometry, used for the detection of acoustic emission generated displacements, has become one of the most active areas for acoustic emission research. Interferometry is the technique by which a beam of coherent light (typically laser light) is split (amplitude splitting interferometry) by a beam splitter and recombined to form interference fringes. One leg of the split beam travels to a reference mirror while the other leg travels to the surface of a specimen; both beams are reflected back along their original paths and are recombined at the beam splitter. If the optical path difference of the returning beams are exactly an integral number of optical wavelengths, such that the waves are in phase, an interference pattern in the form of alternating bright and dark fringes will result. If the specimen surface is displaced, by the passage of a transient elastic wave for example, the path length of the split laser beams will differ by a fraction of an optical wavelength. This difference will create a phase difference between the two beams resulting in a change in the fringe pattern. The resulting pattern will be an exact representation of the surface displacement which initiated the change.

Results obtained from the adaptation of optical interferometry to the detection and characterization of acoustic emission signals have been promising in recent years, [1,4,6-10]. Major advantages of the optical probe include:

a. No direct probe to specimen contact (distance to specimen surface is determined by the focal length of the focusing lens; 4 inches for this work)

b. Very broad, flat frequency response (0 to 5 MHz for this work)

c. No requirements for an impedance matching couplant

d. Ability to probe very small regions (beam diameter 1 millimeter or less, beam to source distance as close as a few hundreths of a millimeter)

Most importantly, the optical probe can be absolutely calibrated and is "virtually free" of mechanical resonance. An effective way of determining if a probe will characterize the waveform of an acoustic emission event is to match the acoustic waveform, recorded by the probe, to the theoretical waveform proposed by Lamb in 1904, Fig. 2, [11]. The infinite half-space is used for this model because a waveform will not be modified by reflections from boundaries. The three-dimensional solution to Lamb's problem for vertical displacement excited by a point source indicates that there is not

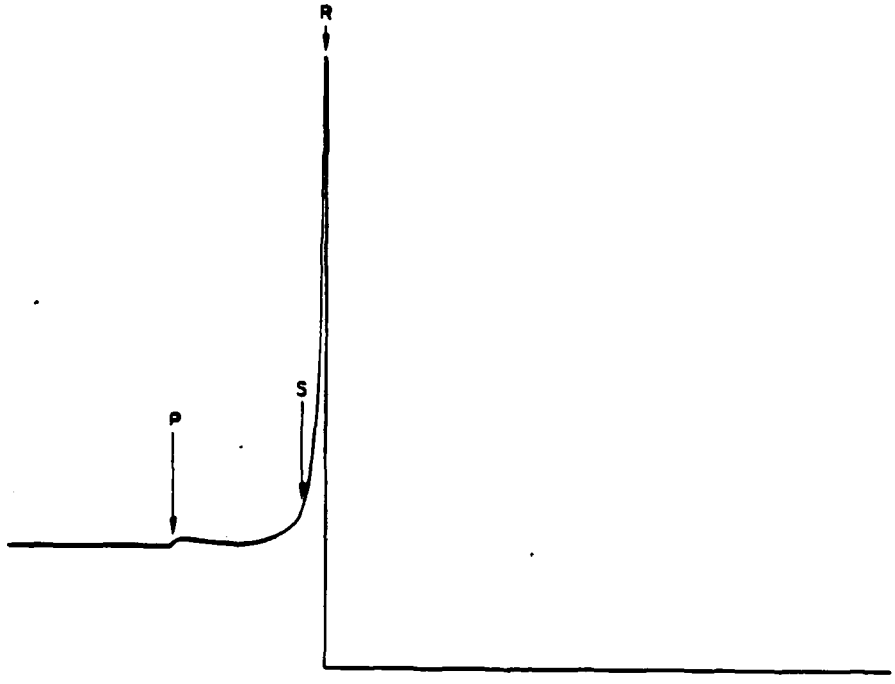

Figure 2. THEORETICAL RECORD OF A STEP-LOADING POINT SOURCE STRIKING AN INFINITE HALF-SPACE

only the pronounced Rayleigh surface acoustic wave, (SAW) designated by (R), but also longitudinal (P) and shear (S) wave components. Experimental results reported by Kline, Fig. 3, and Breckenridge, Fig. 4, show excellent correlation to theory. If a longer time frame were used, specimen displacement will slowly decay to zero due to attenuation. However, Breckenridge showed that before the signal was completely attenuated, the time-displacement record went into long wavelength oscillations, Fig. 5. These oscillations are believed to be the result of long-term normal mode oscillations produced due to the finite specimen dimensions and not the infinite half-space which the theory assumes. No normal mode oscillations are associated with a half-space of infinite size. Proof that these oscillations are caused by resonant frequencies are not at all trivial; in fact, mathematically it cannot be exactly solved for most geometries, [13].

Continuing studies, [14], have shown that acoustic emission research is far from complete. The development of innovative acoustic emission probes at the National Bureau of Standards and The

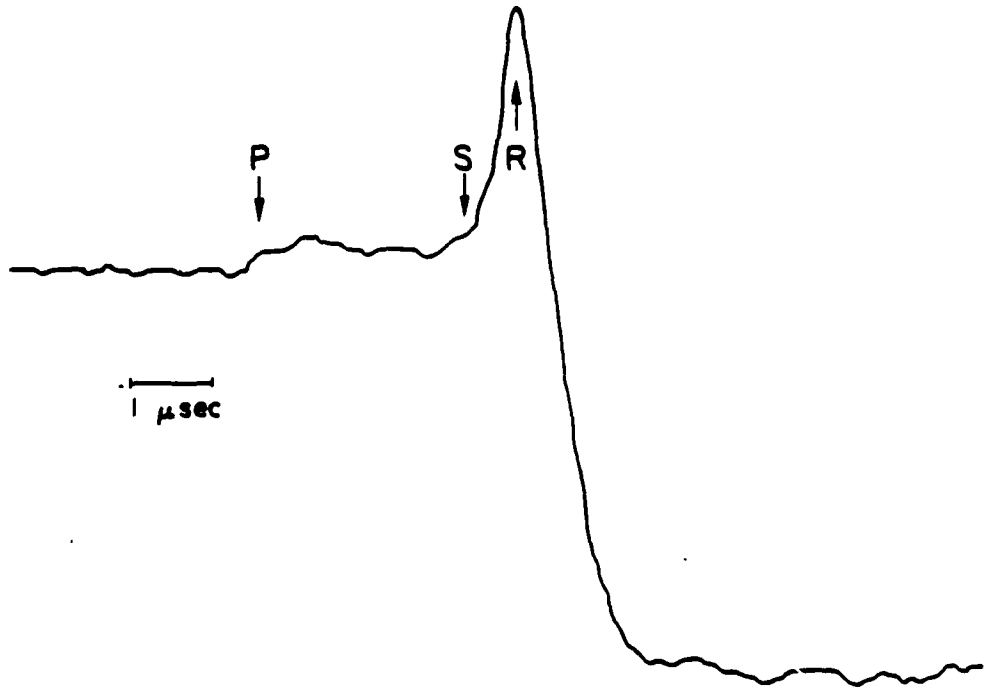

Figure 3. Experimental record of a radial displacement vs. time record for a step-function point source, after Kline, [6].

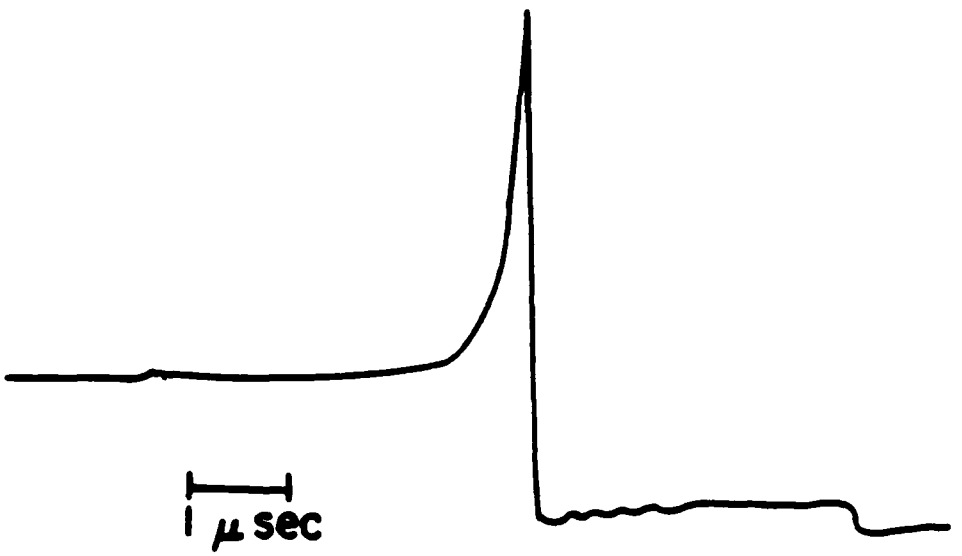

Figure 4. Experimental record of a radial displacement vs. time record for a step-function point source striking an aluminum block, simulating an infinite half-space, after Breckenridge et. al. [12].

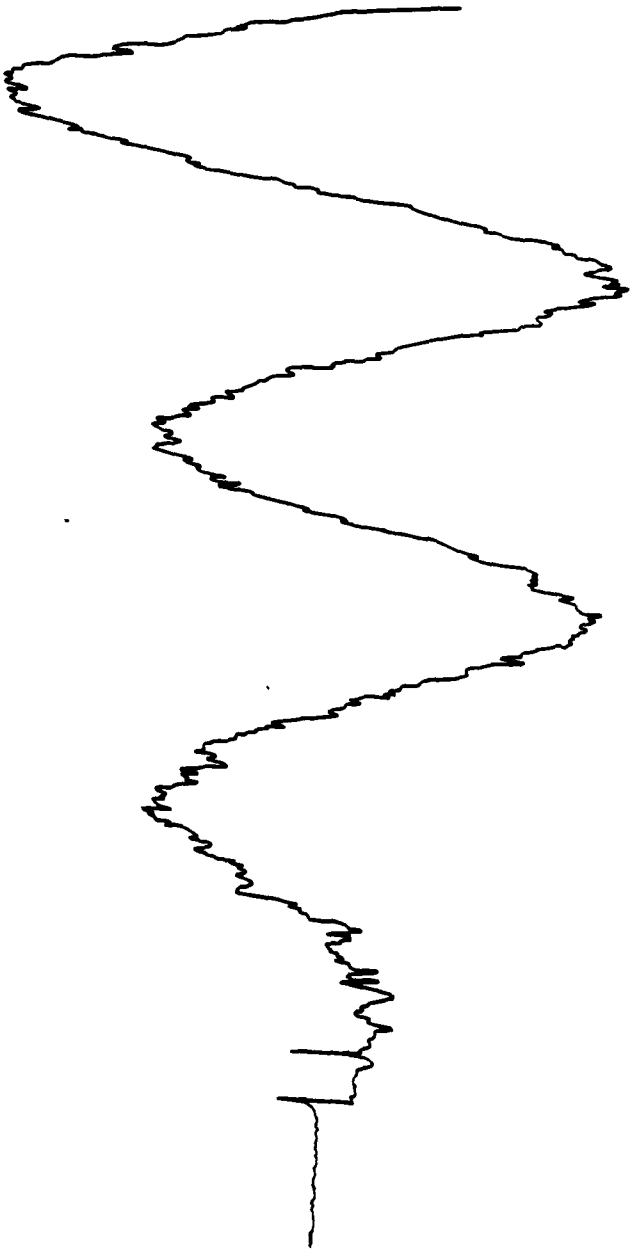

Figure 5. Long term time displacement record of Fig. 4.

Johns Hopkihs University Applied Physics Laboratory allows one to make more accurate records of acoustic emission events, [15,16]. These records are more characteristic of the source mechanism that the probe. A detailed discussion of both systems will be presented later.

A. HISTORICAL WORK IN ACOUSTIC EMISSION

"And there rose up a great noise as if thunder was born from the bowels of the Earth."
-Stephen Majerowicz, 1983.

Seismology was one of the first disciplines to use acoustic emission as a form of analysis. The elastic waves produced by an earthquake were used to characterize fault movement in terms of energy released, location and depth, [3]. But earthquakes were not the only source of acoustic emissions; early observations in metals indicated that deformation mechanisms were also active generators of acoustic emissions. Studies over the past thirty years, [17-24], led to acoustic emission theories relating to twinning, Martensitic transformation, pre-failure emission and grain boundary interface motion. In the late 1950's and early 1960's, intensive acoustic emission work was performed by

Schofield, [25-27] and Tatro, [28,29]. These initial studies led to comprehensive work on the relation between acoustic emission and deformation mechanisms in a large number of materials.

Early work in acoustic emission centered around the deformation of a material in the plastic region. For the most part, investigators operated in a frequency range that was below 60 kHz. A major breakthrough in experimental technique, reported in the mid 1960's [30], was the extension of experiments into the 100 kHz and 1 MHz range. This eliminated the need for extensive laboratory soundproofing by eliminating extraneous noise, thus allowing analysis via acoustic emission to be made practial.

B. EXPERIMENTAL GOALS

The primary goal of acoustic emission research is to be able to gain maximum knowledge of an acoustic emission event. This knowledge would allow researchers to relate the observed elastic waves to the mechanisms responsible for their generation. This goal has extended applications of acoustic emission techniques into areas of materials research and evaluation, non-destructive testing and structural integrity.

Increased demand for more accurate acoustic emission probes has led to the development of innovative sensors capable of reaching previously unexplored areas.

It is necessary to locate and identify acoustic emission sources. Triangulation techniques, utilizing piezoelectric transducers, are effective in locating the region where an acoustic emission event occurred. However, these systems are often large arrays of transducers which cannot always fit into small areas. When access to an area is restricted it is necessary to use remote sensing techniques. The use of laser interferometry in remote sensing is the most innovative technique to become available. Optical interferometers offer special advantages for remote sensing; not only do they allow access to restricted regions, but they do not alter an acoustic emission waveform by direct contact between the probe and specimen. Therefore, the use of a laser interferometer as a remote sensing technique was a basis on which this thesis was undertaken..

There were two goals of the present work. The first, was to characterize several different probes, both piezoelectric and optical, in reference to their ability to record a "true" acoustic emission waveform without significant alteration of the signal. The second, was to determine experimentally the influence different specimen geometries have on the propagation of the same known acoustic emission waveform.

II. PROBE CHARACTERIZATION

A. PROBE SELECTION

Identification, characterization and accurate recording of acoustic emission events is of major importance to researchers. Unfortunately, inherent design flaws in most acoustic emission probes have kept this criteria from being met; therefore, nine different acoustic emission probes were characterized at the onset of this work, Fig. 6, Table I.

Conventional transducers used to record acoustic emission waveforms form a complex structure which is subject to multiple resonances. The wear plate, active element, backing material, case and connector combine to cause large variations in transducer response (unless the wear plate is specifically designed as an impedance transformer), [15]. Limitations in the size of the backing material may cause the piezoelectric element to resonate and dominate the transducer response. The large diameter contact area associated with conventional transducers causes an integration effect when recording waveforms therefore, the conventional transducer does not act as a point receiver.

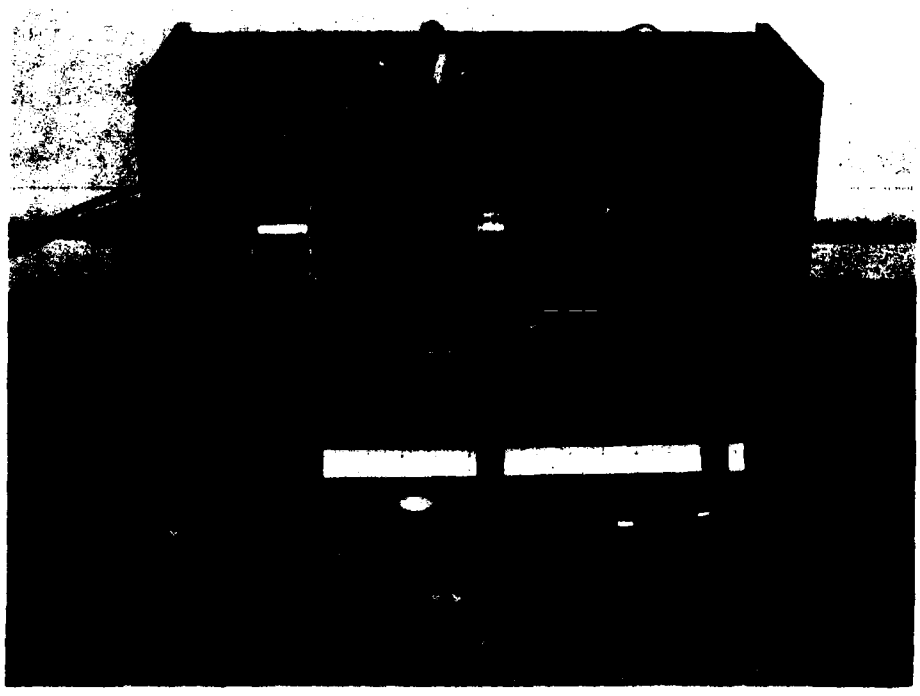

Figure 6. Probes characterized during this work; Rear: a) APL laser interferometer, Front from left: b) NBS-PZT #26, c) NBS-PZT # 36, d) Panametrics A5-0.1-L362, e) Panametrics V3032, f) Panametrics V3031, g) Aerotech Gamma D12618, h) Aerotech Gamma C12634, i) Dunegan/Endevco S9201 AC42. Length between black marks on ruler is six inches.

TABLE I

a. APL-System, modified Michelson laser interferometer

b. NBS-PZT #26, conical transducer
   Active area: 5/64 in.= 2mm diameter

c. NBS-PZT #36, conical transducer
   Active area: 3/64 in.= 1.2mm diameter

d. Panametrics AE - 0.1 - L632
   0.1 MHz conventional transducer
   Active area: 1 in. diameter

e. Panametrics V3032
   0.5 MHz conventional transducer
   Active area: 0.5 in. diameter

f. Panametrics V3031
   1.0 MHz conventional transducer
   Active area: 0.5 in. diameter

g. Aerotech Gamma D12618
   1.0 MHz conventional transducer
   Active area: 0.5 in. diameter

h. Aerotech Gamma C12634
   1.0 MHz conventional transducer
   Active area: 1 in. diameter

i. Dunegan/Endevco S9201 AC42
   1.0 MHz conventional transducer
   Active area: 0.5 in. diameter

An improved transducer, the National Bureau of Standards conical transducer (b and c Table I, hereafter referred to as NBS-PZT), overcomes the problem of a large contact area associated with conventional acoustic emission probes, Fig. 7. The design of this transducer has been kept simple; the contact area is as small as possible, no wear plate has been used and the backing has been extended both radially and axially. The active piezoelectric element, Lead Zirconium Titanate (PZT), is in the shape of a truncated cone, which allows the NBS-PZT to act as a point receiver. A heat cured epoxy resin is used to fix the piezoelectric element to a brass backing plate. The backing plate is designed to prevent any internally reflected waves from interfering with the first arriving signal. The frequency response for this innovative transducer varies less than 3dB over the frequency range of interest (100 kHz to 1 MHz). Because of the flat frequency response and the minimal area of contact, the NBS-PZT models the transient signal exceptionally well, with displacement measurements on the order of 0.1 Å or better, [15].

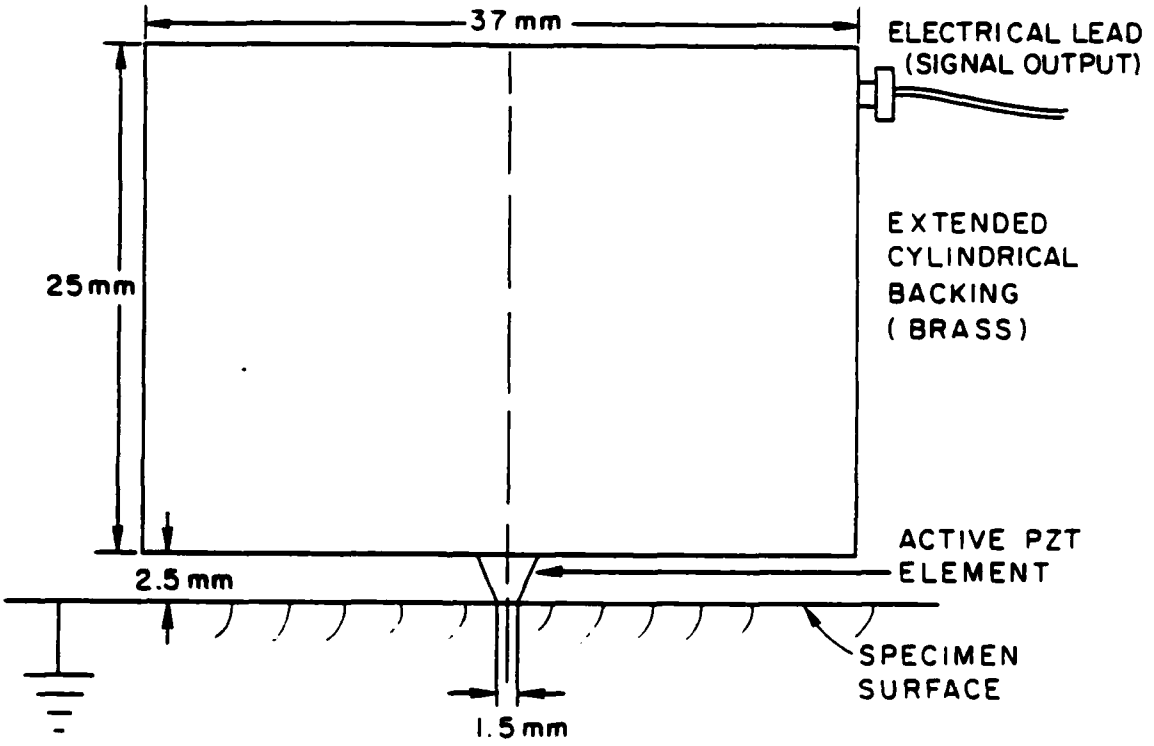

Figure 7. Schematic drawing of the National Bureau of Standards conical transducer.

Since the advent of the laser, optical probing of acoustic emission events has become numerous, [1,4,6-10,14,30-43]. With the development of a new modified Michelson interferometer at The Johns Hopkins University Applied Physics Laboratory, [16], the task of acoustic emission research has become a new art. Hereafter, the laser interferometer will be referred to as the APL-System, (a, Table I). Optical probes used in acoustic emission research offer many advantages for monitoring acoustic emission events. The major advantage of the optical probe is that there is no contact between the probe and specimen surface, therefore, the elastic waves that are to be detected are not mechanically disturbed. A description of the working features for the laser interferometer can be found in Appendix A.

B. PROBE CHARACTERIZATION PROCEDURE

In turn each piezoelectric transducer was coupled to a flat face of an Aluminum 2024-T4 right circular cylinder via an acoustic impedance matching couplant (KB-Aerotech, Batch No. 042480XL01), Fig. 8. The output from the piezoelectric probes was fed through a voltage follower into a Nicolet Explorer Digital Storage

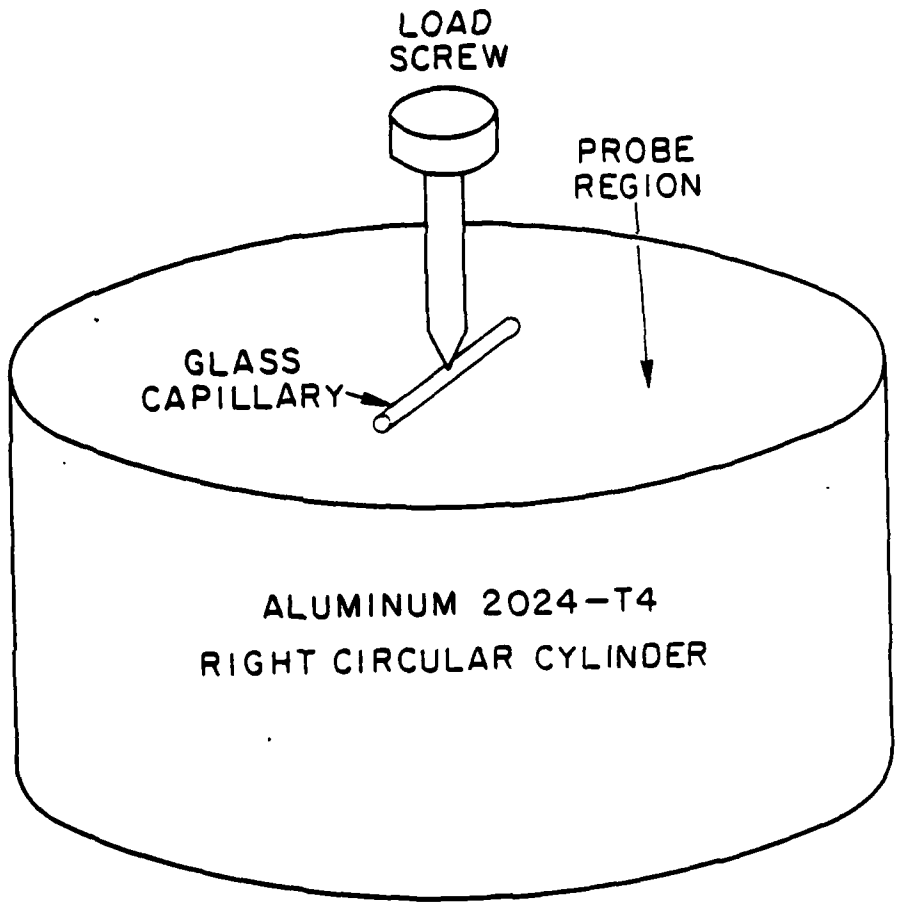

Figure 8. Experimental arrangement used for probe characterization.

Oscilloscope. A voltage follower is a unity gain amplifier which acts as an impedance match between a high output impedance device and a low input impedance recorder; Fig. 9 is a block diagram of the experimental system. The probes were placed two inches from a centrally located Borosilicate glass capillary source, (Kimble type Kimax-51 ICS 46485-1, 0.7 to 1.0 millimeter outside diameter). The glass capillaries were fractured brittlely on the surface of the specimen to generate an acoustic emission waveform. After the transient signal was captured on the Nicolet, the waveform was stored on a magnetic disk for future analysis. This procedure was repeated for each of the nine probes used in this work.

C. PROBE CHARACTERIZATION RESULTS

Characterization of the probes was based on 1) the ability of the probe to capture a waveform closely resembling the theoretically predicted model, Fig. 2 and 2) the ability of the probe to discern the broadest range of frequencies present in the waveform. Using the brittle fracture of the glass capillary as the source for acoustic emission

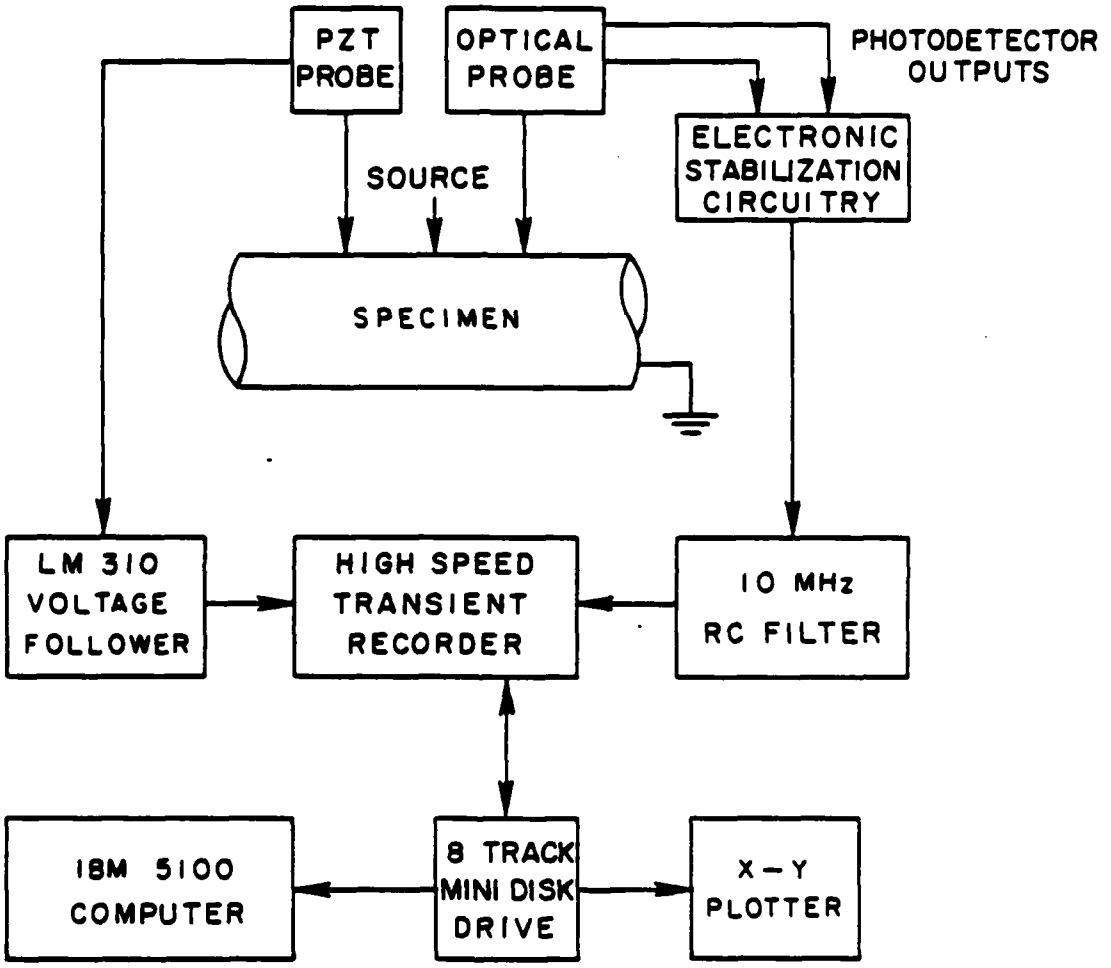

Figure 9. Block diagram of experimental arrangement used in probe and specimen characterization.

events a battery of time-base data was recorded and can be found in Appendix B. The maximum amplitude waveform recorded at the lowest recording sensitivity of the Nicolet was the basis whereby each probe was compared qualitatively to each other. At ±2 volts full scale on the Nicolet, four of the nine probes recorded a waveform with the desired characteristic structure, Figs. B2-B5, but only three probes produced a waveform whose values were consistent with those obtained by theory. Of the remaining five probes, Figs. B5-B10, information obtained in the time domain could not be utilized because the information was not compatible with the theoretical data. It was then decided to increase the sensitivity of the Nicolet from ±2 volts to ±400 millivolts and finally to ±100 millivolts full scale, Figs. B11-B19. Eventually a waveform of approximately the proper structure was observed but there was no practical reason to continue with the conventional transducers.

It was also necessary to determine which probe gave the best frequency response because if the waveform was to be analyzed in the frequency domain it would be desirable to have as large a bandwidth

as possible on the recording probe. Cutoff values were chosen for each of the time-base waveforms such that the frequency spectrum could be generated via the Fourier transform; refer to Appendix C for the cutoff time-base waveforms as well as the corresponding frequency spectra.

Solutions for the response of a system to a particular excitation are not trivial, especially when the excitation waveform is complex. It is possible, however, to take a complex waveform and represent it by a sum of elementary or building-block waveforms. The principle of superposition for linear systems allows the total response to be determined from the responses to the elementary waveforms making up the excitations, [44]. Once the elementary component waveforms are known, a frequency spectrum can be generated from the time domain record. The mechanism for generating a frequency spectrum from a time domain waveform is the Fourier transform. The Discrete Fourier Transform (DFT) is the actual function which changes the time-base information into a frequency spectrum. The Fast Fourier Transform (FFT) is the computer algorithm which runs the DFT.

Data stored on the Nicolet was in the form of a discrete number of points with time and voltage information. Transfer of the stored data was accomplished through an RS-232C interface into an IBM 5100 portable computer. Appendix D contains a listing of the programs used during the data analysis. It was necessary to determine if the time-base data would yield meaningful information in the frequency domain. Ideally a waveform should begin and end at a zero reference level when using the DFT. Characterization of the time-base data could be windowed around the first arriving longitudinal (P) shear (S), and Rayleigh surface wave (R). By windowing around these waves it was possible to standardize the information processing.

The Fourier transform was made on each cutoff time plot and two frequency spectra were generated. The normalized amplitude spectra respresents the largest voltage value, for each frequency spectra, divided by itself such that the corresponding greatest value equals one. The relative amplitude spectra represents the voltage values of each frequency spectra divided by 1.9667 millivolts, for this series. Upon observation of the time domain

and frequency domain information it was decided that the APL laser interferometer and NBS-PZT #26 were the probes which would yield accurate representations of the acoustic emission waveforms. Figures 10 and 11 show the time-base first arriving P, S, and R waves quite clearly. Observation of the frequency spectra for these probes indicated that the APL-System was able to discern a broader range of Frequencies, Figs. 12 and 13. With this information it was decided that both probes would be used for the characterization of the specimens. NBS-PZT #26 would be used to obtain time-base waveforms because it was able to capture more of the waveforms than any of the other probes. The APL-System would also be used because its broad bandwidth allowed one to cover a greater frequency range.

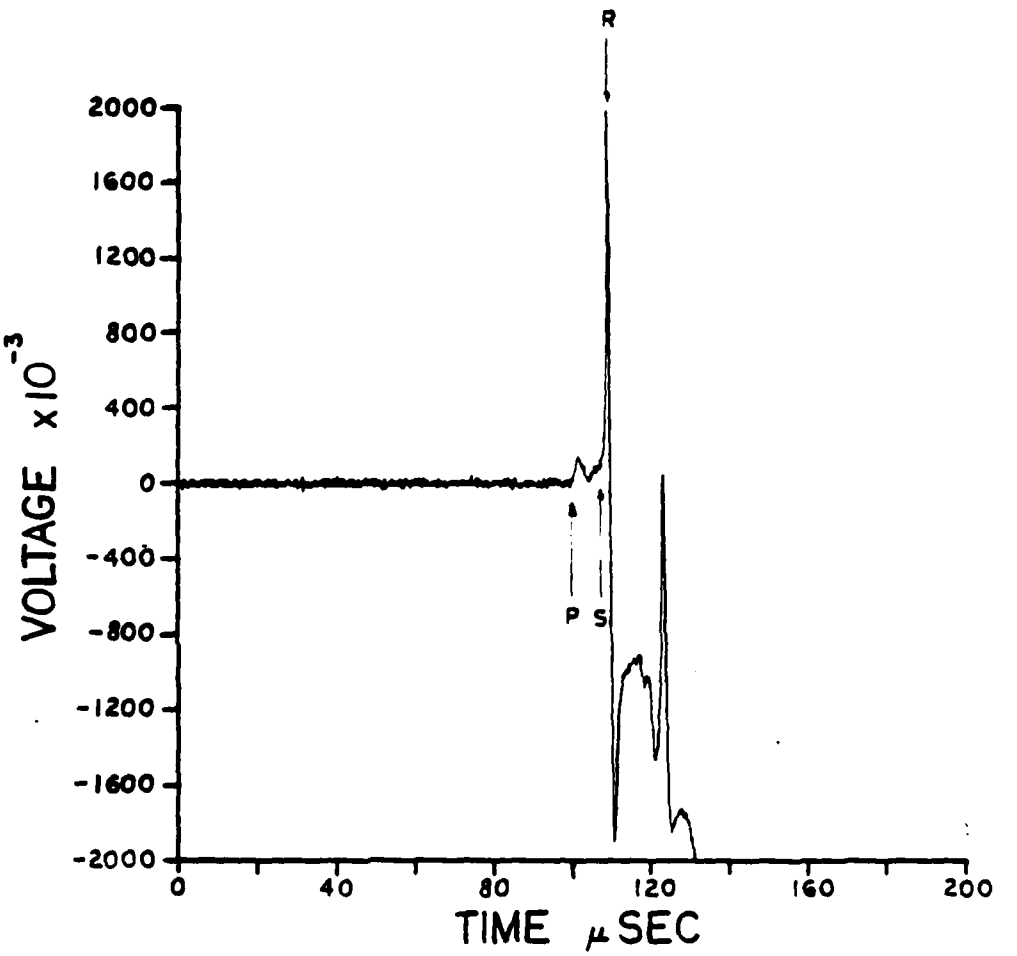

Figure 10. Time domain waveform recorded by the APL laser interferometer located two inches from a glass capillary source on an Aluminum 2024-T4 right circular cylinder.

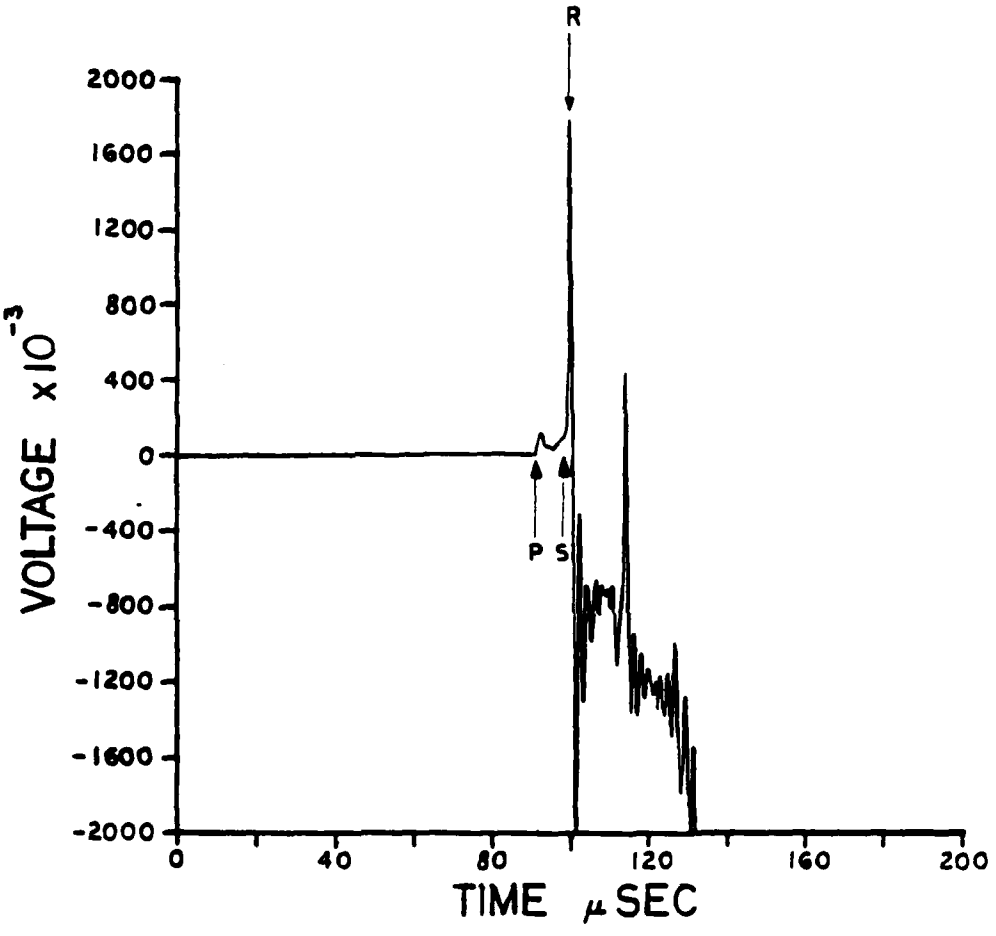

Figure 11. Time domain waveform recorded by the NBS-PZT #26 conical transducer located two inches from a glass capillary source on an Aluminum 2024-T4 right circular cylinder.

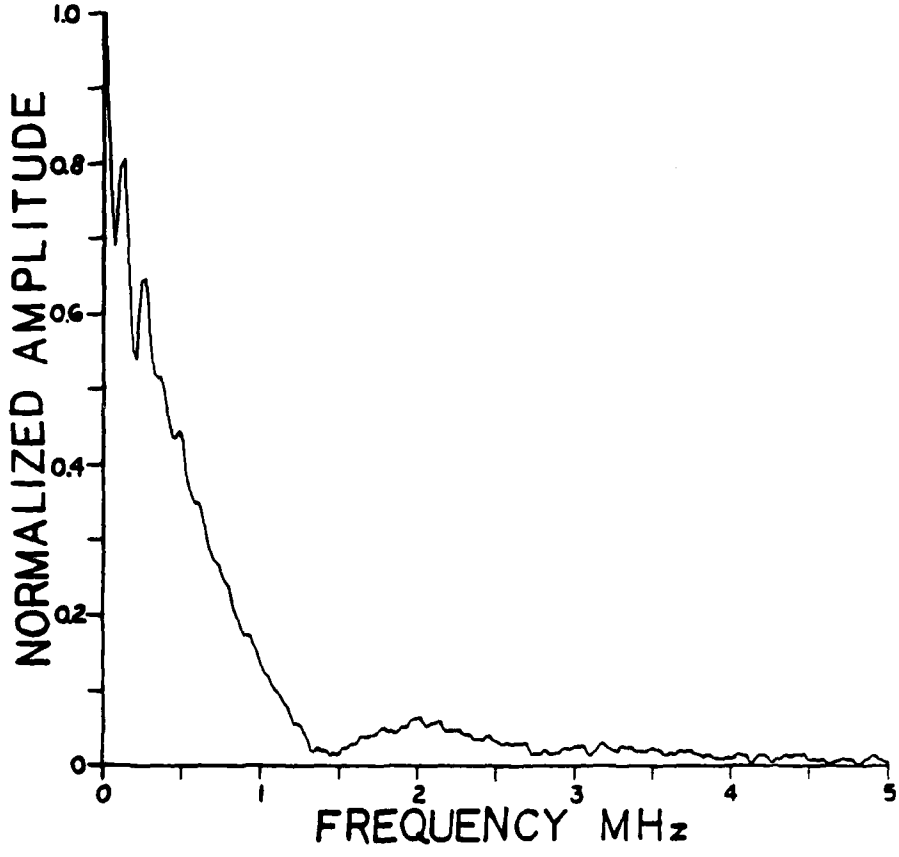

Figure 12. Frequency spectrum generated from waveform in Fig. 10.

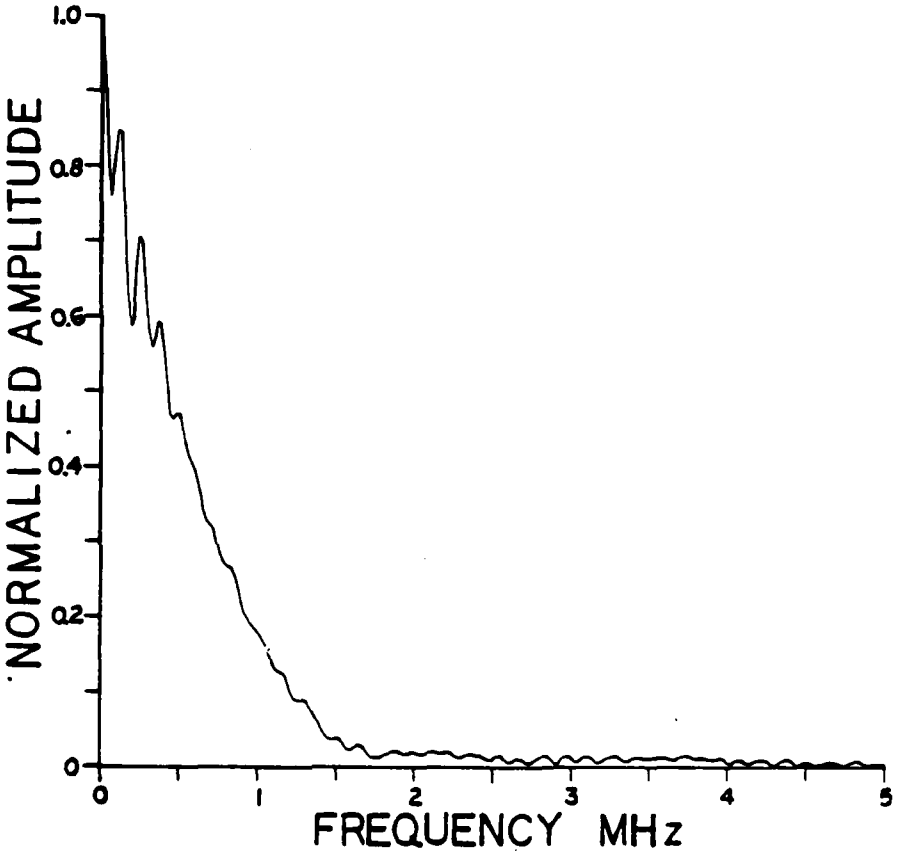

Figure 13. Frequency spectrum generated from waveform in Fig. 11.

III. SPECIMEN CHARACTERIZATION

A. SPECIMEN SELECTION

Specimens used in this work were chosen to represent several different geometries. The specimens chosen fell into two categories, Fig. 14:

1. Solid Geometries
2. Open Geometries

Table II contains a description of the specimens used throughout this work. The outer surface of each specimen was removed to a depth of approximately 1/64 in. by machining. The surface was then buffed with an Iron Oxide buffing compound and polished with a Chromium Oxide polishing compound until a mirror-like finish was achieved. A highly reflective surface was needed in order to optimally use the interferometric technique. By polishing the surface of the specimens, any rough areas were reduced thus minimizing scattering of the laser light. Before any experiments were performed, the surface of the specimen was cleaned of dust with a 95% Ethanol solution and allowed to dry.

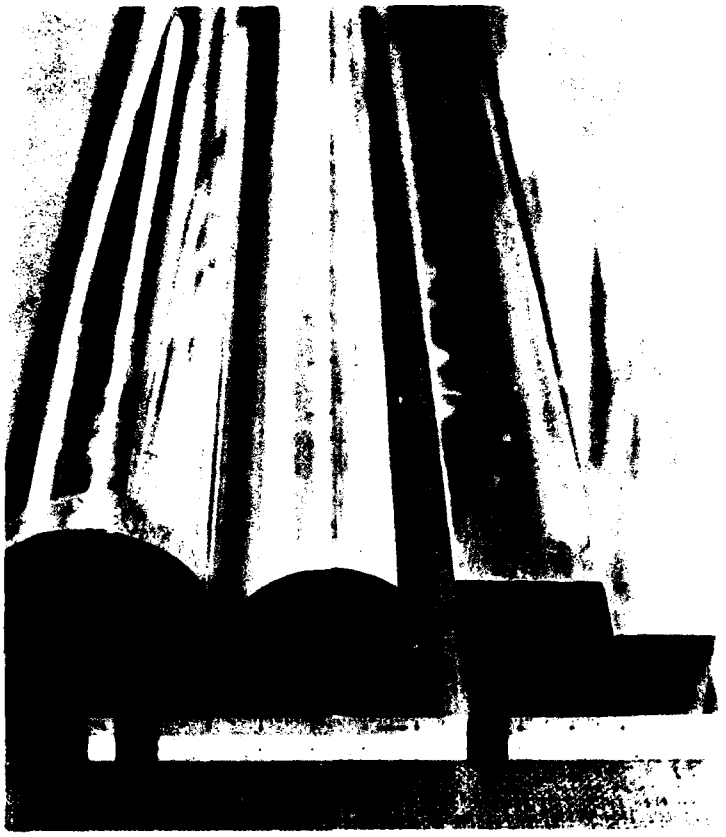

Figure 14. Specimens characterized in this work; from the left: a) Solid cylindrical beam, b) Pipe, c) I-beam, d) Rectangular beam. Length between black marks on ruler is six inches.

TABLE II

1. Solid Geometries

   a. Cylindrical Beam
      2024-ST4 Aluminum
      5 in. Diameter x 44 in. Long

   b. Rectangular Beam
      2024-T351 Aluminum
      2.5 in. High x 2 in. Wide x 71 in. Long

2. Open Geometries

   a. Pipe
      6061 Aluminum
      3.25 in. Inside Diameter x 3.875 in.
      Outside Diameter x 56 in. Long
      Wall Thickness: 0.625 in. (5/8 in.)

   b. I-Beam
      6061 Aluminum
      3.75 in. High x 2.75 in. Wide x 56 in. Long
      Rib and Wing thickness: 3/16 in.

B. SPECIMEN CHARACTERIZATION PROCEDURE

Each specimen in turn was placed on an air suspension table in order to minimize extraneous vibrations. At a point four inches from one end a glass capillary was fractured to produce an acoustic emission waveform. Both the APL laser interferometer and the NBS-PZT #26 were, in turn, positioned two inches from the source. After each acoustic emission event was recorded, the probe was translated in two inch increments down the entire length of the specimen. Figures 15 and 16 show the experimental arrangement of both the APL-System and NBS-PZT #26. Each specimen was tested with the sensitivity level of the Nicolet set at ±4 volts full scale and the sample rate set at 50 nanoseconds per point for the 4096 total points. With this arrangement the total recording window was 204.8 μsec. Because the data received from the solid cylinder was exceptionally good a second test at 200 nanoseconds per point was run yielding a total recording window of 819.2 μsec.

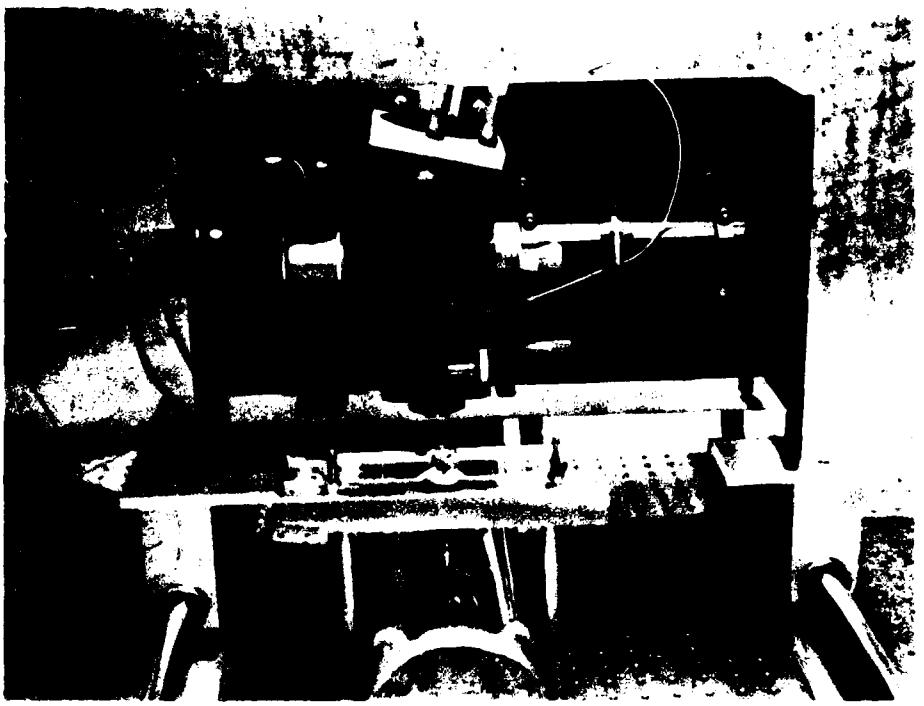

Figure 15. Experimental arrangement of the APL laser interferometer. Length between black marks on ruler is six inches.

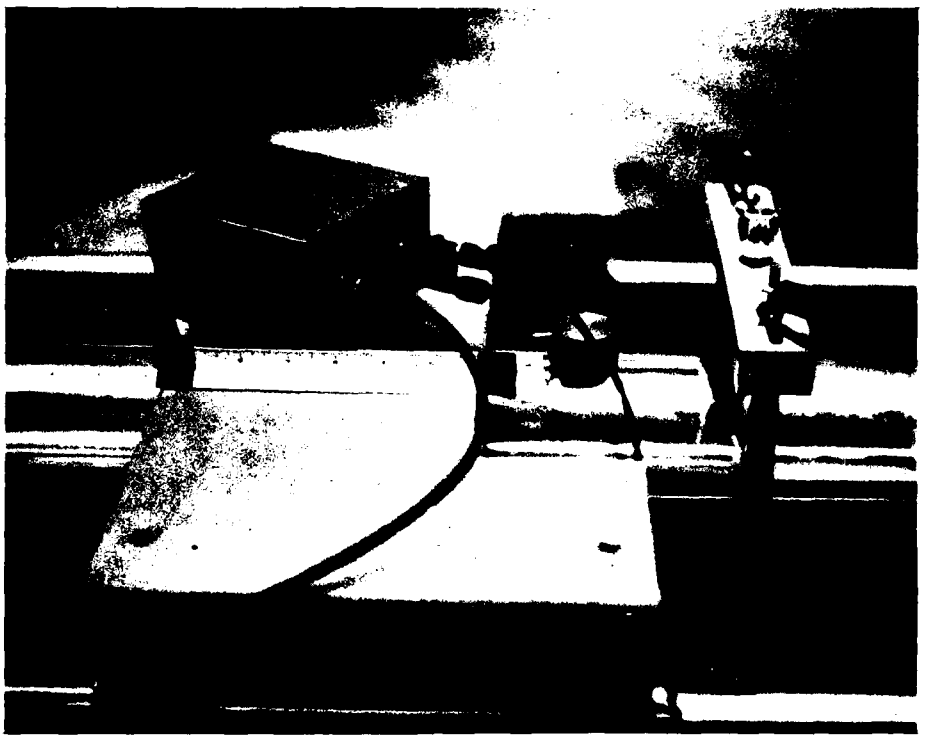

Figure 16. Experimental arrangement of the NBS-PZT conical transducer. Length between the black marks on ruler is six inches.

C. SPECIMEN CHARACTERIZATION RESULTS

1. SOLID CYLINDER

Appendix E contains the time-base waveforms for the experiments performed on all of the specimens. Figures E1-E15 show the time-base records of two inch incremental placements of NBS-PZT #26 along the length of the solid cylinder and Figs. E16-E29 show the time-base records of two inch incremental placements of the APL laser interferometer. Fig. 17 shows the waveform recorded by NBS-PZT #26 two inches from the source. The first arriving P, S, and R waves are clearly evident as well as multiple mode converted waves. At fourteen inches from the source, the first arriving waves have been modified such that the shear (S) wave is not as well defined as before, Fig. 18. Finally, at thirty inches from the source, only the first arriving Rayleigh wave can be identified, Fig. 19, mode converted waves have increased in number but identification of them is difficult.

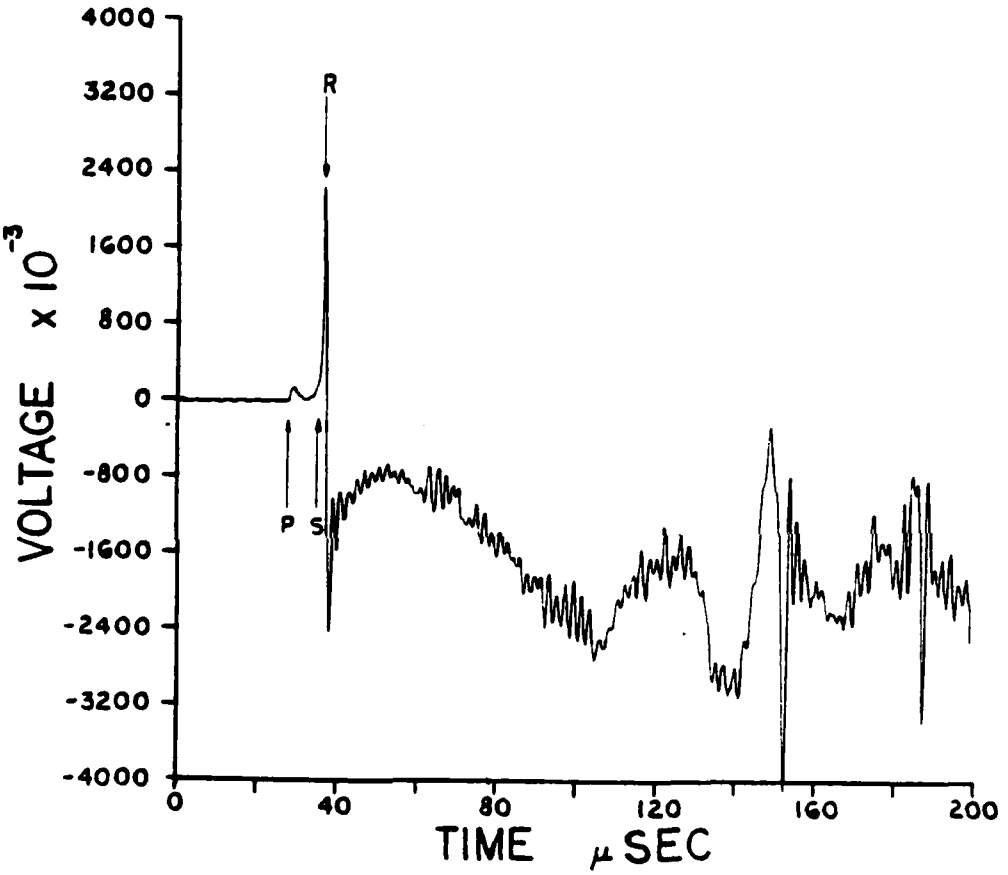

Figure 17. Time domain waveform recorded by NBS-PZT #26 two inches from the source on the solid cylindrical beam.

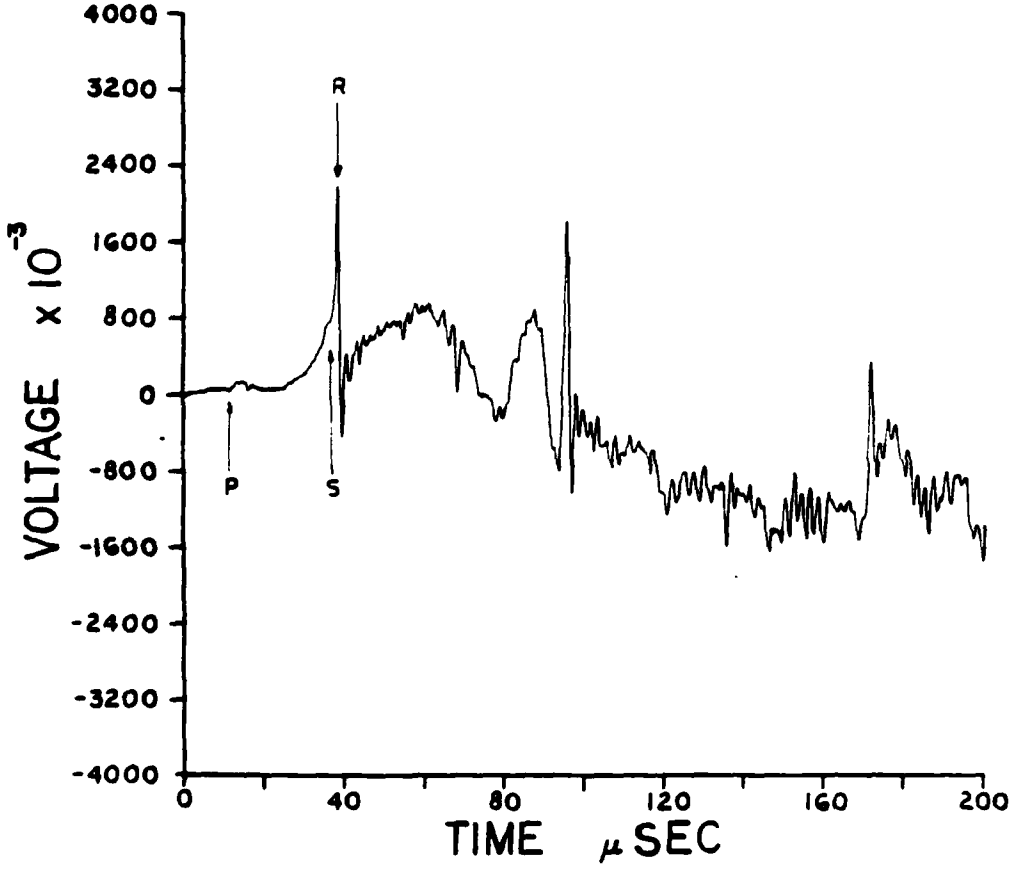

Figure 18. Time domain waveform recorded by NBS-PZT #26 fourteen inches from the source on the solid cylindrical beam.

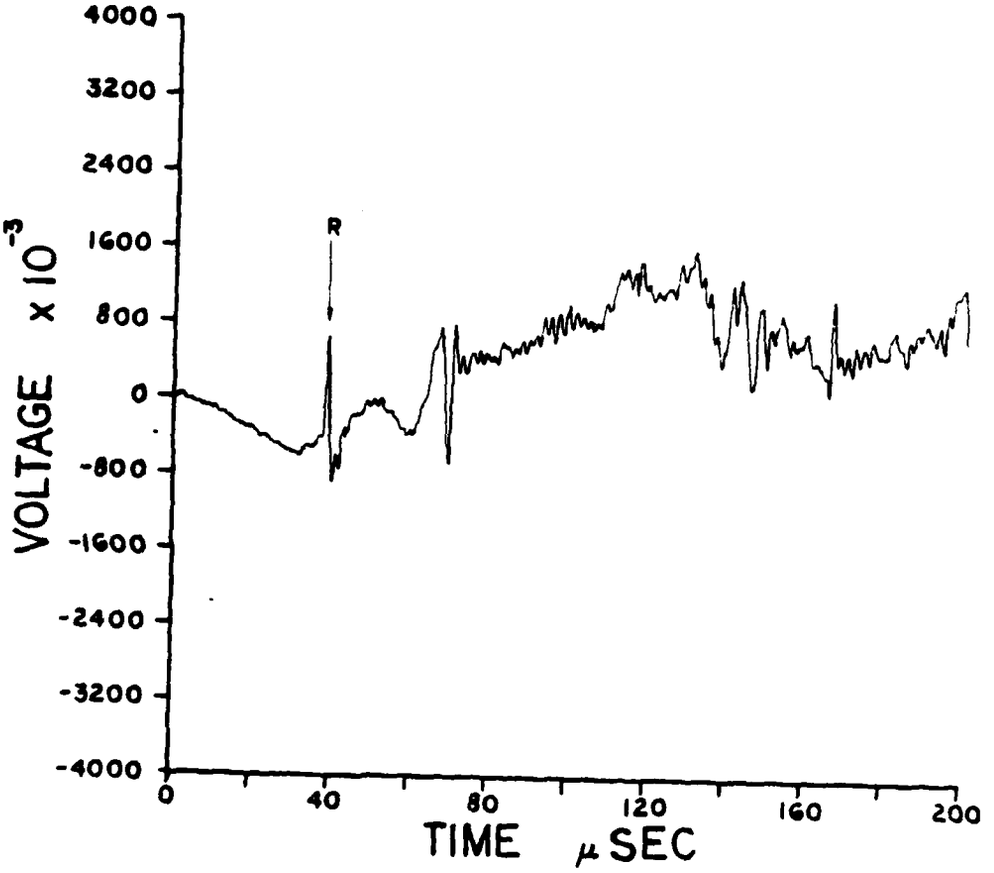

Figure 19. Time domain waveform recorded by NBS-PZT #26 thirty inches from the source on the solid cylindrical beam.

2. RECTANGULAR BAR

Figures E45-E59 reveal a markedly different structure than was observed from the cylindrical bar. The smaller dimensions as well as sharper angles have modified the waveform such that beyond the first arriving P, S and R waves, at two inches from the source, there were reflections which saturated the signal, Fig. 20. At fourteen inches from the source, mode converted waves overshadow the first arriving P and S waves significantly decreasing the amplitude of the region prior to the first arriving R wave, Fig. 21. Finally, at thirty inches from the source, no appreciable information about the source was obtained, Fig. 22; the first arriving R wave was observed but mode converted waves still cannot be identified.

3. I-BEAM

Figures E60-E67 show the corresponding waveforms for experiments conducted on the I-beam. At two inches from the source, the only identifiable features were the first arriving P and R waves, Fig. 23. Mode conversions, from reflections, have

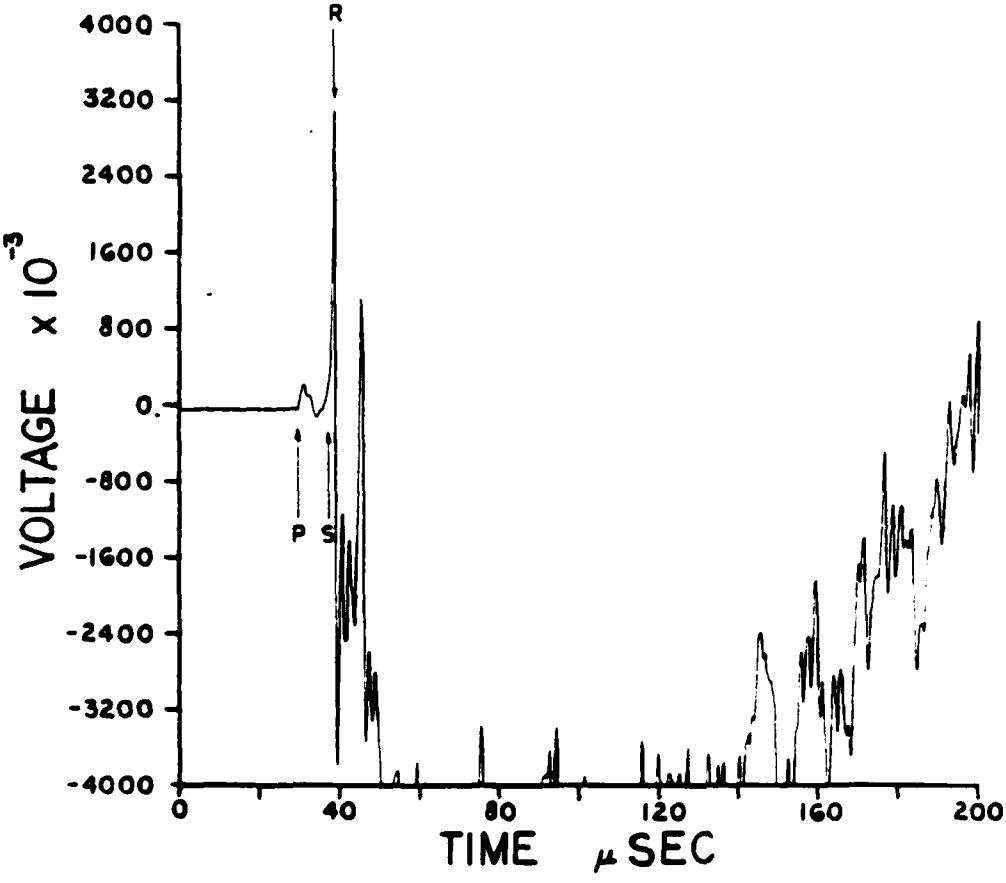

Figure 20. Time domain waveform recorded by NBS-PZT #26 two inches from the source on the rectangular beam.

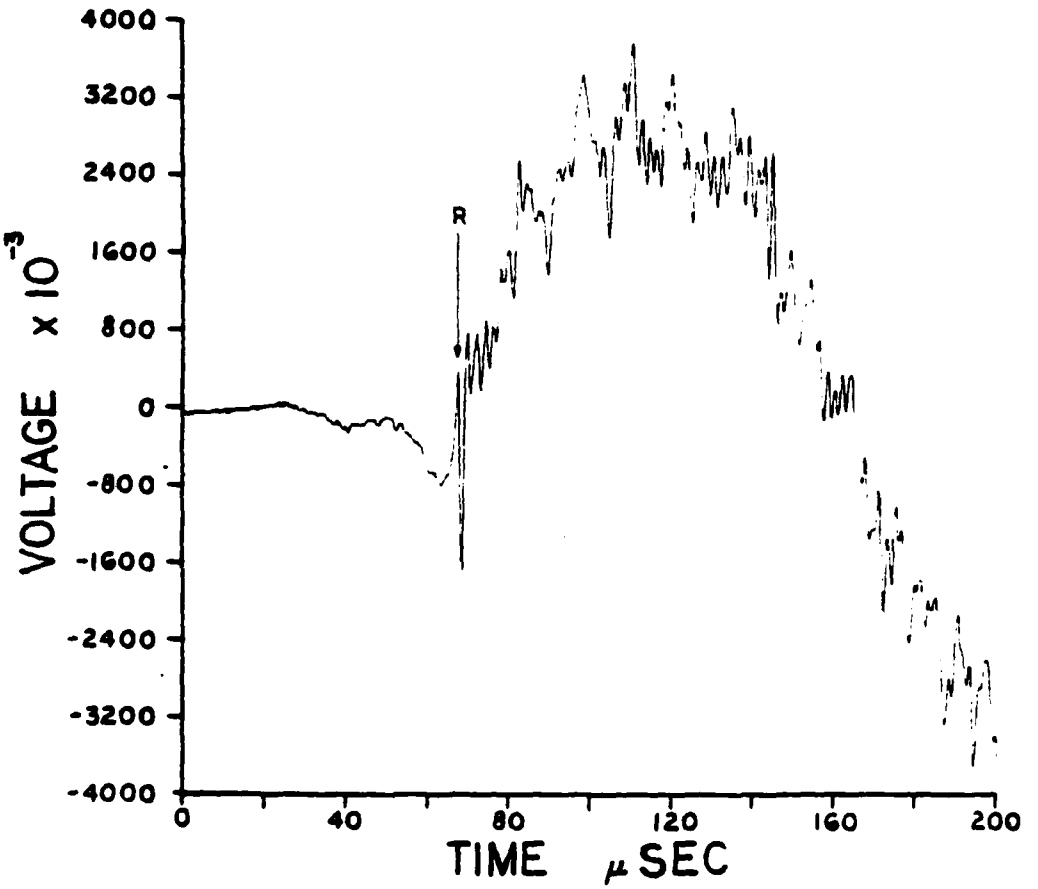

Figure 21. Time domain waveform recorded by NBS-PZT #26 fourteen inches from the source on the rectangular beam.

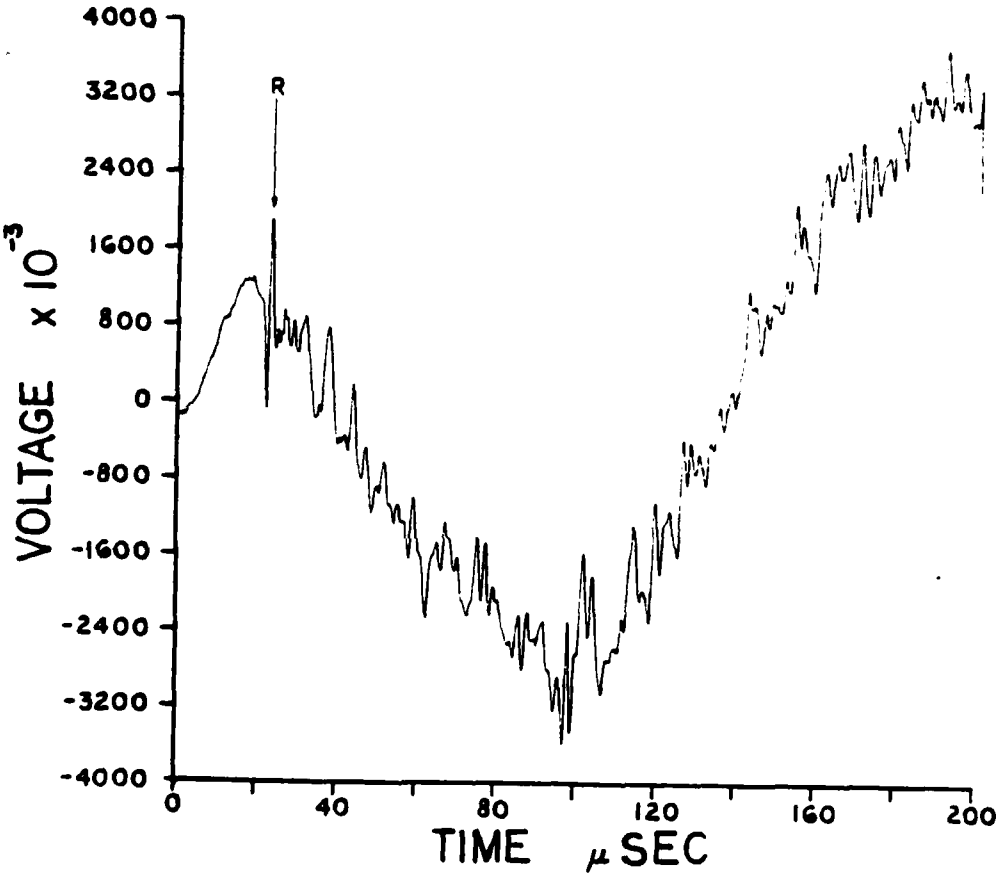

Figure 22. Time domain waveform recorded by NBS-PZT #26 thirty inches from the source on the rectangular beam.

forced large scale oscillations into the time domain. No tangible information could be discerned from the represented data. At eight inches from the source, more structure in the waveform was observed but only the first arriving Rayleigh wave could be identified, Fig. 24. Finally, at sixteen inches from the source, a large amount of structure was observed but identification of the waves, primarily due to mode converted reflections was impossible, Fig. 25.

4. PIPE

Figures E68-E75 show the corresponding waveforms recorded for experiments performed on the aluminum pipe. Observations made two inches from the source clearly show the first arriving P and R waves, Fig. 26. Again, beyond the first arriving R wave, large scale oscillations have saturated the signal. Eight inches from the source, more structure is observed in the waveform expecially in the region prior to the first arriving R wave, Fig. 27. Finally, at sixteen inches from the source, a great deal of structure is observed but identification of each mode converted is impossible, Fig. 28.

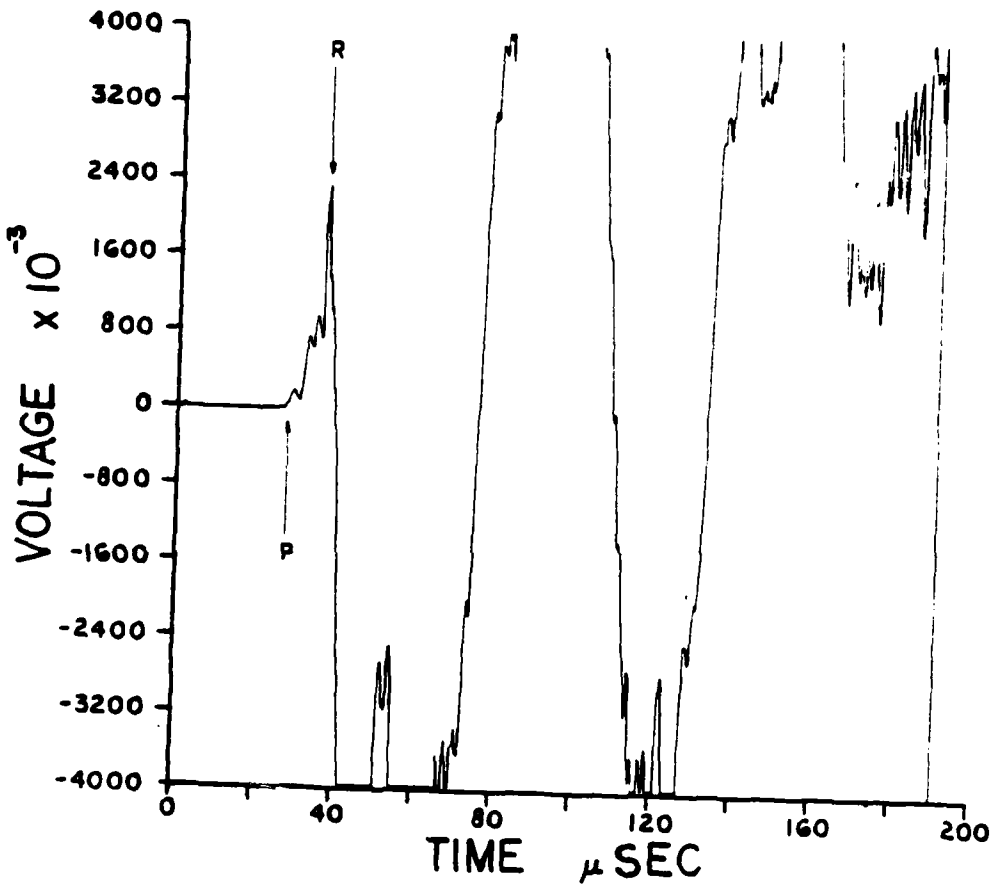

Figure 23. Time domain waveform recorded by NBS-PZT #26 two inches from the source on the I-beam.

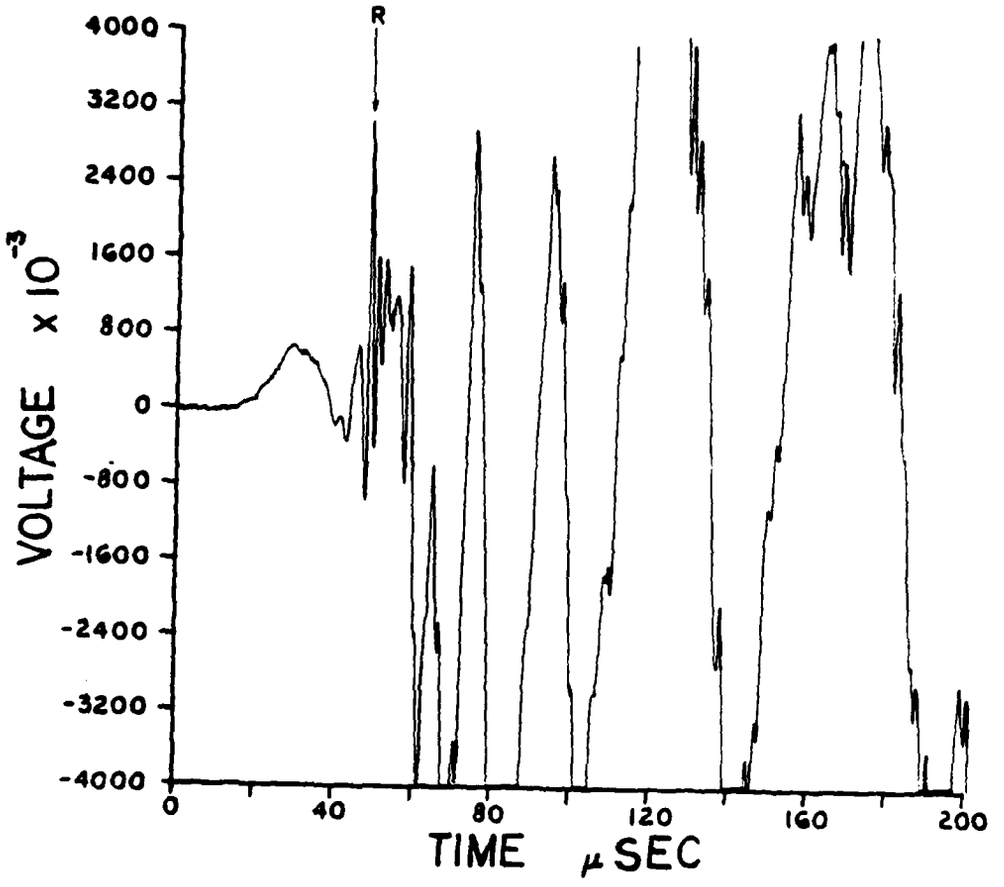

Figure 24. Time domain waveform recorded by NBS-PZT #26 eight inches from the source on the I-beam.

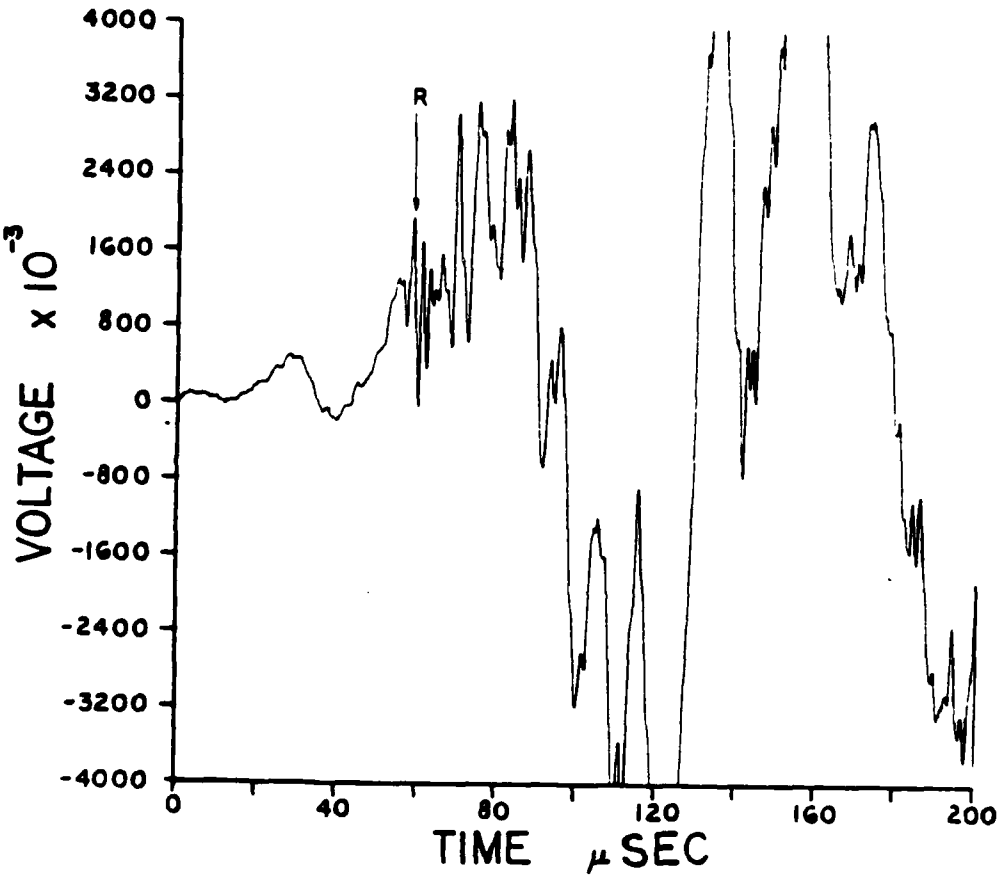

Figure 25. Time domain waveform recorded by NBS-PZT #26 sixteen inches from the source on the I-beam.

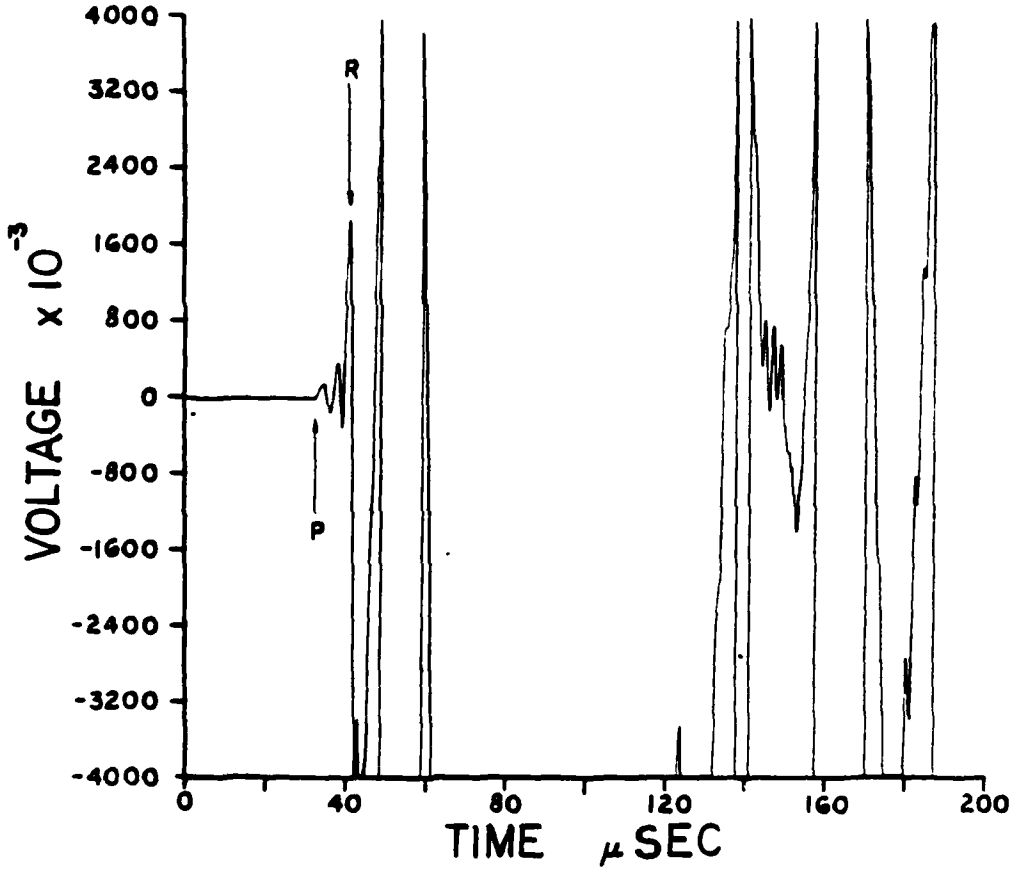

Figure 26. Time domain waveform recorded by NBS-PZT #26 two inches from the source on the pipe.

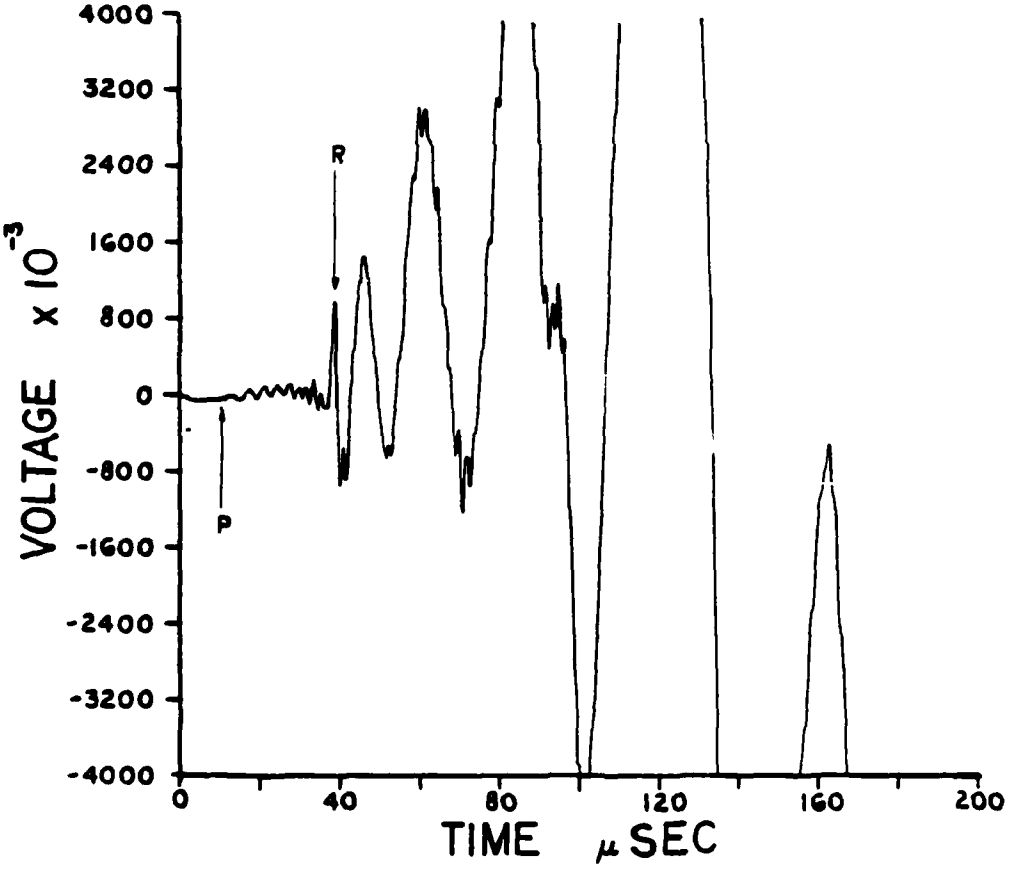

Figure 27. Time domain waveform recorded by NBS-PZT #26 eight inches from the source on the pipe.

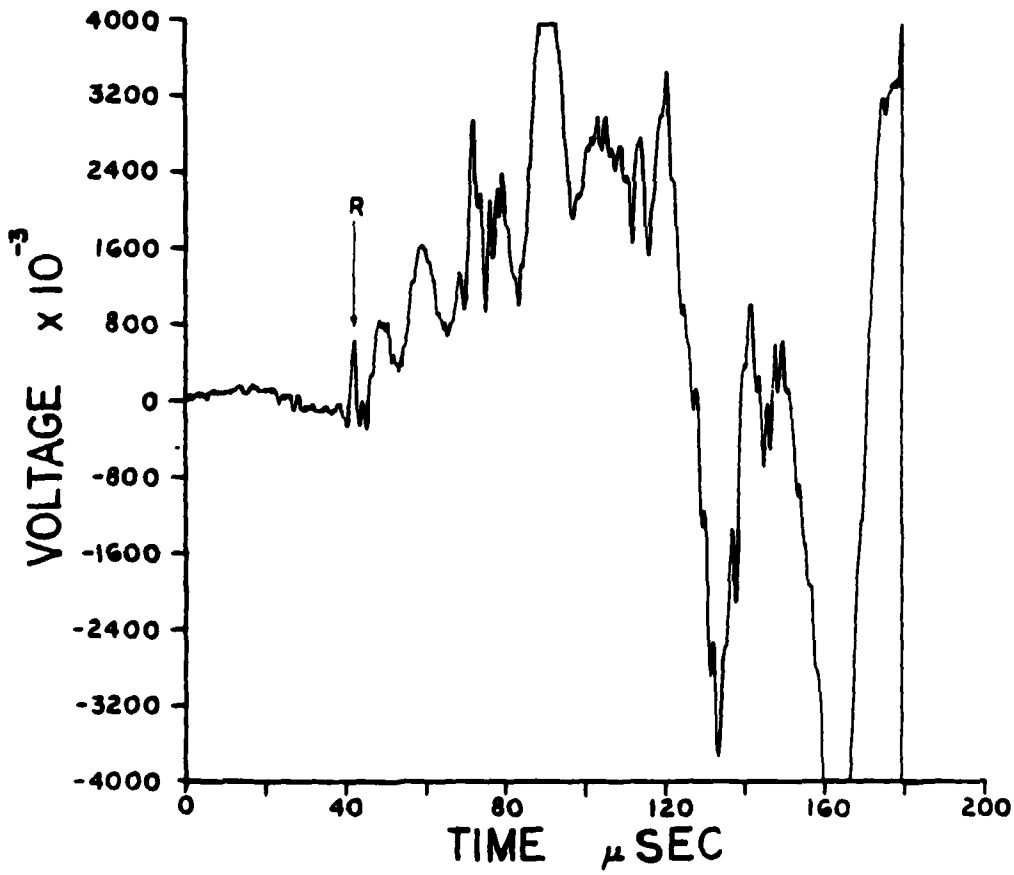

Figure 28. Time domain waveform recorded by NBS-PZT #26 sixteen inches from the source on the pipe.

From the information obtained in the time-base it was observed that the solid geometries were able to propagate the waveform over greater distances before attenuation of the signal. Bulk specimens allow the wave to travel without interference effects from reflections or mode converted waves. The open type geometries are prone to create massive interference effects due to the finite size of ribbing or webbing, walls and angles. When looking at data only in the time domain it is these geometrical effects which must be taken into account. There is also a question as to how the frequency content of a waveform is affected as a function of distance from the source.

The APL laser interferometer was employed for the specimen characterization in the frequency domain because of the broad bandwidth the system possessed. Appendix F shows the time-base data and the corresponding frequency spectra for two inch incremental translations down the length of the solid cylindrical bar. Cutoff values were chosen such that the last point of the time-base data crossed the zero reference line. For this series the relative amplitude was found by dividing the

voltage values of each frequency spectrum by 5.9035 millivolts. The normalized data for this series show the higher frequencies damping out faster as distance from the source is increased. The relative amplitude data corroborates this finding but also indicates that the low frequency content of the waveform increases as distance from the source is increased. This effect is caused by an increase in long wavelength oscillations through the bulk of the specimen.

IV. DISCUSSION

Theories for determining the arrival time of wavefronts, at a point, in geometries other than a sphere or a plate have not been sufficiently constructed. Without theoretical models, with which to compare experimental results, analysis of complex geometries is virtually impossible. Rough calculations can be made to estimate when certain waves should arrive, but complex geometries produce such a great number of mode coverted reflections that detailed analysis of a waveform is impossible. Because of the complexity in analysis of the entire waveform, it was decided to specifically look for the first arriving P, S, and R waves. By close observation of these waves any modifications in their features could be noted. Two procedures were followed for the analysis; analysis in the time domain and analysis in the frequency domain.

Results obtained from the conventional acoustic emission transducers indicated several discrepancies with established practice. In the time domain the conventional transducers were extremely inefficient when recording highly energetic glass capillary fractures. The conventional transducers were able

to indicate an event occurred but they revealed little of the characteristic surface wave structure which was used as the basis for the probe comparison. Observations in the time domain revealed the overall superiority of the NBS-PZT and the APL-System in sensitivity as well as definition of characteristic features. When observations were made in the frequency domain it was noticed that because the conventional piezoelectric transducers were damped to increase their frequency response there was a marked decrease in their sensitivity. Frequency spectra obtained from the laser interferometer showed a greater frequency content than any of the other probes tested.

With the information obtained from the probe characterization it was decided to characterize the geometrical specimens with both the APL laser interferometer and NBS-PZT #26. The laser was used because it discerned a broader frequency range than the conical transducer. For time-base information NBS-PZT #26 was chosen because it was more sensitive to transient wave surface displacements. Time domain waveforms obtained by NBS-PZT #26, on the four specimens, revealed markedly different

structures. For the open type geometries, the closer the probe was to the source the worse the information was beyond the first arriving waves. This was due to massive internal reflections, in the thin walls of the specimens saturating the recording equipment. When the probe was moved further from the source the first arriving waves decayed but the latter waves revealed a slight increase in structure. On the solid type geometries the time domain records revealed recognizable features as far away as thirty inches from the source. The closer the probe was to the source the larger the signal amplitude, likewise, the further the probe from the source the smaller the signal amplitude.

From these time domain observations it was noted that open geometries revealed no easily identifiable features other than the first arriving P and R waves. Due to the sharp corners and the intricacy of structure it was impossible to determine where the waves originated. Mode converted reflections created a vast number of waverforms which, without previous theoretical modeling, could not be identified. Observations made on the solid geometries were more promising. The rectangular beam, with its sharp corners, produced a large number of mode

converted reflections but it was still possible to observe the first arriving R wave thirty inches from the source. It was the solid cylindrical beam that produced the most useable data. Without sharp edges to mode convert waveforms it was possible to identify the first arriving P, S and R waves as far away as eight inches from the source. Because massive reflections did not saturate the captured waveform, it was possible to record time domain information with the laser interferometer, window it and run the FFT. The frequency information obtained from the translation of the laser probe down the lengths of the solid cylindrical beam revealed two interesting features:

1. The higher frequencies dropped out as the distance from the source was increased, and
2. The lower frequencies increased in amplitude as the distance from the source was increased.

Because conventional probes are most sensitive in the lower frequency range they would tend to pick up large amplitude low frequency information. When the frequency spectra was generated, researchers might think the event occurred close to the probe; this work shows that their inference would be incorrect.

The present work leads one to believe that structural information for the characterization of a specimen should be performed in the time domain. Frequency information cannot always be utilized because of the fundamental flaws associated with performing the Fourier transform. The greatest misconception associated with the generation of the Fourier transform is where the data should be windowed. If the windowing is not consistent or if the waveform does not begin and end at zero one will find the generated frequency spectra to be in error.

V. CONCLUSION

This work has dealt with the influence that a specimen's structural geometry had on a simulated acoustic emission signal. At the onset of this investigation nine different probes were compared in both the time and frequency domains. It was determined that the NBS-PZT conical transducer recorded the most information with the least amount of waveform modification in the time domain. It was also found that the APL laser interferometer was able to distinguish a broader range of frequencies when the FFT was performed. Because of these findings it was determined that specimen characterization must be performed utilizing both the NBS-PZT transducer and the APL laser interferometer.

Identification of every wave in systems which have not been theoretically solved is a near impossible task. For open geometries, such as the I-beam and pipe, mode converted waves produced massive reflections which saturated the electronic components of the NBS-PZT support equipment as well as the amplifiers in the APL laser interferometer. The waveforms recorded for these specimens revealed no useful information; one can only say that open

type geometries are the most difficult to characterize. For the solid geometries, such as the rectangular beam and the cylindrical beam, probes could be placed thirty inches away from the source and still record a characteristic R wave; this is compared to the sixteen inch distance acquired on the open geometries. Large scale reflections were not prevalent on the cylindrical beam waveforms due to the rounded shape of the specimens, yet there were waveform features which indicated bulk reflections took place.

The combination of optical and piezoelectric probes for the task of acoustic emission source and specimen characterization has provided an indicator which will point future research in more productive directions. It is the convenience of the NBS-PZT transducer, however, which makes it the most attractive probe to use for acoustic emission work. Yet, with the increase in technological breakthroughs a more efficient system will undoubtedly come along; high-tech developments in stable laser interferometric systems could conceivably make the optical probe the most powerful tool for acoustic emission research.

APPENDIX A

DESCRIPTION OF LASER INTERFEROMETER

The APL-System is a modified Michelson interferometer with the output beam originating from a 200 milliwatt polarized Helium-Neon laser (Tropel model 200, λ = 6328 Å). Figures A1 and A2 show schematic representations of the APL-System. Legs on the laser rack are fitted into depressions drilled into a translation carriage. When postioned in these alignment holes, the specimen beam from the laser remained in a fixed area on the specimen surface. The laser is mounted on the back side of the support rack and its output beam is steered to the front of the support by two beam position mirrors, (dielectrically coated for a reflectivity of 99.5% at λ = 6328 Å). If the laser light is linearly polarized, with its components normal to each other, any reflections from mirrors will not alter the polarization components.

Linearly polarized light can be split into two components $\vec{E}_x$ and $\vec{E}_y$; where $\vec{E}_x$ will be the P-polarization component, with its electric vector perpendicular to the X-axis, $\perp_o$, and $\vec{E}_y$ will be the S-polarization component, with its electric vector parallel with the X-axis, $||_o$, Fig. A3.

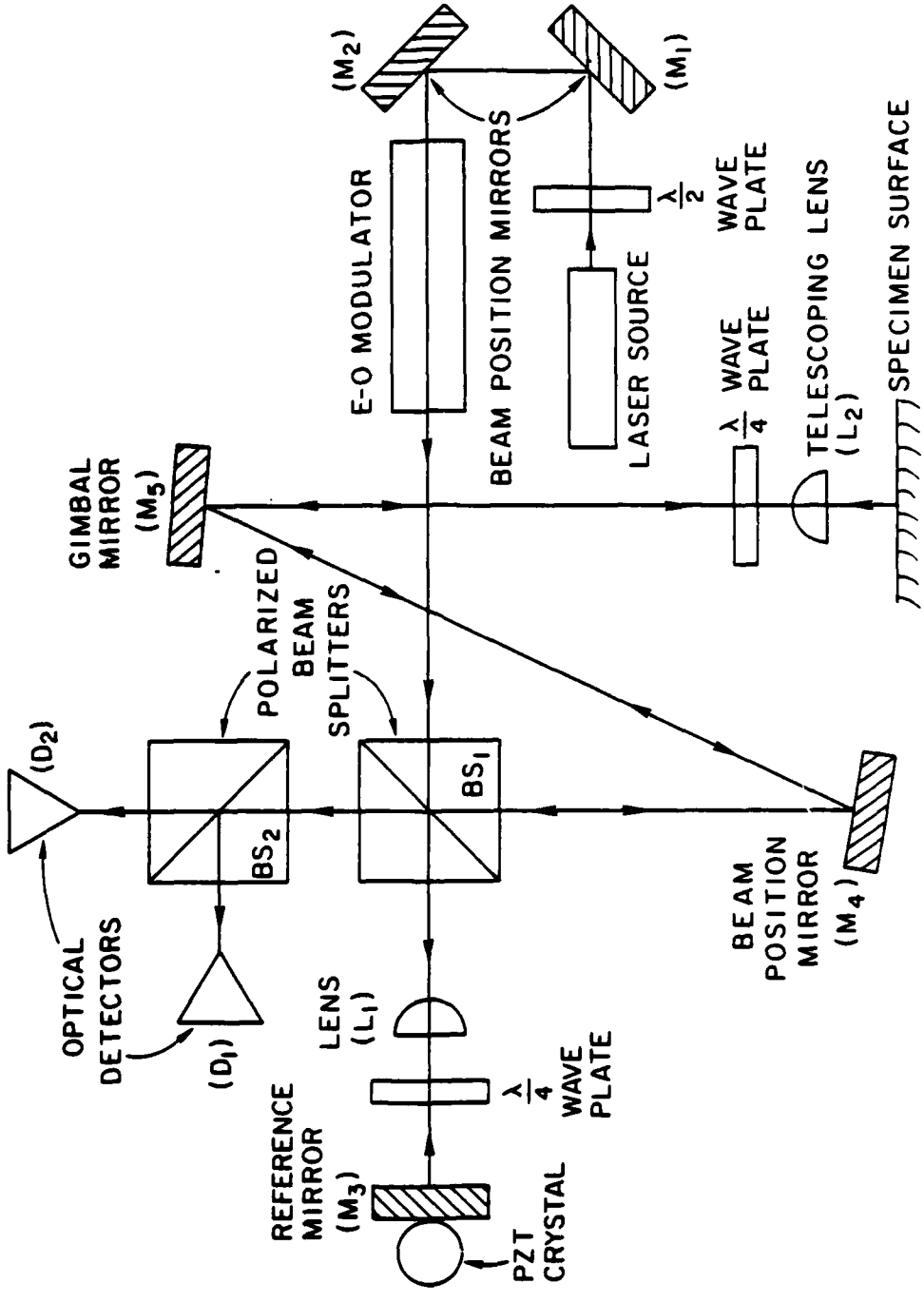

Figure A1. Schematic representation of APL laser interferometer.

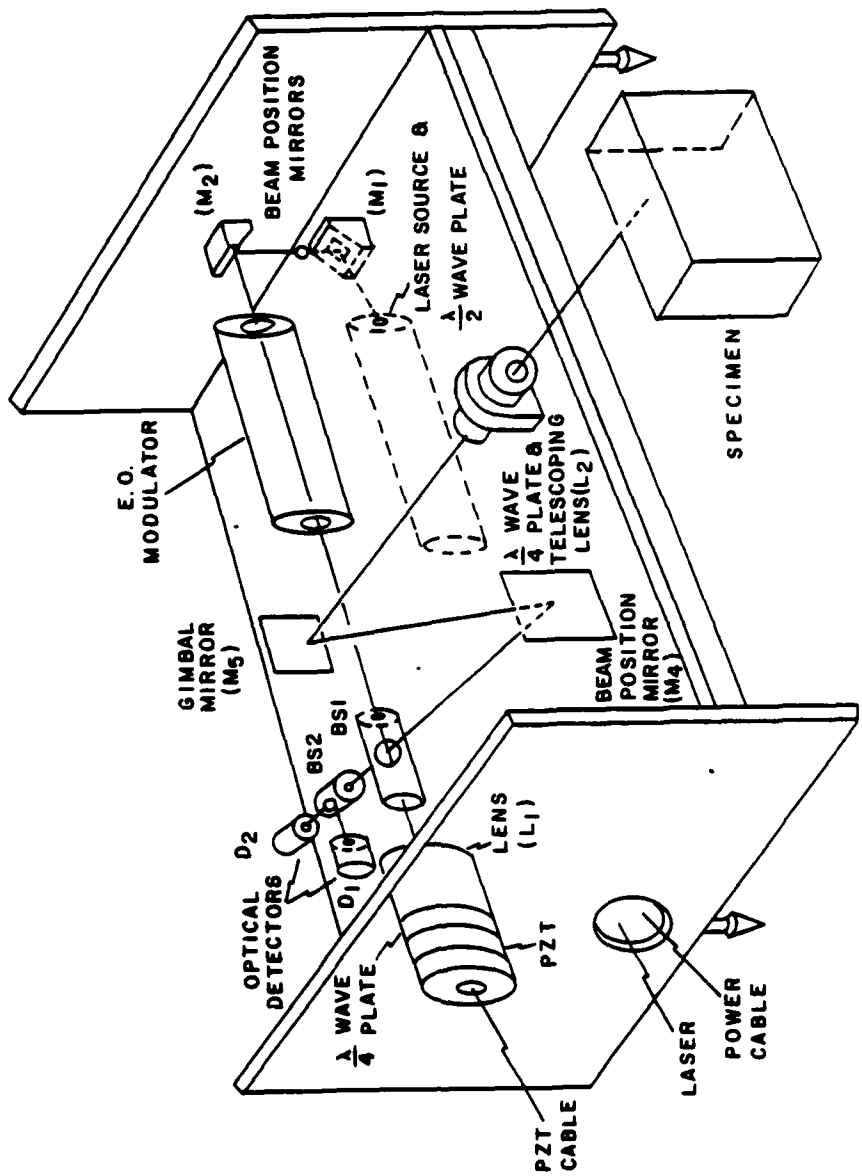

Figure A2. Block diagram of AFL laser interferometer.

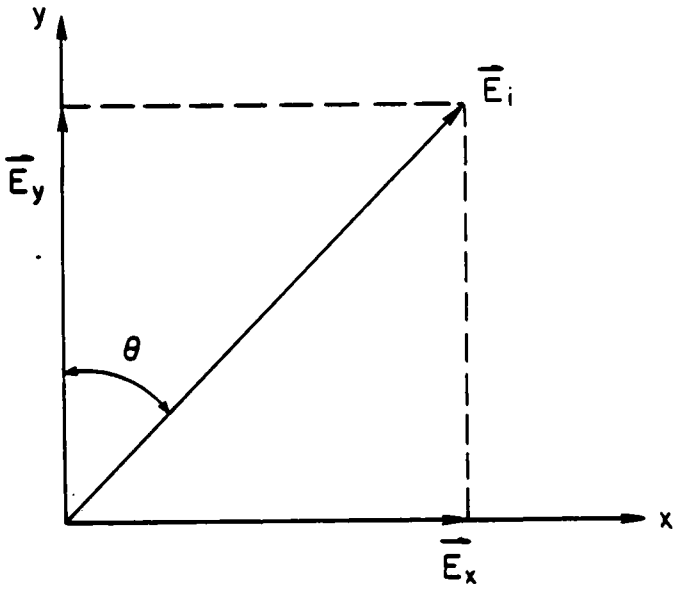

$$\vec{E}_x = E_i \sin\theta \cos(\omega t - k_o Z)$$

$$\vec{E}_y = E_i \cos\theta \cos(\omega t - k Z + \phi)$$

Figure A3. Component representation of linearly polarized light.

The half-wave plate is orientated to allow maximum transmission of the linearly polarized laser light while prohibiting stray laser light from entering the laser cavity. An explanation of polarization is given at the end of this appendix.

Once the laser light is brought in front of the support rack it passes through an electro-optic (E-O) modulator. The E-O modulator is a modulated wave plate which acts as a half-wave plate when biased at 125 VDC. This modulation allows the E-O modulator to stabilize the signal path by introducing a phase shift corresponding to the extraneous vibrations around the system. The signal to the E-O modulator comes from a differential amplifier in the electronics system; the electronics package will be explained later.

When the beam emerges from the E-O modulator it enters a polarized beam splitter (BS_1) which is oriented such that the transmitted light is almost entirely plane polarized in the P-direction ($\perp_o$), while the reflected beam is almost entirely plane polarized in the S-direction ($\|_o$). The reflected component travels to the specimen surface via two beam position mirrors, a quarter-wave plate, and a telescoping lens. Since the quarter-wave plate

elliptically polarizes linearly polarized light, and because the $||_o$ component is linearly polarized at a 45° angle, the light emerges from the quarter-wave plate circularly polarized, i.e. the $||_o$ component is split into two components which are equal by virtue of circular polarity. The light passes through a telescoping lens which allows the beam to be focused over a four inch range. After passing through the lens, the beam is reflected back from the specimen surface along its original path. When circularly polarized light passes through a quarter-wave plate it becomes linearly polarized, therefore, when the reflected beam passes through the quarter-wave plate its phase is shifted 90° with respect to the light which initially passed through. The phase shift on the light, changing the $||_o$ component to $\perp_1$ is very important because the light must return through the polarized beam splitter. If the change did not occur then the light would be reflected back into the laser. Once through the quarter-wave plate, the light (now $\perp_1$) will be transmitted through BS_1 and BS_2 to optical detector D_2.

A similar operation occurs on the $\perp_o$ component of light as it is transmitted through BS_1. The beam passes through a fixed lens and a quarter-wave

plate. Circulary polarized, the beam travels to a dielectric coated reference mirror which is mounted to a Burleigh PZT-Pusher, model PZ-40. The PZT-Pusher is a miniature electro-mechanical actuator used to make ultra-high resolution positioning adjustments remotely and continuously. PZ-40 provides a 15 μM/1000V motion and has a frequency response of 5kHz. The PZT-Pusher acts to eliminate low frequency noise, its operation will be discusses in a later section. The mirror is driven by the PZT-Pusher at a rate determined by the output of the optical detectors. After the beam is reflected from the reference mirror it passes through the quarter-wave plate in the opposite direction. The light undergoes a phase shift whereby the $\perp_o$ component becomes $\|_1$. This assures that the majority of the light will be reflected, as it passes through BS_1 and BS_2, into optical detector D_1. This is the second leg of the design which completes the interferometric path. Photoconductive diodes (EG & G Inc. model SGD160) were used as the optical detectors in the APL-System. The active area of each diode was approximately 4 mm in diameter and the bandwidth was 45 MHz at an RC of 50Ω; sensor resistance 300Ω, capacitance 9pf. Outputs from these

detectors were the source for the feedback loops, Fig. A4.

There are two outputs which come from each of the two optical detectors. The first output set; i.e. one output from each detector, was fed into a high frequency differential video amplifier (Fairchild μA733). A differential amplifier is an amplifier whose output is a function of the difference between two input voltages. Ideally, the output of a differential amplifier is not responsive to common mode voltages, temperature variations, and supply voltage fluctuations. A common mode voltage is the average of the two input voltages. A differential video amplifier was used because of its variable gain and large bandwidth. For this work the gain was set at the lowest value of 10x with a corresponding bandwidth of 120 MHz.

Outputs from the two optical detectors were in phase and equal in voltage. When such a signal is fed into a differential amplifier the output is zero as is given by Eqn. A1:

$$V = K(V_2 - V_1) \qquad \text{(A1)}$$

Where V_1 and V_2 are the input voltages and K is a proportionality constant equivalent to the gain of

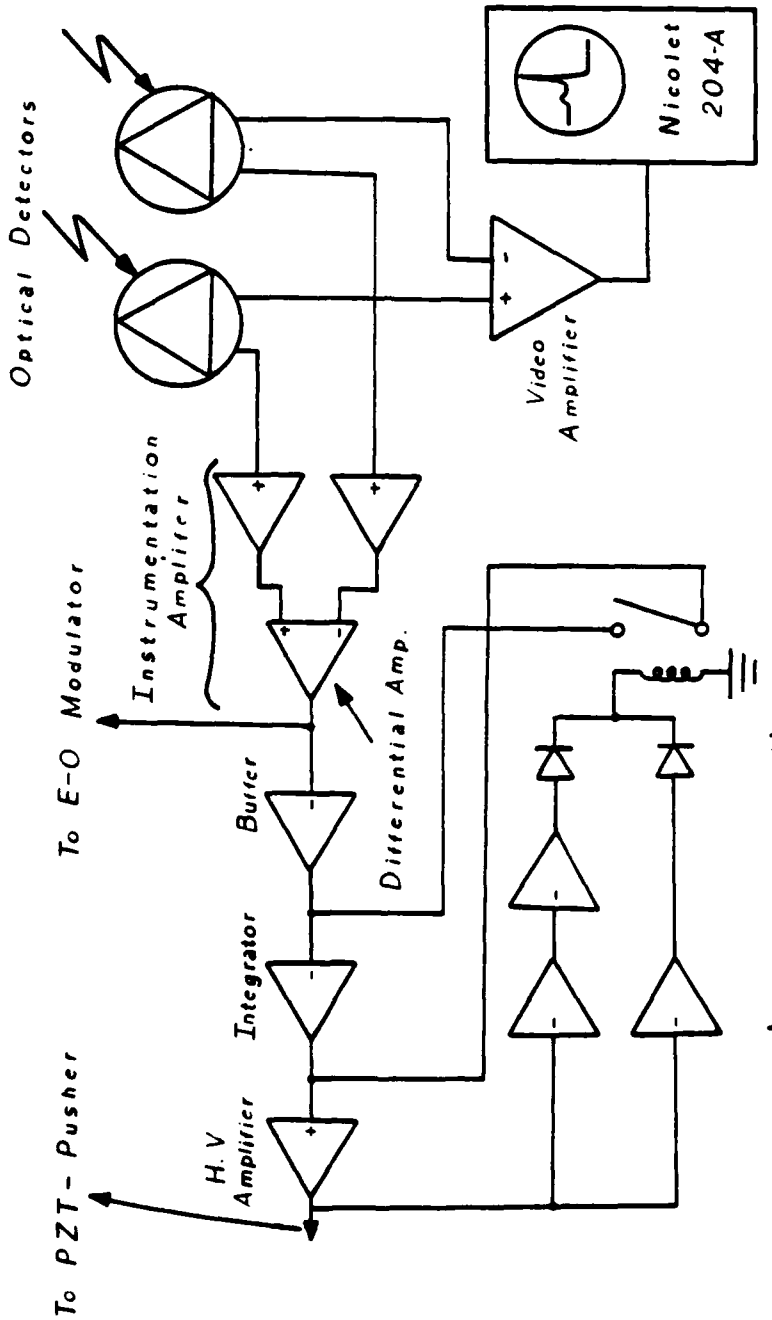

Figure A4. Block diagram of electronics package for APL laser interferometer.

the amplifier. When the APL-System is in equilibrium, the output of the differential video amplifier remains at a zero value. When a change occurs in one of the optical path lengths, proportionally larger than the background noise, the difference in the light intensity will cause a variation at the optical detectors. Output from the optical detectors will no longer be equivalent, therefore the differential video amplifier will no longer output zero but will yield a voltage value corresponding to the event which initiated the change. This information was recorded on a Nicolet Explorer Digital Oscilloscope for future analysis.

A second set of outputs from the optical detectors, also in phase and equal voltage, were fed into an instrumentation amplifier. (NOTE: all amplifiers in this description are Fairchild μA3140's except for the high voltage amplifier which is a Burr-Brown 3584 JM). Hereafter, the instrumentation amplifier will be referred to as the differential amplifier. This is the beginning of the two feedback stabilization loops which are located in the electronics package of the laser system, Fig. A4.

The stabilization circuit involves two active loops which control the difference in signal beam

and reference beam path lengths. The first loop operates using the PZT-Pusher as a low frequency (F_{max} = 6kHz) filter, effectively eliminating any associated low frequency interference. The second loop operates using the E-O modulator as a high frequency (F_{max} = 100kHz) filter, effectively eliminating any associated high frequency interference. The control signal for both loops comes from the differential amplifier. The following description traces the control of the stabilization circuit loops, again refer to Fig. A4.

Output from the differential amplifier directly controls the second loop of the stabilization circuit, the E-O modulator. The output of the differential amplifier is also fed into a buffer amplifier which acts as an impedance match between the differential amplifier and an integrator amplifier. The integrator amplifier tells a high voltage amplifier at what voltage the PZT-Pusher is to be driven. When the high voltage amplifier reaches approximately 140 volts, a relay is reset which results in the integrator output going to zero. When the integrator is zero the high voltage amplifier output is zero thus the PZT-Pusher is reset to its starting point. The stabilization of the laser

interferometer is complete, when these two loops are active, and associated frequencies, which would interfere with the stability of the APL-System, are effectively eliminated.

Proper alignment of the laser interferometer is achieved in a series of beam positioning steps which result in a bullseye structure fringe pattern. The bullseye pattern consists of either a bright or dark central fringe surrounded by alternating bright and dark fringes. Adjustments are initially made by focusing the specimen beam spot with the telescoping lens to bring it near the reference beam spot. Once the specimen beam is properly focused it is necessary to bring the two light beams into coincidence, this is achieved by adjustments made to the gimbal mirror M5, Fig. A1. The gimbal mirror allows the specimen beam to be moved in both horizontal and vertical planes.

To calibrate the APL-System, a 6kHz sine wave is generated by a function generator in the electronics package. The voltage output of the oscillator is fed into the high voltage amplifier, and by measuring the output voltage (0.3 - 0.5 volts) and knowing the calibration of the PZT-Pusher (15 μM/1000V), it is possible to calculate a voltage/displacement

relation. For example:

$$P \times V = D \qquad (A2)$$

where P is the PZT-Pusher calibration, V_o is the oscillator voltage output and D is the displacement of the PZT-Pusher. By monitoring the 6kHz sine wave it is possible to maximize the signal via adjustments made to the gimbal mirror and telescoping lens. When a maximum signal is obtained for the 6kHz sine wave, V_o is measured from the oscillator output. If the peak-to-peak voltage of the 6kHz sine wave is, for example, 0.2 volts and V_o is measured to be 0.33 volts, then Eqn. A2 yields:

$$\frac{15\ M}{1000V} \times 0.33V = 50\ \mathring{A}$$

Therefore, a 200 millivolt peak-to-peak sine wave corresponds to a 50 Å displacement of the PZT-Pusher and also a 50 Å displacement in the reference mirror.

POLARIZATION OF LIGHT

Let a vibration be taking place along the X-Y axes with a phase difference of ϕ between them, Fig. A5. Assume $X = a \sin(\omega t)$, and $Y = b \sin(\omega t+\phi)$. By using the trigonometric identity:

$$\text{Sin}(\alpha+\beta) = \text{Sin}\ \alpha\ \ \text{Cos}\ \beta\ \ + \text{Cos}\ \alpha\ \ \text{Sin}\ \beta$$

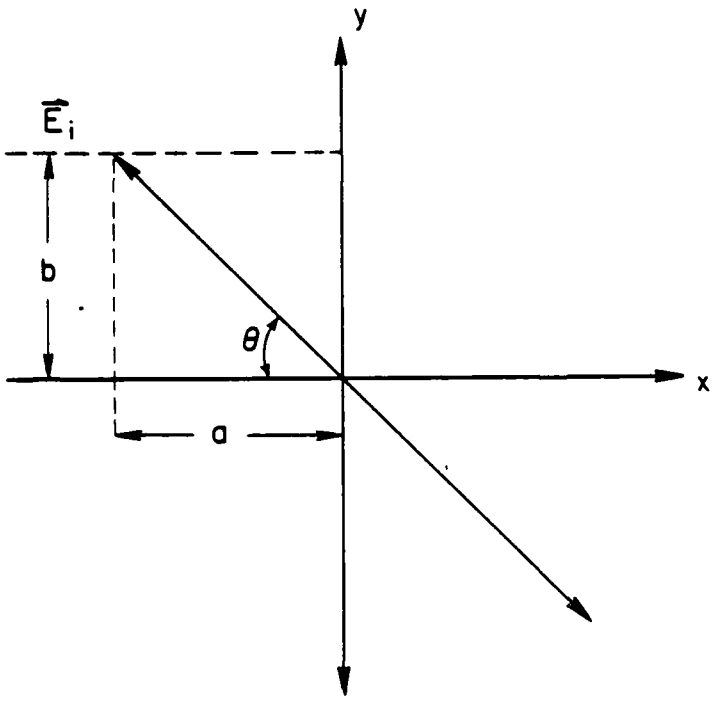

$$x = a \text{ Sin } (\omega t)$$

$$y = b \text{ Sin } (\omega t + \phi)$$

Figure A5. Component representation of the polarization of light.

one can write Eqn. A3 as follows:

$$y/b = \text{Sin}(\omega t)\ \text{Cos}\ \phi + \text{Cos}(\omega t)\ \text{Sin}\ \phi \qquad \text{(A3)}$$

One can now substitute x/a for Sin(ωt) and using the trigonometric identity $\text{Sin}^2\ x + \text{Cos}^2\ x = 1$ one can write; $\text{Cos}\ x = \sqrt{1-\text{Sin}^2 x}$. Letting x=ωt one can write:

$$\text{Cos}(\omega t) = \sqrt{1-\text{Sin}^2(\omega t)} = \sqrt{1-x^2/a^2} \qquad \text{(A4)}$$

Substituting Egn. A4 into Eqn. A3 one sees:

$$y/b = x/a\ \text{Cos}\ \phi + \sqrt{1-x^2/a^2}\ \text{Sin}\ \phi \qquad \text{(A5)}$$

Upon rearrangement one sees:

$$y/b - x/a\ \text{Cos}\ \phi = \sqrt{1-x^2/a^2}\ \text{Sin}\ \phi \qquad \text{(A6)}$$

Squaring and grouping terms yields:

$$y^2/b^2 + x^2/a^2\ \text{Cos}^2\ \phi - \frac{2xy}{ab}\ \text{Cos}\ \phi = (1-x^2/a^2)\ \text{Sin}^2\ \phi \qquad \text{(A7)}$$

$$x^2/a^2\ (\text{Cos}^2\phi + \text{Sin}^2\phi) + y^2/b^2 - \frac{2xy}{ab}\ \text{Cos}\ \phi = \text{Sin}^2\ \phi \qquad \text{(A8)}$$

Because $\text{Cos}^2\ \phi + \text{Sin}^2\phi = 1$, Eqn. A8 becomes;

$$x^2/a^2 + y^2/b^2 - \frac{2xy}{ab}\ \text{Cos}\ \phi = \text{Sin}^2\ \phi \qquad \text{(A9)}$$

Equation A9 is the general equation of an ellipse, where the major and minor axes do not coincide with the X and Y axes. Thus, the particle always has X

and Y coordinates such that the point they define lies on an ellipse; the particle then follows an elliptical path.

When $\phi = \pi/2, 3\pi/2, 5\pi/2, \ldots$, the equation of the path, Eqn. A9, becomes:

$$(x^2/a^2) + (y^2/b^2) = 1 \qquad \text{(A10)}$$

which is an ellipse with the major and minor axes coincident with the coordinate axes.

When $\phi = \pi, 2\pi, 3\pi, \ldots$, the equation of the path, Eqn. A9 becomes:

$$(x^2/a^2) + (y^2/b^2) + \left(\frac{2xy}{ab}\right) = 0 \qquad \text{(A11)}$$

or

$$(x/a + y/b)^2 = 0 \qquad \text{(A12)}$$

Equation A12 is the equation of two coincident straight lines $x/a = -y/b$, inclined to the negative X-axis at an angle:

$$\theta = \text{Tan}^{-1}\ (b/a). \qquad \text{(A13)}$$

APPENDIX B

PROBE CHARACTERIZATION WAVEFORMS

The following figures were generated from each of the nine probes placed two inches from the source on a flat face of the Aluminum right circular cylinder. Figures B1-B10 were recorded at ±2 volts full scale at a rate of 50 nanoseconds per point.

Fig. B1 Calibration sine wave for APL laser, peak-to-peak voltage corresponds to 50 Å displacement.

Fig. B2 APL laser interferometer

Fig. B3 NBS-PZT #26 conical transducer

Fig. B4 NBS-PZT #36 conical transducer

Fig. B5 Panametrics AE-0.1-1632 coventional transducer

Fig. B6 Panametrics V3032 0.5MHz/0.5 in. conventional transducer

Fig. B7 Panametrics V3031 1.0MHz/0.5 in. conventional transducer

Fig. B8 Dunegan/Endevco S9201 AC42 conventional transducer

Fig. B9 Aerotech Gamma D12618 1.0MHz/0.5 in. conventional transducer

Fig. B10 Aerotech Gamma C12634 1.00MHz/1.0 in. conventional transducer

The following figures were recorded at ±400 millivolts full scale at a recording speed of 50 nanoseconds per point.

Fig. B11 Panametrics 0.5MHz/0.5 in. conventional transducer

Fig. B12 Panametrics 1.0MHz/0.5 in. conventional transducer

Fig. B13 Dunegan/Endevco S9201 AC42 conventional transducer

Fig. B14 Aerotech Gamma D12618 1.0MHz/0.5 in. conventional transducer

Fig. B15 Aerotech Gamma C12634 1.00MHz/1.0 in. conventional transducer

The following figures were recorded at ±100 millivolts full scale at a recording speed of 50 nanoseconds per point.

Fig. B16 Aerotech Gamma D12618 1.0MHz/0.5 in. conventional transducer

Fig. B17 Aerotech Gamma C12634 1.00MHz/1.0 in. conventional transducer

Fig. B18 Fig. B16 expanded 8x

Fig. B19 Fig. B17 expanded 8x

B1

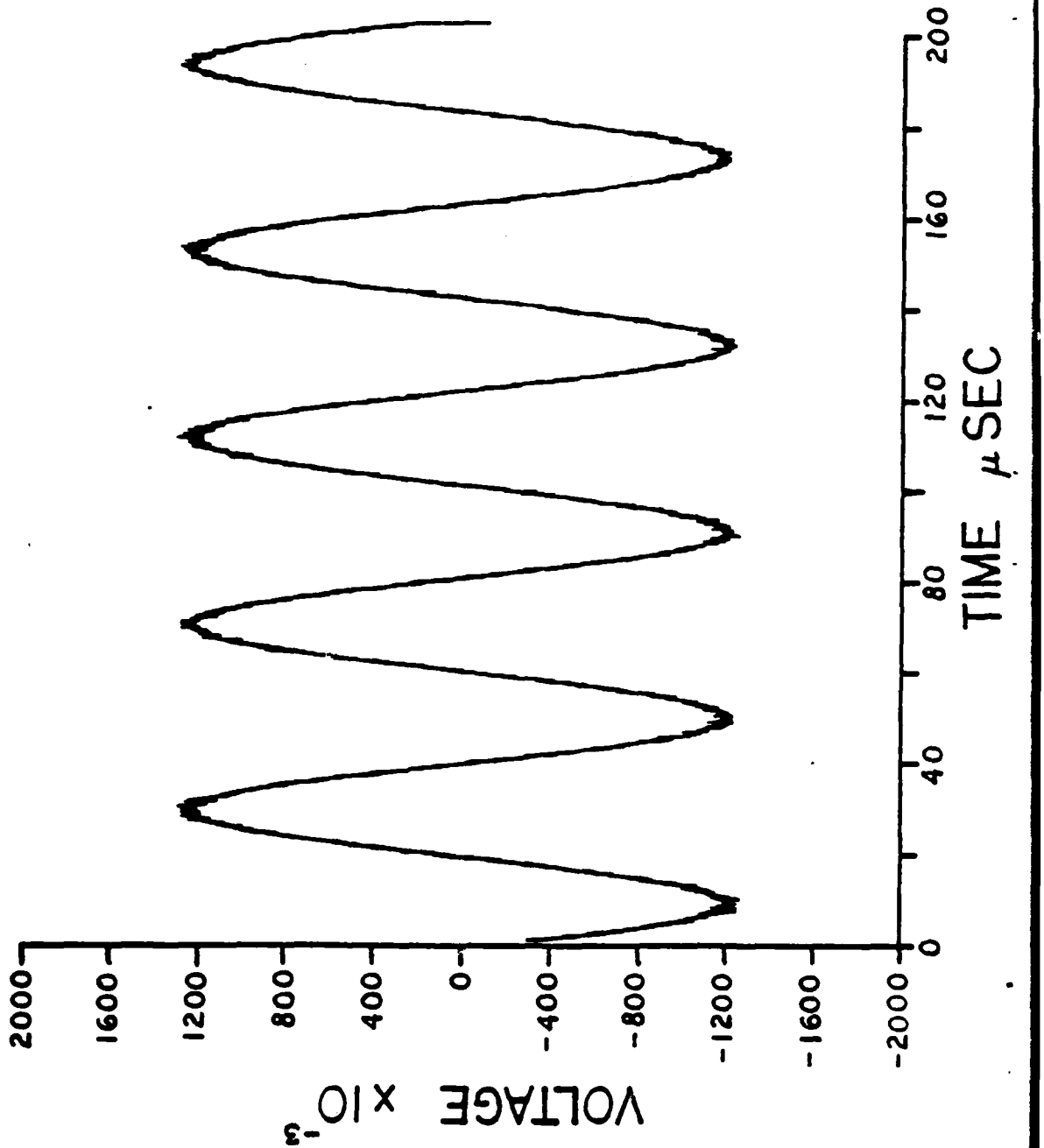
VOLTAGE x10^-3
2000
1600
1200
800
400
0
-400
-800
-1200
-1600
-2000
0
40
80
120
160
200
TIME μSEC

B2

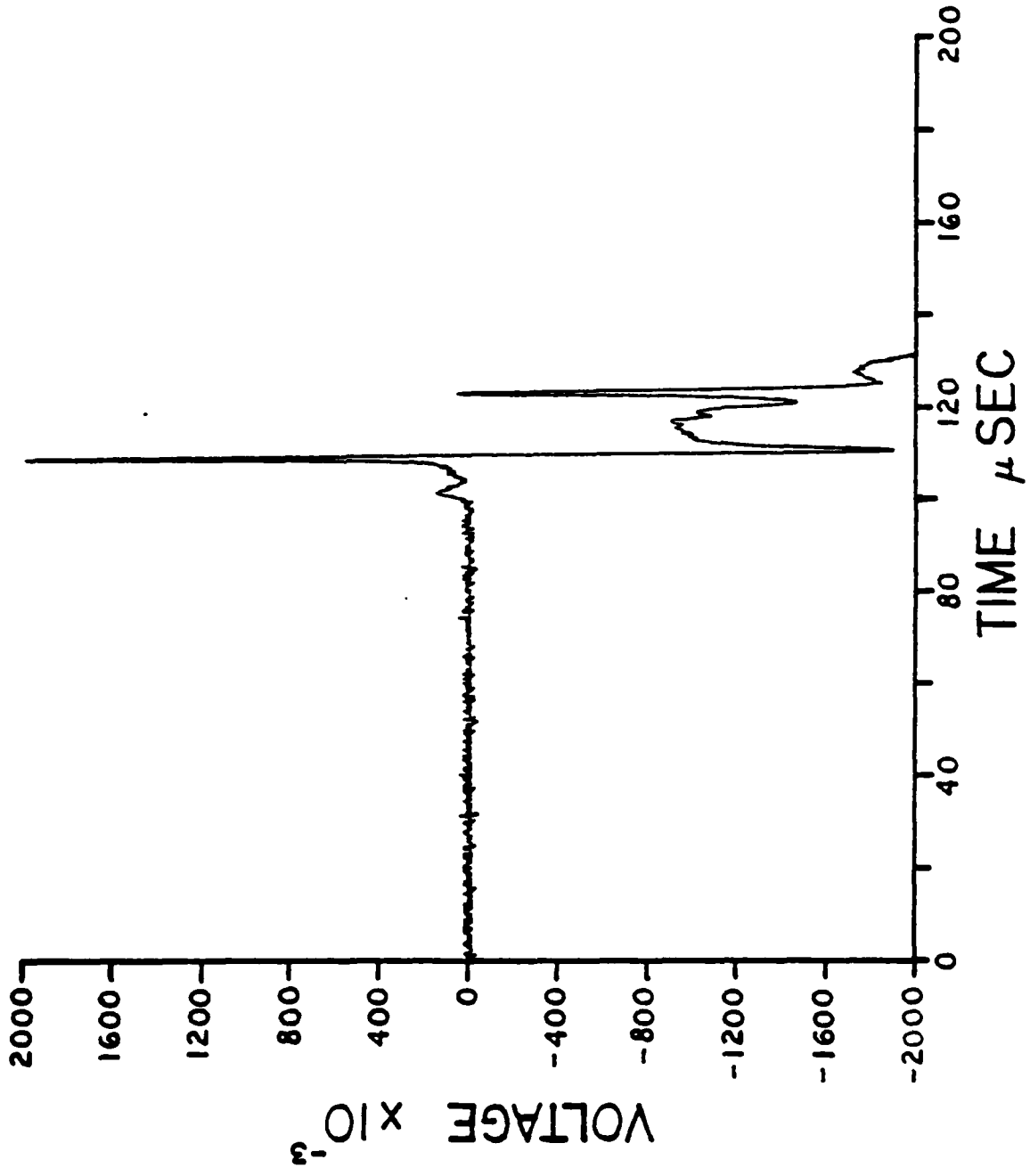
VOLTAGE x10⁻³
2000
1600
1200
800
400
0
-400
-800
-1200
-1600
-2000
0
40
80
120
160
200
TIME μSEC

B3

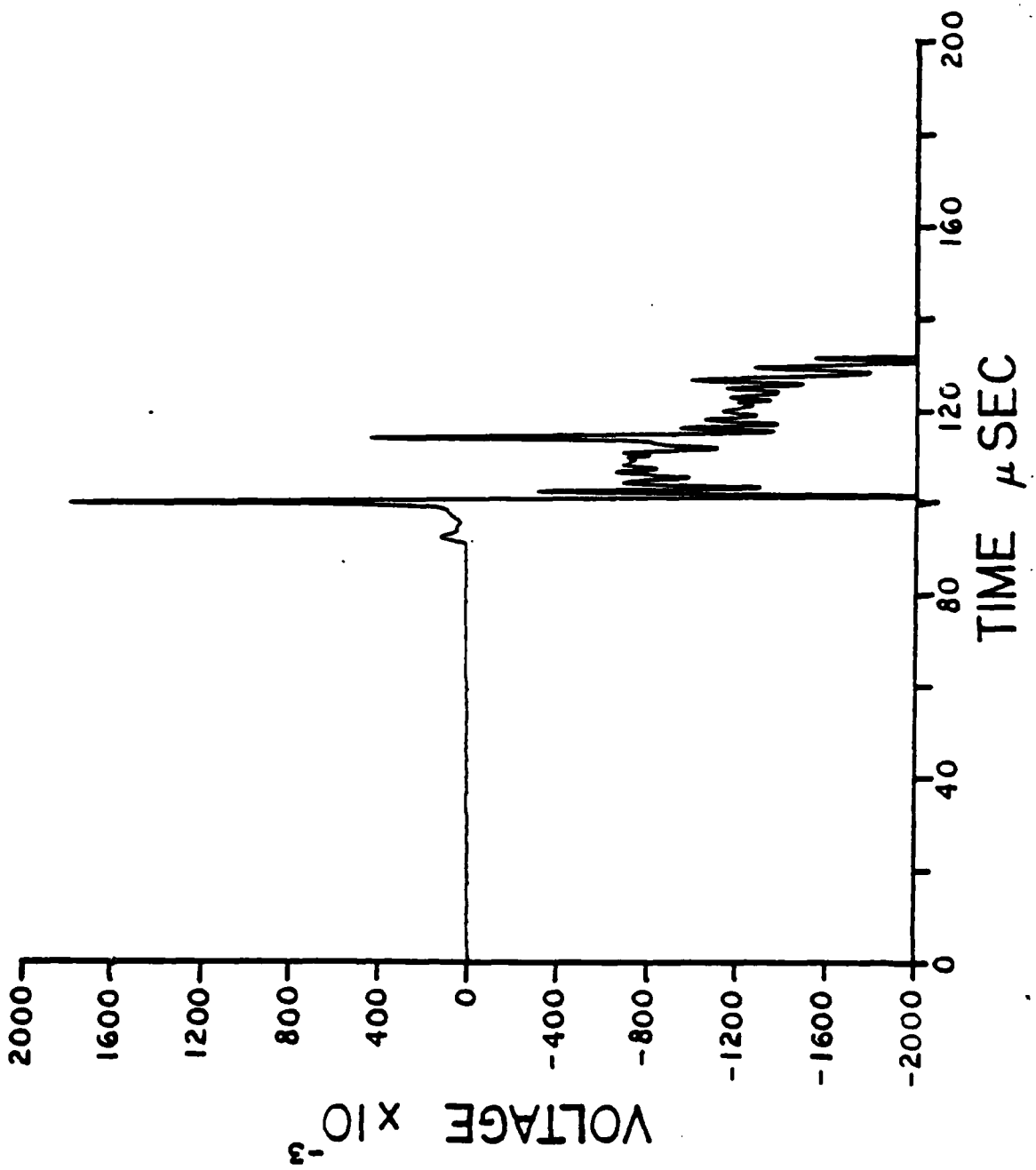
VOLTAGE x10^-3
2000
1600
1200
800
400
0
-400
-800
-1200
-1600
-2000
0
40
80
120
160
200
TIME μSEC

B4

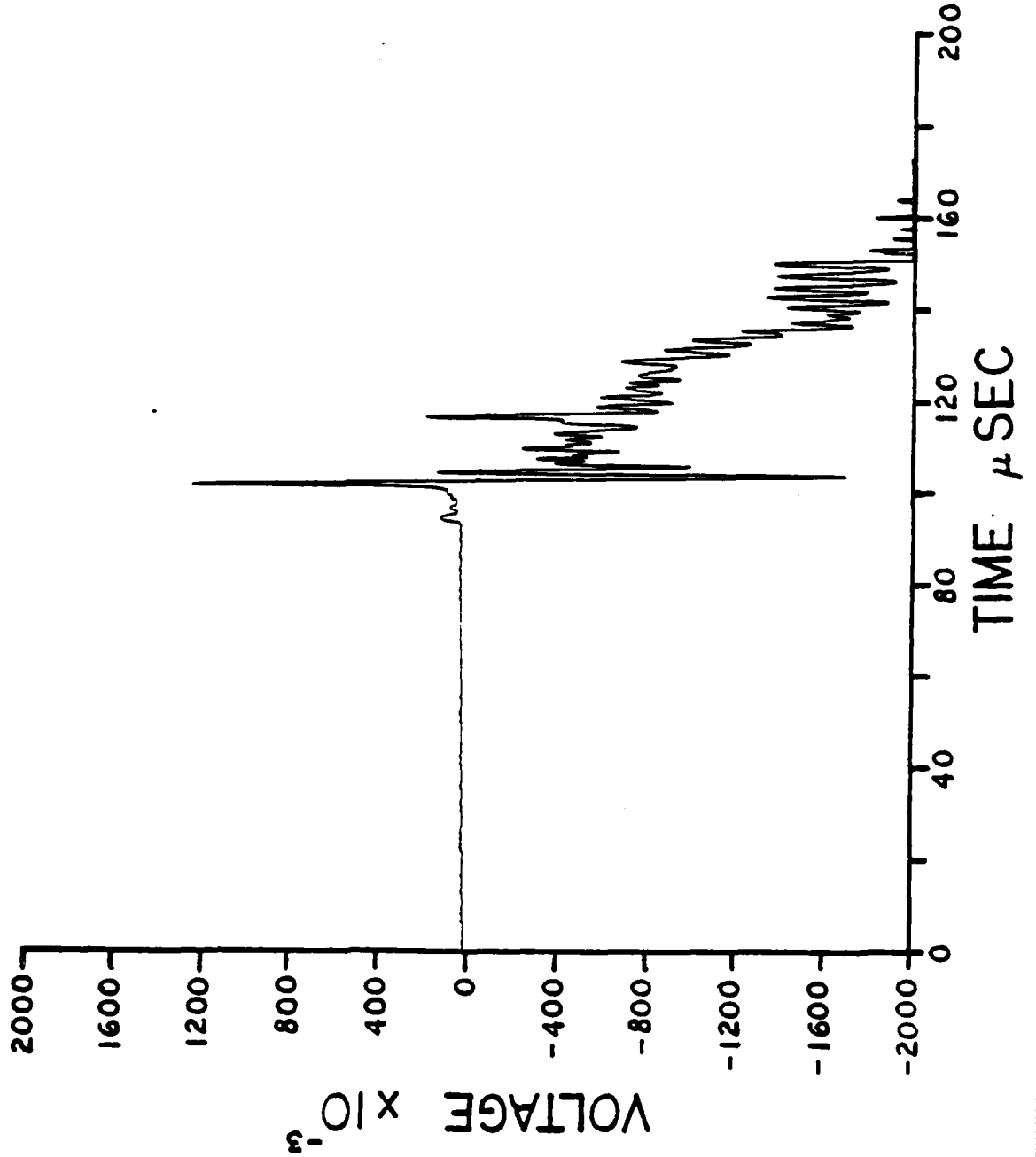
VOLTAGE x10⁻³
2000
1600
1200
800
400
0
-400
-800
-1200
-1600
-2000
0
40
80
120
160
200
TIME μSEC

B5

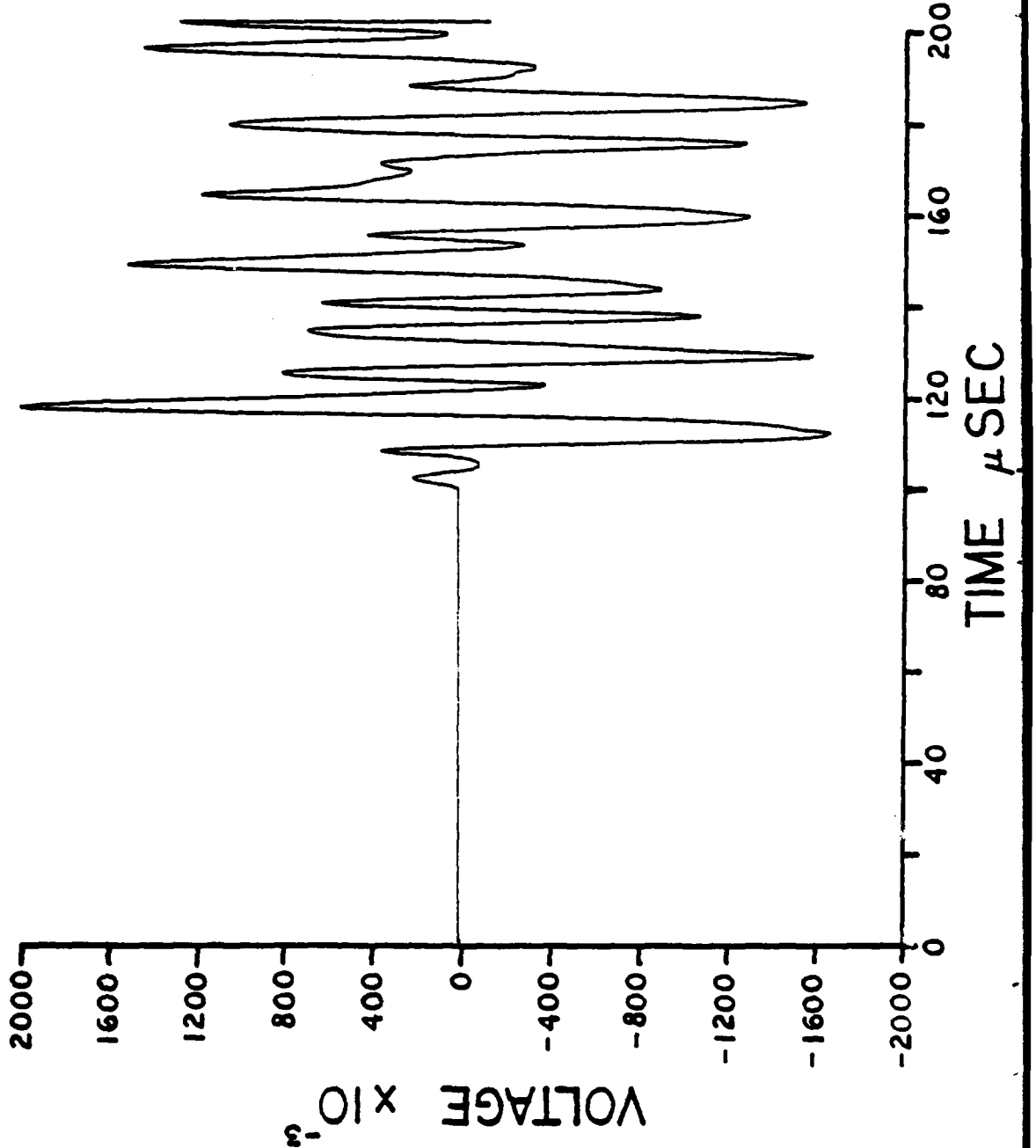
VOLTAGE x10^-3
2000
1600
1200
800
400
0
-400
-800
-1200
-1600
-2000
0
40
80
120
160
200
TIME μSEC

B6

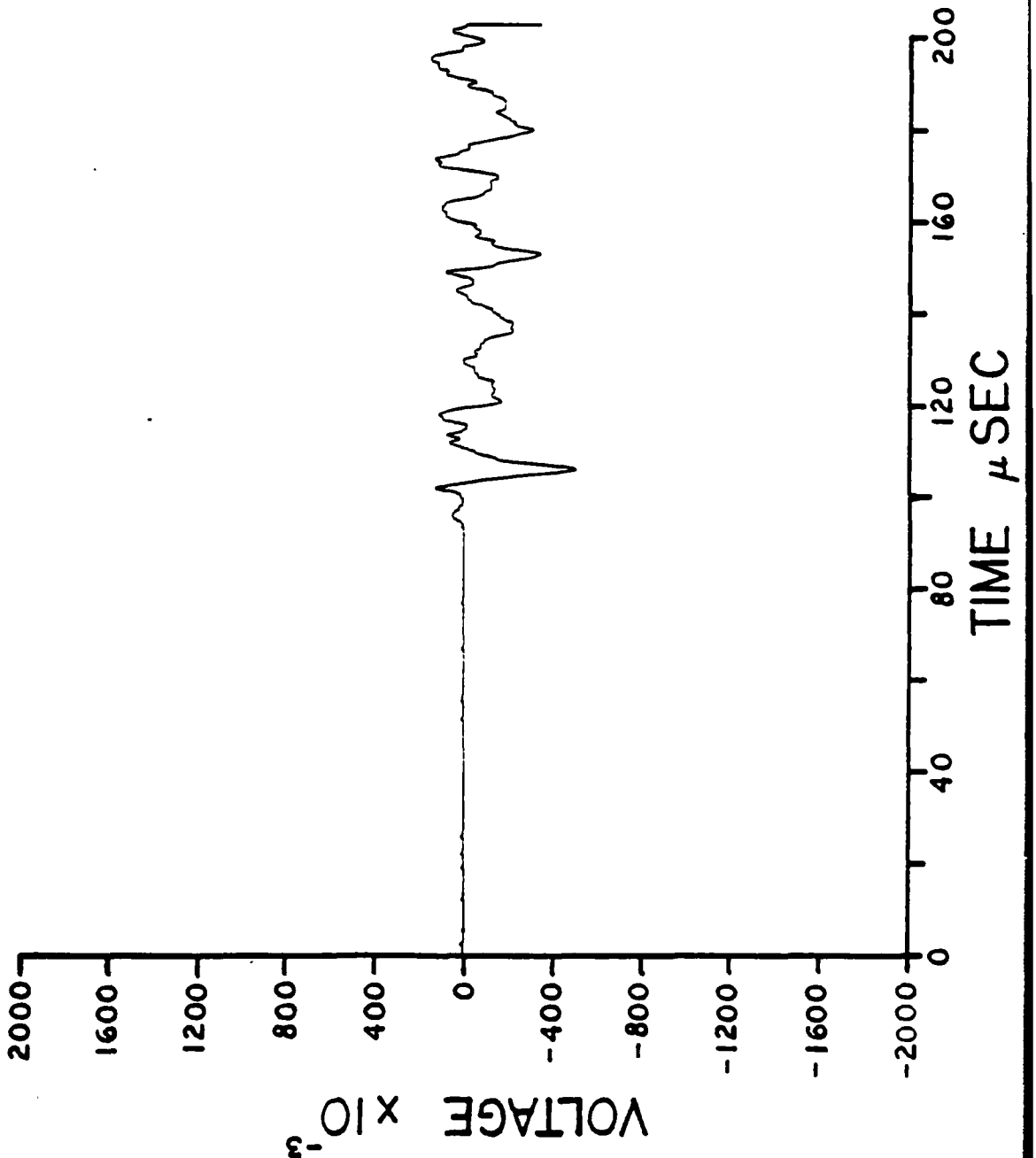
VOLTAGE x10^-3
2000
1600
1200
800
400
0
-400
-800
-1200
-1600
-2000
0
40
80
120
160
200
TIME μSEC

B7

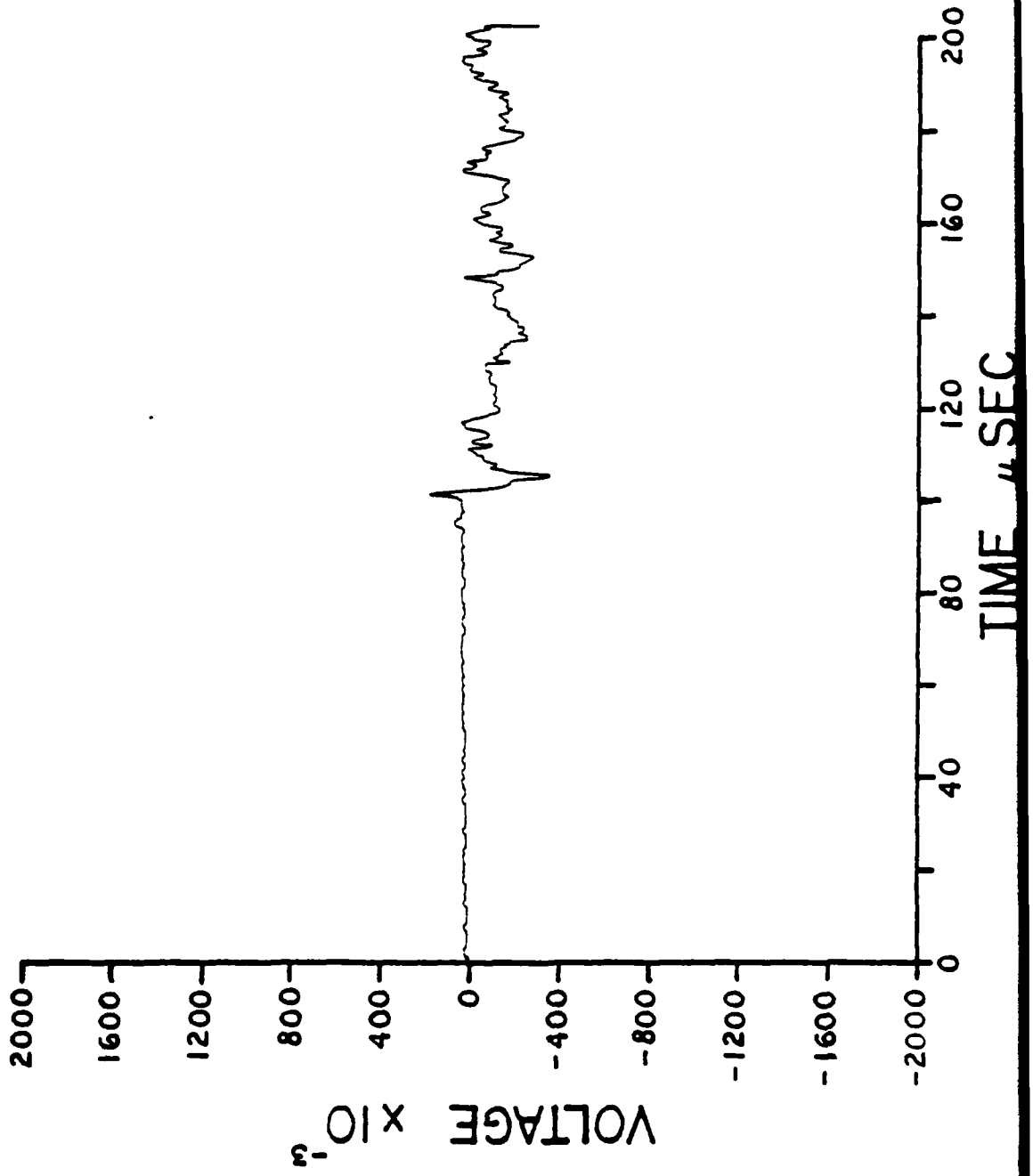
VOLTAGE x10⁻³
2000
1600
1200
800
400
0
-400
-800
-1200
-1600
-2000
0
40
80
120
160
200
TIME μSEC

B8

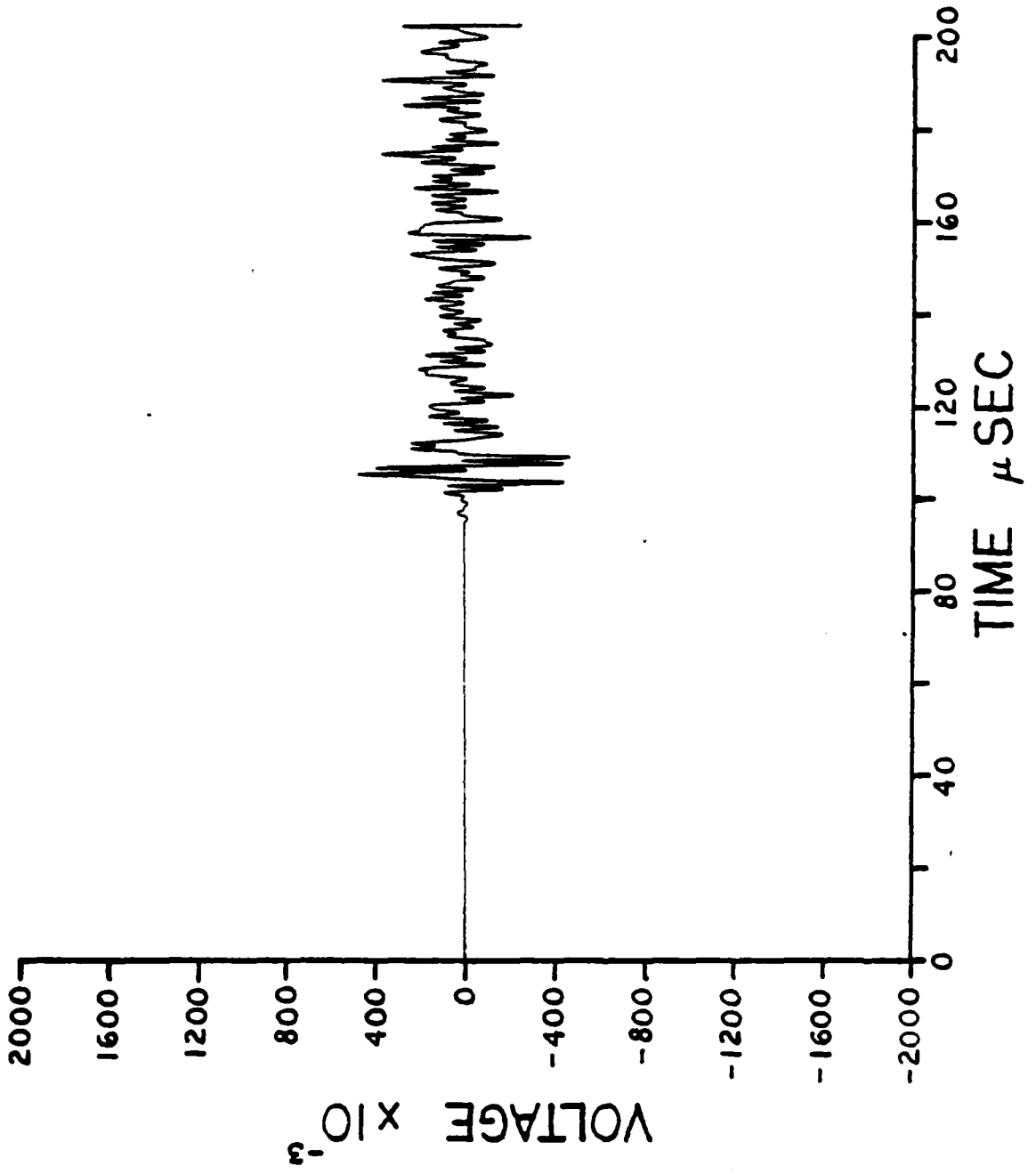
VOLTAGE x10⁻³
2000
1600
1200
800
400
0
-400
-800
-1200
-1600
-2000
0
40
80
120
160
200
TIME μSEC

B9

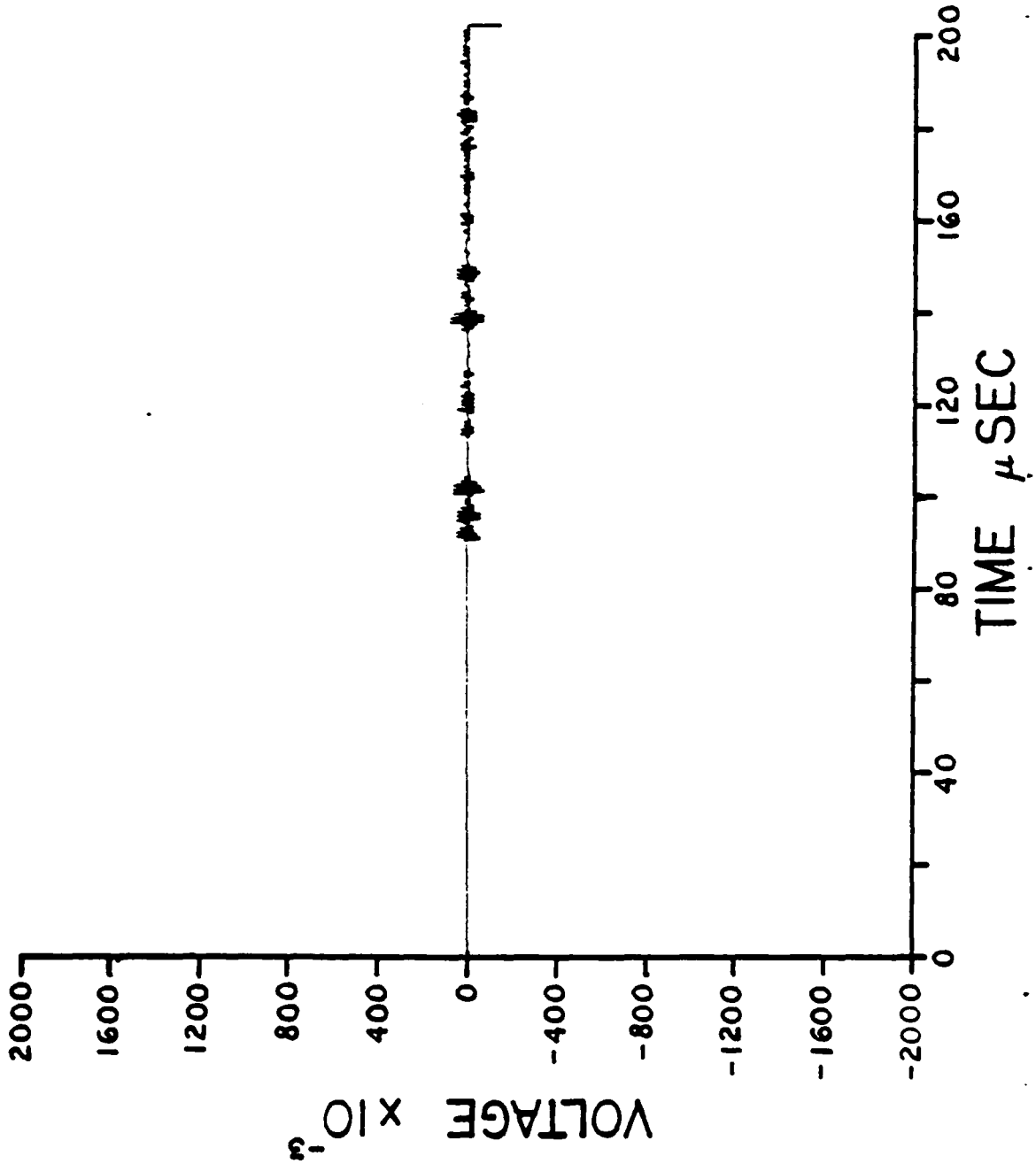
VOLTAGE x10⁻³
2000
1600
1200
800
400
0
-400
-800
-1200
-1600
-2000
0
40
80
120
160
200
TIME μSEC

B10

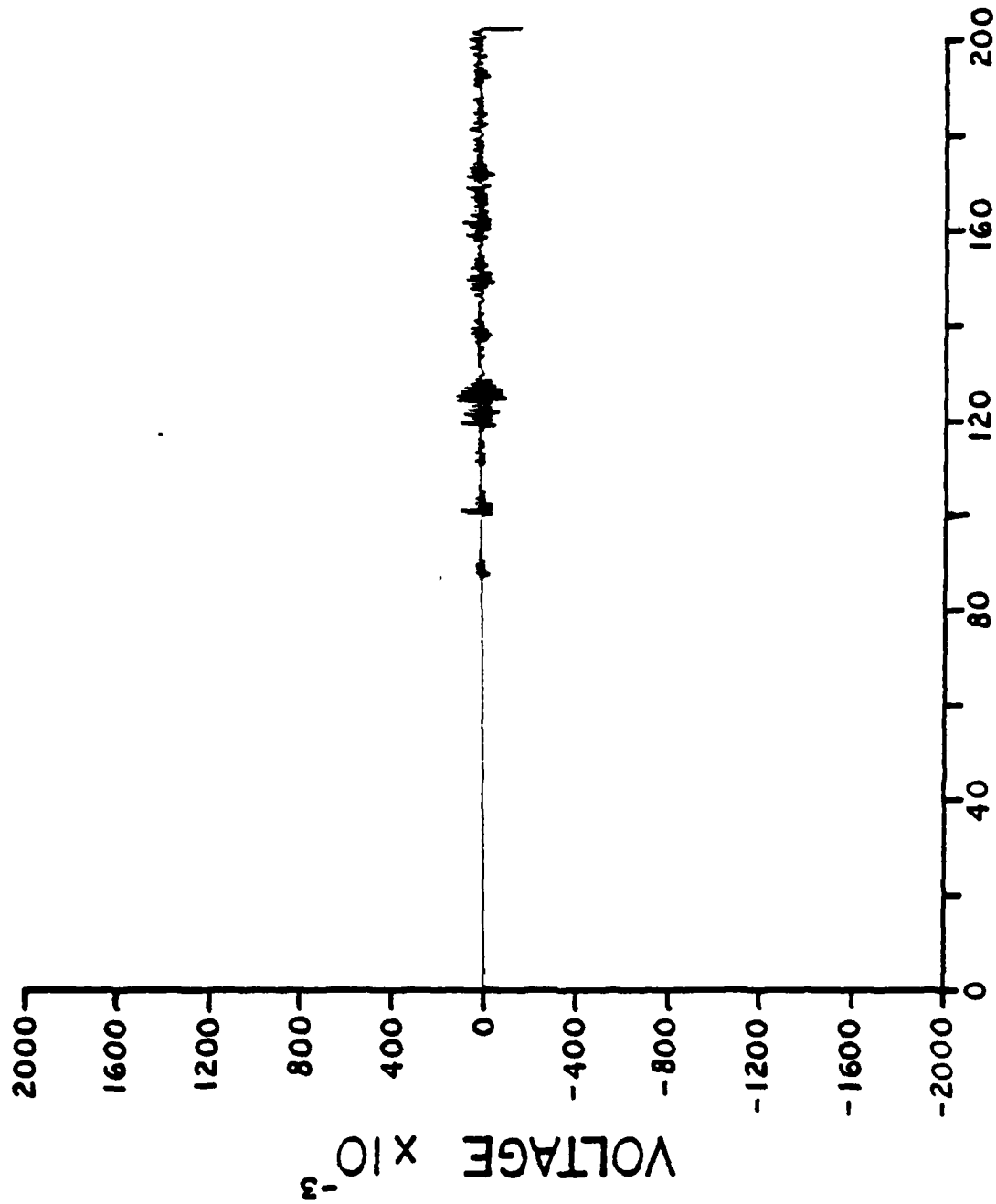
VOLTAGE x10⁻³
2000
1600
1200
800
400
0
-400
-800
-1200
-1600
-2000
0
40
80
120
160
200
TIME μSEC

B11

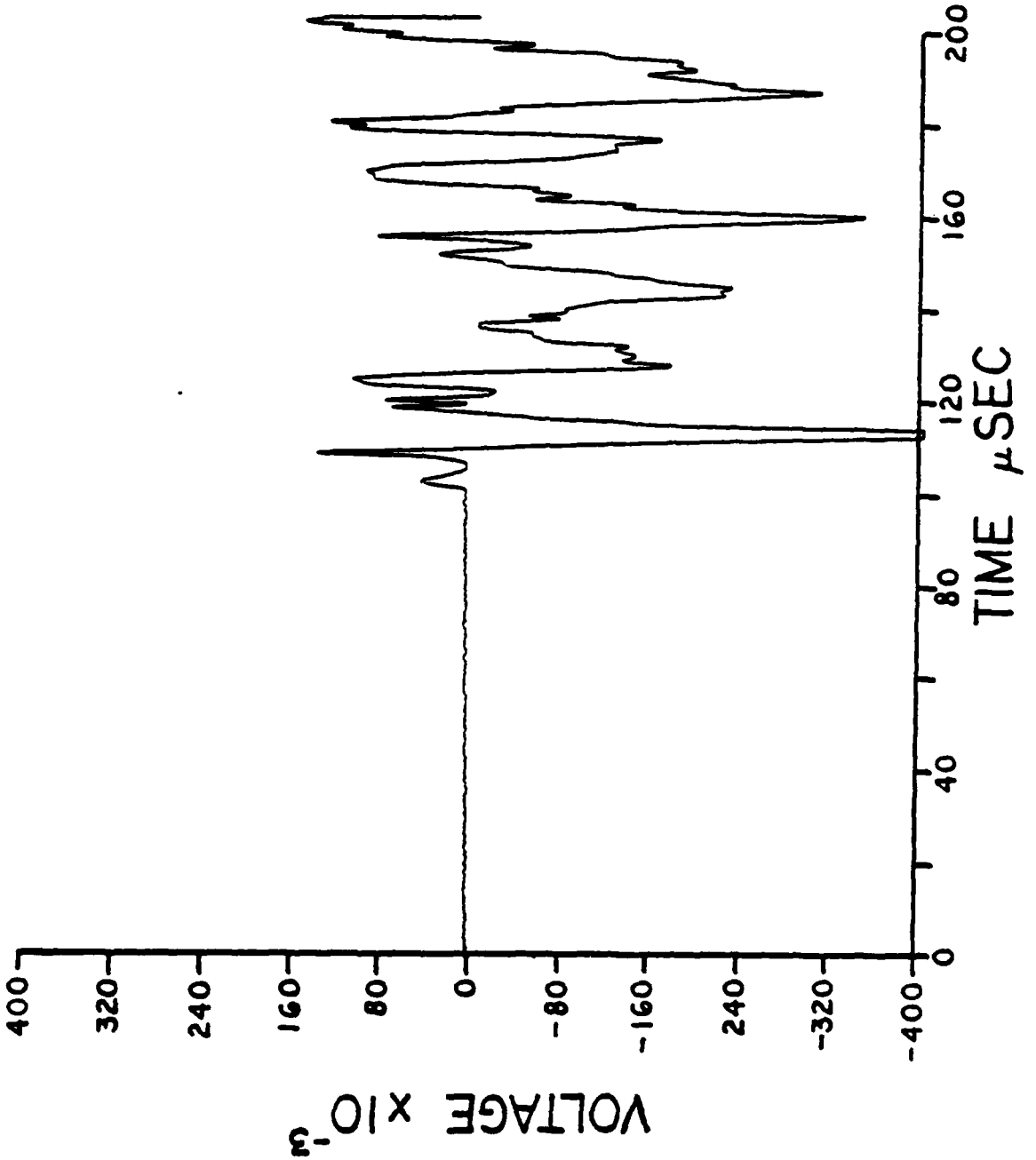
VOLTAGE x10⁻³
400
320
240
160
80
0
-80
-160
240
-320
-400
0
40
80
120
160
200
TIME μSEC

B12

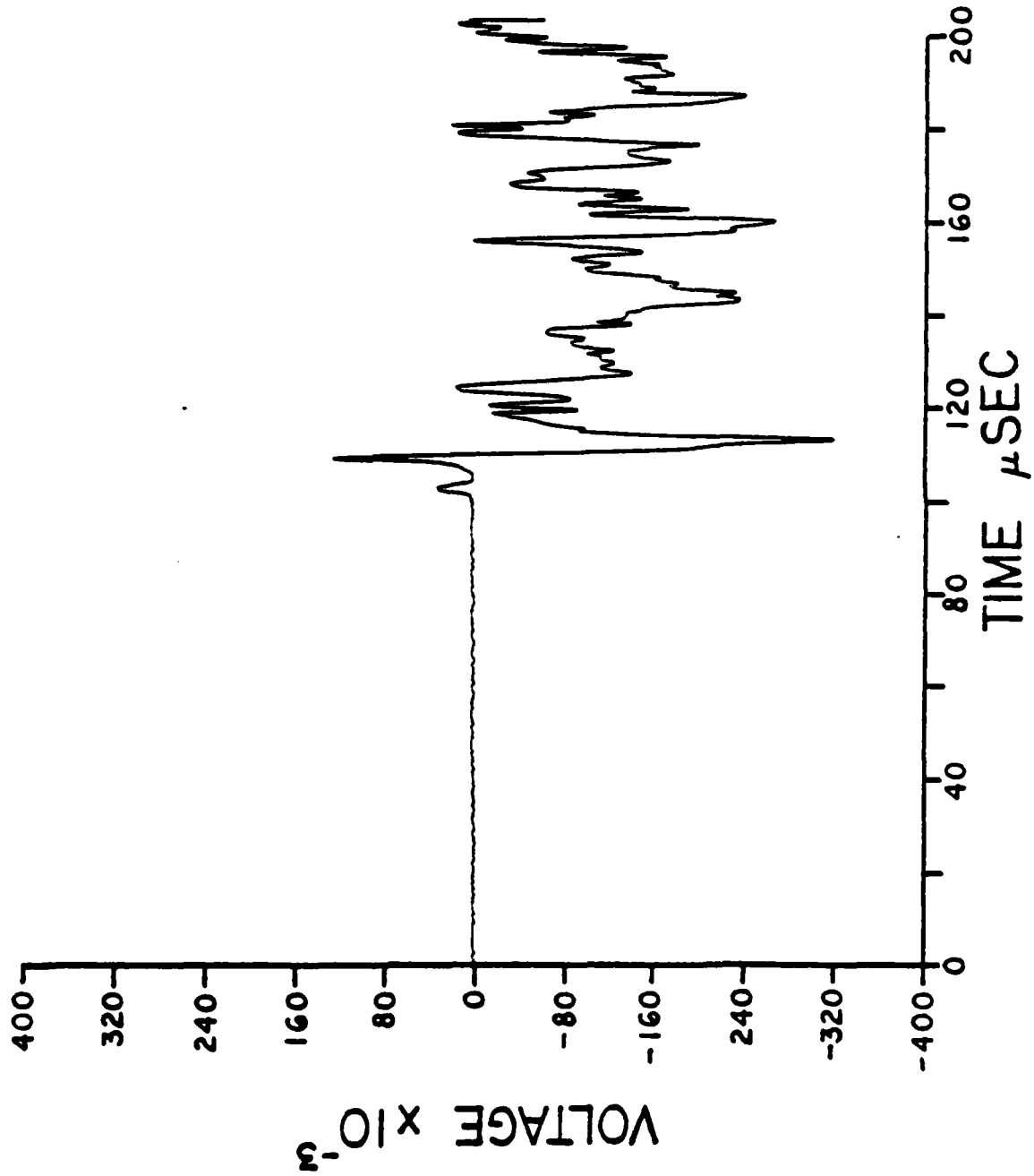
VOLTAGE x10⁻³
400
320
240
160
80
0
-80
-160
240
-320
-400
0
40
80
120
160
200
TIME μSEC

B13

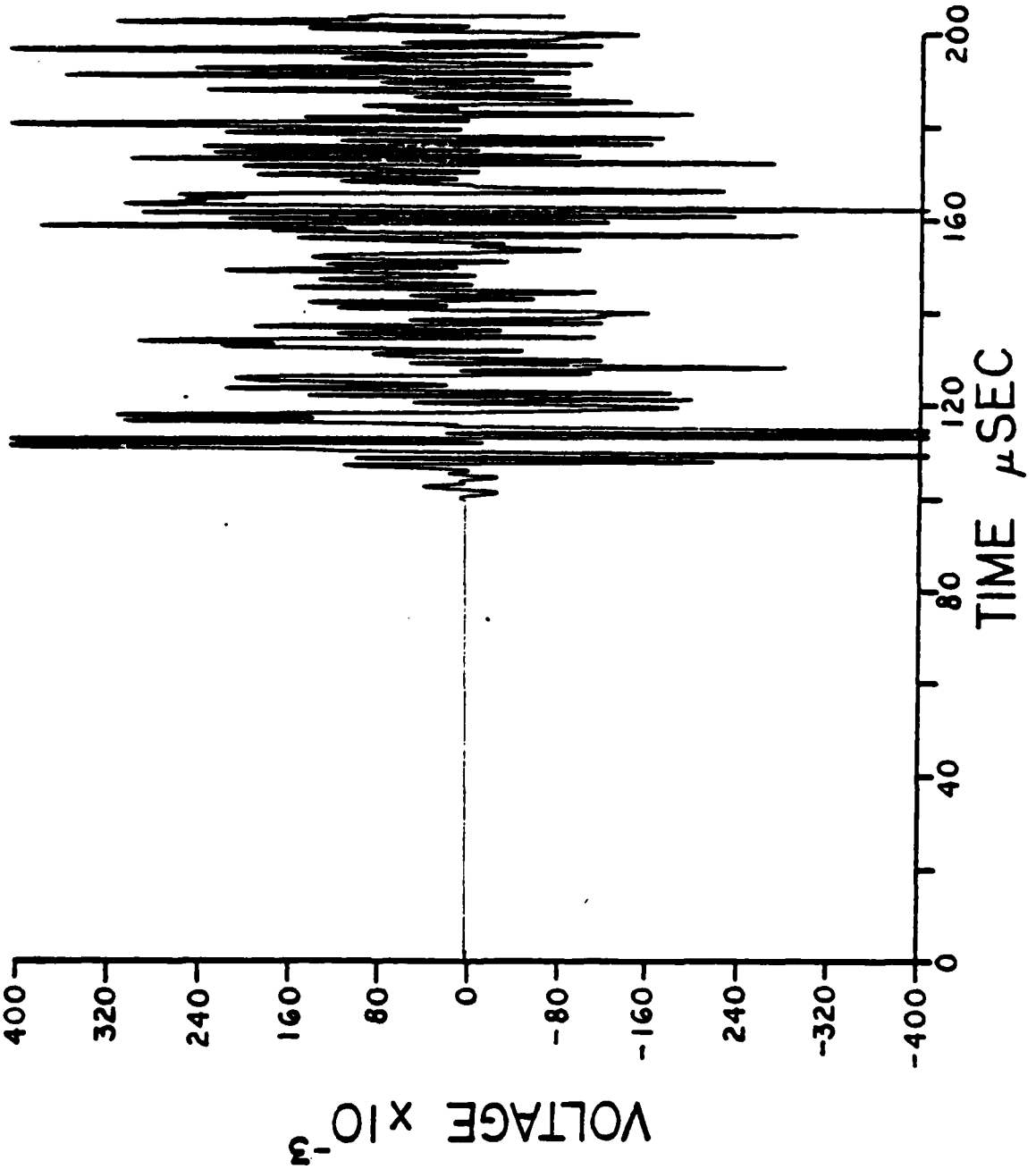
VOLTAGE x10^-3
400
320
240
160
80
0
-80
-160
240
-320
-400
0
40
80
120
160
200
TIME μSEC

B14

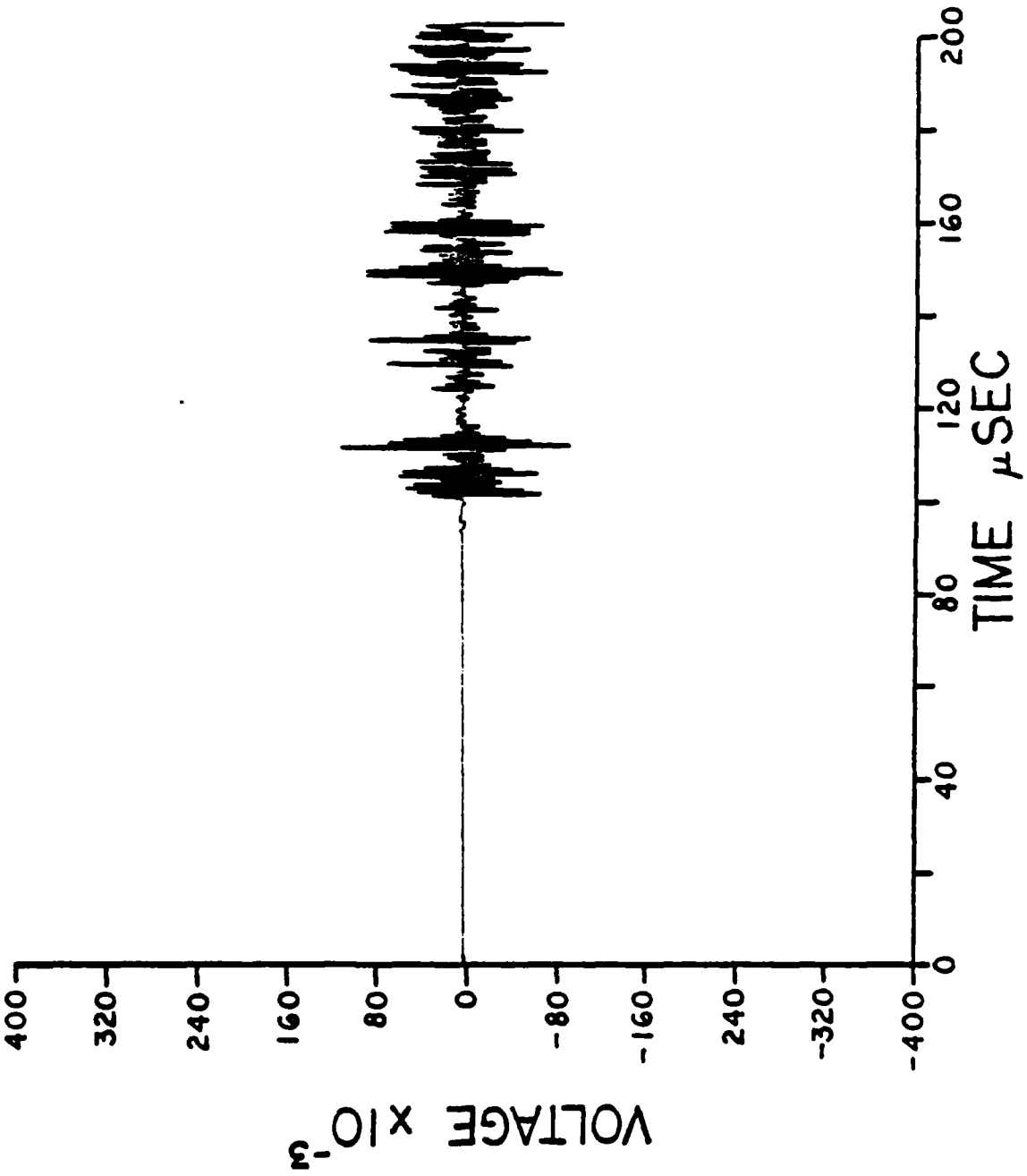
VOLTAGE x10⁻³
400
320
240
160
80
0
-80
-160
240
-320
-400
0
40
80
120
160
200
TIME μSEC

B15

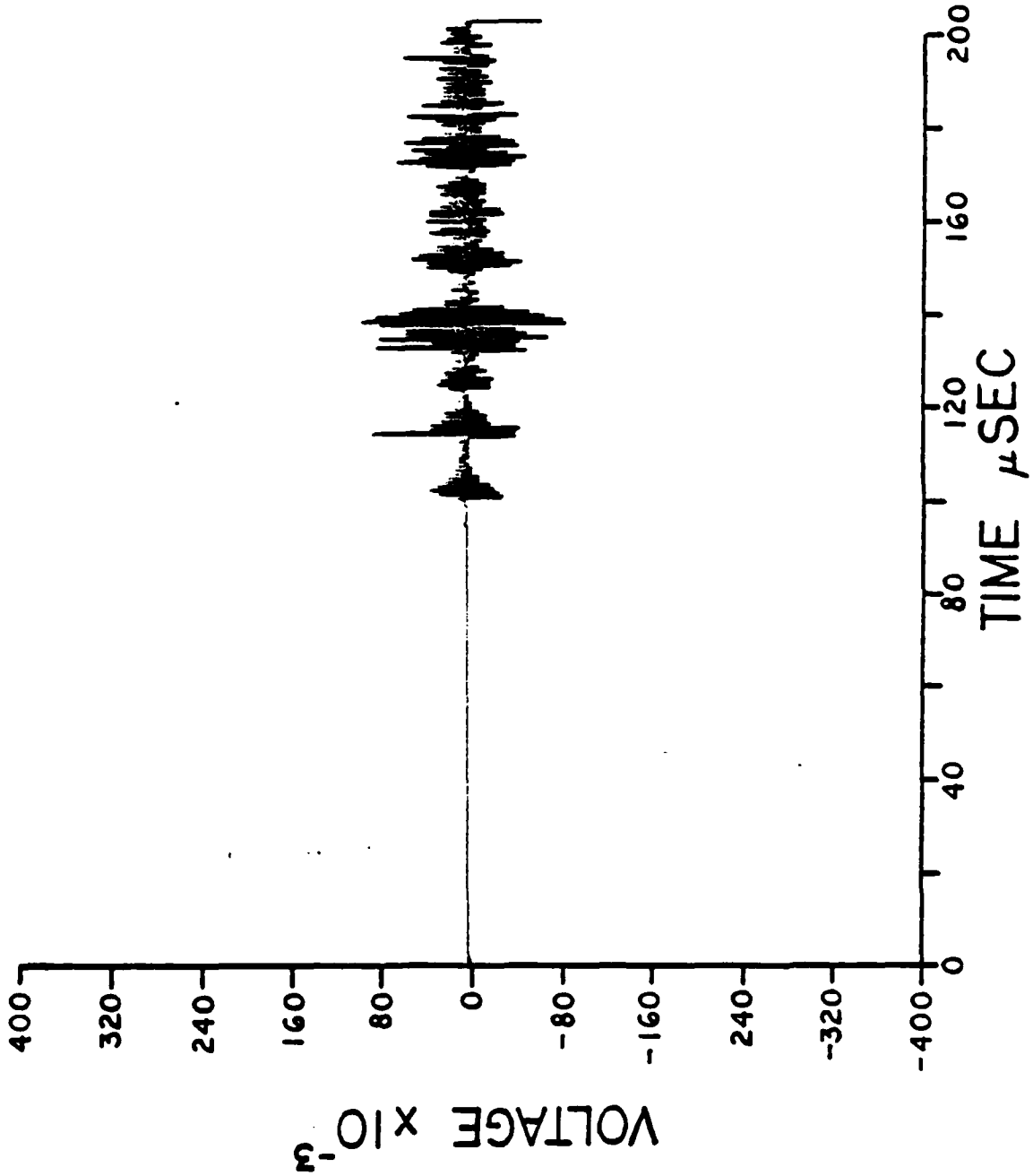
VOLTAGE x10⁻³
400
320
240
160
80
0
-80
-160
240
-320
-400
0
40
80
120
160
200
TIME μSEC

B16

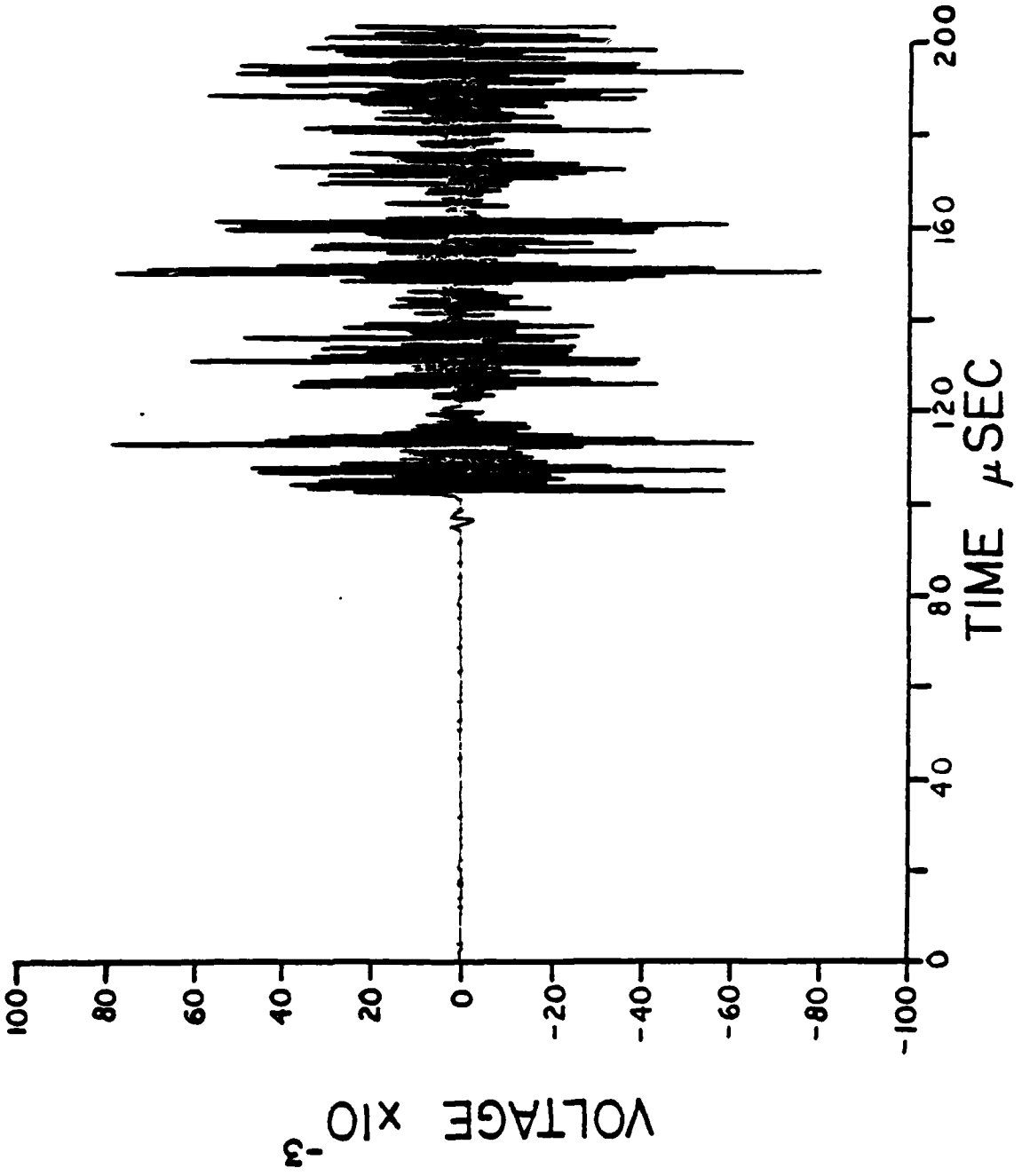
VOLTAGE x10^{-3}
100
80
60
40
20
0
-20
-40
-60
-80
-100
0
40
80
120
160
200
TIME μSEC

B17

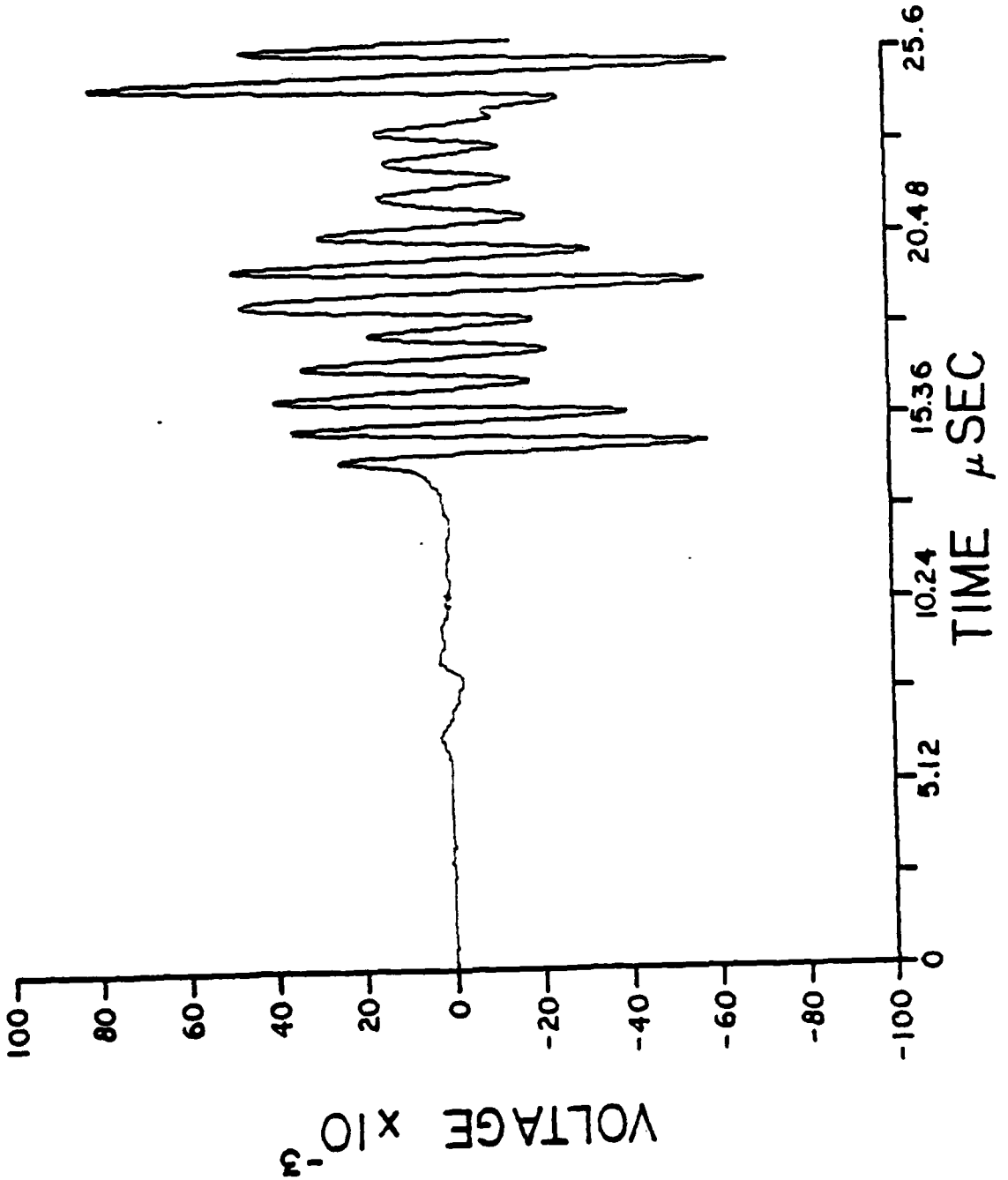
VOLTAGE x10^{-3}
100
80
60
40
20
0
-20
-40
-60
-80
-100
0
5.12
10.24
15.36
20.48
25.6
TIME μSEC

B18

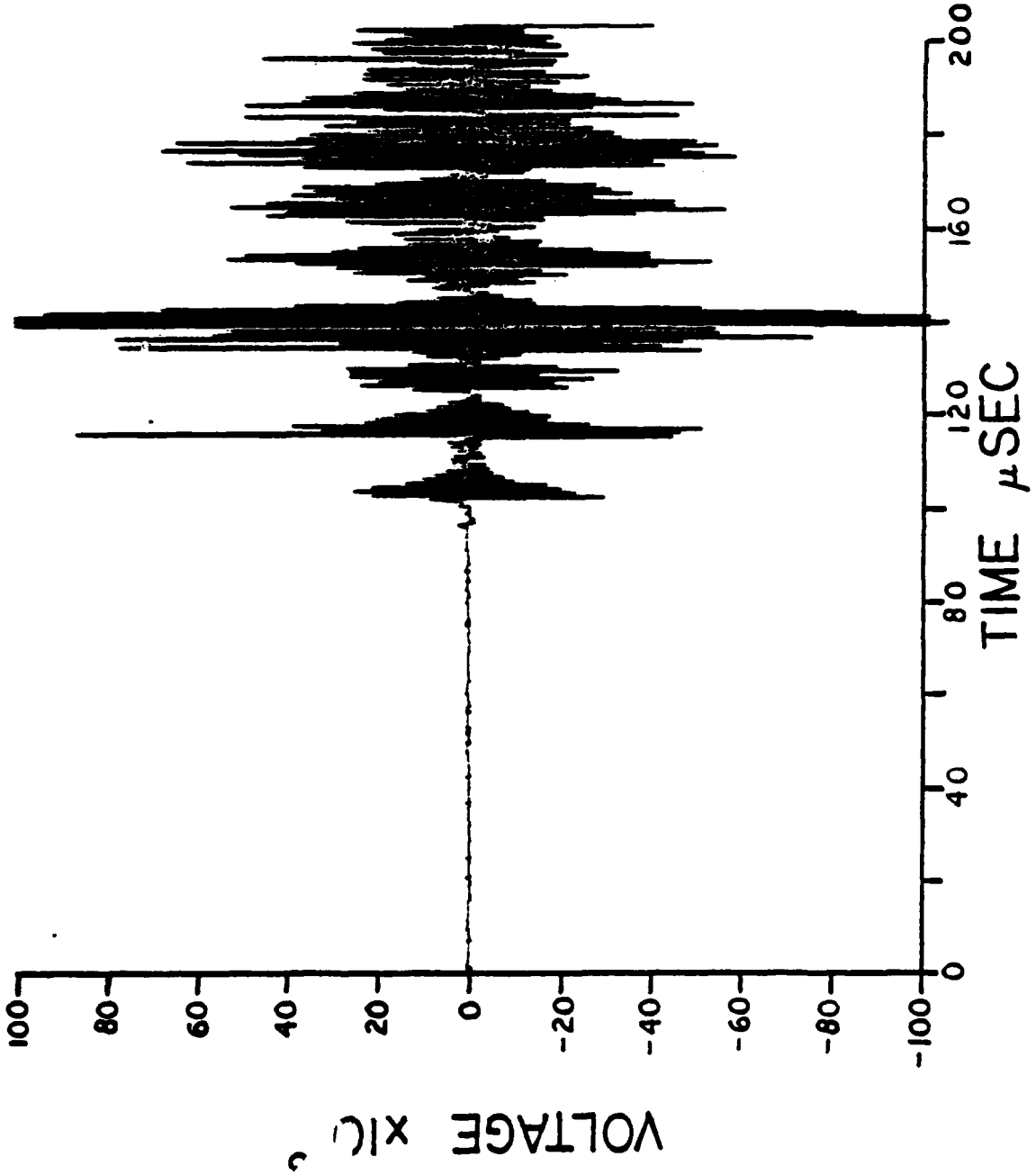
VOLTAGE x10^3
100
80
60
40
20
0
-20
-40
-60
-80
-100
0
40
80
120
160
200
TIME μSEC

B19

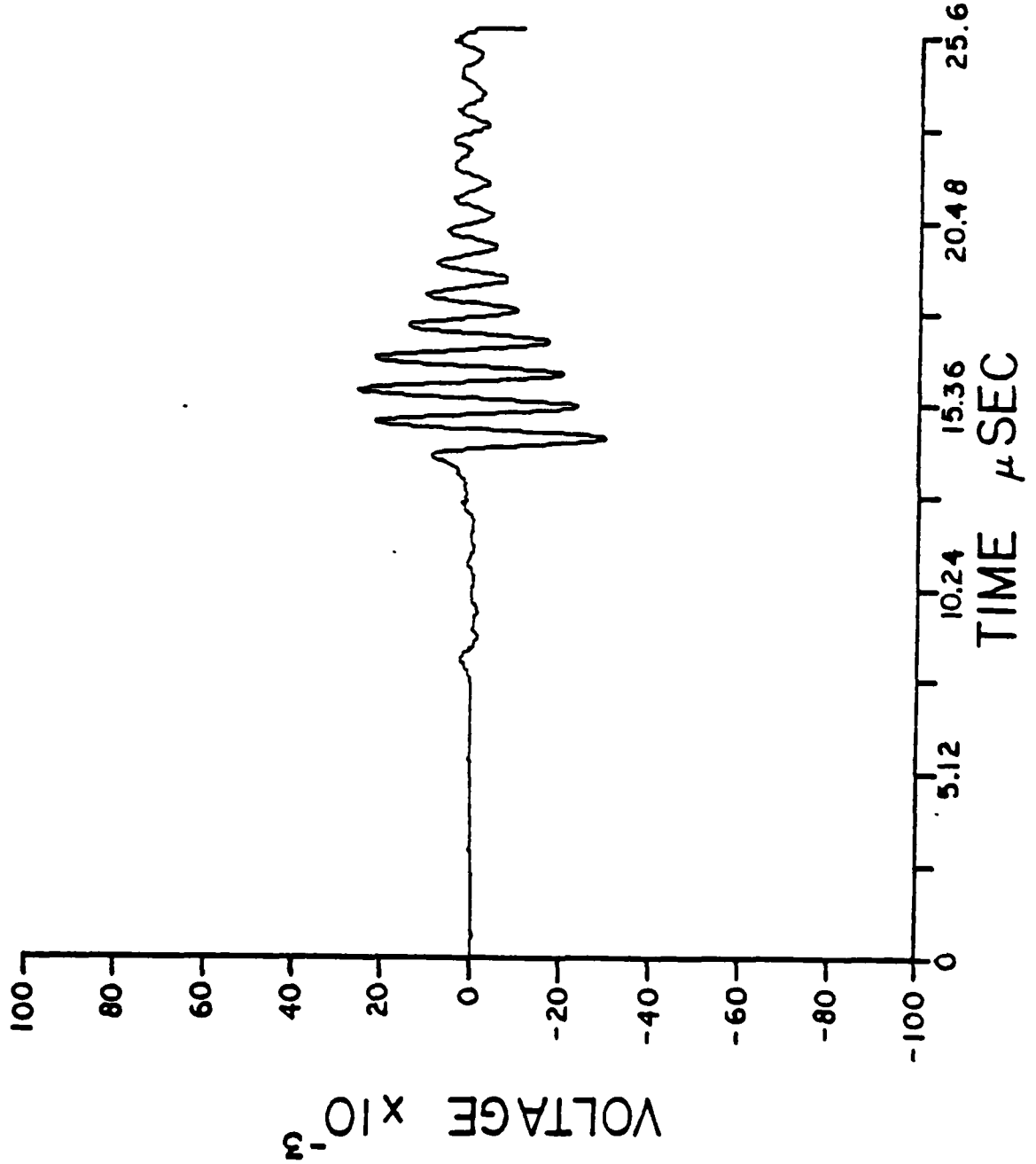
VOLTAGE x10⁻³
100
80
60
40
20
0
-20
-40
-60
-80
-100
0
5.12
10.24
15.36
20.48
25.6
TIME μSEC

APPENDIX C

PROBE CHARACTERIZATION FREQUENCY SPECTRA

The following figures are the time domain waveforms from which the frequency spectra were generated for the characterization of the nine acoustic emission probes.

Figs. C1-C3	APL laser interferometer
Figs. C4-C6	NBS-PZT #26 conventional transducer
Figs. C7-C9	NBS-PZT #36 conventional transducer
Figs. C10-C12	Panametrics AE-0.1-L632 conventional transducer
Figs. C13-C15	Panametrics V3032 0.5MHz/0.5 in. conventional transducer
Figs. C16-C18	Panametrics V3031 1.0MHz/0.5 in. conventional transducer
Figs. C19-C21	Dunegan/Endevco S9201 AC42 conventional transducer
Figs. C22-C24	Aerotech Gamma D12618 1.0MHz/0.5 in. conventional transducer
Figs. C25-C27	Aerotech Gamma C12634 1.00MHz/1.0 in. conventional transducer

C1

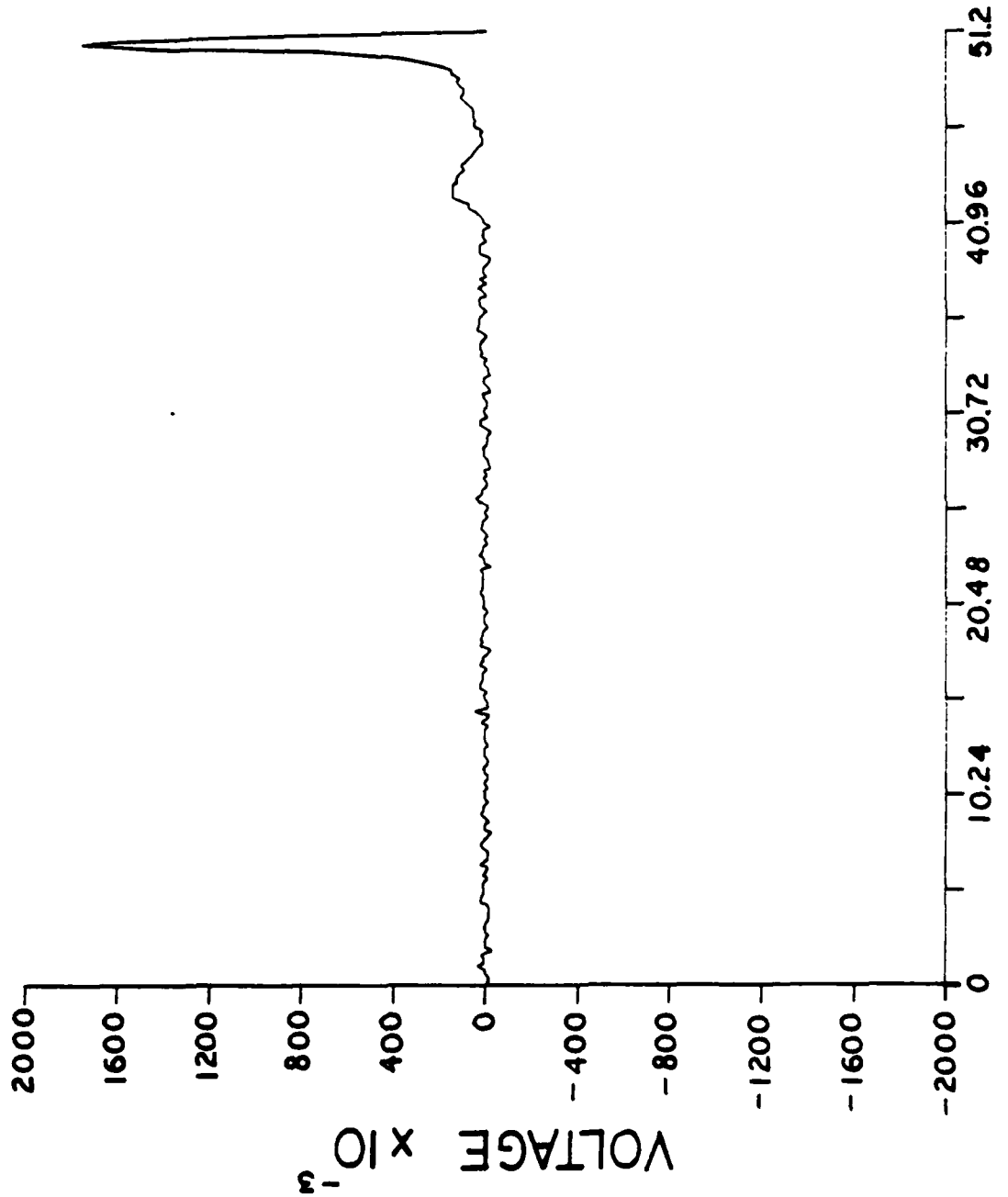
2000
1600
1200
800
400
0
-400
-800
-1200
-1600
-2000
VOLTAGE x 10⁻³
0
10.24
20.48
30.72
40.96
51.2
TIME μSEC

C2

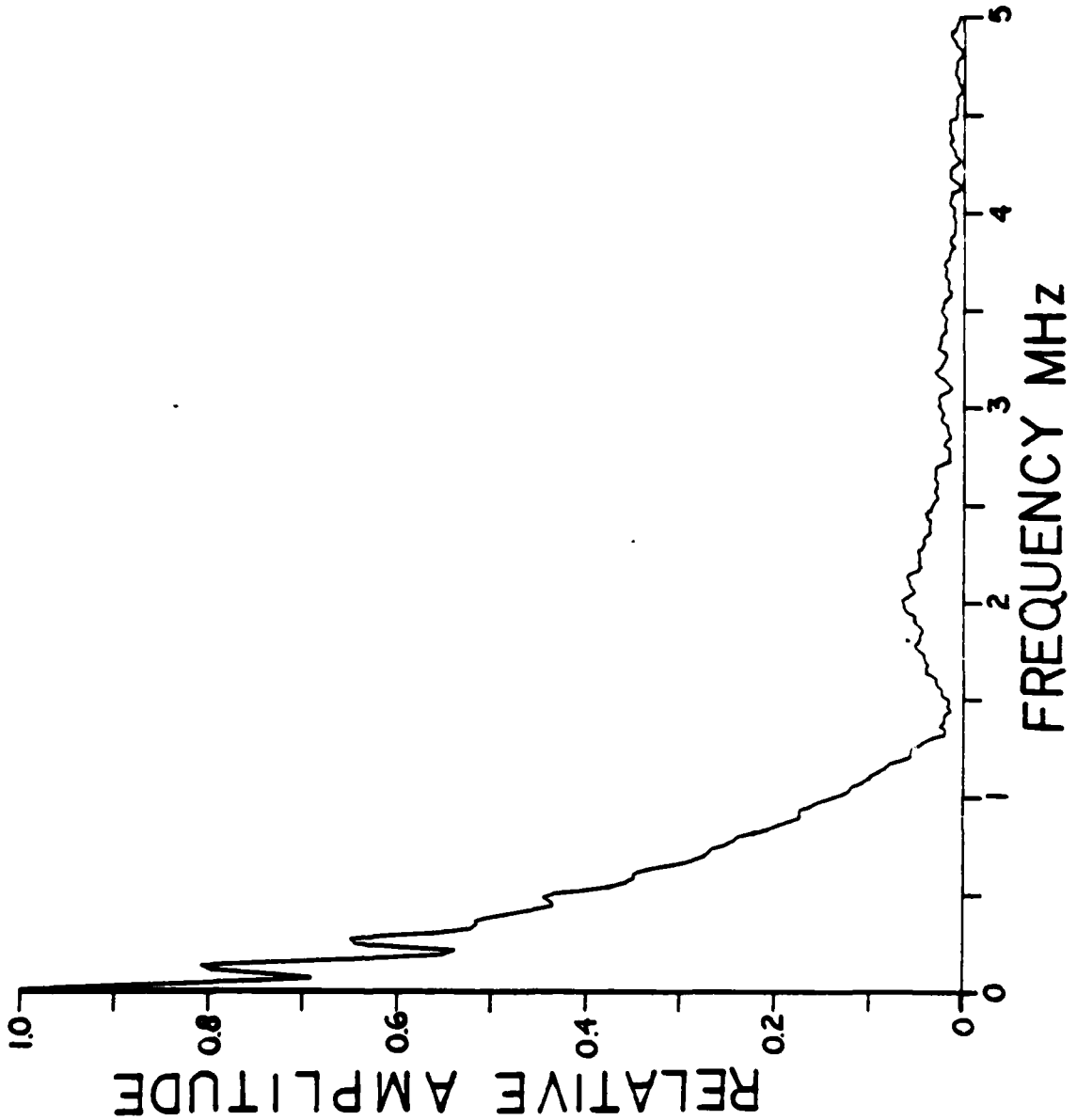

C3

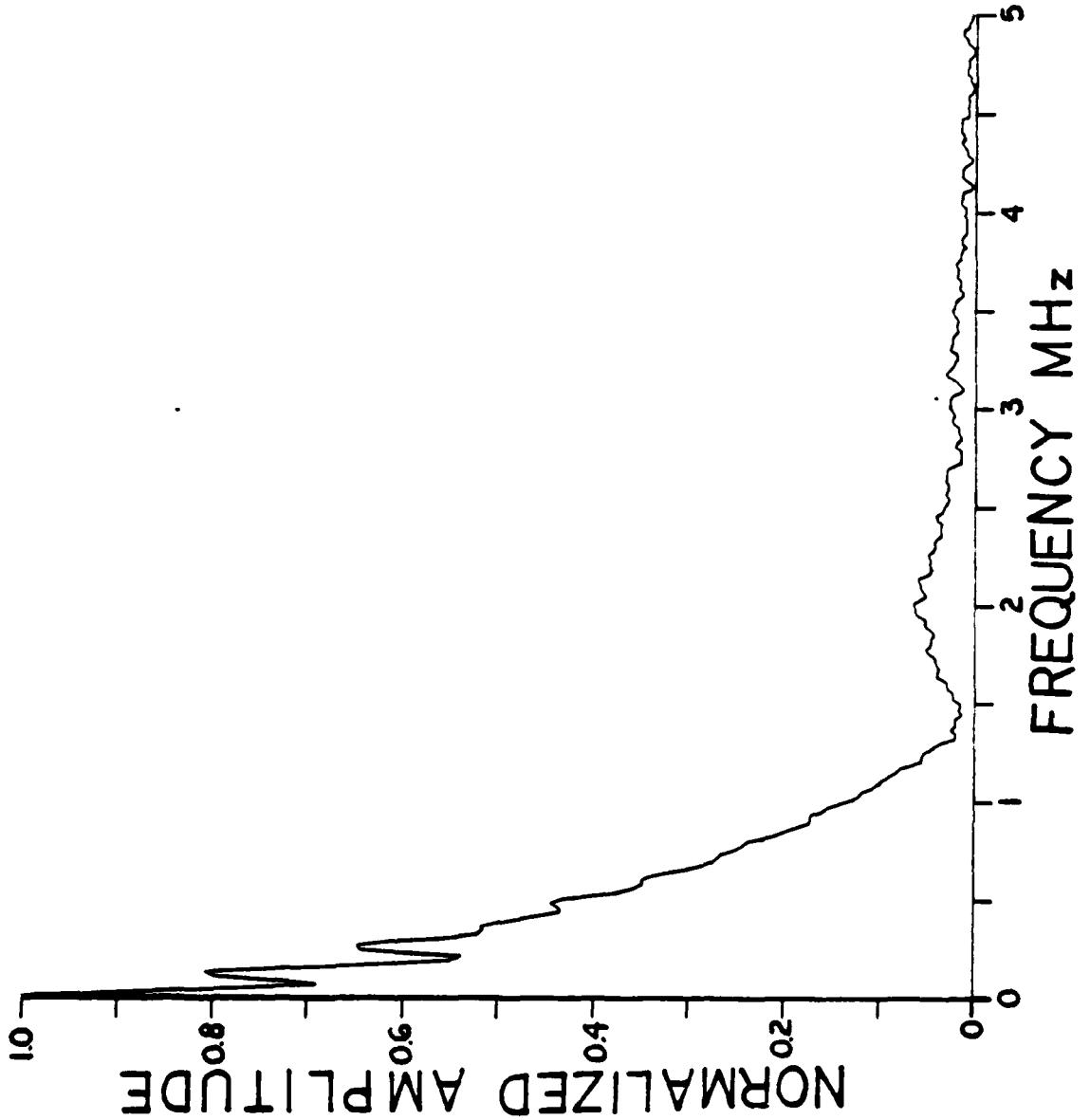

C4

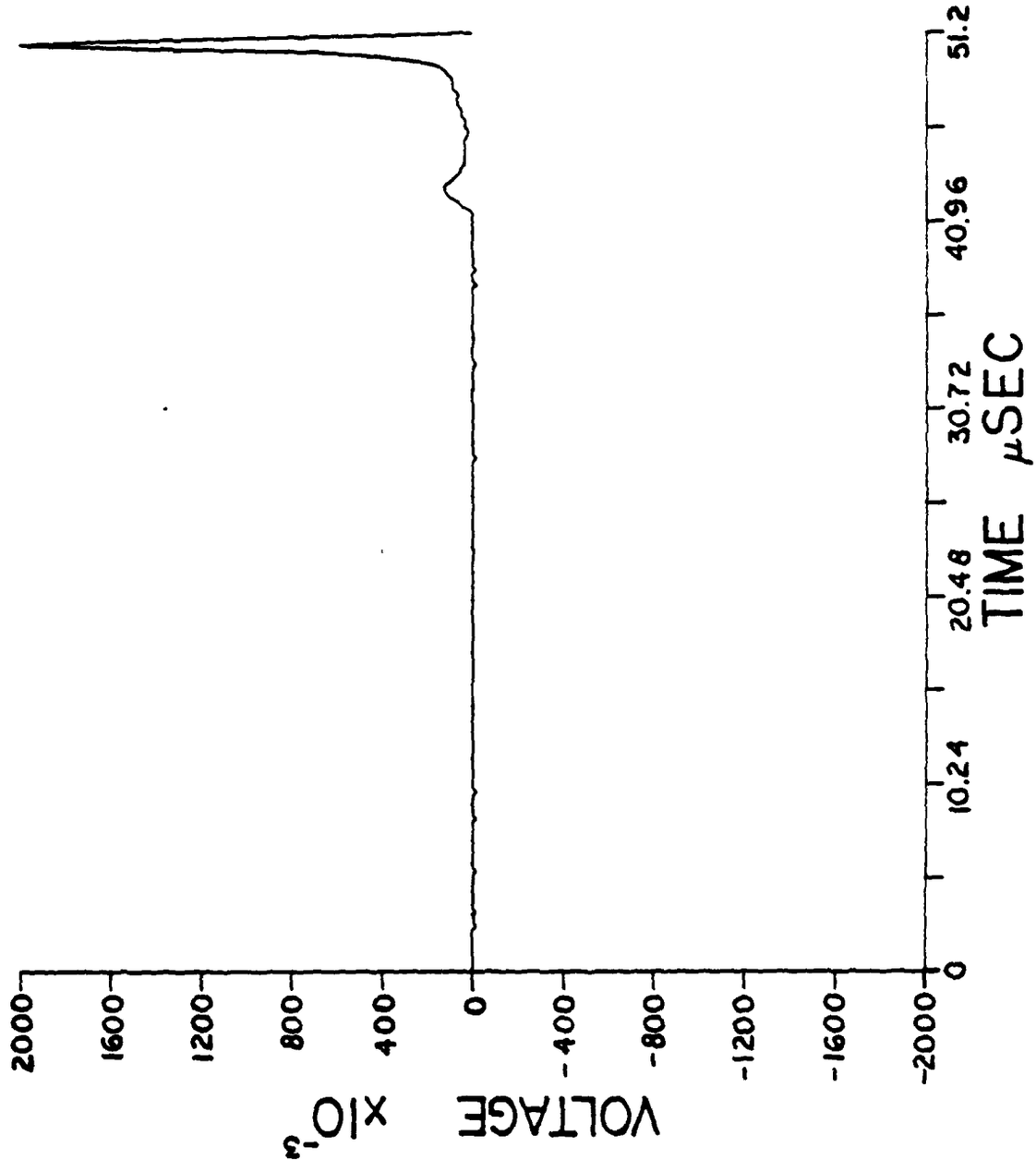
VOLTAGE x10⁻³
2000
1600
1200
800
400
0
-400
-800
-1200
-1600
-2000
0
10.24
20.48
30.72
40.96
51.2
TIME μSEC

C5

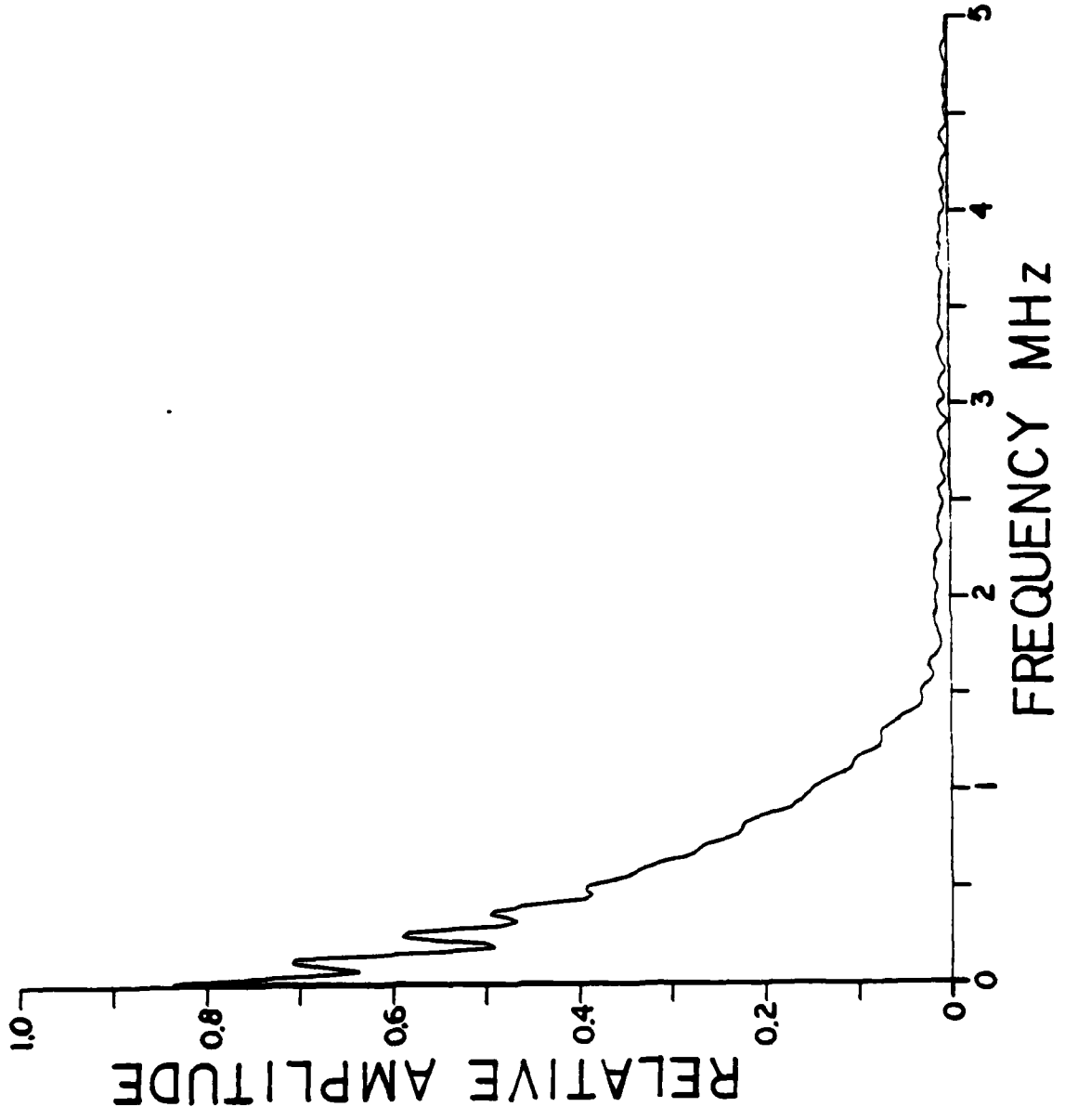

C6

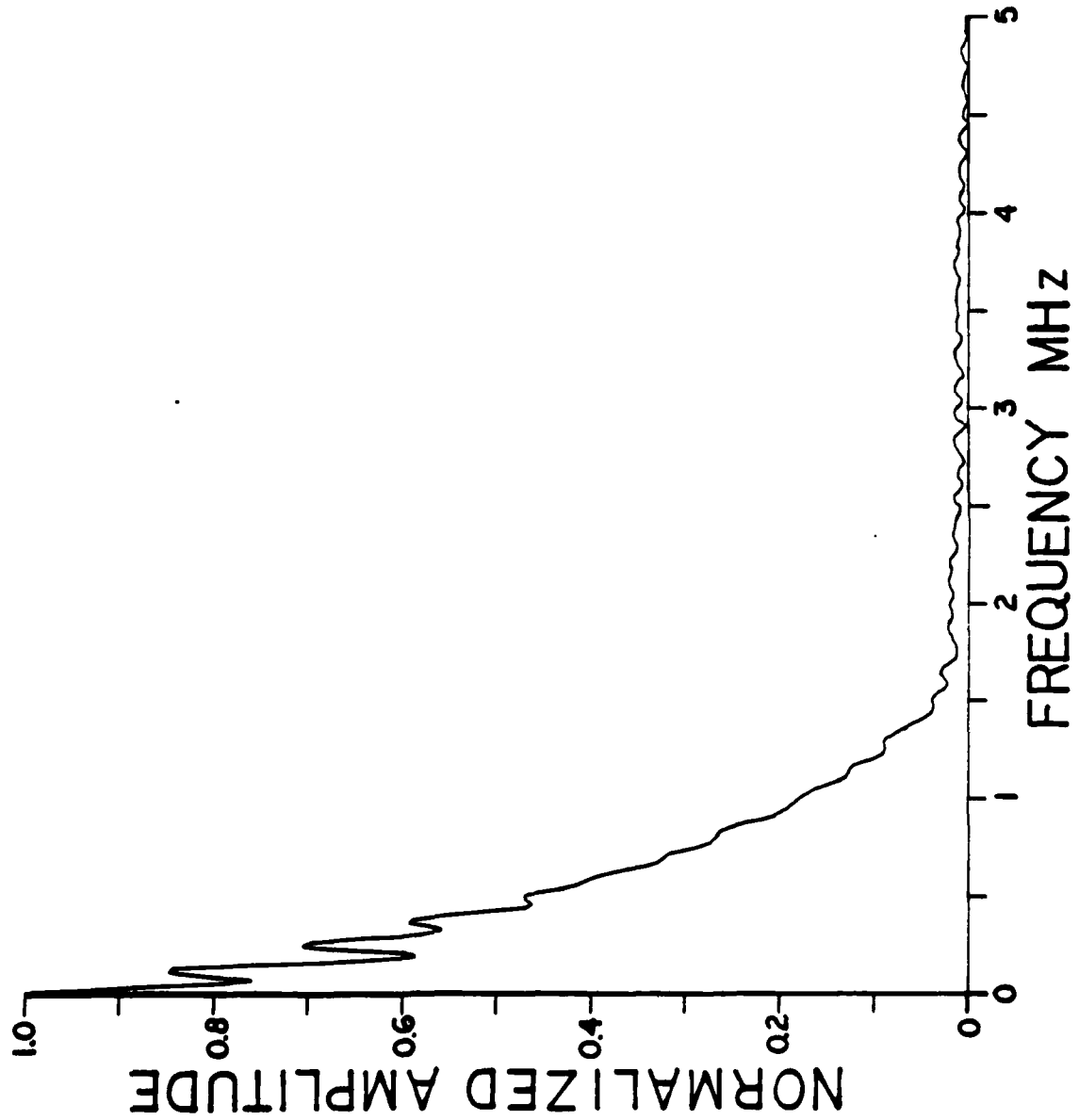

C7

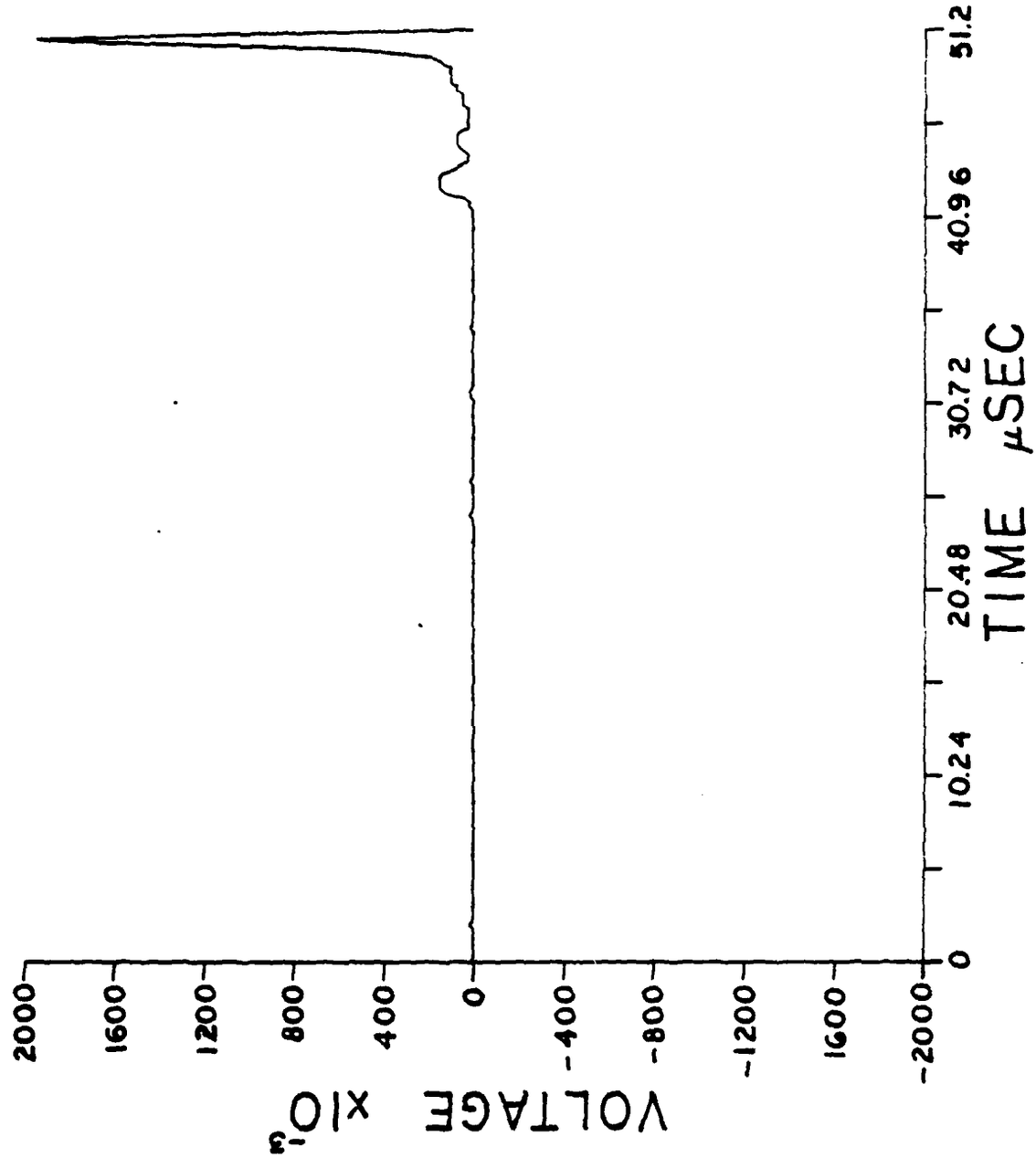
VOLTAGE x10⁻³
2000
1600
1200
800
400
0
-400
-800
-1200
1600
-2000
0
10.24
20.48
30.72
40.96
51.2
TIME μSEC

C8

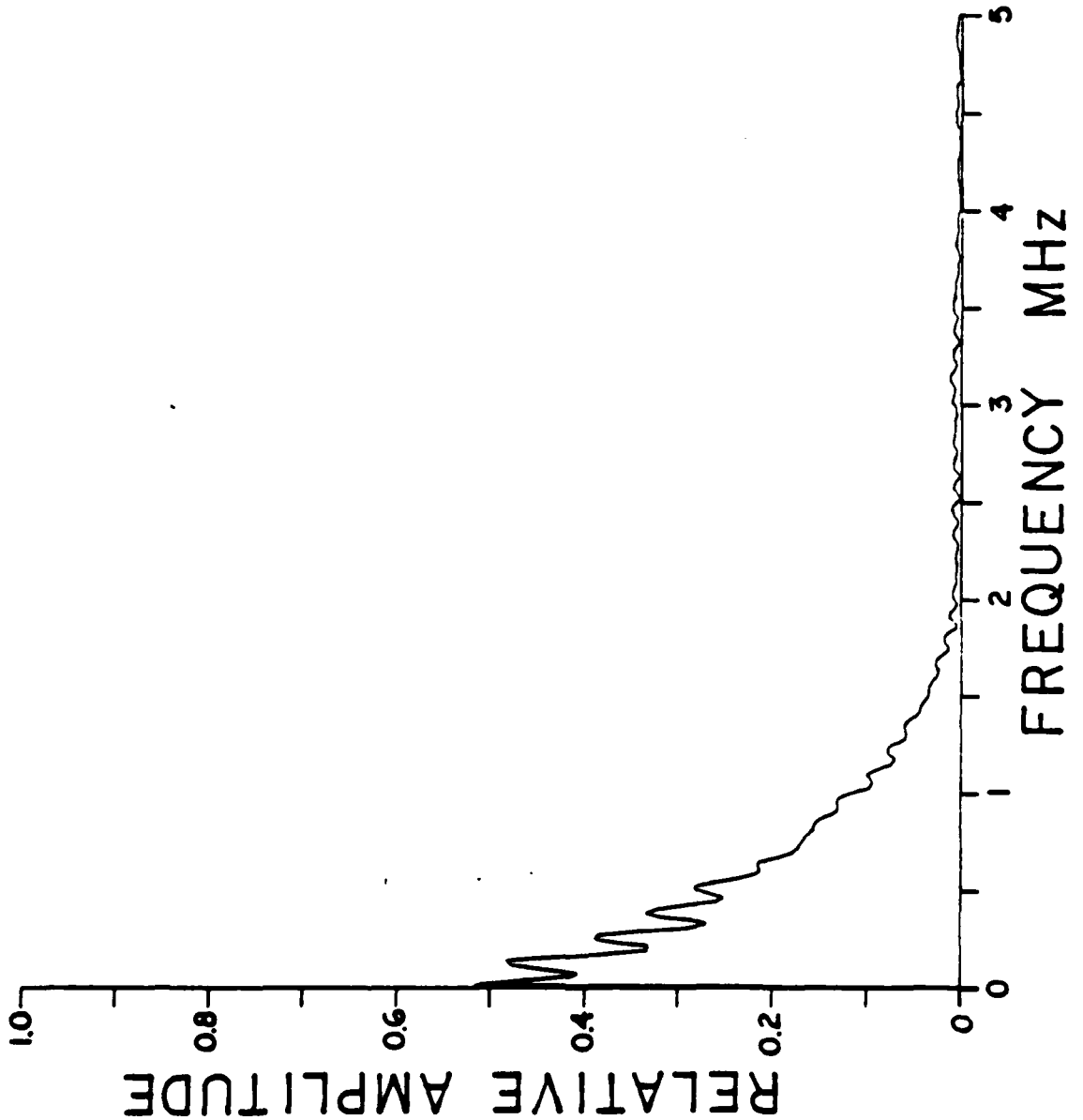

C9

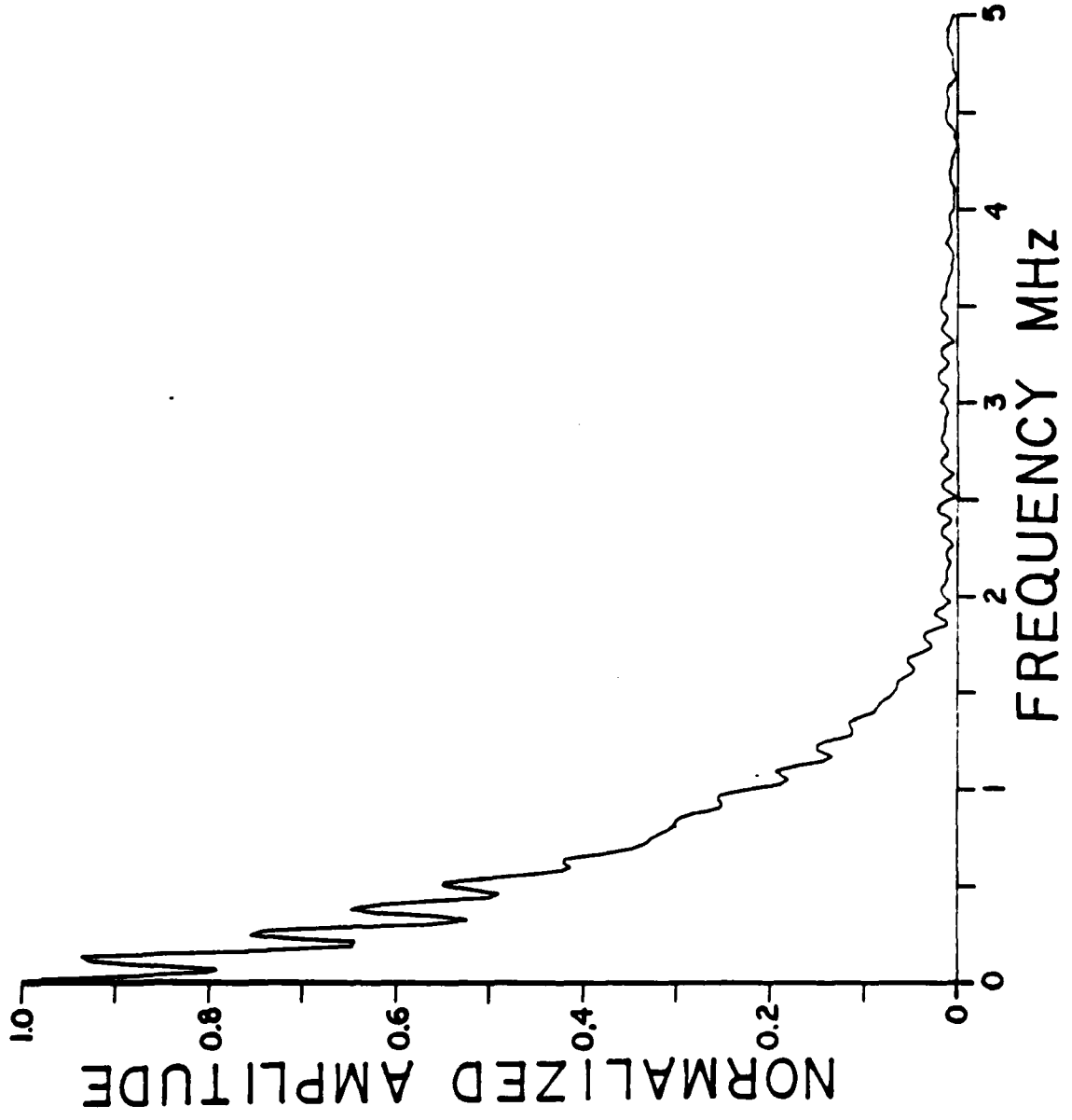

C10

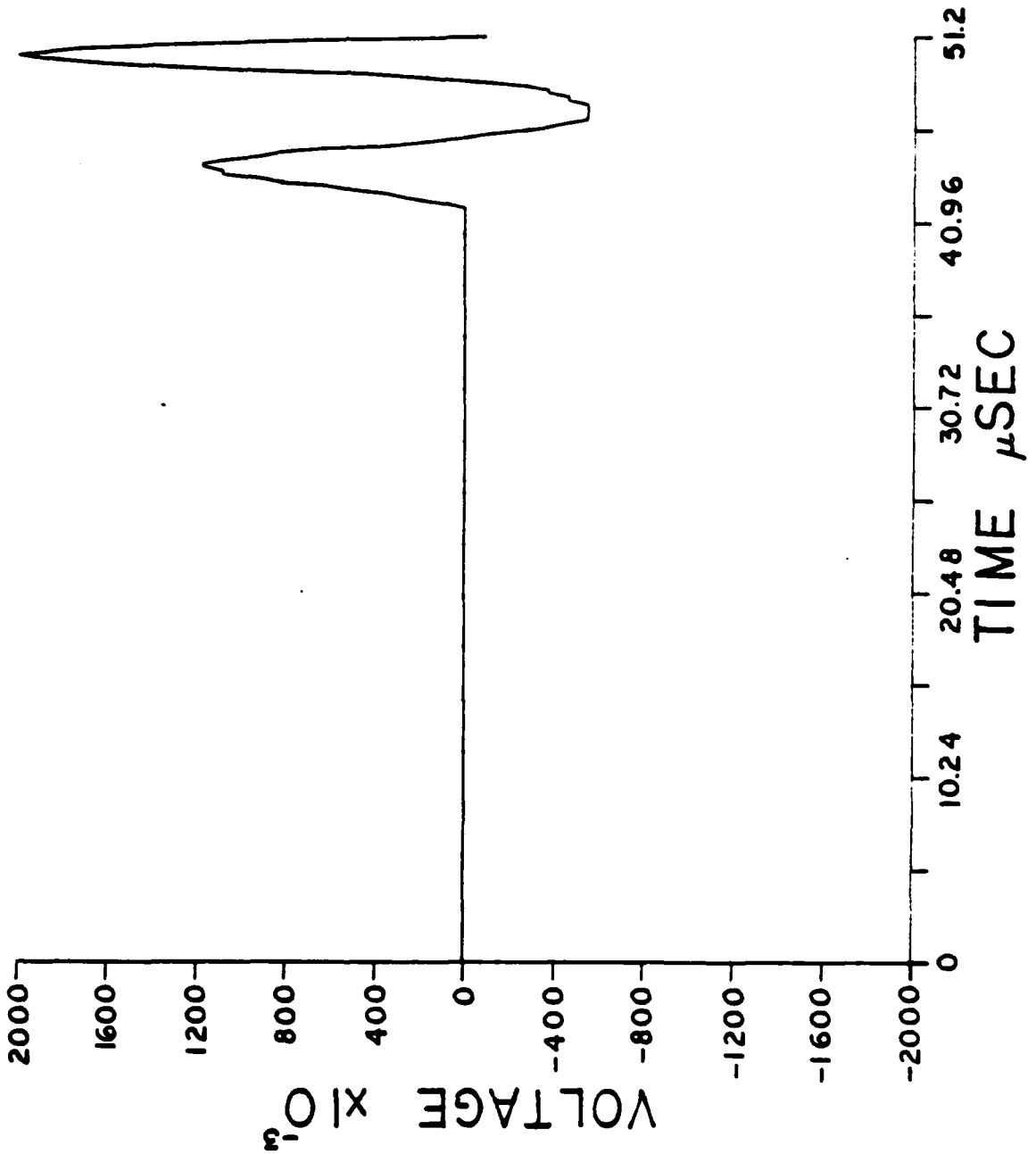
VOLTAGE x10⁻³
2000
1600
1200
800
400
0
-400
-800
-1200
-1600
-2000
0
10.24
20.48
30.72
40.96
51.2
TIME μSEC

C11

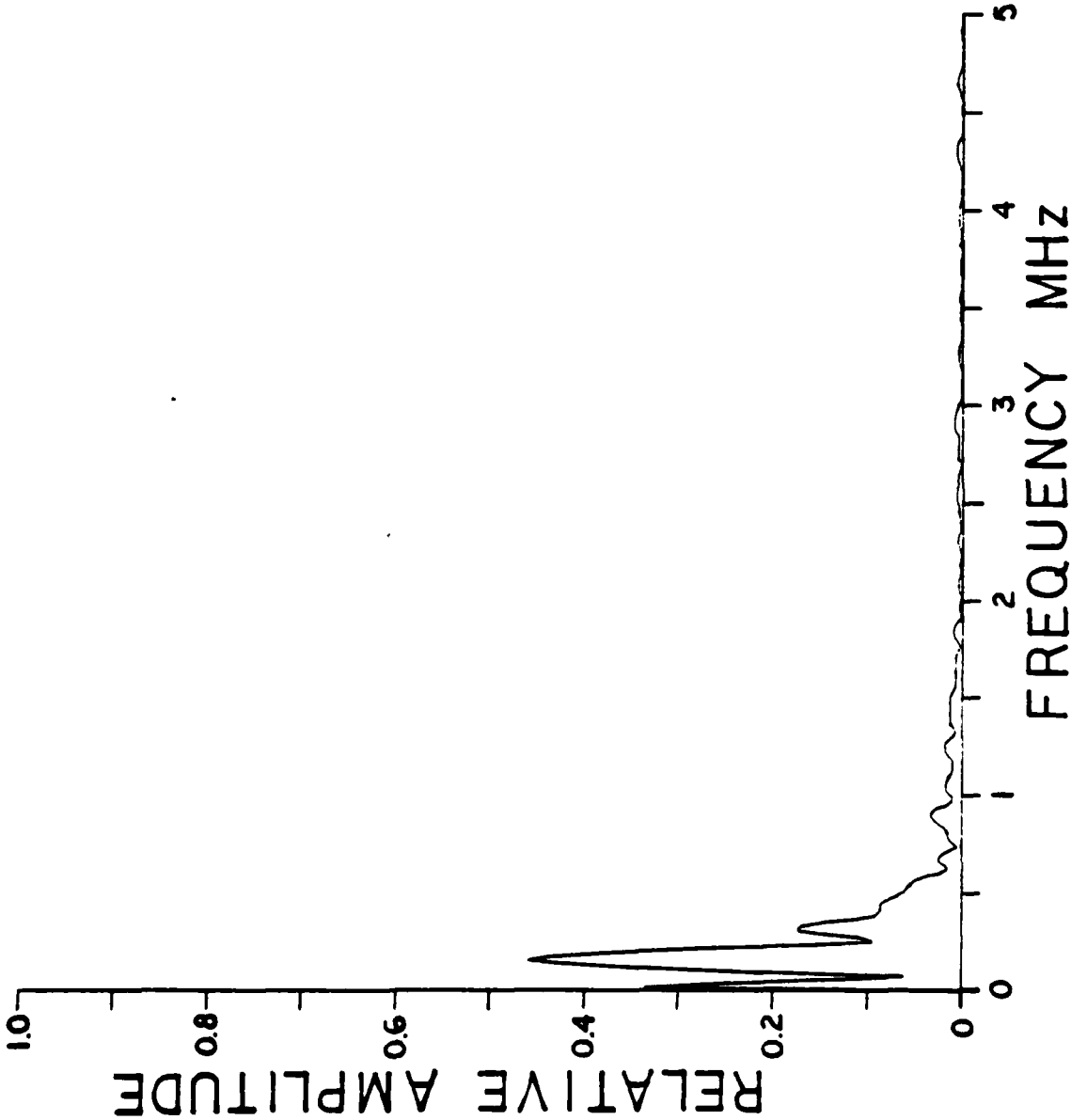

C12

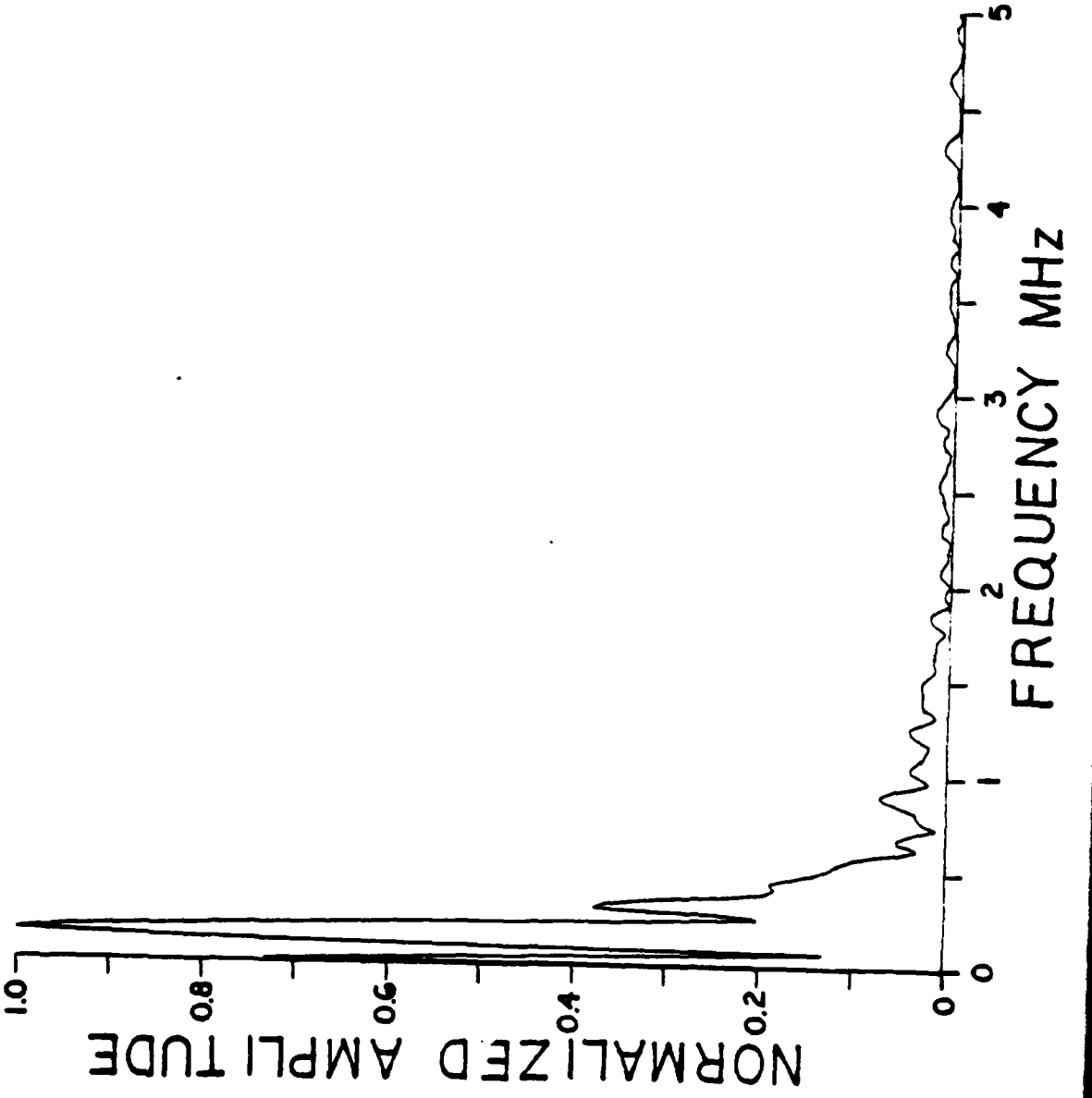

C13

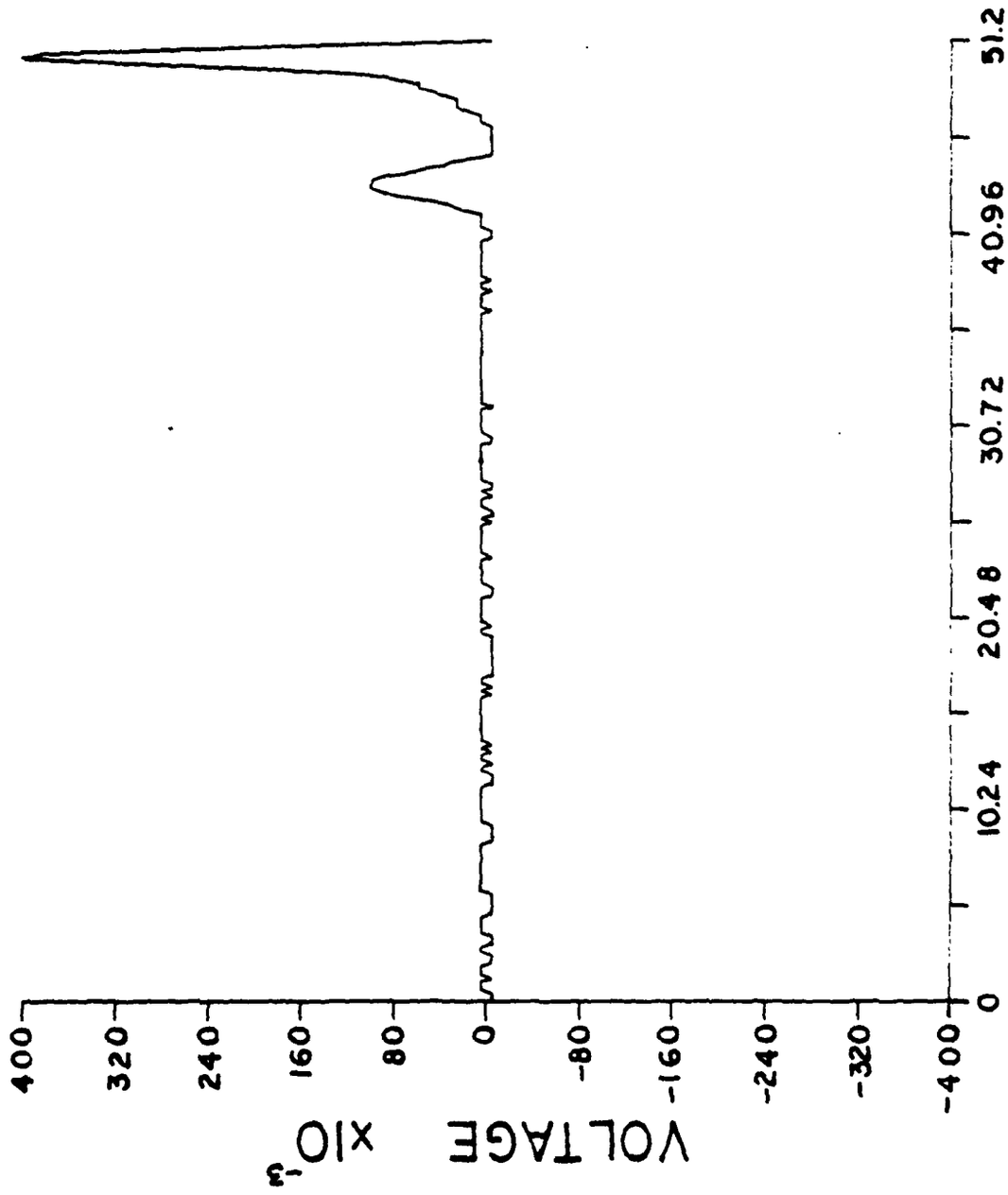
VOLTAGE x10⁻³
400
320
240
160
80
0
-80
-160
-240
-320
-400
0
10.24
20.48
30.72
40.96
51.2
TIME μSEC

C14

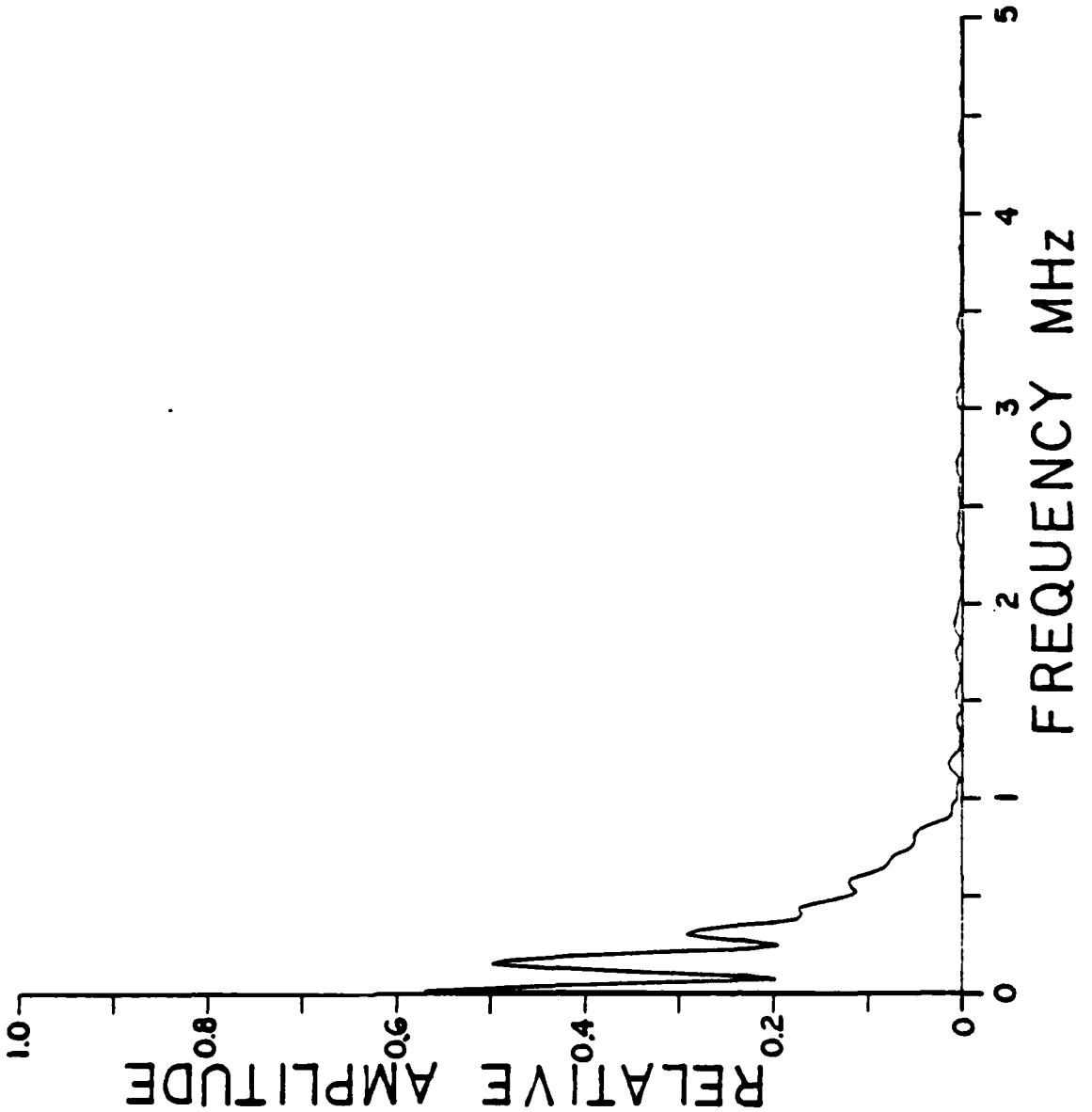

C15

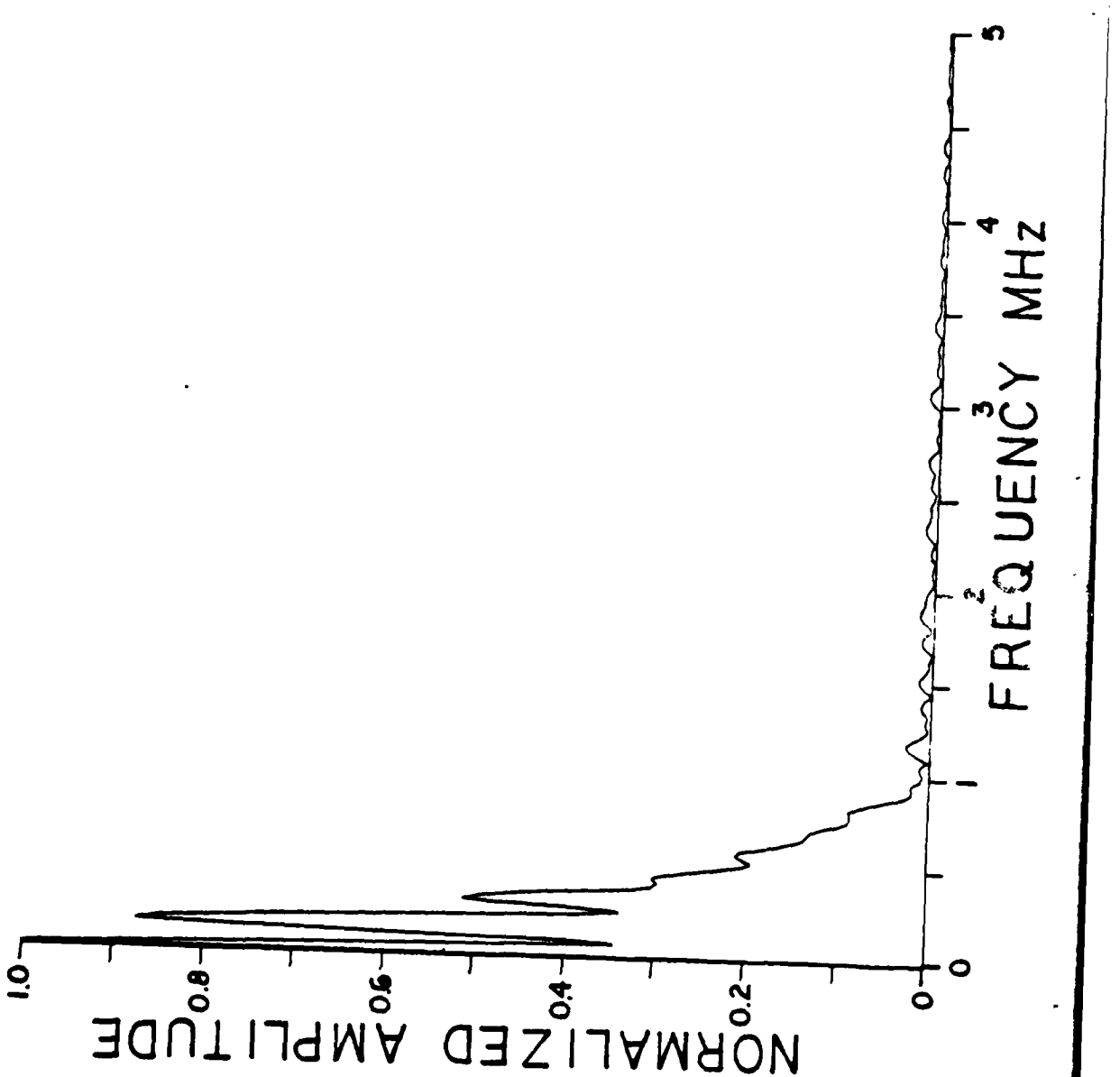

C16

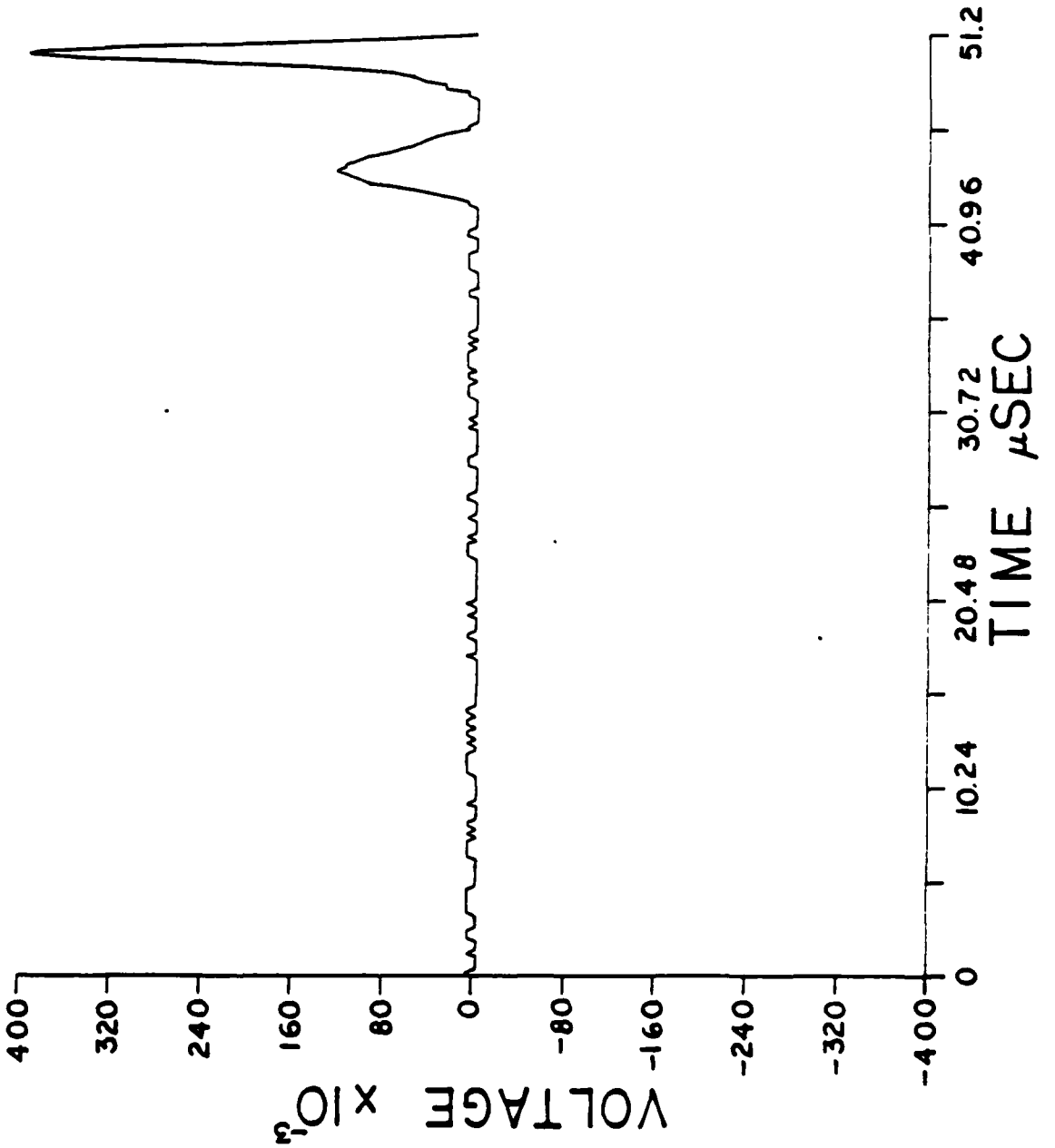
VOLTAGE x10³
400
320
240
160
80
0
-80
-160
-240
-320
-400
0
10.24
20.48
30.72
40.96
51.2
TIME μSEC

C17

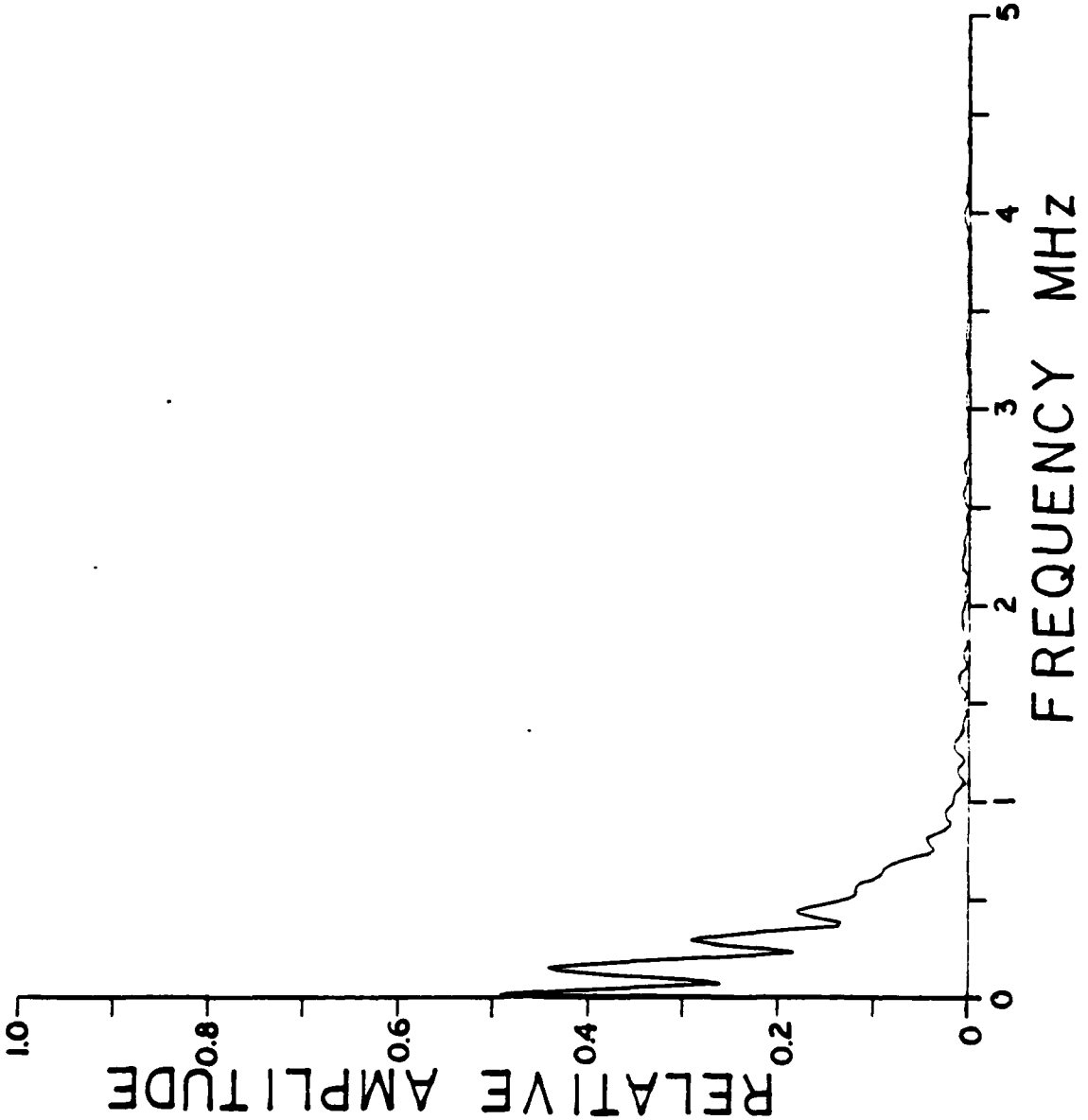

C18

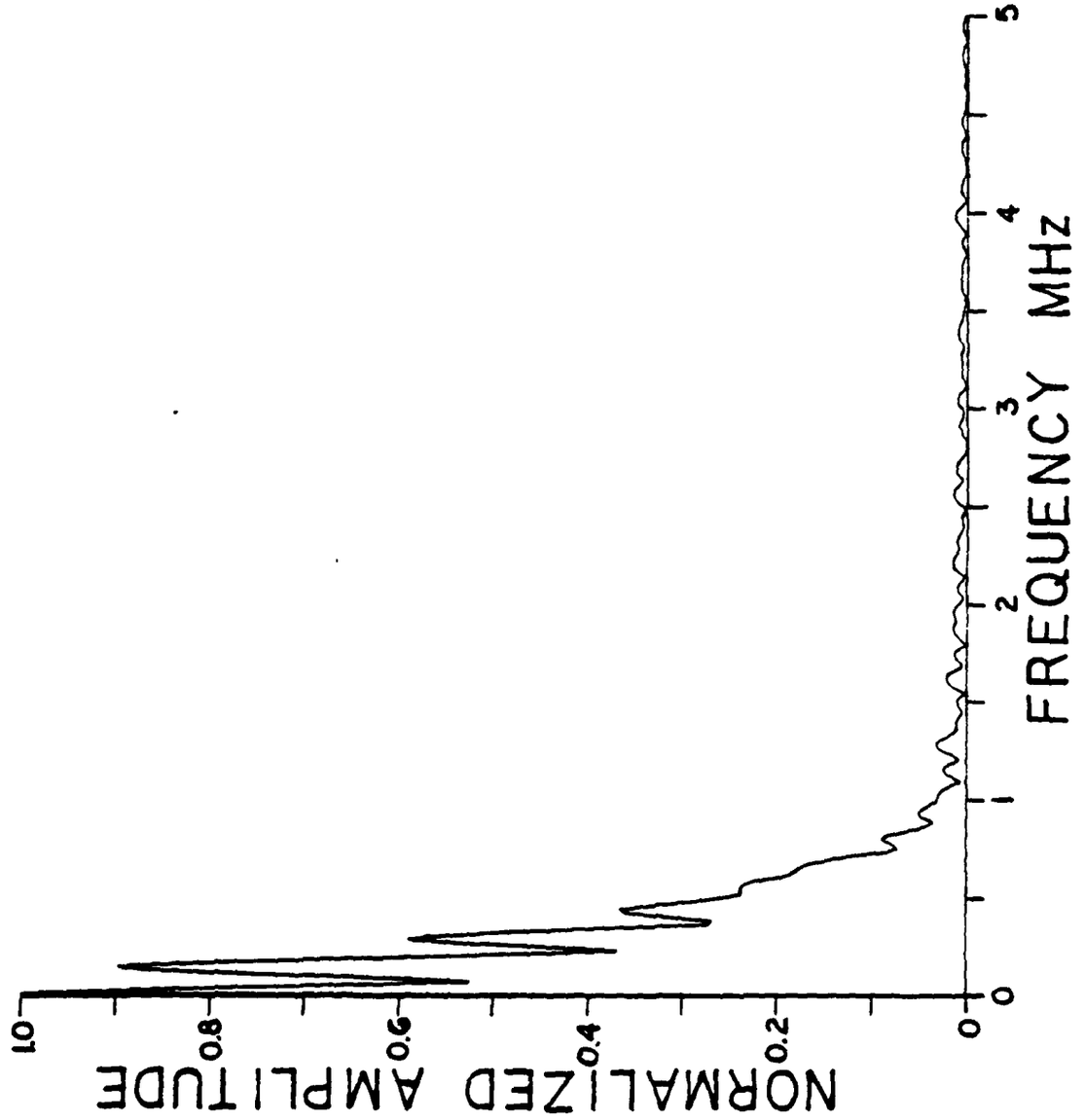

C19

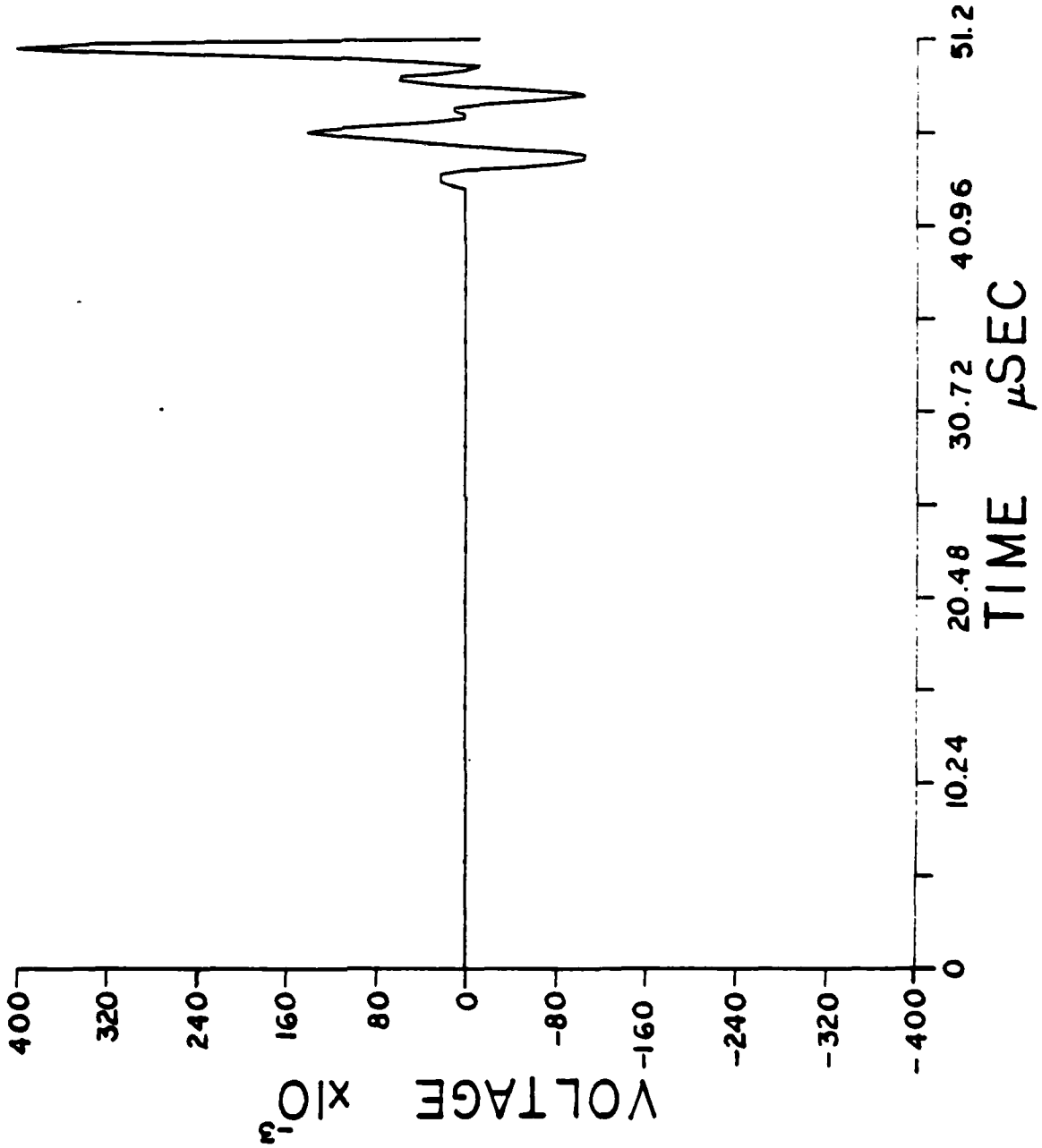
VOLTAGE x10⁻³
400
320
240
160
80
0
-80
-160
-240
-320
-400
0
10.24
20.48
30.72
40.96
51.2
TIME μSEC

C20

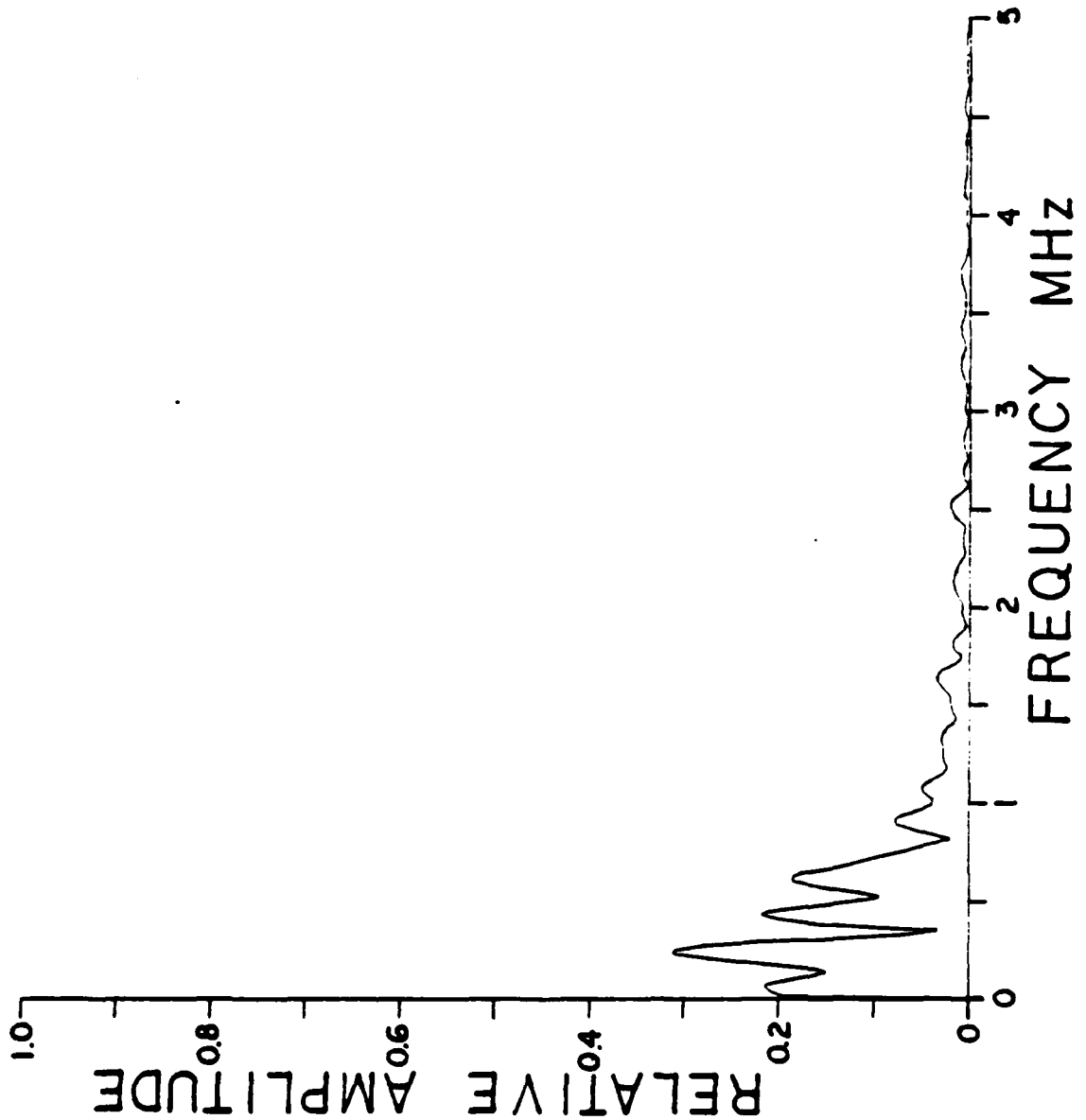

C21

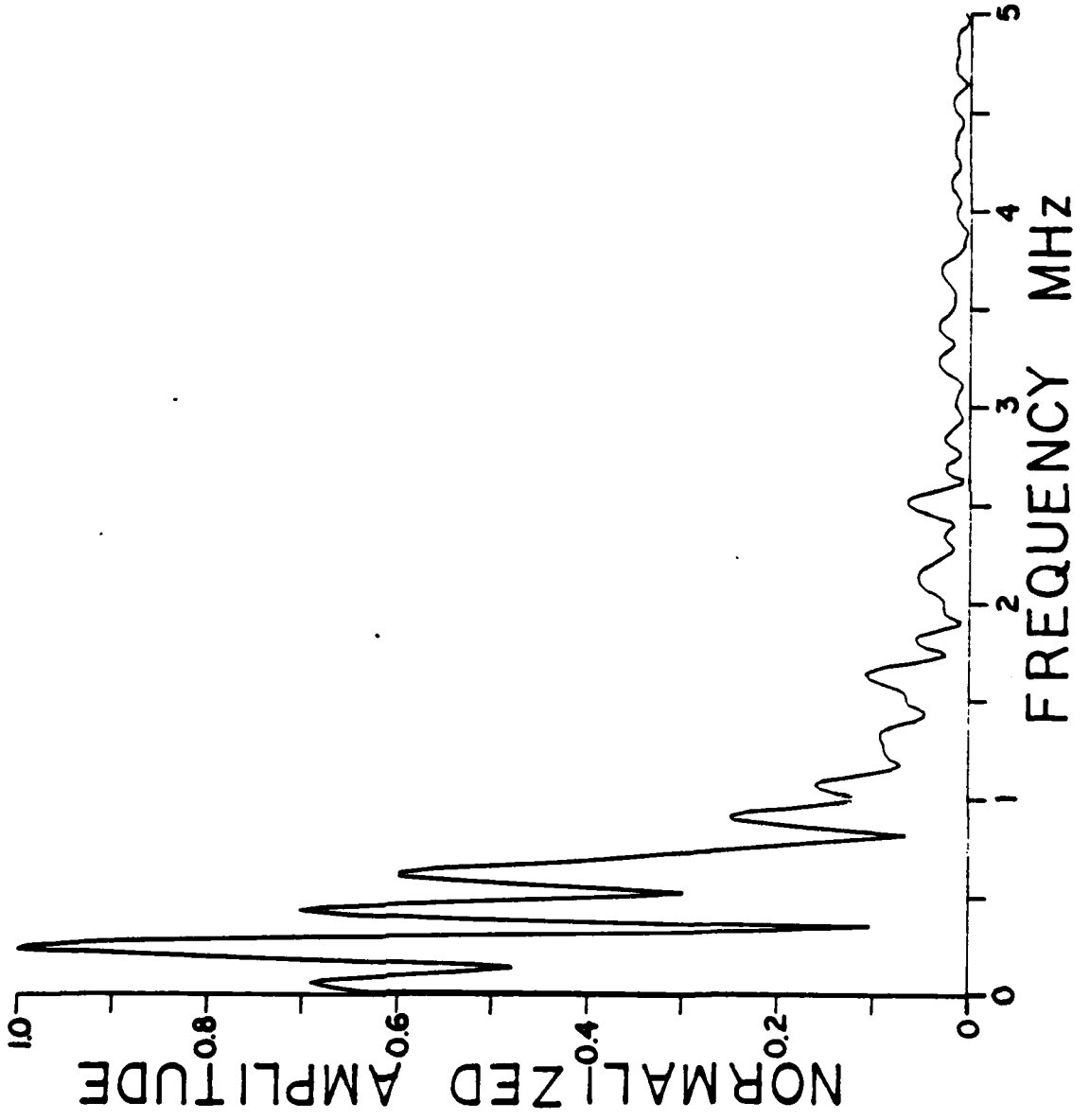

C22

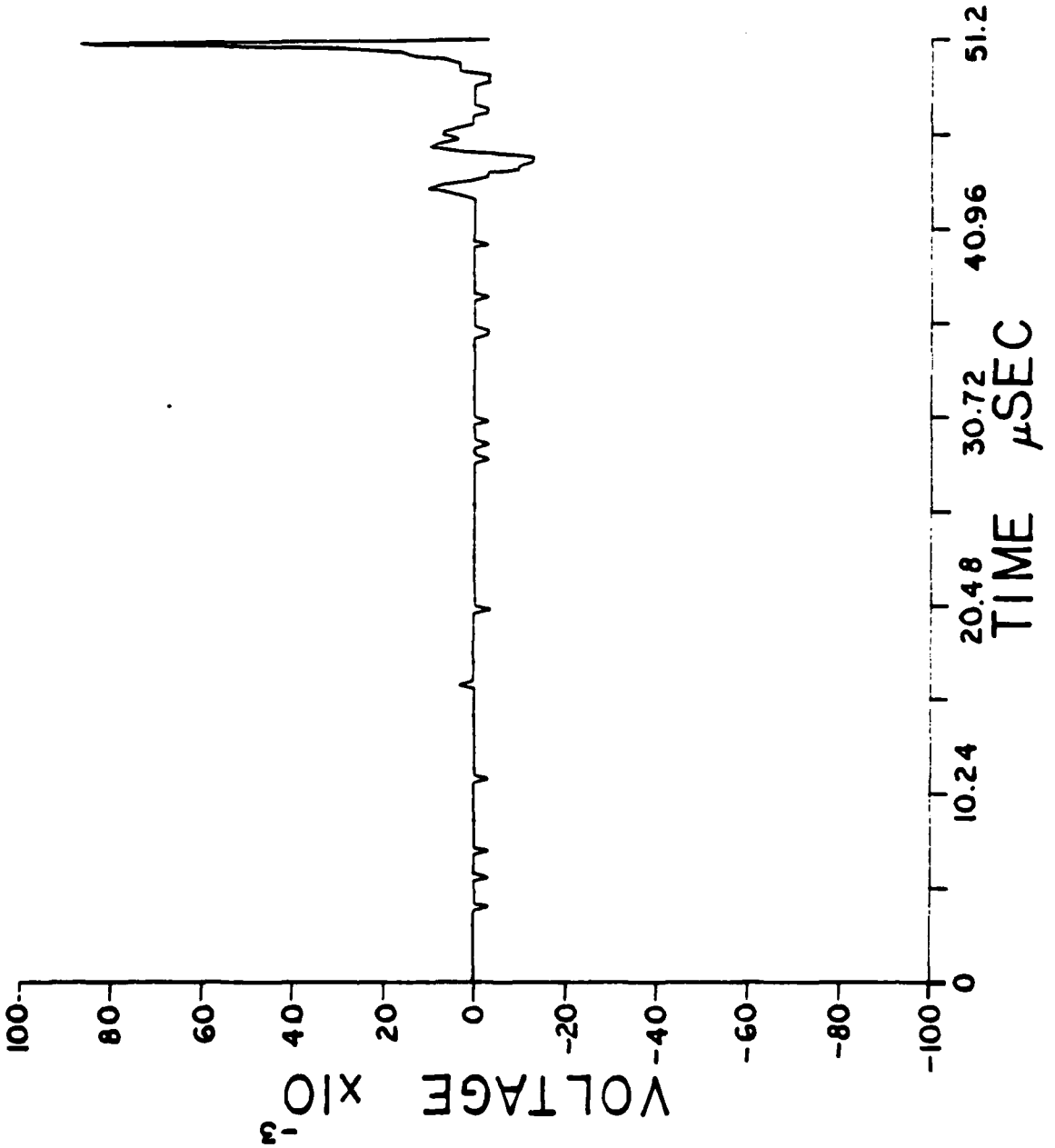
VOLTAGE x10^-3
100
80
60
40
20
0
-20
-40
-60
-80
-100
0
10.24
20.48
30.72
40.96
51.2
TIME μSEC

C23

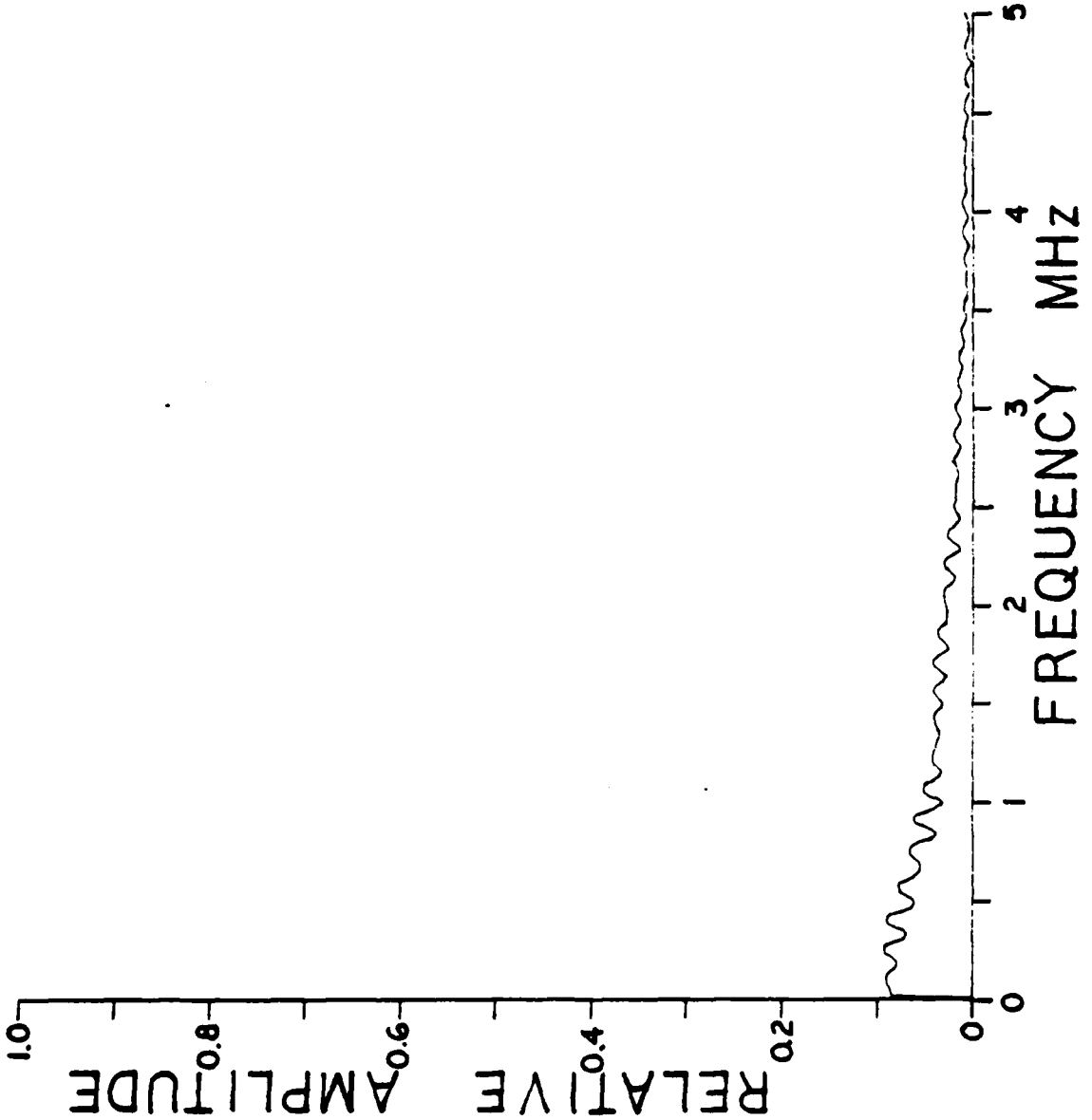

C24

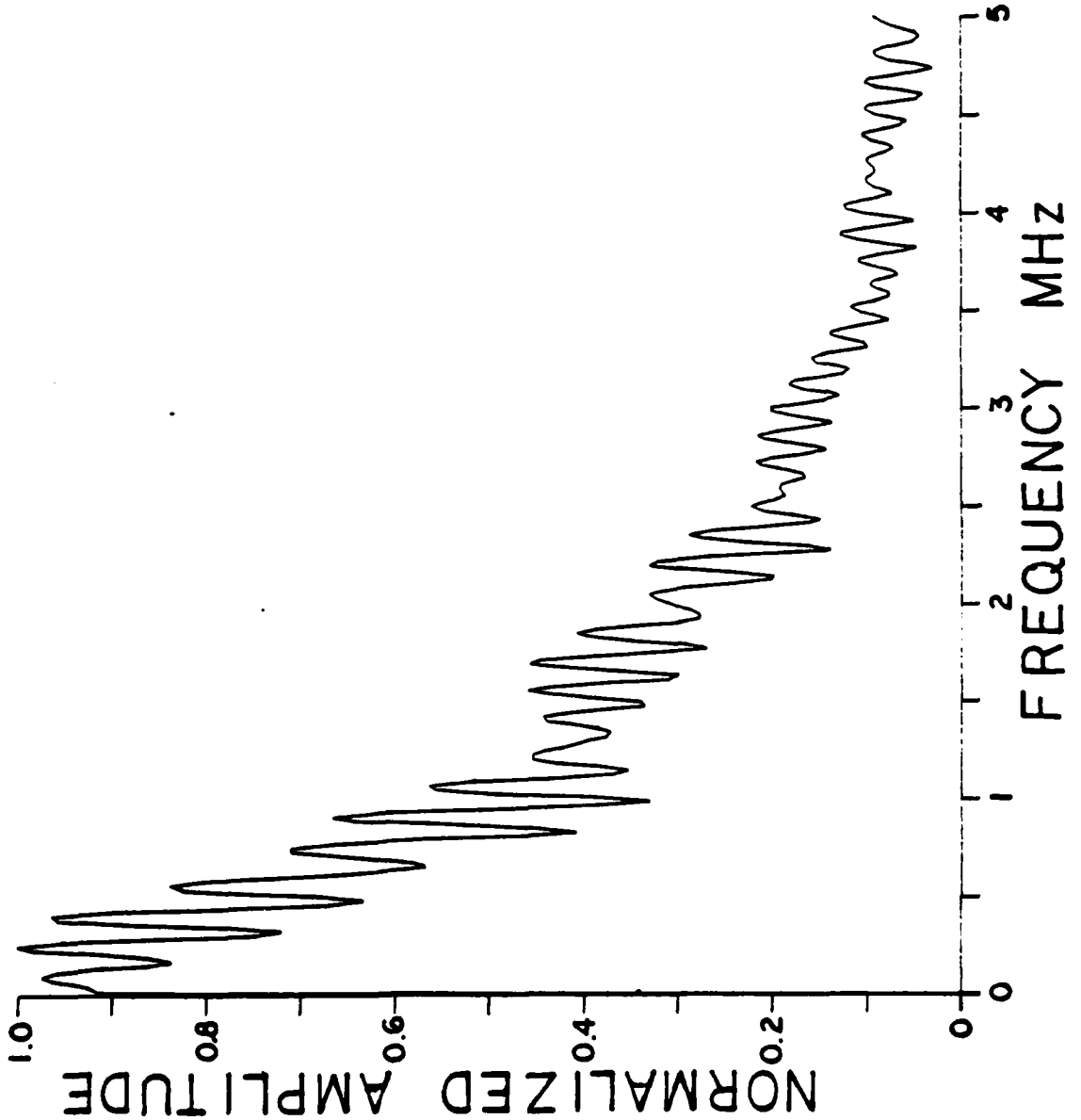

C25

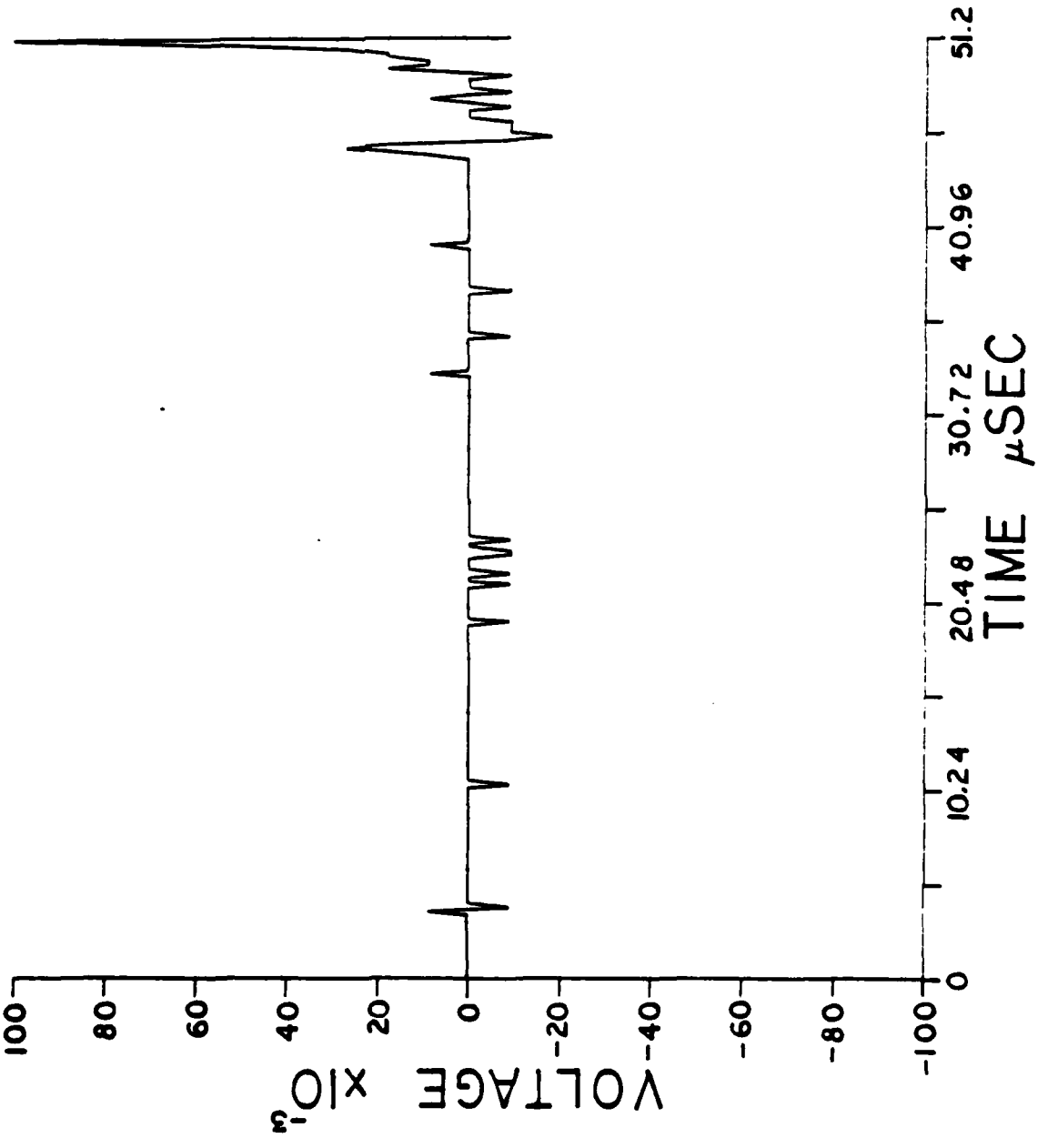
VOLTAGE x10⁻³
100
80
60
40
20
0
-20
-40
-60
-80
-100
0
10.24
20.48
30.72
40.96
51.2
TIME μSEC

C26

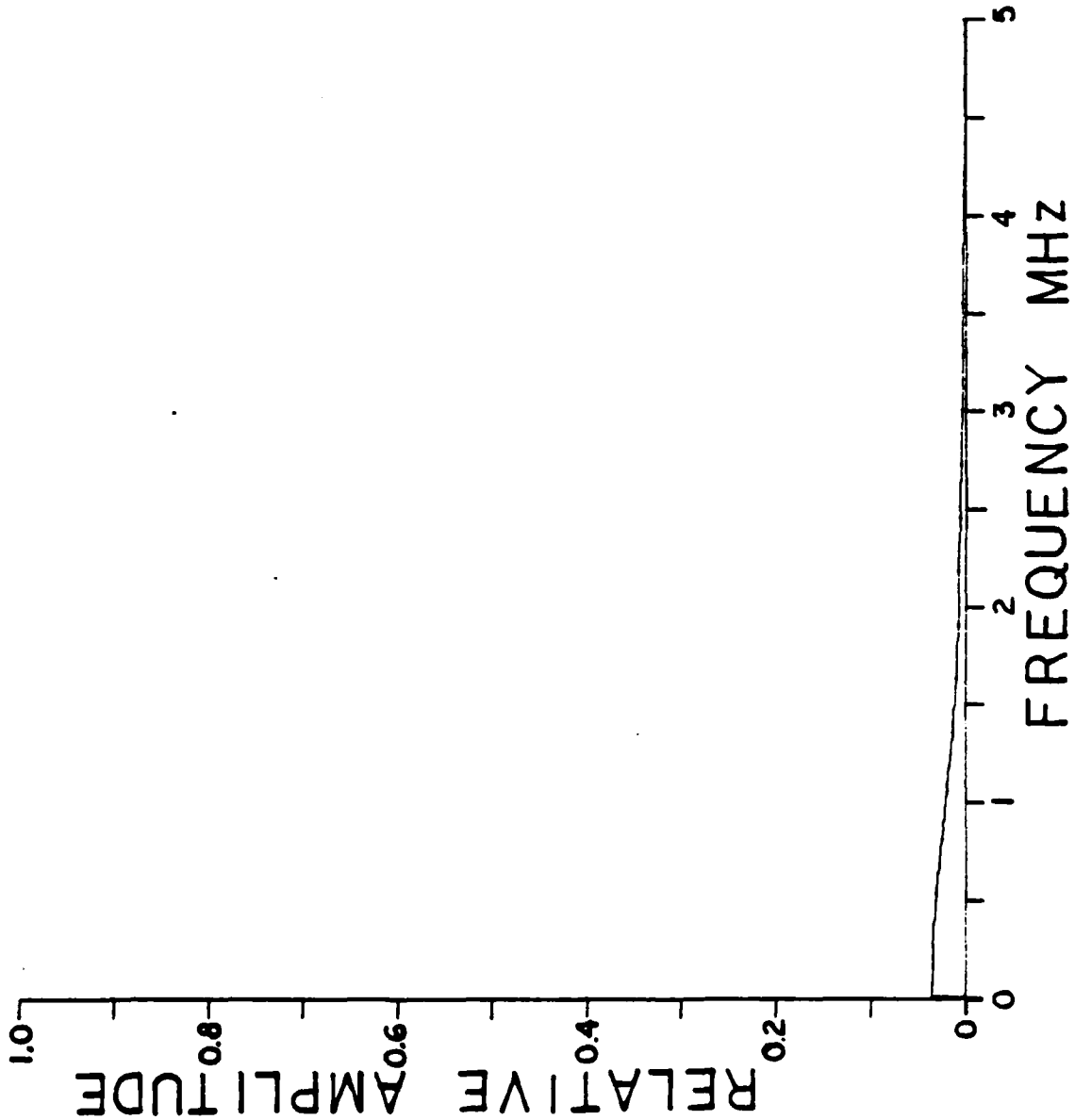

C27

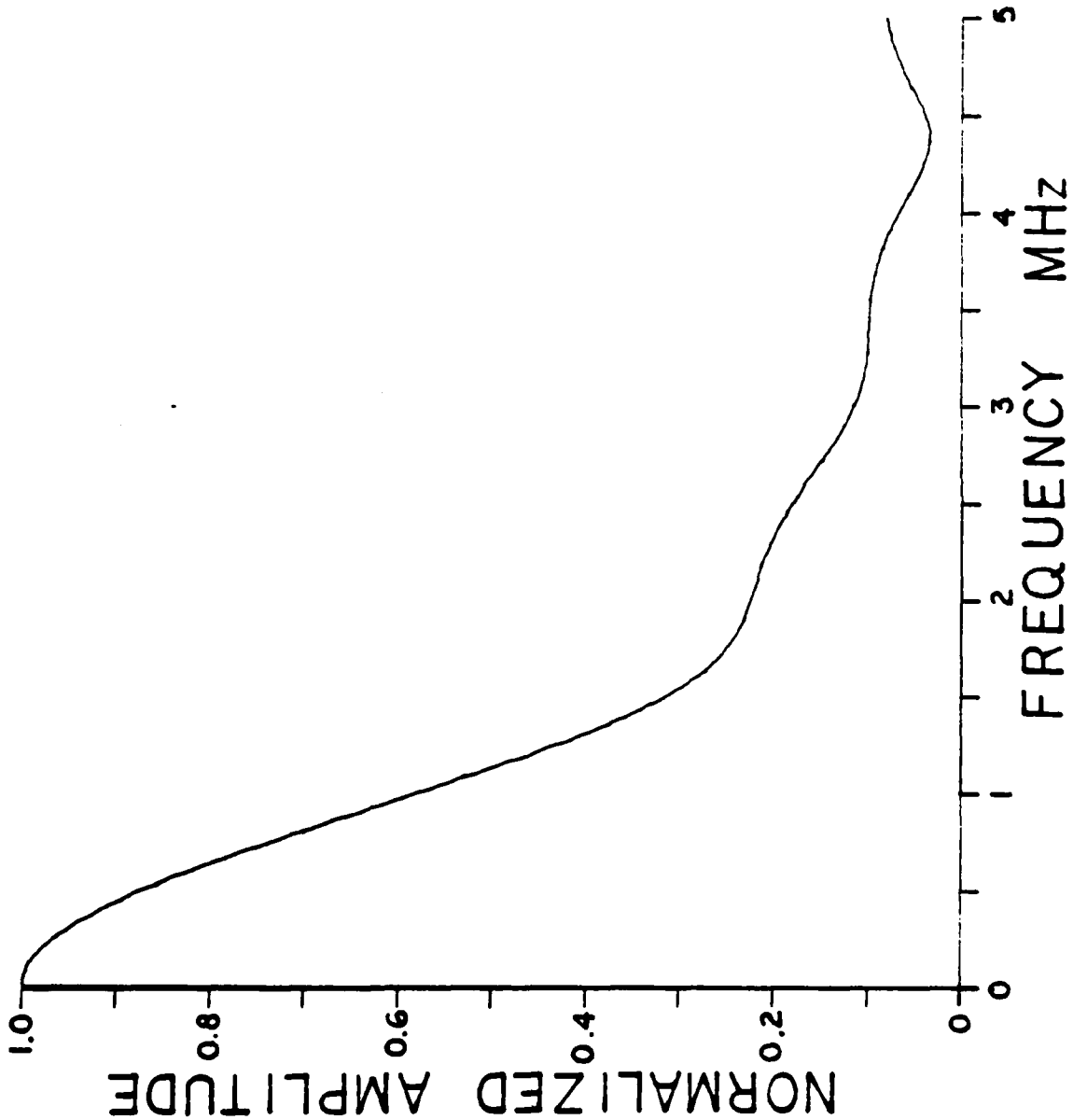

APPENDIX D

COMPUTER PROGRAMS

When preparing the Nicolet for proper interfacing with the IBM 5100 several initializing procedures must be performed to complete the link. The first change to make is in the Nicolet RS-232C interface; the "Dip" switches should be set as follows:

1	2	3	4	5	6	7	8
ON	ON	ON	ON	OFF	ON	ON	ON

(1 2 3) . Sets the band or transfer rate for this case - 9600 bps.

(4) Not used

(5) Parity Check 5 used when switch 5 is off.

(6) Sets the parity, ON = even, OFF = odd -used only if bit 5 = OFF.

(7) Sets number of stop bits, ON = 2 stop bits, OFF = 1 stop bit.

(8) Not used

When the RS-232C interface is set up as in the example, the Nicolet will dump its data at a transfer rate of 9600 bits per second with an even parity and two stop bits at the end of the file. Before the Nicolet will begin to transfer data it

must be given the proper sequence of commands. The command string which must be issued to the Nicolet is:

▼D1D0E300256

For an explanation of the command characters refer to the "IBM 5100 Serial I/O Adapter Feature User's Manual" and the "Operations Manual For Series 2090 Digital Oscilloscopes Nicolet Instrument Corporation."

The following program, written in APL, not only sets up the shared variable used in the APL command structure but also initiates the process whereby the Nicolet dumps its data into the buffer of the IBM 5100:

```
      ∇LOAD
    ∇ LOAD
[1]   J←1 ⎕SVO 'D1'
[2]   D1←'IN 33001'
[3]   J←D1
[4]   J←1 ⎕SVO 'D2'
[5]   D2←'OUT 31001'
[6]   D2←'I/1282,R/9600,H/P,C/T, <013,
      ¯<213'
[7]   D2←⍳0
[8]   D2←'OUT 32001 TYPE=I'
[9]   D2←'▼D1D0E300256'
[10]  D2←⍳0
[11]  DATA←⍬,(256 5 ⍴D1),(256⍴' ')
[12]  N←1
[13]  RPT:D2←'OUT 32001 TYPE=I'
[14]  D2←'▼D0E300256'
[15]  D2←⍳0
[16]  DATA←DATA,⍬,(256 5 ⍴D1),(256⍴' ')
[17]  →(15≥N←N+1)/RPT
[18]  J←⎕EX 'D1'
[19]  J←⎕EX 'D2'
[20]  TOTAPE
    ∇
```

To begin the transfer process insert the Serial I/O tape and issue the command)MODE COM. When the option menu is displayed select 7 for the track that is to be transferred and type LOAD on the IBM 5100. The I/O Active light, on the Nicolet, will come on for approximately five seconds and then go off for approximately ten seconds, this process is repeated fifteen times and indicates that the data is being transferred at a rate of 256 points per I/O Active. It is necessary to have the process repeated fifteen times during the transfer so the buffer on the IBM 5100 will not be exceeded. At the end of the process one track of data will have been stored in the IBM 5100.

To generate a frequency spectrum of the data the following program was initiated by typing MASTER on the IBM 5100:

```
      ∇MASTER
    ∇ MASTER;J;N;FIO;D;DATA
[1]  LBL1:⎕EX 'D2'
[2]   J←1 ⎕SVO 'D'
[3]   'ENTER FILE NUMBER'
[4]   N←⎕
[5]   'ENTER FILE ID'
[6]   FID←⍞
[7]   D←'IN ',(⍕1000+N),' ID=(',FID,')'
[8]   J←D
[9]   DATA←D
[10]  D
[11]  J←⎕EX 'D'
[12]  'ENTER CUTOFF VALUE'
[13]  N←⎕
```

```
[14]   DATA←1↓DATA[(N-1024)+⍳1024],0
[15]   'ZERO AVG=';(+/DATA[⍳100])÷100
[16]   'ENTER OFFSET VALUE'
[17]   N←⍞
[18]   DATA←DATA-N
[19]   'DO YOU WANT A TIMEPLOT? 0=NO, 1=YES'
[20]   →(0=⍞)/LBL3
[21]   ERASE
[22]   1000 2 TEKPLT(1+DATA[24+4×⍳250]÷⌈/|DATA) VS
       4×⍳250
[23]   AXIS
[24]  LBL3:'DO YOU WANT AN FFT? 0=NO, 1=YES'
[25]   →(0=⍞)/NEXT
[26]   DATA←GLITCH DATA
[27]   ERASE
[28]   DATA←RFFT DATA
[29]   DATA[1;1]←0
[30]   'DO YOU WANT TO PLOT THE FFT? 0=NO, 1=YES'
[31]   →(0=⍞)/LBL5
[32]   (5000000,⌈/DATA[1;]) TEKPLTΦ⍉ 2 257 ↑DATA
[33]   AXIS
[34]  LBL5:'DO YOU WANT TO STORE THE FFT ON TAPE?
       0=NO, 1=YES'
[35]   →(0=⍞)/NEXT
[36]  LBL4:TOTAPE
[37]  NEXT:'DO YOU WANT TO REDO THE TIME PLOT?
       0=NO, 1=YES'
[38]   →(1=⍞)/LBL1
[39]   'DO YOU WANT TO DO ANOTHER DATA FILE? 0=NO,
       1=YES'
[40]   →(1=⍞)/LBL1
[41]  LBL2:'YOU HAVE FINISHED !!!!!'
      ∇
```

Several variables and functions are necessary for both the LOAD program and the MASTER program to run properly. The following programs should be included in the work space of the IBM 5100 for the proper execution of MASTER and LOAD:

```
      ∇RFFT[□]∇
     ∇ Z←RFFT A;N;N1;N2;N3;N4;X;SAMPFREQ
[1]    ⍝
[2]    SAMPFREQ←20000000
[3]    A←⍉((N←0.5×⍴A),2)⍴A
[4]    A←¯1⌽⊖A÷N
[5]    FFT
[6]    Z←Z, 2 1 ↑Z←A
[7]    A←0
[8]    Z←(0,N4)⌽((N1↑Z)+⌽((-N1)↑Z))-⌽(-N1←2,
       N4←1+N2←N÷2)↑Z
[9]    Z[;N3]←(-⌿Z[;N3]×X),[0-0.5]++⌿Z[;N3←N4
       +⍳N4]×⌽[1] X←2 1 ∘.○0-0.5-((0←⍳1)-⍳N4)÷N
[10]   Z←0.5×((N1↑Z)+(-N1)↑Z, 0 1 ↓⌽(N1↑Z)-
       (-N1)↑Z
[11]   Z[0+1;⍳N4]←-Z[0+1;⍳N4]
[12]   Z←N×(+/[1] Z*2)*0.5
[13]   Z←(2,⍴Z)⍴(Z÷SAMPFREQ),SAMPFREQ×(÷2×N)
       ×0,⍳(⍴Z)-1
     ∇


      ∇FFT[□]∇
     ∇ FFT;K;L;M;N;O;P;Q;R;S;T;W
[1]    A←(2,R←(M←⌊2⊛N←¯1↑⍴A)⍴2)⍉⍴A
[2]    W←R⍴⍉ 2 1 ∘.○(-(O←⍳1)-⍳K)÷1↑S←(K←N÷2),T←2
[3]    →((M=1)/L3),L2,Q←(P←O+M-0.5)-L←1
[4]   L1:W←R⍴⍉(T,N÷T←T×2)⍴⍉(K⍴T↑1)⌿S⍴W
[5]   L2:A←(+⌿A),[P-L](-/W×-⌿A),[Q]+/W×⌽-⌿A
[6]    →(M>L←L+1)/L1
[7]   L3:A←⍉(N,2) (+⌿A),[0-0.5]-⌿A
     ∇


      ∇Q[□]∇
     ∇ Q
[1]   LBL:□EX 'D'
[2]    J←1 □SVO 'D'
[3]    'ENTER FILE NUMBER'
[4]    N←□
[5]    'ENTER FILE ID'
[6]    FID←□
[7]    D←'IN ',(⍕1000+N),' ID=(',FID,')'
[8]    J←D
[9]    ⌈/D
[10]   'DO YOU WANT TO DO ANOTHER FILE? 0=NO,
       1=YES'
[11]   →(1=□)/LBL
[12]   'YOU HAVE FINISHED !!!!'
     ∇
```

```
      ∇FUN[□]∇
    ∇ FUN C
[1]   D2←TEK[30]
[2]   →(15≥(ρC)[1])/6
[3]   D2←TEK[1+(XMC 15 2 ↑C)]
[4]   C← 14 0 ↓C
[5]   →2
[6]   D2←TEK[1+(XMC C)]
[7]   D2←TEK[32]
    ∇


      ∇PCHAR[□]∇
    ∇ V PCHAR C;X
[1]   ⍝L IS A GLOBAL CHARACTER VARIABLE
[2]   C[;1]←273+C[;1]×546÷V[1]
[3]   C[;2]←137+C[;2]×546÷V[2]
[4]   X←XMC 1 2 ↑C
[5]   CIBM[1+(,29,X),31],L
[6]   C← 1 0 ↓C
[7]   →(1≤(ρC)[1])/4
    ∇


      ∇PGRAF[□]∇
    ∇ V PGRAF C;X
[1]   C[;1]←273+C[;1]×546÷V[1]
[2]   C[;2]←137+C[;2]×546÷V[2]
[3]   →(10≥(ρC)[1])/8
[4]   X← 10 4 ρXMC 10 2 ↑C
[5]   CIBM[1+(,29,X,X[;4]),31]
[6]   C← 10 0 ↓C
[7]   →3
[8]   X←((ρC)[1],4)ρXMC C
[9]   CIBM[1+(,29,X,X[;4]),31]
    ∇


      ∇TOTAPE[□]∇
    ∇ TOTAPE
[1]   J←1 □SVO 'T'
[2]   'ENTER FILE NUMBER'
[3]   N←□
[4]   'ENTER FILE ID'
[5]   FID←□
[6]   T←'OUT ',(▼2000+N),' ID=(',FID,') TYPE=A'
[7]   T←DATA
[8]   T←⍳0
[9]   J←□EX 'T'
[10]  □EX 'DATA'
    ∇
```

```
        ∇TIMEPLOT[□]∇
      ∇ TIMEPLOT
[1]     J←1 □SVO 'D'
[2]     'ENTER FILE NUMBER'
[3]     N←□
[4]     'ENTER FILE ID'
[5]     FID←⍞
[6]     D←'IN ',(▼1000+N),' ID=(',FID,')'
[7]     J←D
[8]     DATA←D
[9]     D
[10]    J←□EX 'D'
[11]    4096 4096 TEKPLT(2048+DATA) VS↓4096
      ∇


        ∇FPLT[□]∇
      ∇ FPLT
[1]     □EX 'D2'
[2]    LBL:J←1 □SVO 'D'
[3]     'ENTER FILE NUMBER'
[4]     N←□
[5]     'ENTER FILE ID'
[6]     FID←⍞
[7]     D←'IN ',(▼1000+N),' ID=(',FID,')'
[8]     J←D
[9]     DATA←D
[10]    J←□EX 'D'
[11]    'GET PLOTTER READY AND TYPE A 1'
[12]    (5000000,⌈/DATA[1;]) TEKPLTΦQ 2 257 ↑DATA
[13]    AXIS
[14]    □EX 'DATA'
[15]    'DO YOU WANT TO DO ANOTHER DATA SET?
        0=NO, 1=YES'
[16]    →(1=□)/LBL
[17]    'YOU HAVE FINISHED !!!!!'
      ∇


        ∇GRAPH[□]∇
      ∇ V GRAPH X
[1]     X[;1]←273+X[;1]×546÷V[1]
[2]     X[;2]←137+X[;2]×546÷V[2]
[3]     FUN X
      ∇


        ∇GLITCH[□]∇
      ∇ T←GLITCH TEST
[1]     T←TEST×-¯1+(|TEST)≤48
      ∇
```

```
      ∇BPLOT[□]∇
    ∇ V BPLOT X;N;XLBL;YLBL;A
[1]   AXIS∆
[2]   XLBL←,XAXISLABEL,[1.5] 11 6 ↑(0,(((~×+/
      [1] ' '≠A)ι0)-1))↓A←⍕ 11 1 ρ0,(V[1]÷10)×ι10
[3]   YLBL←,YAXISLABEL,[1.5] 6 6 ↑(0,(((~×+/[1] ' '
      ≠A)ι0)-1))↓A←⍕ 6 1 ρ0,(V[2]÷5)×ι5
[4]   N←1
[5]  RPT:60↑XLBL
[6]   XLBL←60↓XLBL
[7]   60↑YLBL
[8]   YLBL←60↓YLBL
[9]   →(3≥N←N+1)/RPT
[10]  X[;1]←273+X[;1]×546÷V[1]
[11]  X[;2]←137+X[;2]×546÷V[2]
[12]  FUN X
    ∇


      ∇FPLOT[□]∇
    ∇ FPLOT
[1]   □EX 'D2'
[2]  LBL:J←1 □SVO 'D'
[3]   'ENTER FILE NUMBER'
[4]   N←□
[5]   'ENTER FILE ID'
[6]   FID←⍞
[7]   D←'IN ',(⍕1000+N),' ID=(',FID,')'
[8]   J←D
[9]   DATA←D
[10]  DATA[1;]←DATA[1;]÷0.0019667
[11]  J←□EX 'D'
[12]  'GET PLOTTER READY AND TYPE A 1'
[13]  5000000 1 TEKPLTΦQ 2 257 ↑DATA
[14]  AXIS
[15]  □EX 'DATA'
[16]  'DO YOU WANT TO DO ANOTHER DATA SET? 0=NO,
      1=YES'
[17]  →(1=□)/LBL
[18]  'YOU HAVE FINISHED !!!!!'
    ∇


      ∇PLOT[□]∇
    ∇ PLOT
[1]   N←1
[2]  RPT: 4096 4096 TEKPLT(2048+X[(256×N-1)+
      ι257]) VS(256×N-1)+ι257
[3]   →(16≥N←N+1)/RPT
    ∇
```

```
      ∇TEKPLT[□]∇
    ∇ V TEKPLT X
[1]   DIGPLT
[2]   X[;1]←225+X[;1]×700÷V[1]
[3]   X[;2]←75+X[;2]×700÷V[2]
[4]   FUN X
[5]   J←□EX 'D1'
[6]   J←□EX 'D2'
    ∇


      ∇DIGPLT[□]∇
    ∇ DIGPLT
[1]   J←1 □SVO 'D1'
[2]   D1←'OUT 31001'
[3]   D1←'R/1200'
[4]   D1←⍳0
[5]   J←1 □SVO 'D2'
[6]   D2←'OUT 34001 TYPE=I'
    ∇


      ∇AXIS[□]∇
    ∇ AXIS
[1]   V←30⍴ 0 0  2
[2]   B← 0 10 10 10 20 20 20 30 30 30 40 40 40 50
      50 50 60 60 60 70 70 70 80 80 80 90 90 90
      100 100
[3]   100 100 TEKPLT V VS B
[4]   100 100 TEKPLT B VS V
    ∇


      ∇FFT[□]∇
    ∇ Z←FFT A
[1]   FFT
[2]   Z←A
    ∇


      ∇XMC[□]∇
    ∇ Z←XMC X
[1]   ΔXML←Z←,((⍴X)⍴(32 96 32 64))+X←(⌊(X÷32),
      32|X)[;2 4 1 3]
    ∇


      ∇VS[□]∇
    ∇ Z←Y VS X
[1]   Z←X,[1.5] Y
    ∇
```

```
        B
0 10 10 10 20 20 20 30 30 30 40 40 40 50 50 50 60 60
       60 70 70 70 80 80 80 90 90 90 100 100


        V
0 0 ¯2 0 0 ¯2 0 0 ¯2 0 0 ¯2 0 0 ¯2 0 0 ¯2 0 0 ¯2 0 0
      ¯2 0 0 ¯2 0 0 ¯2


        AXIS∆
≤I∨?≤I9⌈ ≤I∨?≤D∨? ≤I≠∆≤D≠∆ ≤I÷≥≤D÷≥ ≤I+↓≤D+↓ ≤I/'≤D/'
≤I⊥≤D⊥ ≤I2↑≤D2↑ ≤I4○≤D4○ ≤I6_≤D6_ ≤I7#≤D7# ≤I9⌈≤D9⌈
≤I∨?5K∨? ≤I∨?≤I∨□ >%∨?>%∨□ ]V∨?]V∨□ ∧M∨?∧M∨□ ÷C∨?÷C∨□
,Z∨?,Z∨□ .Q∨?.Q∨□ 0G∨?0G∨□ 1$∨?1$∨□ 3T∨?3T∨□ 5K∨?5K∨□


        GRID
≤I∨?5K∨? ≤I≠∆5K≠∆ ≤I÷≥5K÷≥ ≤I+↓5K+↓ ≤I/'5K/' ≤I⊥5K1⊥ ≤I2↑
≤I2↑5K2↑ ≤I4○5K4○ ≤I6_5K6_ ≤I7#5K7# ≤I9⌈5K9⌈ ≤I∨?≤I9⌈ >%∨?
>%∨?>%9⌈ ]V∨?]V9⌈ ∧M∨?∧M9⌈ ÷C∨?÷C9⌈ ,Z∨?,Z9⌈ .Q∨?.Q9⌈ 0G∨?
0G∨?0G9⌈ 1$∨?1$9⌈ 3T∨?3T9⌈ 5K∨?5K9⌈ 7@


        TEK                ∈ ρ !¨#$%&'()*+,-./0123456789:;<=>?
@ABCDEFGHIJKLMNOPQRSTUVWXYZ[\]∧_∆ABCDEFGHIJKLMNOPQRSTUVWXY
Z≤≠≥=~ω


        ∆XML
56 103 39 65 103 38 83


        X
1 2 3 4 5 6 7 8 9 10


        CIBM - Use this when plotting on graphics terminal.
                                  ¨)<≤=>]∨∧≠÷,+./0123456789([;×:\
¯α⊥∩⌊∈∇∆ι○'□|TO*?ρ⌈~↓∪ω⊃↑⊂←#→≥-%ABCDEFGHIJKLMNOPQRSTUVWXY
Z-"&$@

        XAXISLABEL      YAXISLABEL      ERASE
        <K]#            ≤A>'
        )U∧⌈            ]N>'
        <K÷ι            ≠->'
        )U+¯            .I>'
        <K.∪            1V>'
        )U0←            5C>'
        <K2⌊
        )U3⊂
        <K5?
        )U7∇
        <K8≥
```

APPENDIX E

SPECIMEN CHARACTERIZATION WAVEFORMS

The following figures are the waveforms recorded from the various specimens characterized. In each case two inch incremental placements of the probe were made beginning at two inches from the source. The waveforms were recorded at ±4 volts full scale for NBS-PZT #26 and ±2 volts full scale for the APL laser interferometer. Recording time was 50 nanoseconds per point for all figures except Figs. E16-E29 where the recording time was 200 nanoseconds per point.

Figs. E1-E15	NBS-PZT #26 on solid cylinder
Figs. E16-E29	APL laser interferometer on solid cylinder
Figs. E30-E44	NBS-PZT #26 on solid cylinder
Figs. E45-E59	NBS-PZT #26 on rectangular bar
Figs. E60-E67	NBS-PZT #26 on I-beam
Figs. E68-E75	NBS-PZT #26 on pipe

E1

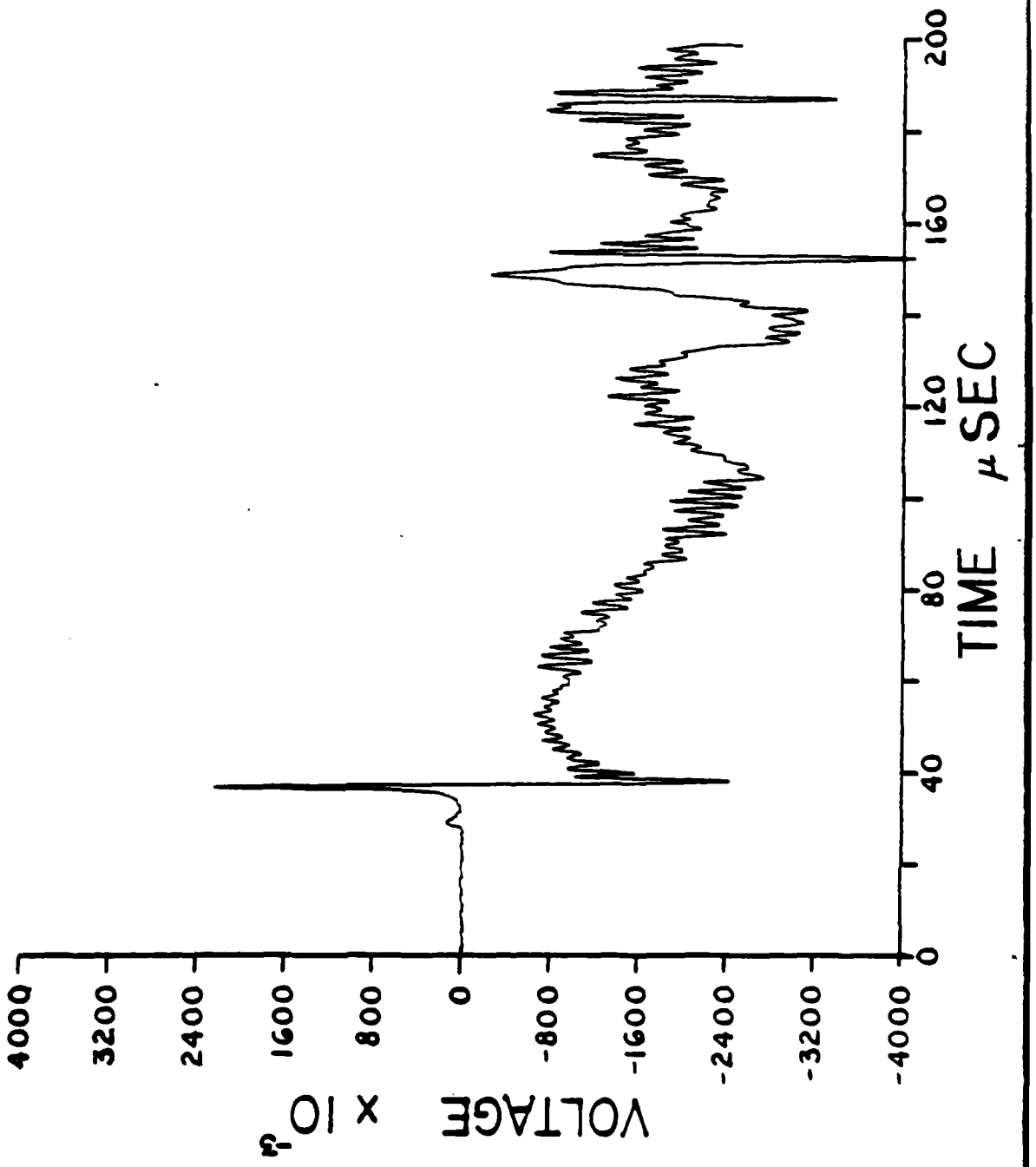
VOLTAGE x 10^-3
4000
3200
2400
1600
800
0
-800
-1600
-2400
-3200
-4000
0
40
80
120
160
200
TIME μSEC

E2

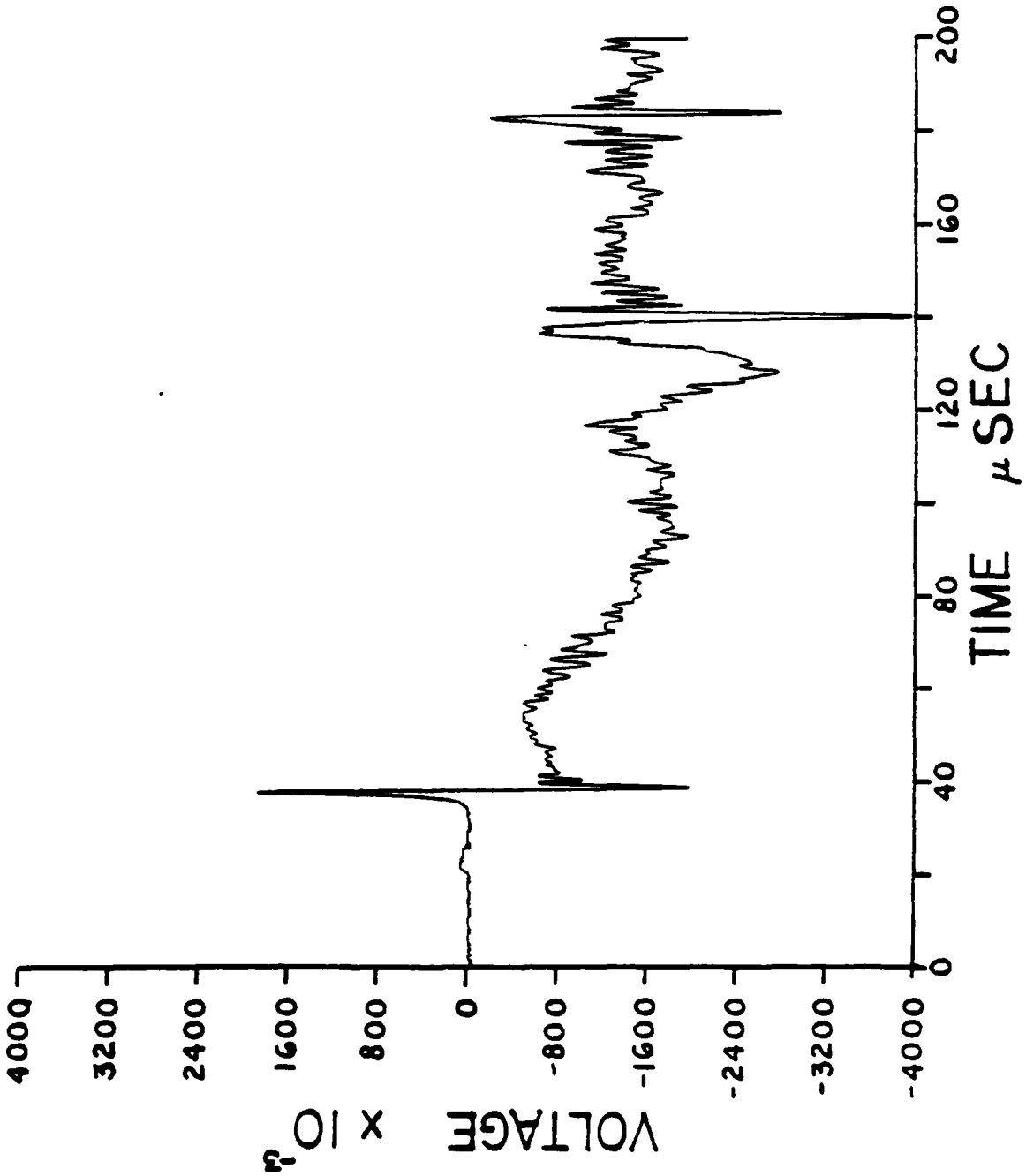
VOLTAGE x 10³
4000
3200
2400
1600
800
0
-800
-1600
-2400
-3200
-4000
0
40
80
120
160
200
TIME μSEC

E3

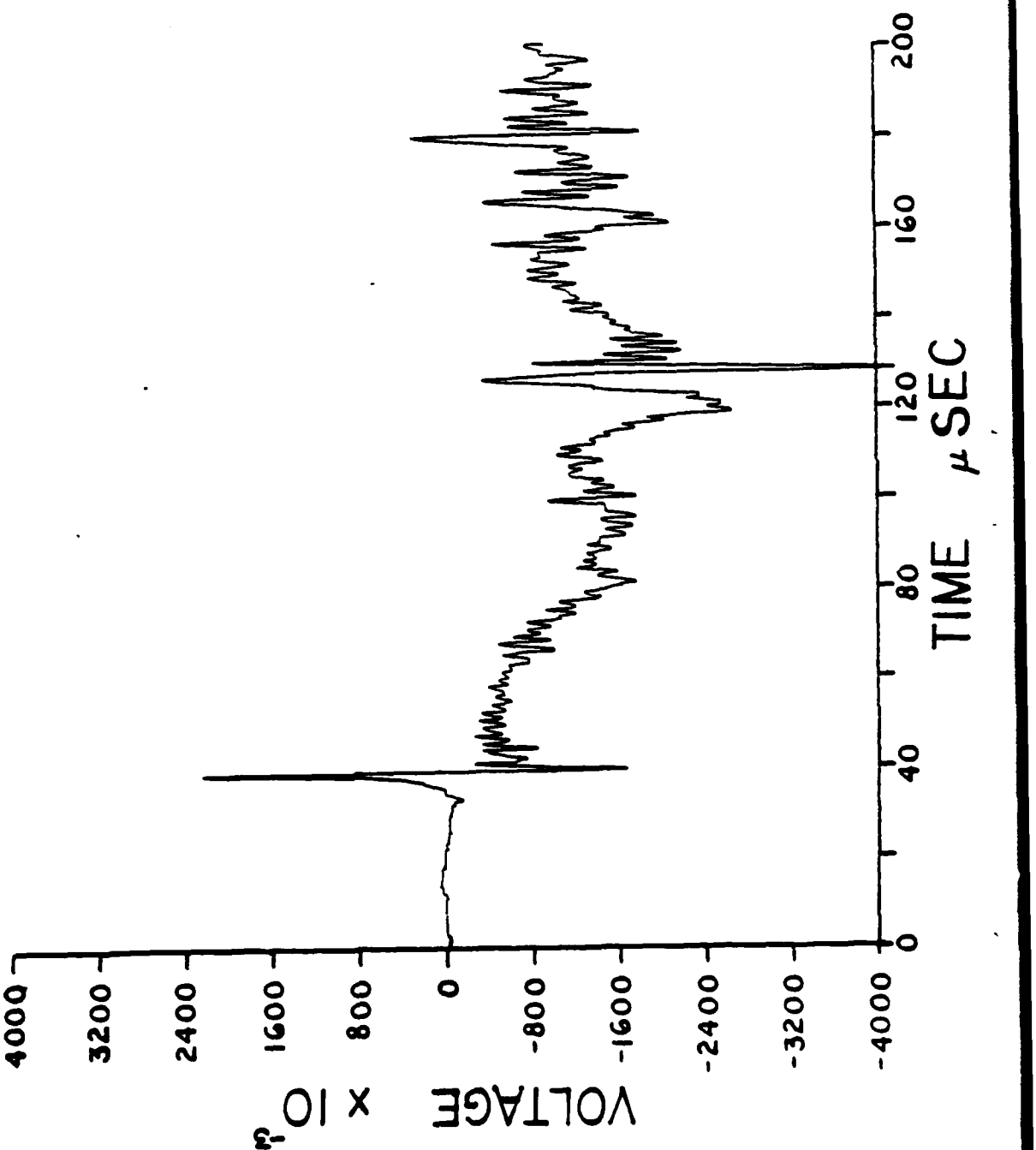
VOLTAGE x 10³
4000
3200
2400
1600
800
0
-800
-1600
-2400
-3200
-4000
0
40
80
120
160
200
TIME μSEC

E4

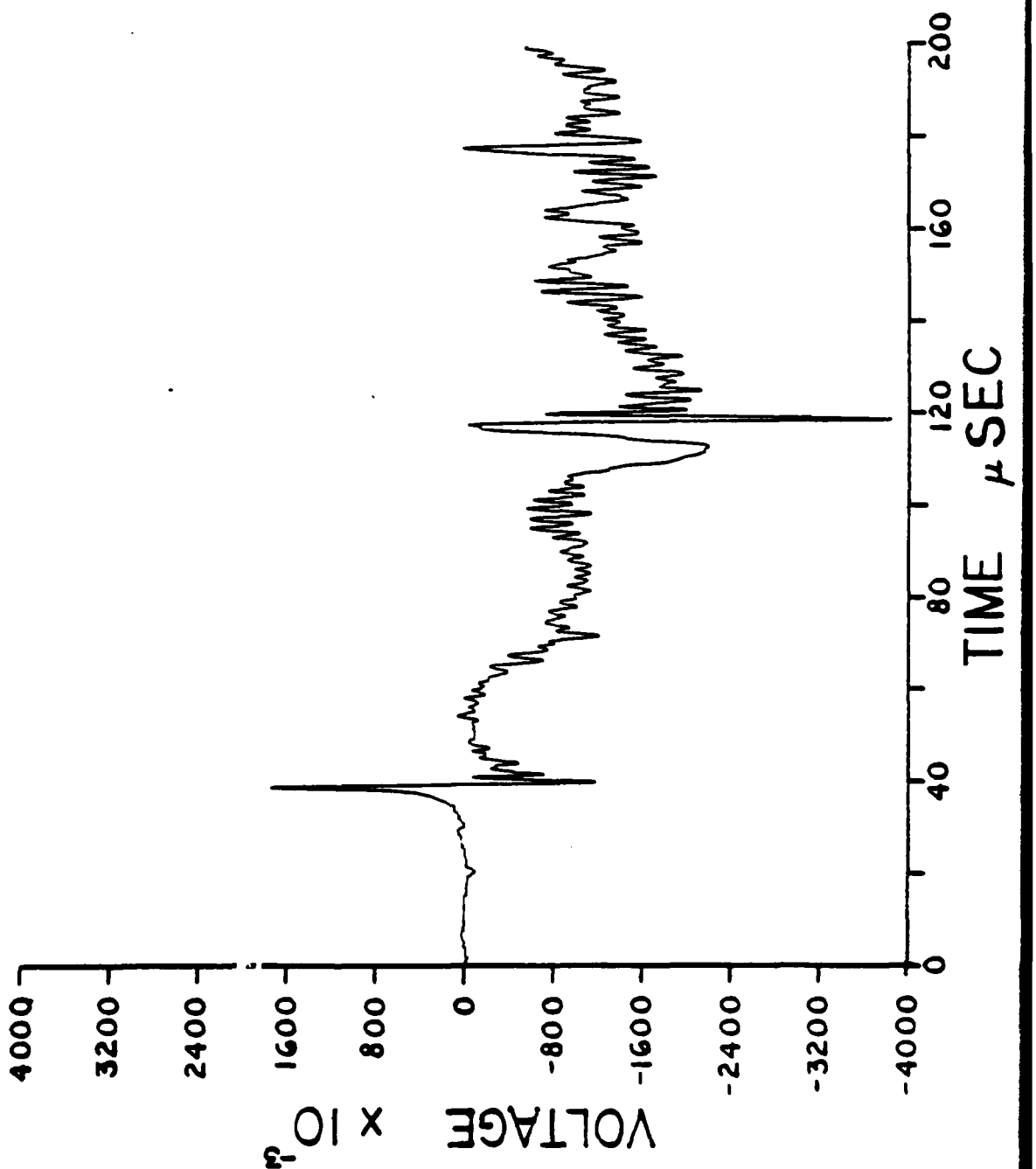
4000
3200
2400
1600
800
0
-800
-1600
-2400
-3200
-4000
VOLTAGE x 10^-3
0
40
80
120
160
200
TIME μSEC

E5

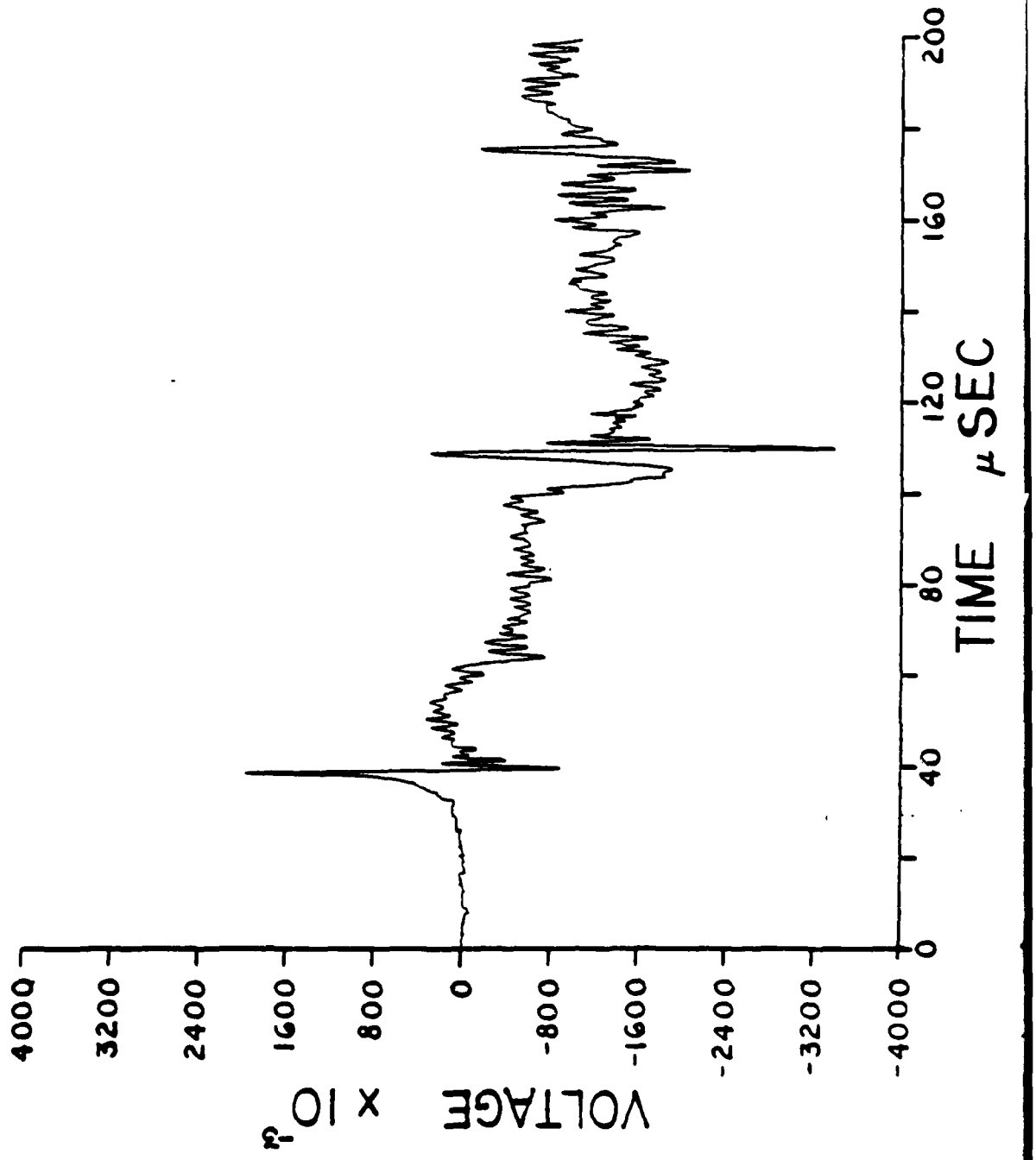
VOLTAGE x 10⁻³
4000
3200
2400
1600
800
0
-800
-1600
-2400
-3200
-4000
0
40
80
120
160
200
TIME μSEC

E6

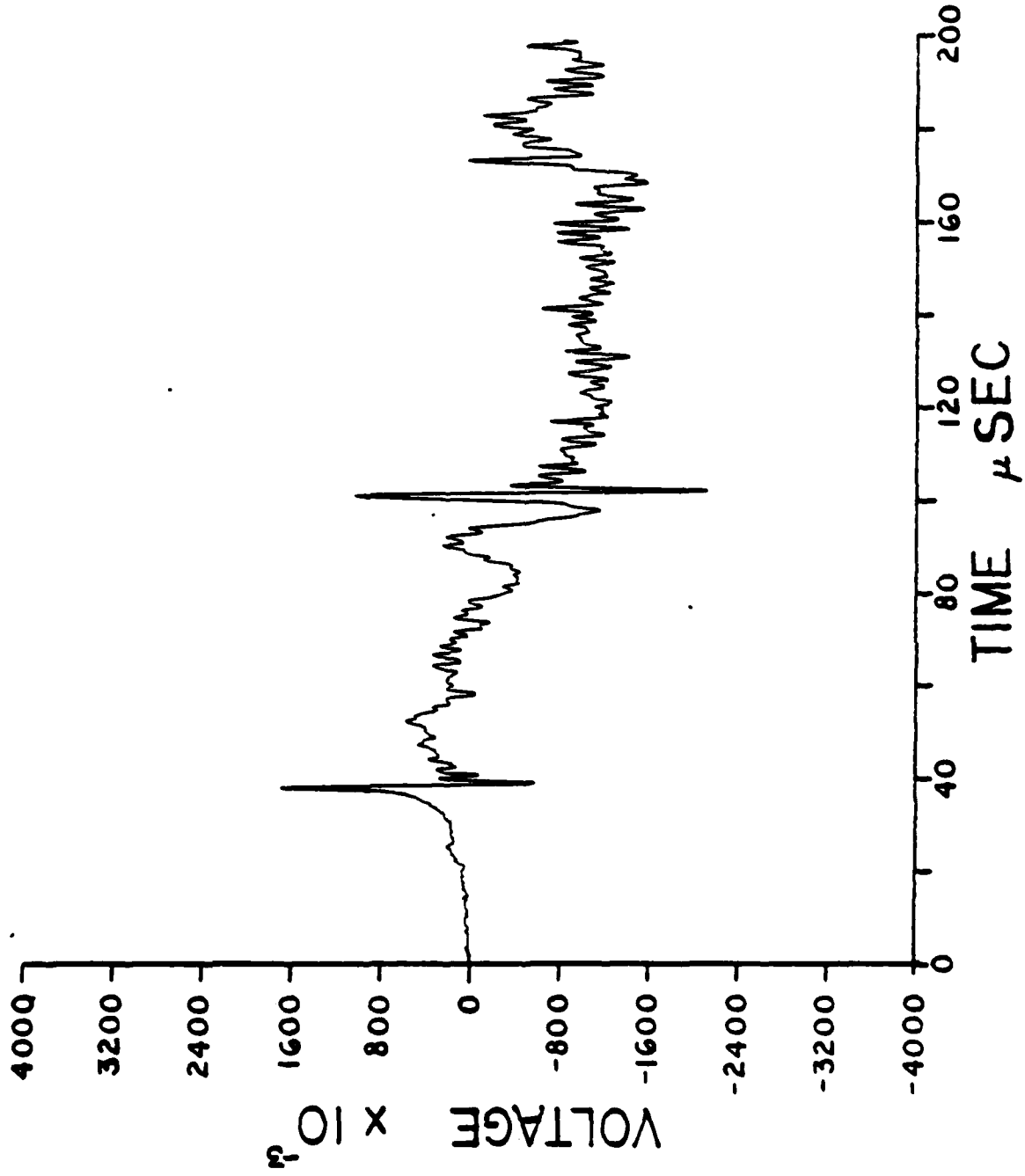
VOLTAGE x 10^{-3}
4000
3200
2400
1600
800
0
-800
-1600
-2400
-3200
-4000
0
40
80
120
160
200
TIME μSEC

E7

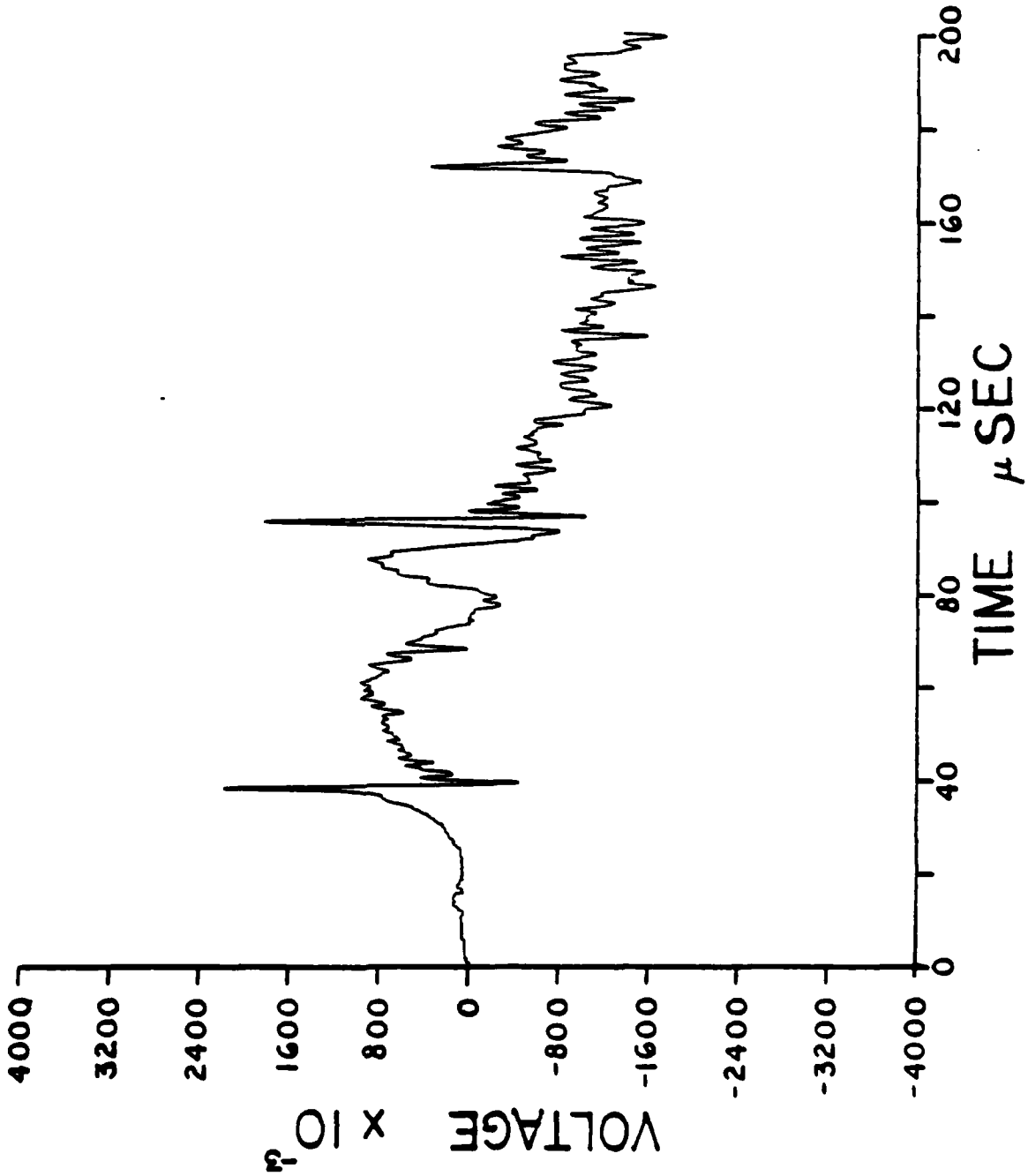
VOLTAGE x 10^{-3}
4000
3200
2400
1600
800
0
-800
-1600
-2400
-3200
-4000
0
40
80
120
160
200
TIME μSEC

E8

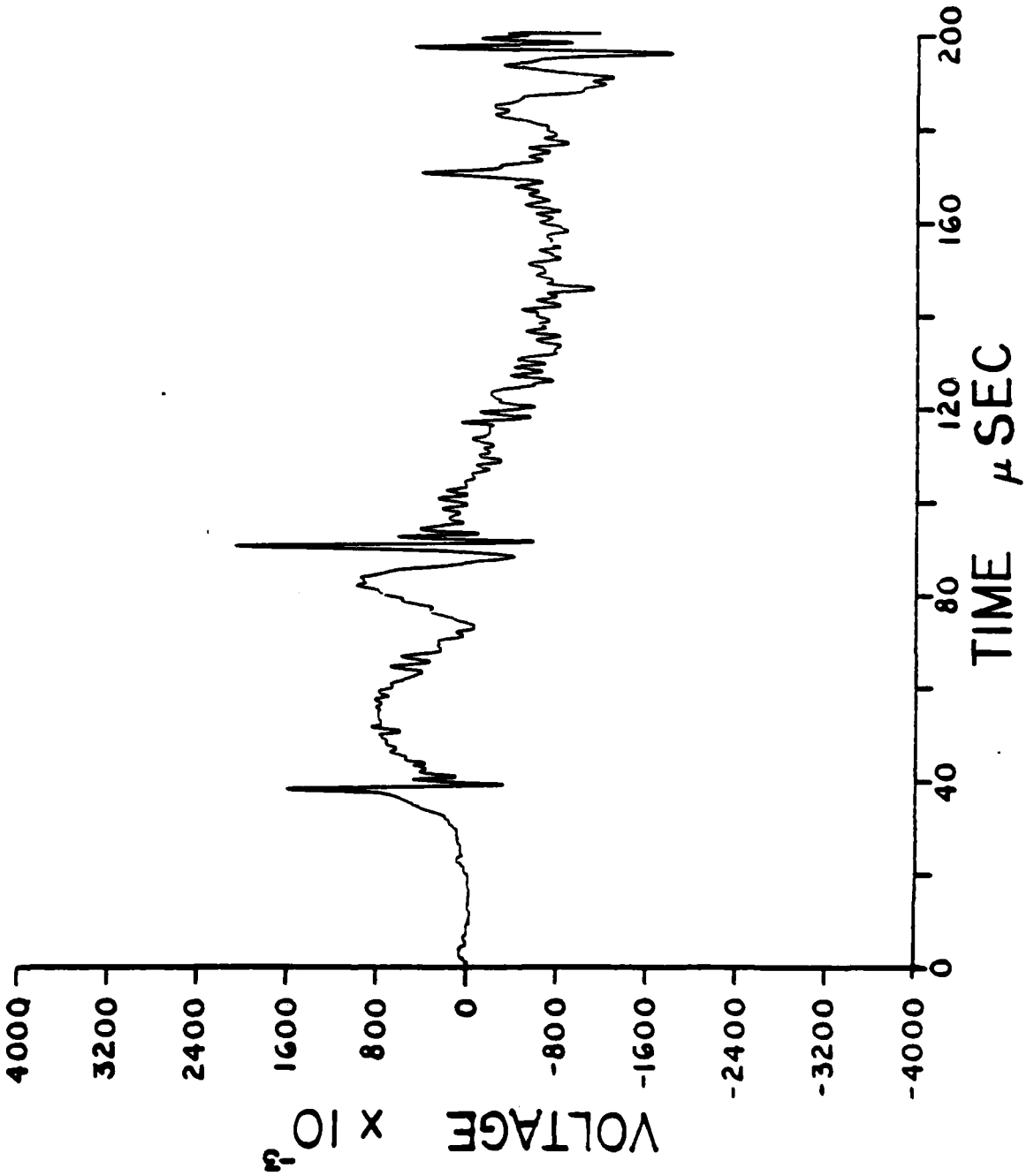
4000
3200
2400
1600
800
0
-800
-1600
-2400
-3200
-4000
VOLTAGE x 10³
0
40
80
120
160
200
TIME μSEC

E9

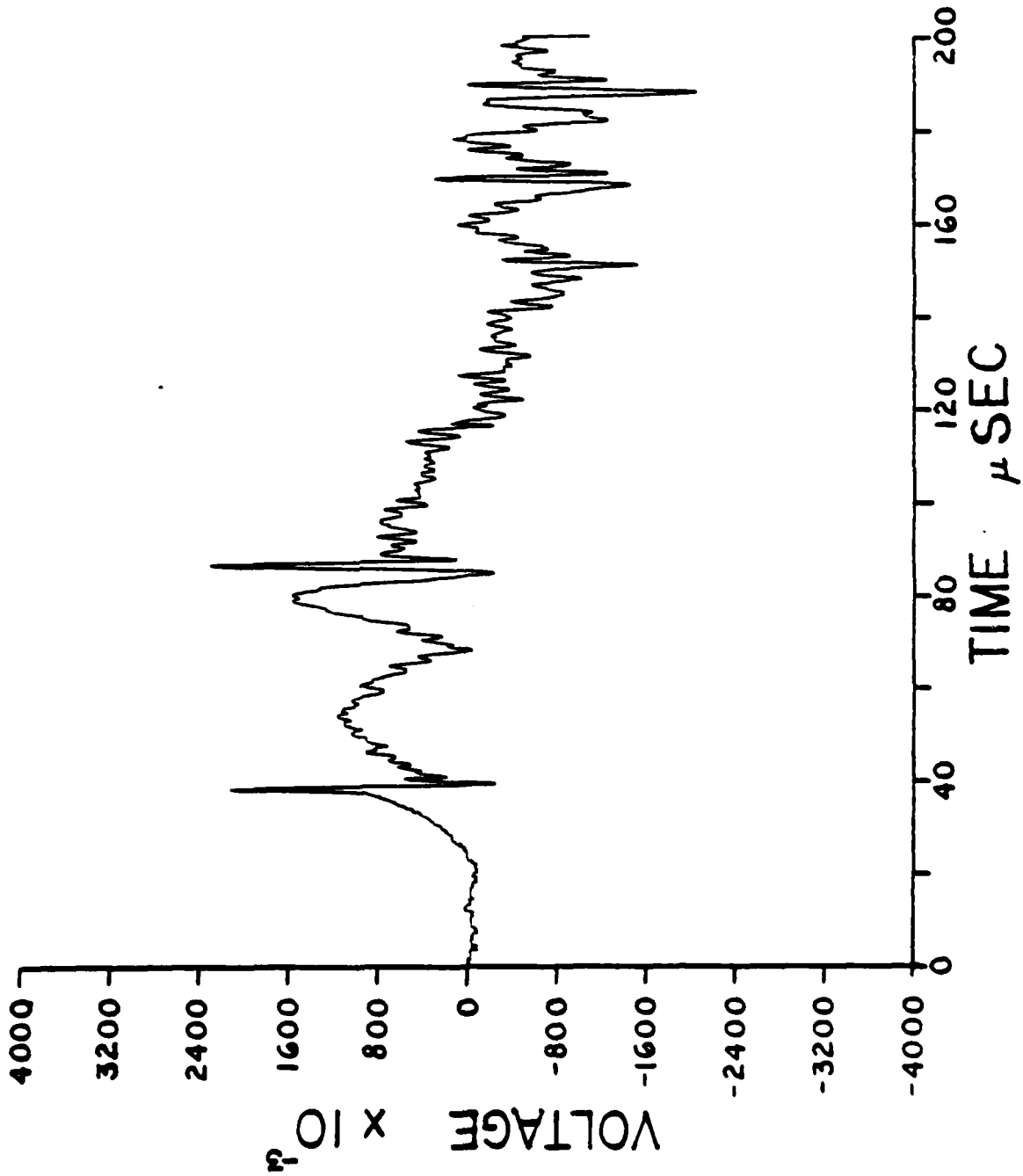
VOLTAGE x 10^p
4000
3200
2400
1600
800
0
-800
-1600
-2400
-3200
-4000
0
40
80
120
160
200
TIME μSEC

E10

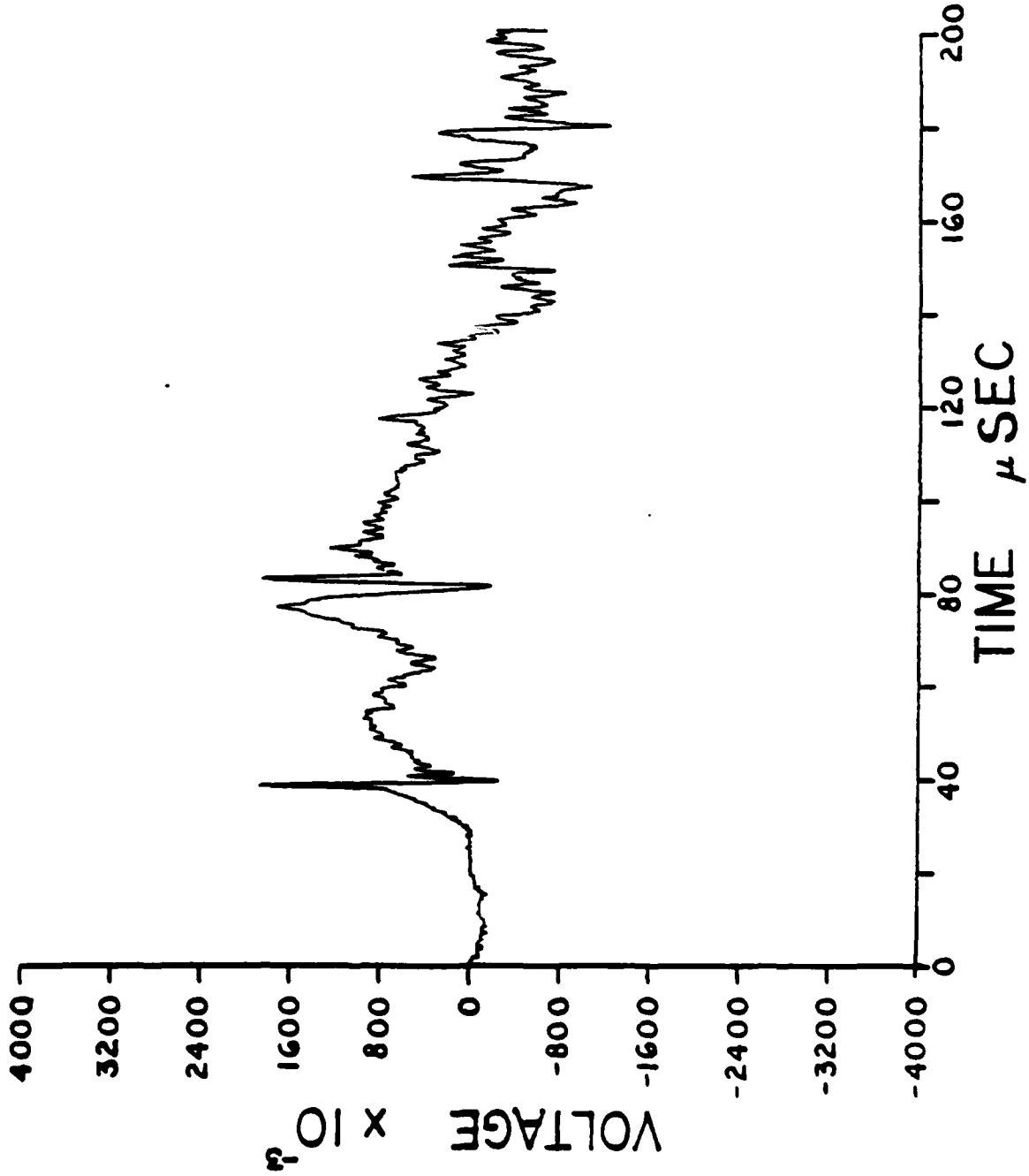
VOLTAGE x 10³
4000
3200
2400
1600
800
0
-800
-1600
-2400
-3200
-4000
0
40
80
120
160
200
TIME μSEC

E11

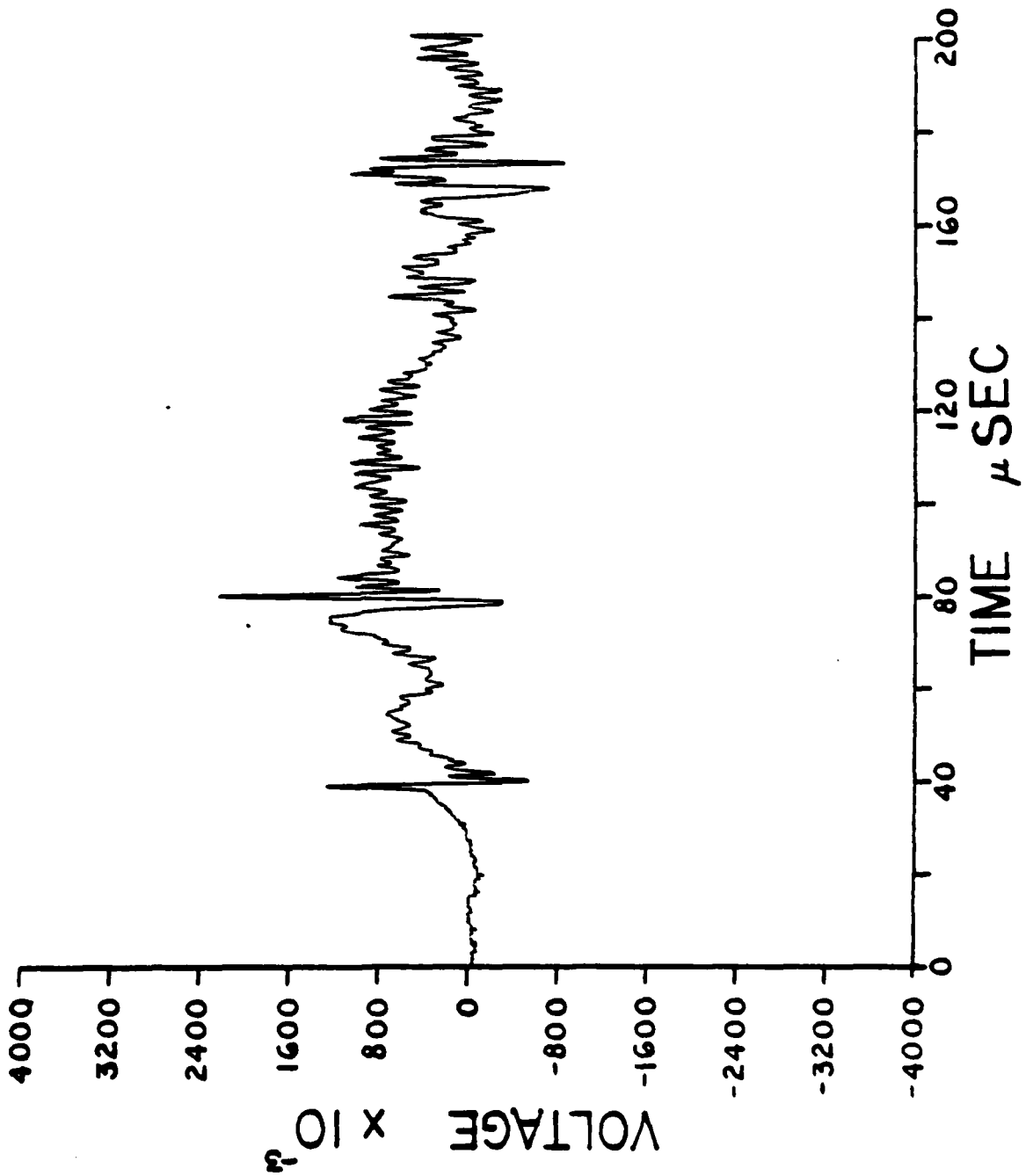
VOLTAGE x 10^3
4000
3200
2400
1600
800
0
-800
-1600
-2400
-3200
-4000
0
40
80
120
160
200
TIME μSEC

E12

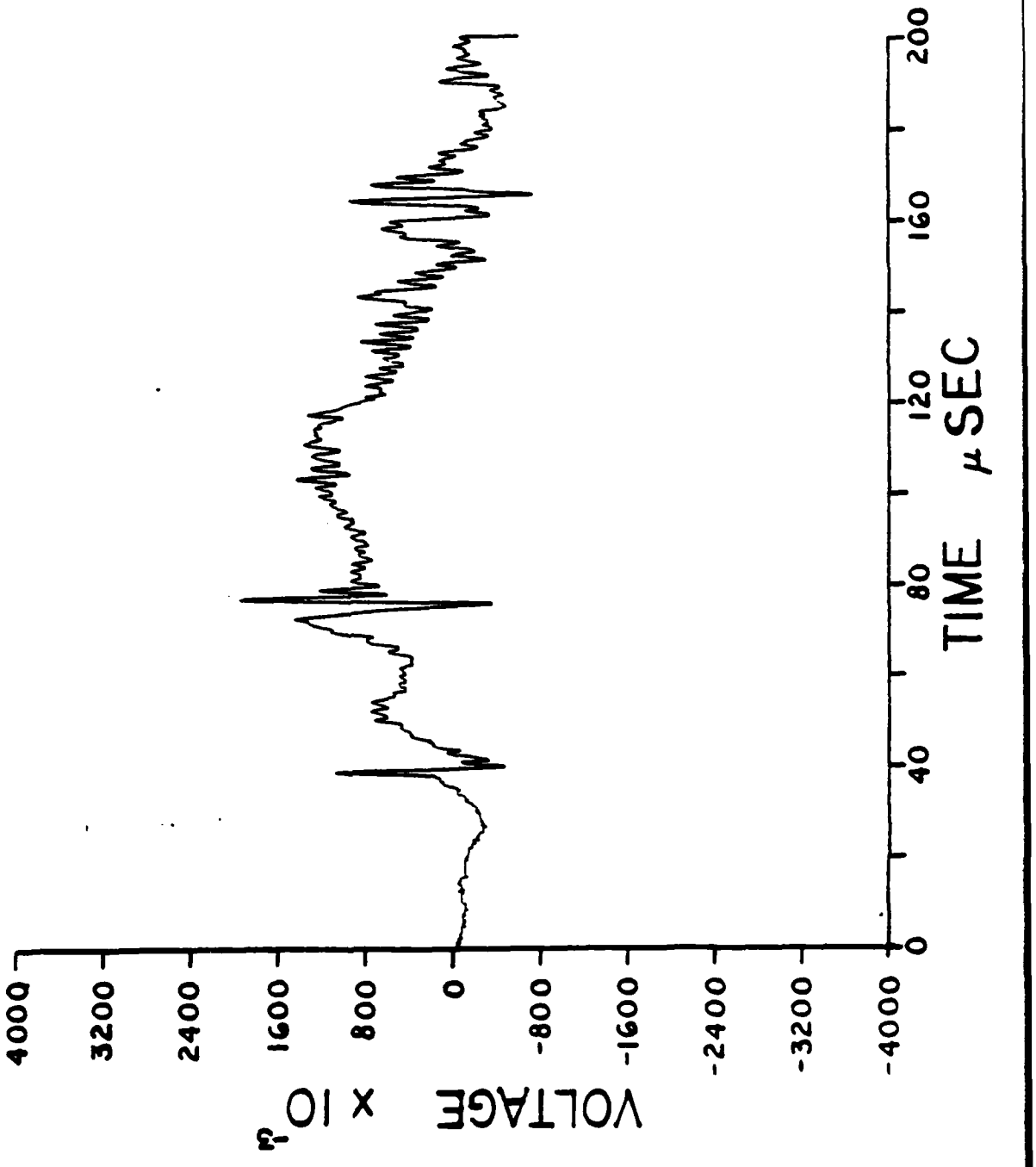
4000
3200
2400
1600
800
0
-800
-1600
-2400
-3200
-4000
VOLTAGE x 10
0
40
80
120
160
200
TIME μSEC

E13

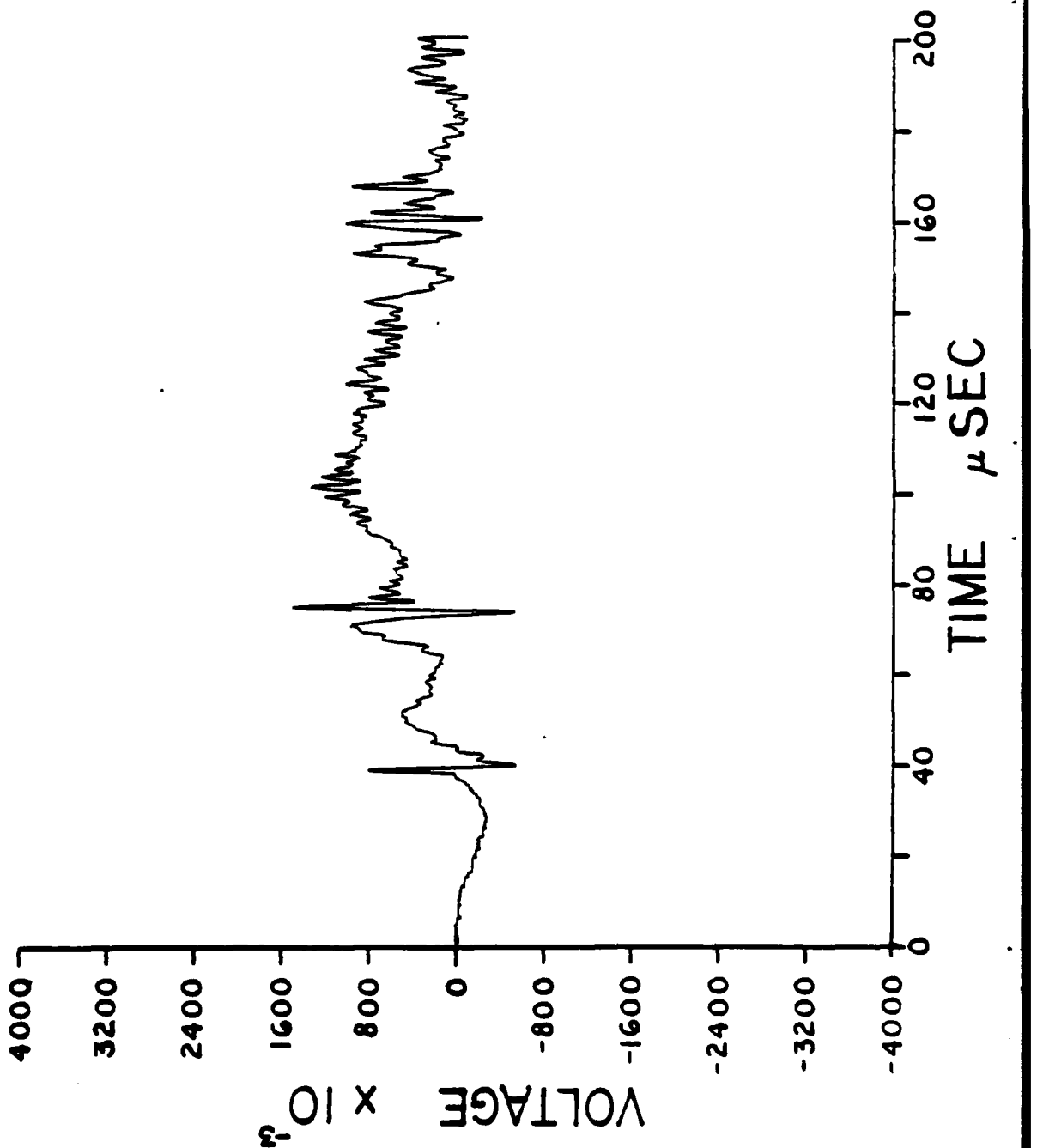
4000
3200
2400
1600
800
0
-800
-1600
-2400
-3200
-4000
VOLTAGE x 10
0
40
80
120
160
200
TIME μSEC

E14

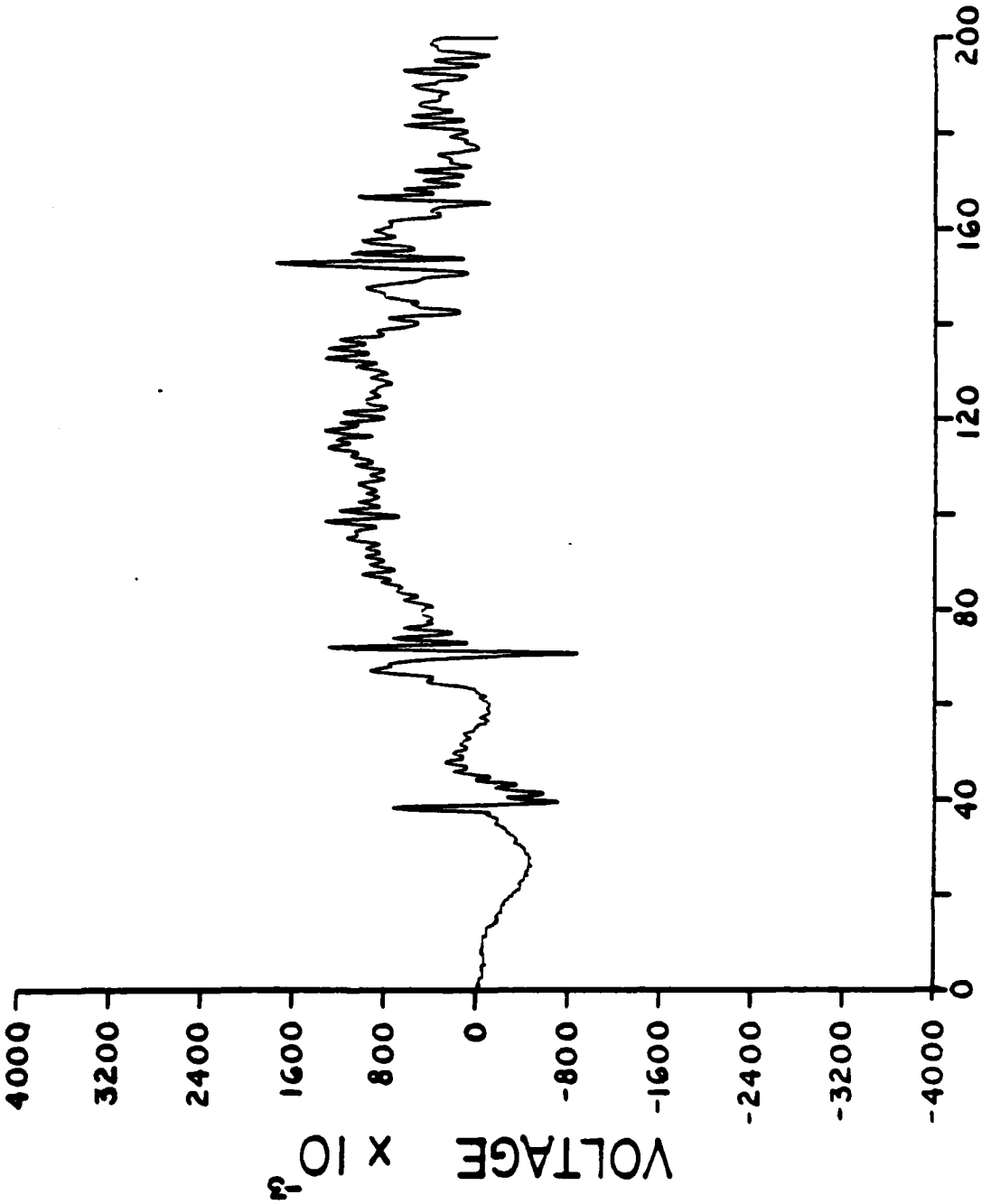
4000
3200
2400
1600
800
0
-800
-1600
-2400
-3200
-4000
VOLTAGE x 10³
0
40
80
120
160
200
TIME μSEC

E15

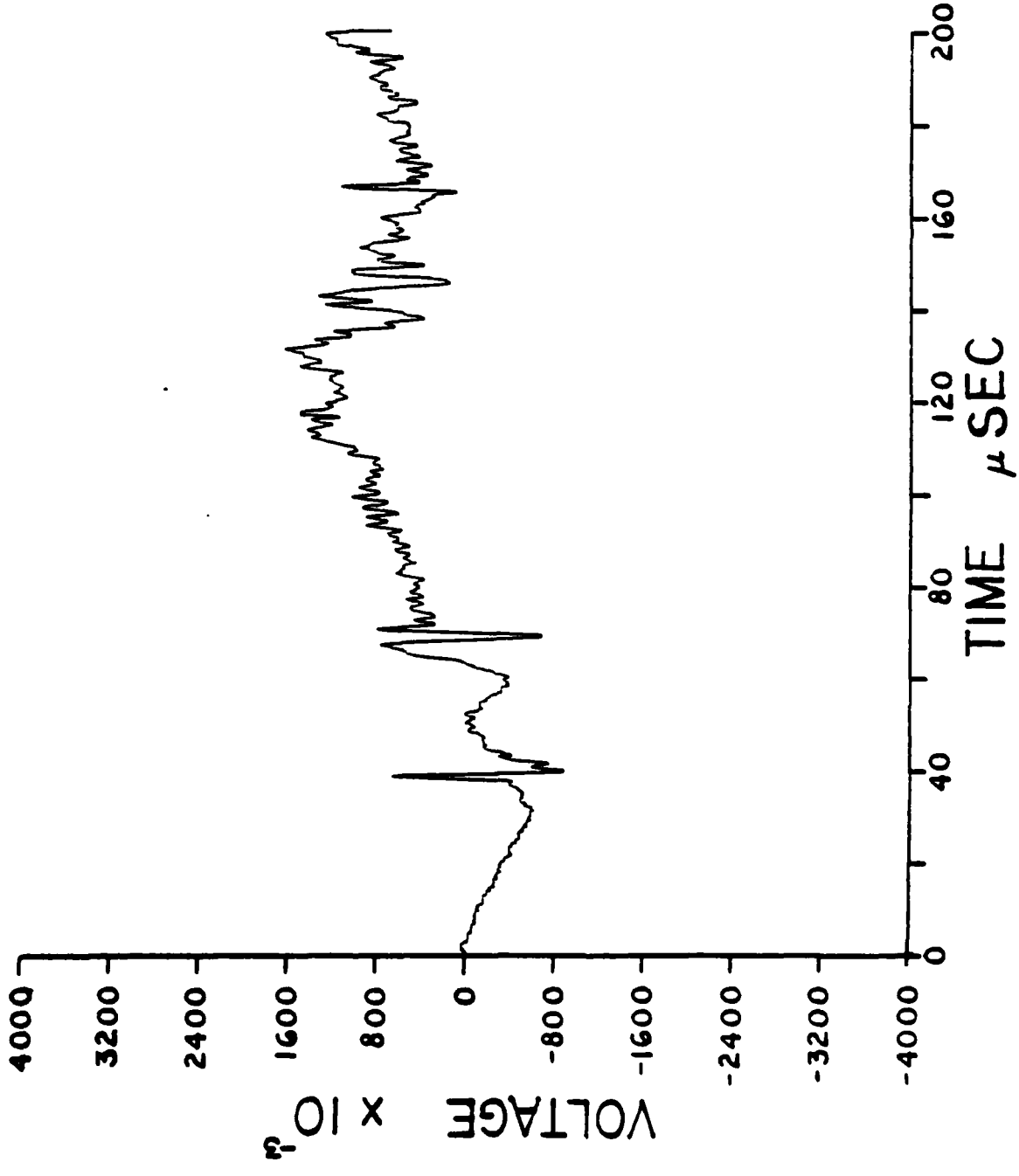
4000
3200
2400
1600
800
0
-800
-1600
-2400
-3200
-4000
VOLTAGE x 10
0
40
80
120
160
200
TIME μSEC

E16

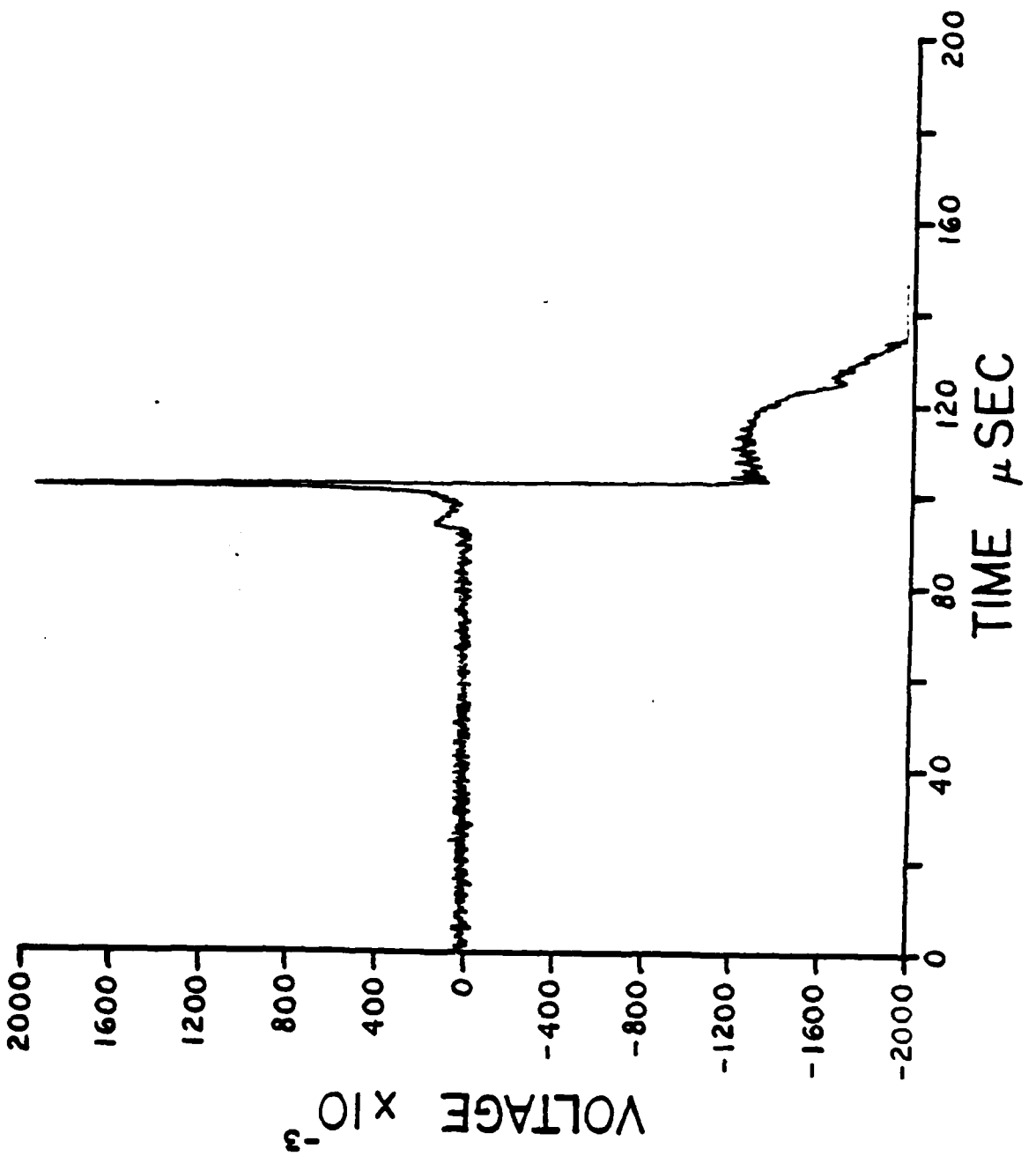
VOLTAGE x10⁻³
2000
1600
1200
800
400
0
-400
-800
-1200
-1600
-2000
0
40
80
120
160
200
TIME μSEC

E17

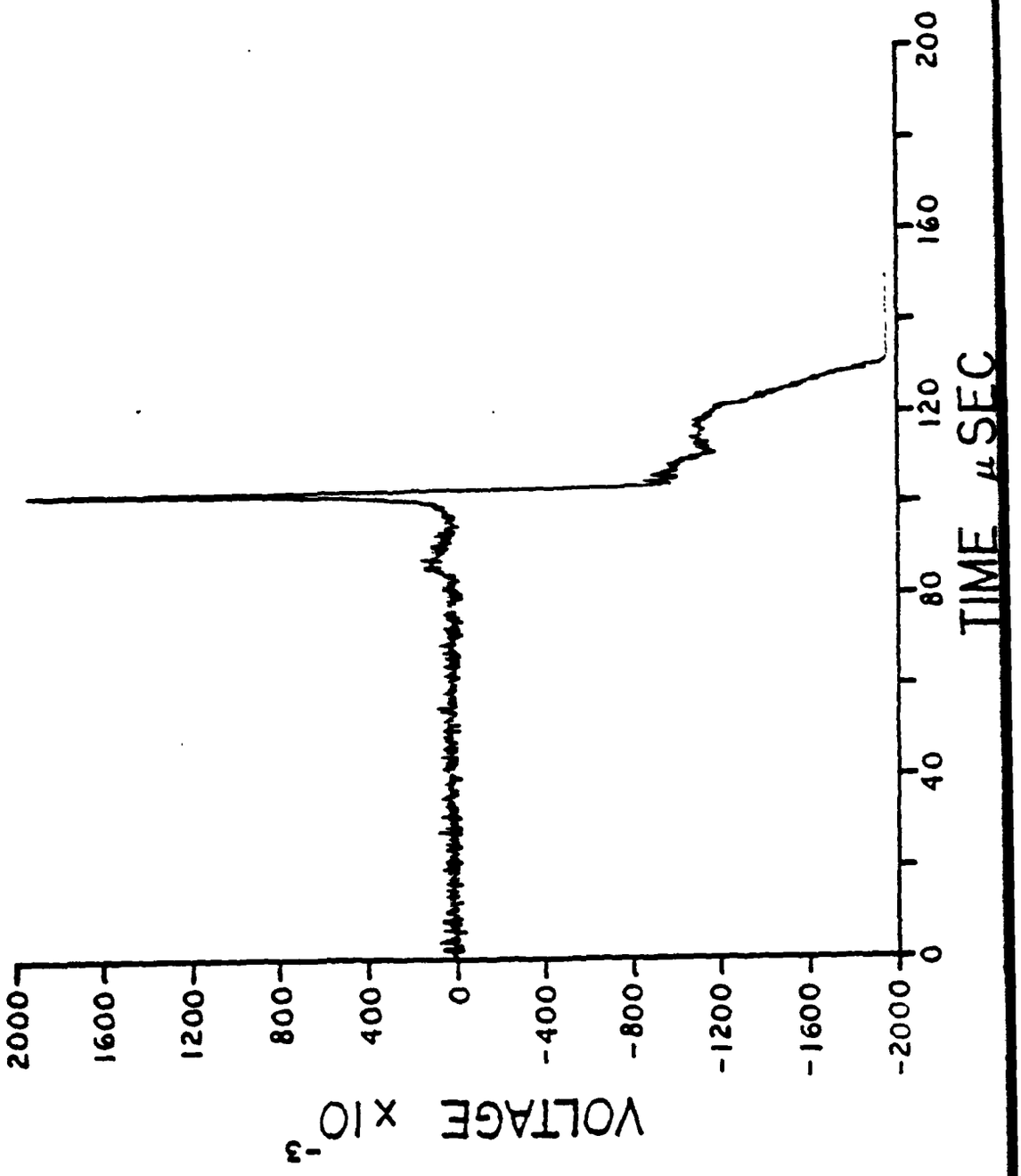
VOLTAGE x10⁻³
2000
1600
1200
800
400
0
-400
-800
-1200
-1600
-2000
0
40
80
120
160
200
TIME μSEC

E18

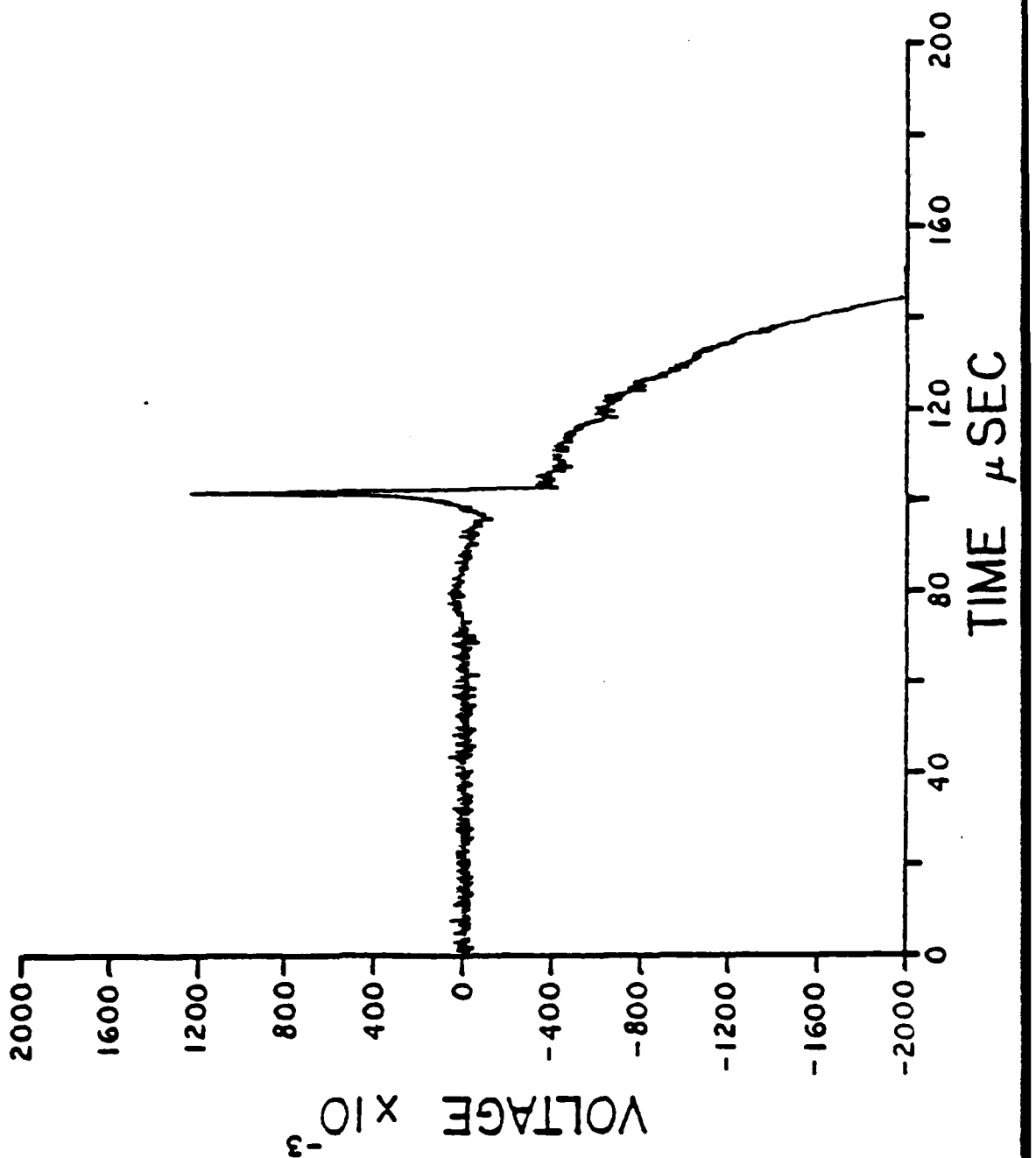
VOLTAGE x10^{-3}
2000
1600
1200
800
400
0
-400
-800
-1200
-1600
-2000
0
40
80
120
160
200
TIME μSEC

E19

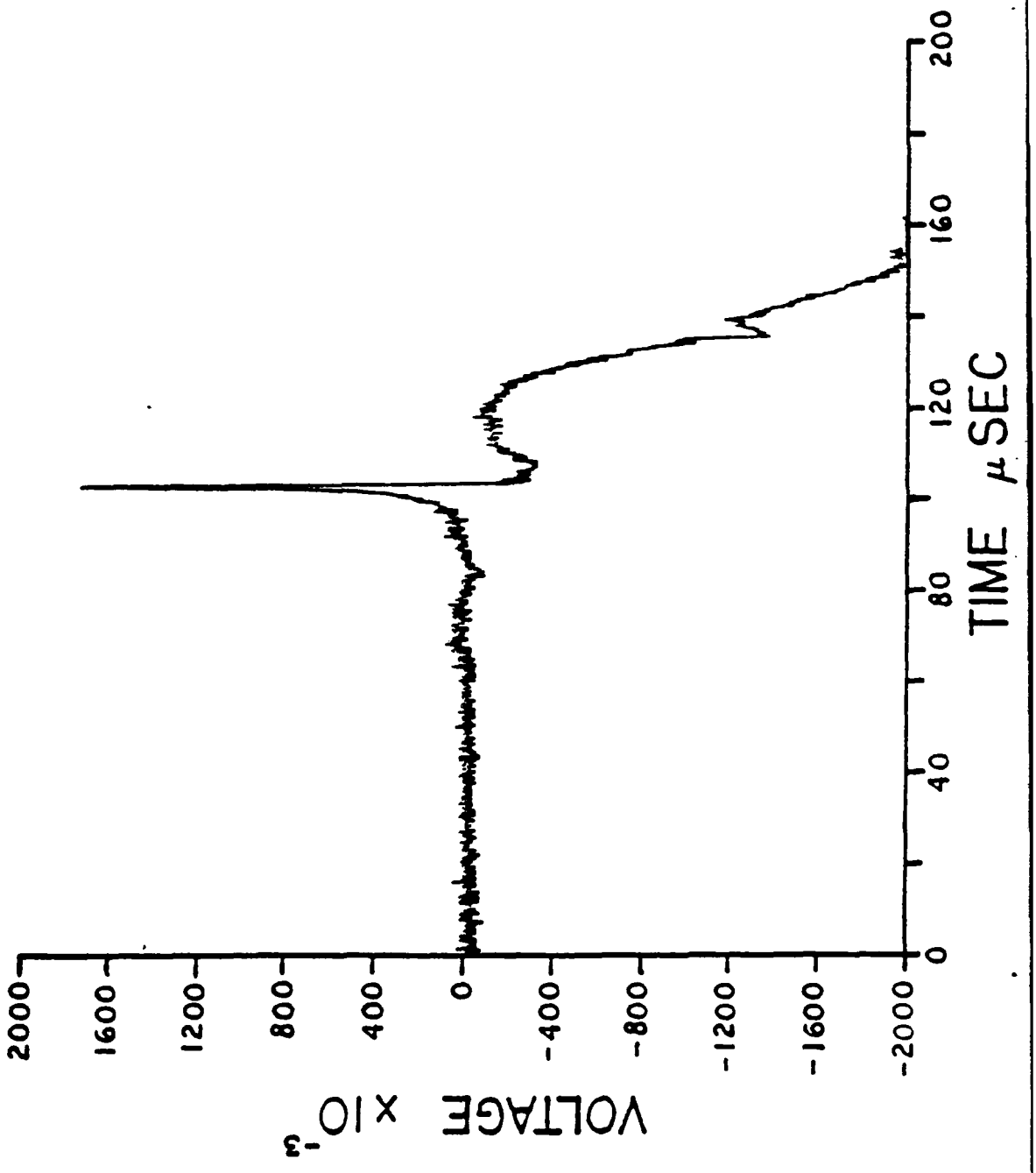
VOLTAGE x10^-3
2000
1600
1200
800
400
0
-400
-800
-1200
-1600
-2000
0
40
80
120
160
200
TIME μSEC

E20

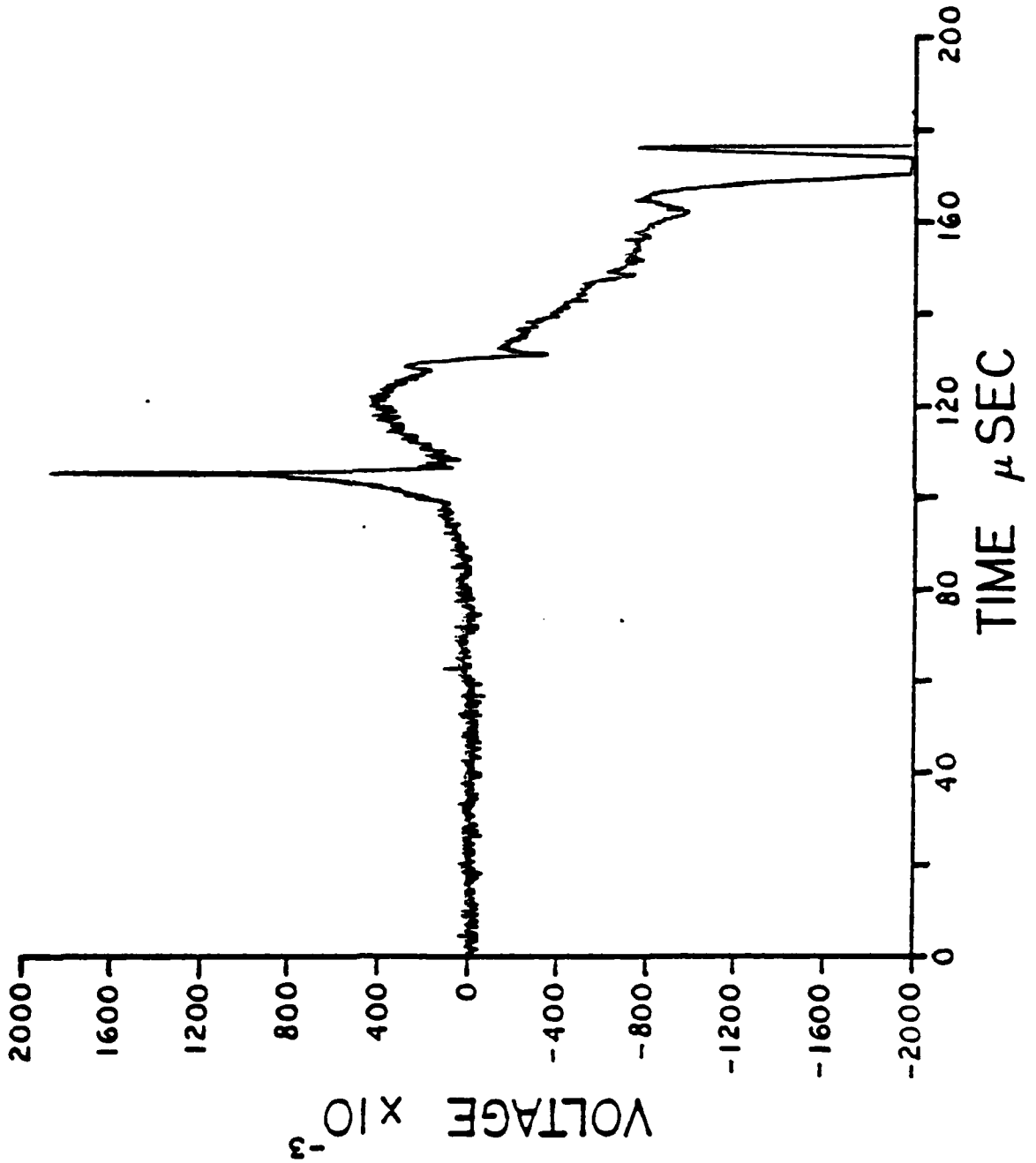
VOLTAGE x10⁻³
2000
1600
1200
800
400
0
-400
-800
-1200
-1600
-2000
0
40
80
120
160
200
TIME μSEC

E21

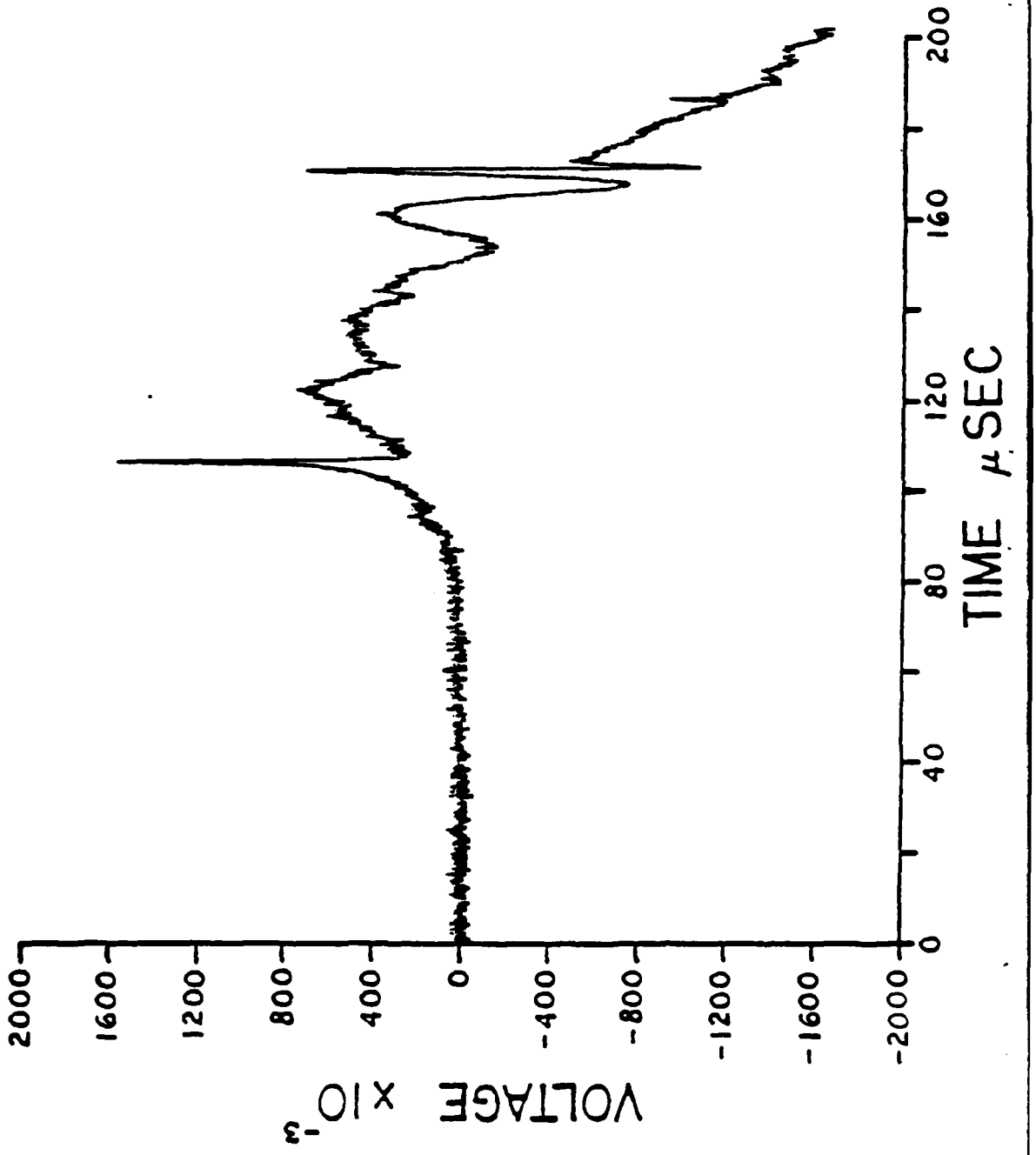
VOLTAGE x10^-3
2000
1600
1200
800
400
0
-400
-800
-1200
-1600
-2000
0
40
80
120
160
200
TIME μSEC

E22

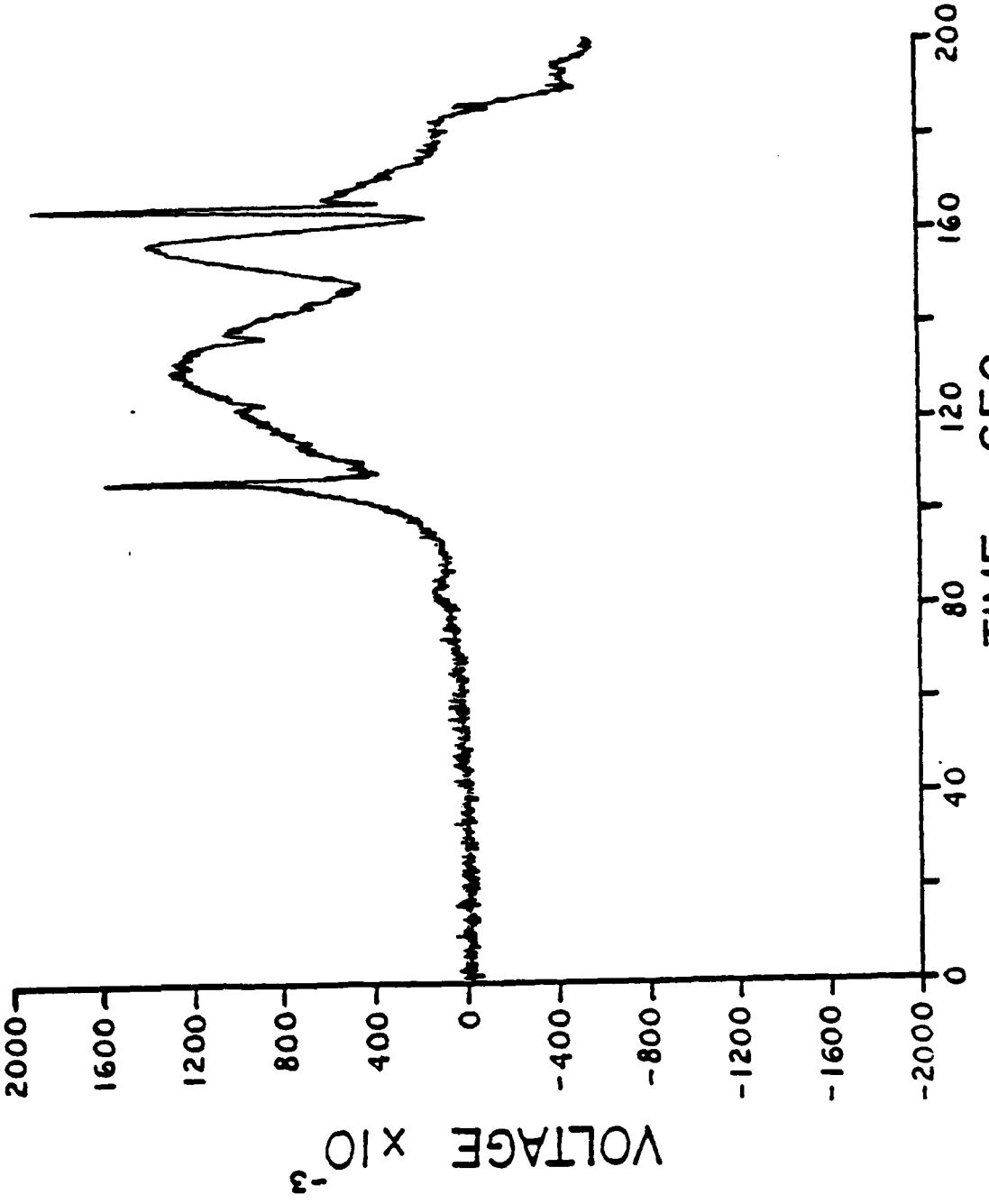
VOLTAGE x10^{-3}
2000
1600
1200
800
400
0
-400
-800
-1200
-1600
-2000
0
40
80
120
160
200
TIME μSEC

E23

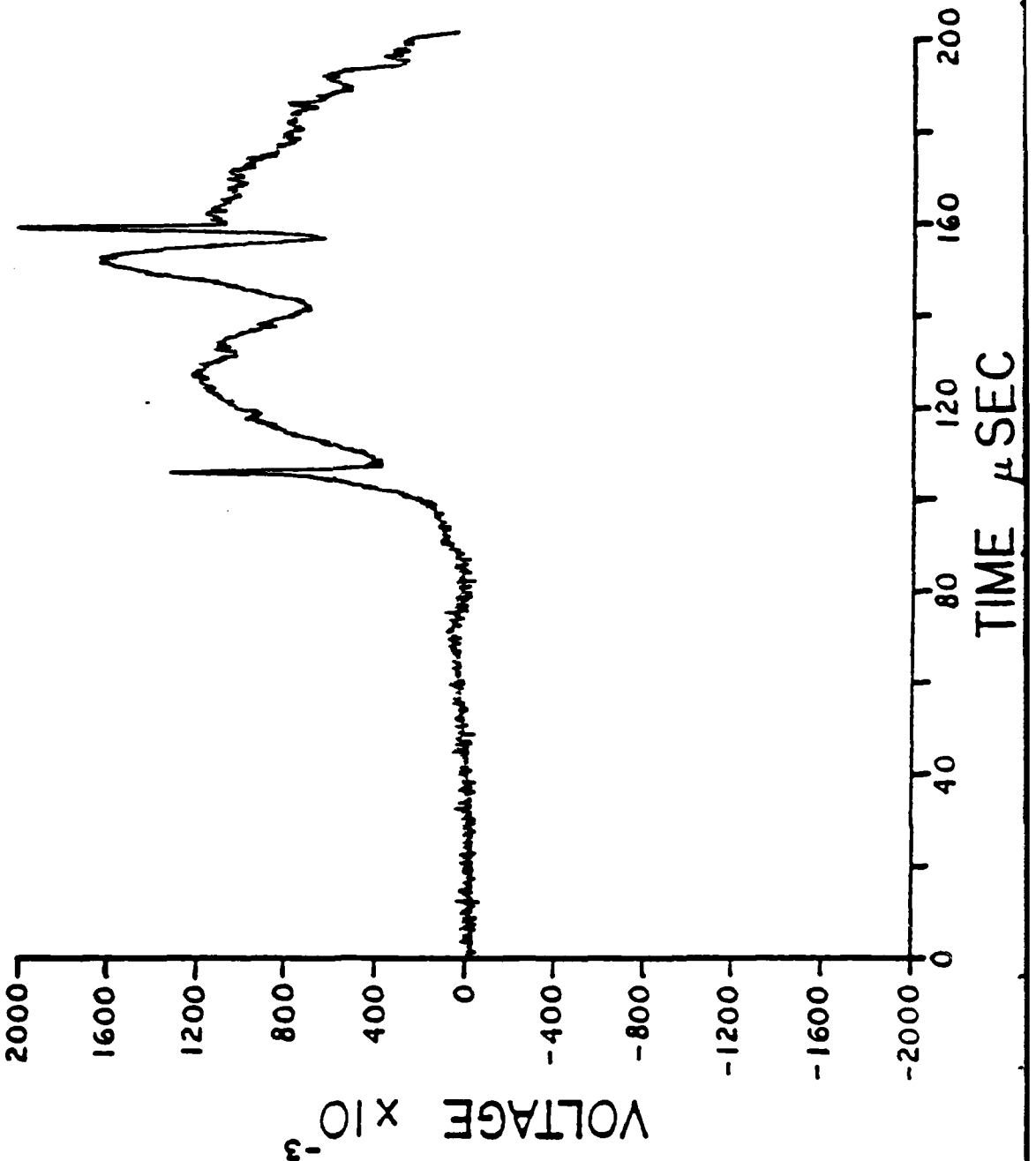
VOLTAGE x10⁻³
2000
1600
1200
800
400
0
-400
-800
-1200
-1600
-2000
0
40
80
120
160
200
TIME μSEC

E24

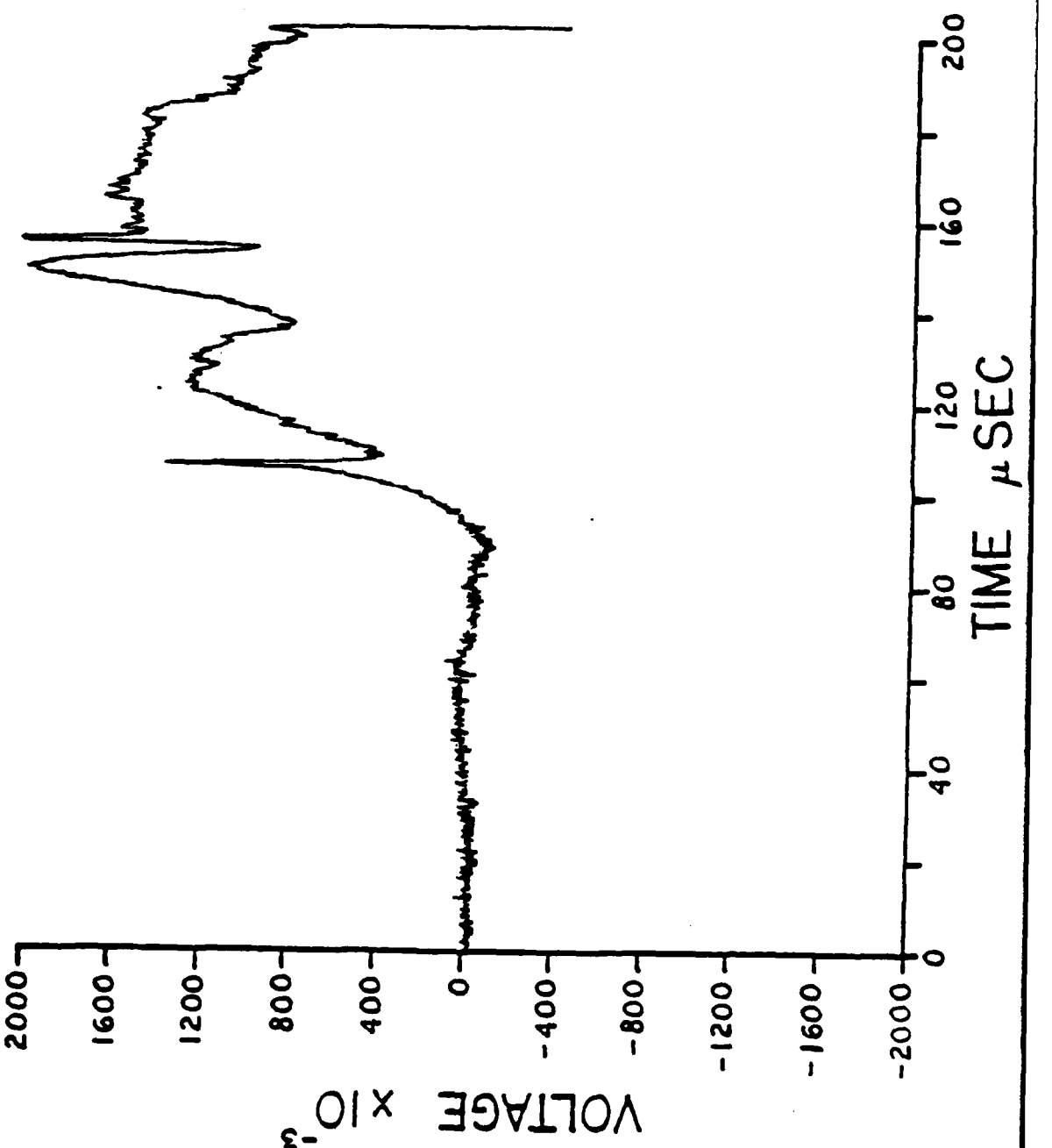
VOLTAGE x10^-3
2000
1600
1200
800
400
0
-400
-800
-1200
-1600
-2000
0
40
80
120
160
200
TIME μSEC

E25

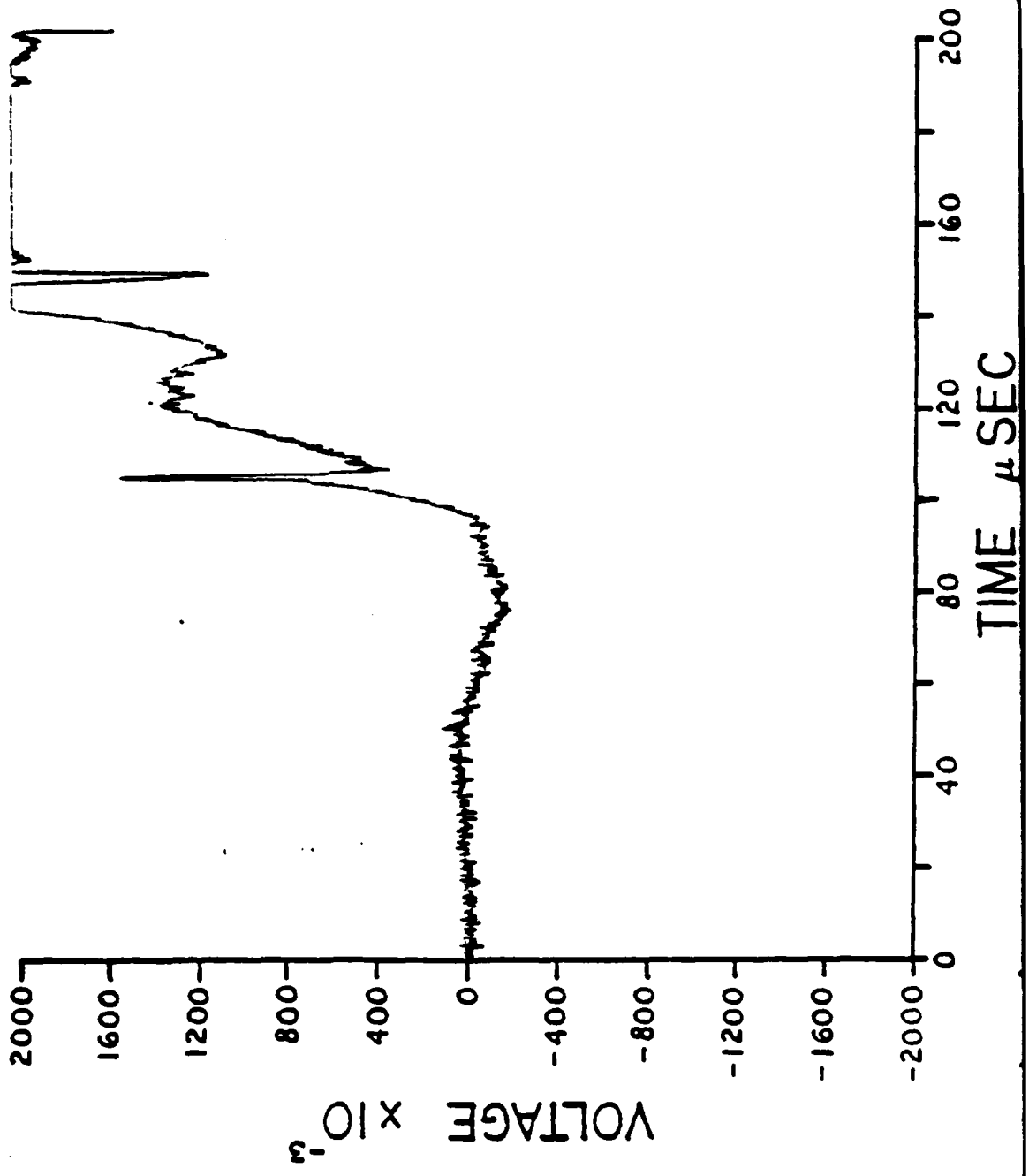
VOLTAGE x 10⁻³
2000
1600
1200
800
400
0
-400
-800
-1200
-1600
-2000
0
40
80
120
160
200
TIME μSEC

E26

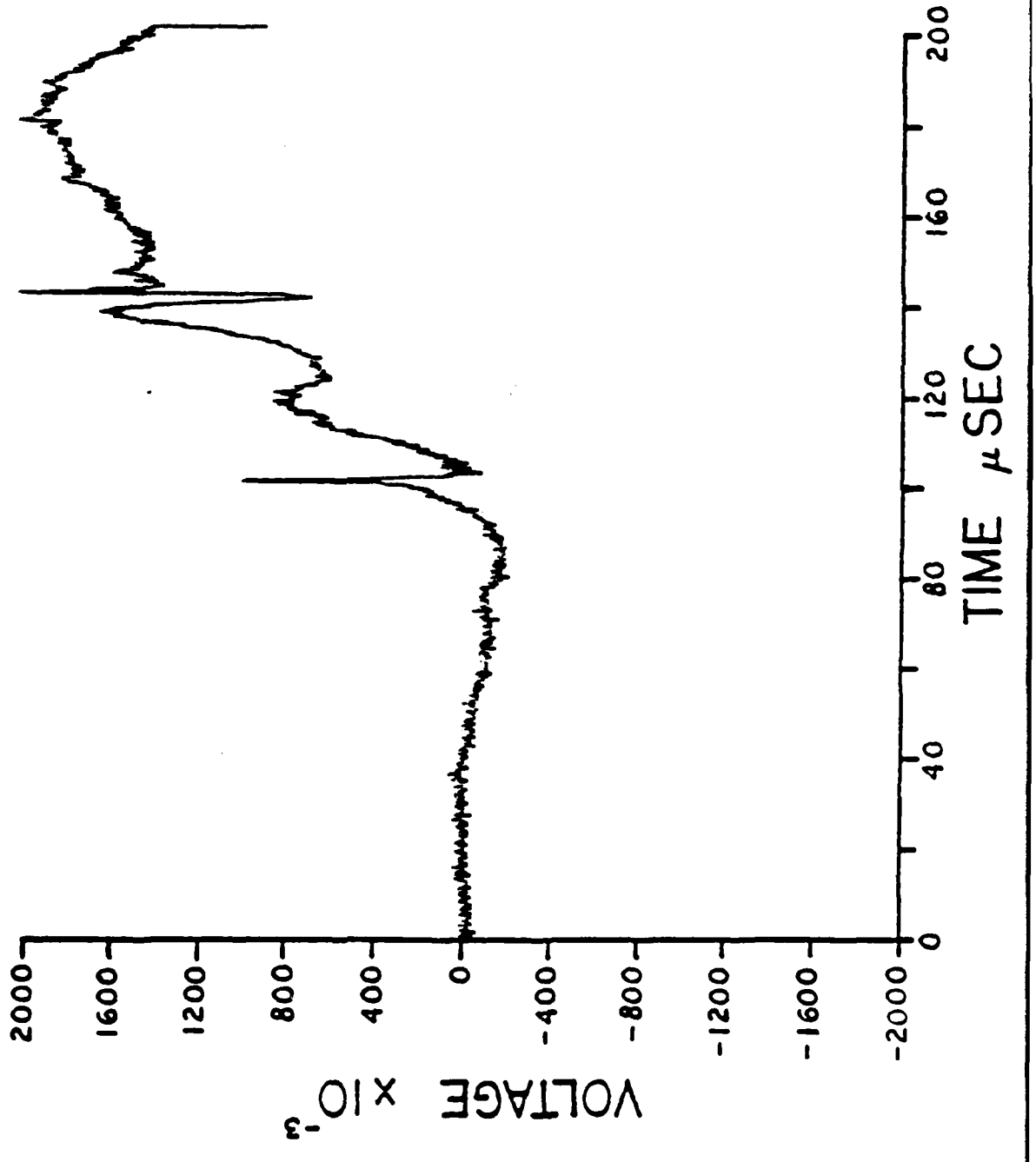
VOLTAGE x10⁻³
2000
1600
1200
800
400
0
-400
-800
-1200
-1600
-2000
0
40
80
120
160
200
TIME μSEC

E27

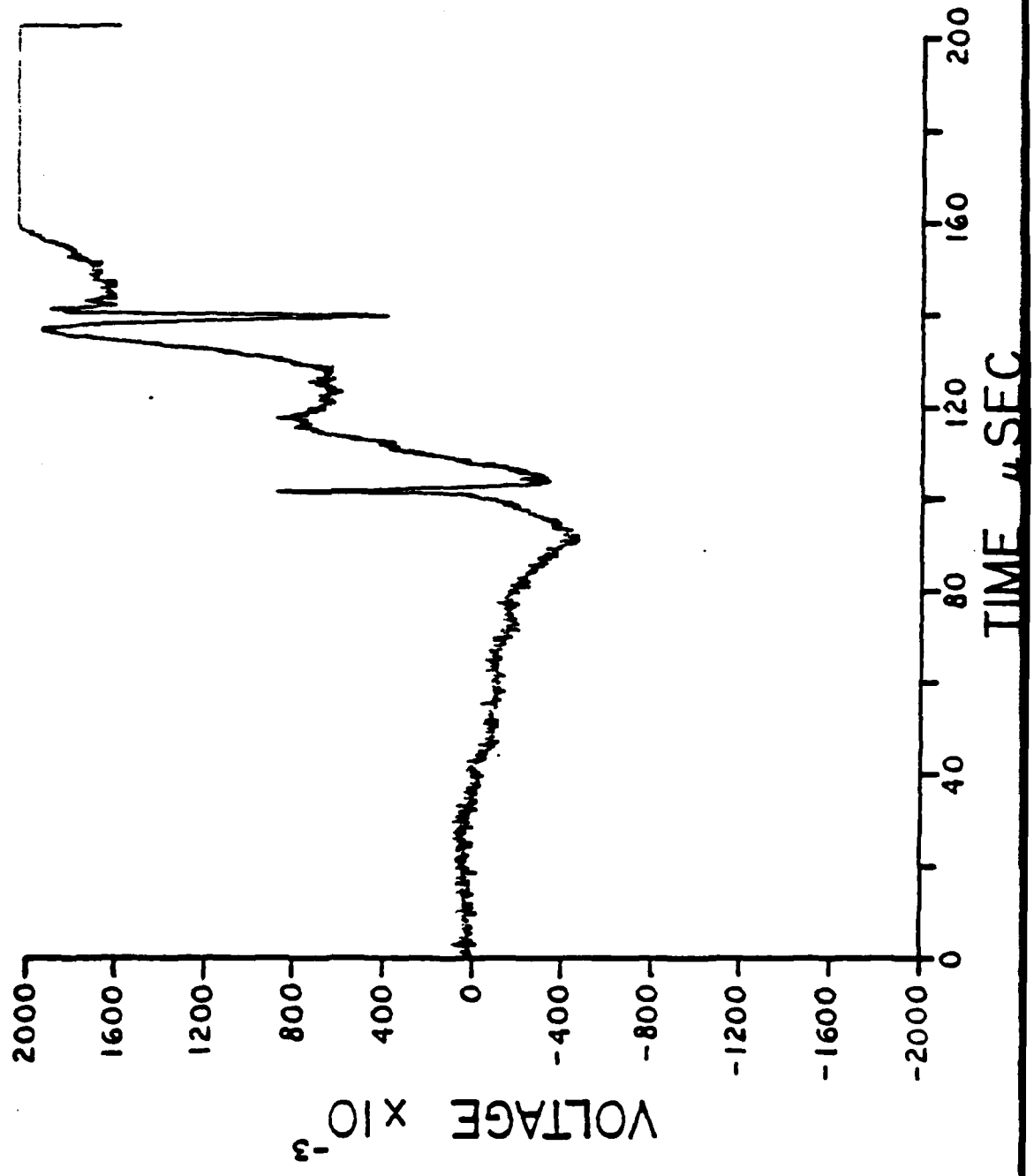
VOLTAGE x10^-3
2000
1600
1200
800
400
0
-400
-800
-1200
-1600
-2000
0
40
80
120
160
200
TIME μSEC

E28

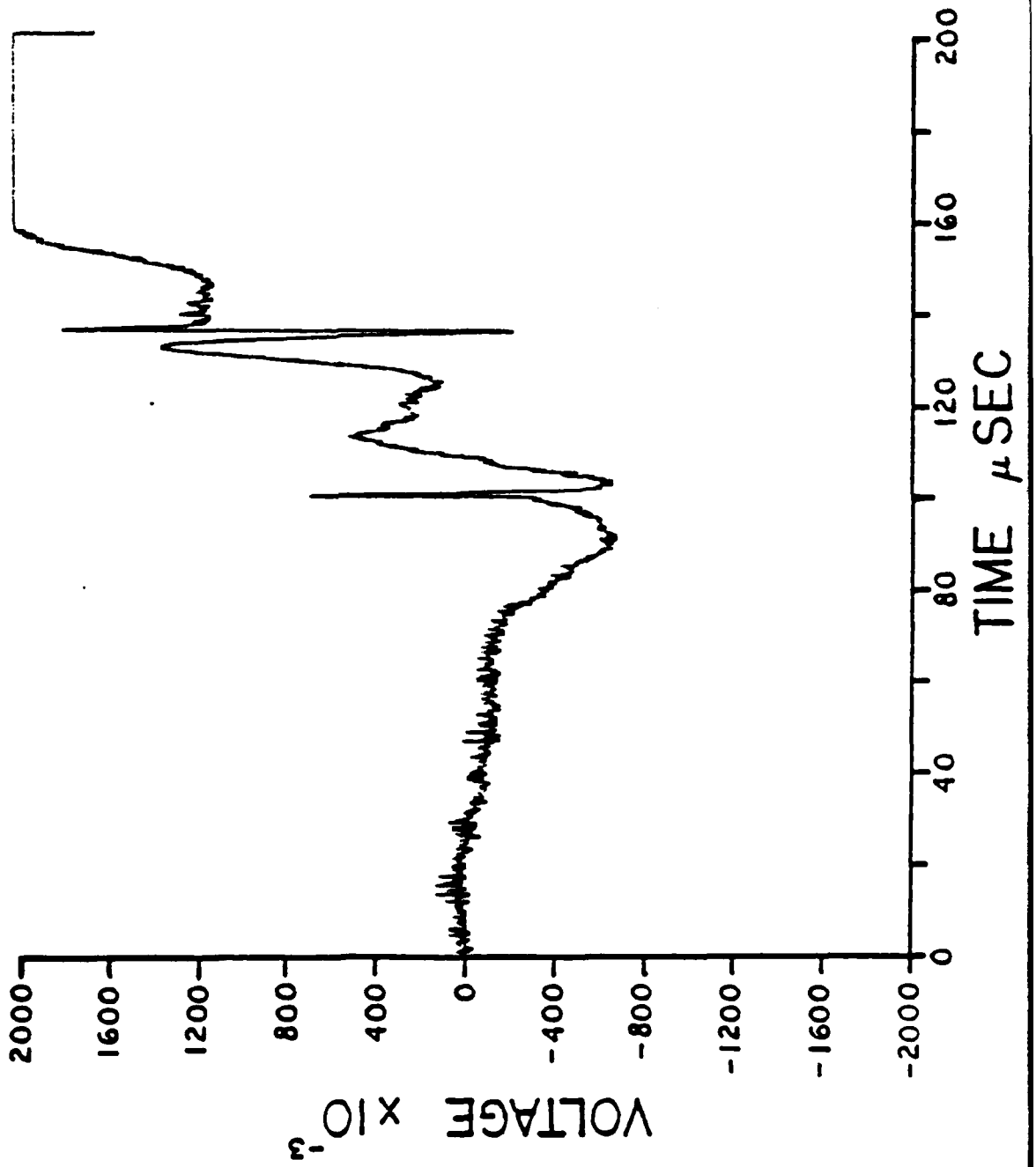
VOLTAGE x10^-3
2000
1600
1200
800
400
0
-400
-800
-1200
-1600
-2000
0
40
80
120
160
200
TIME μSEC

E29

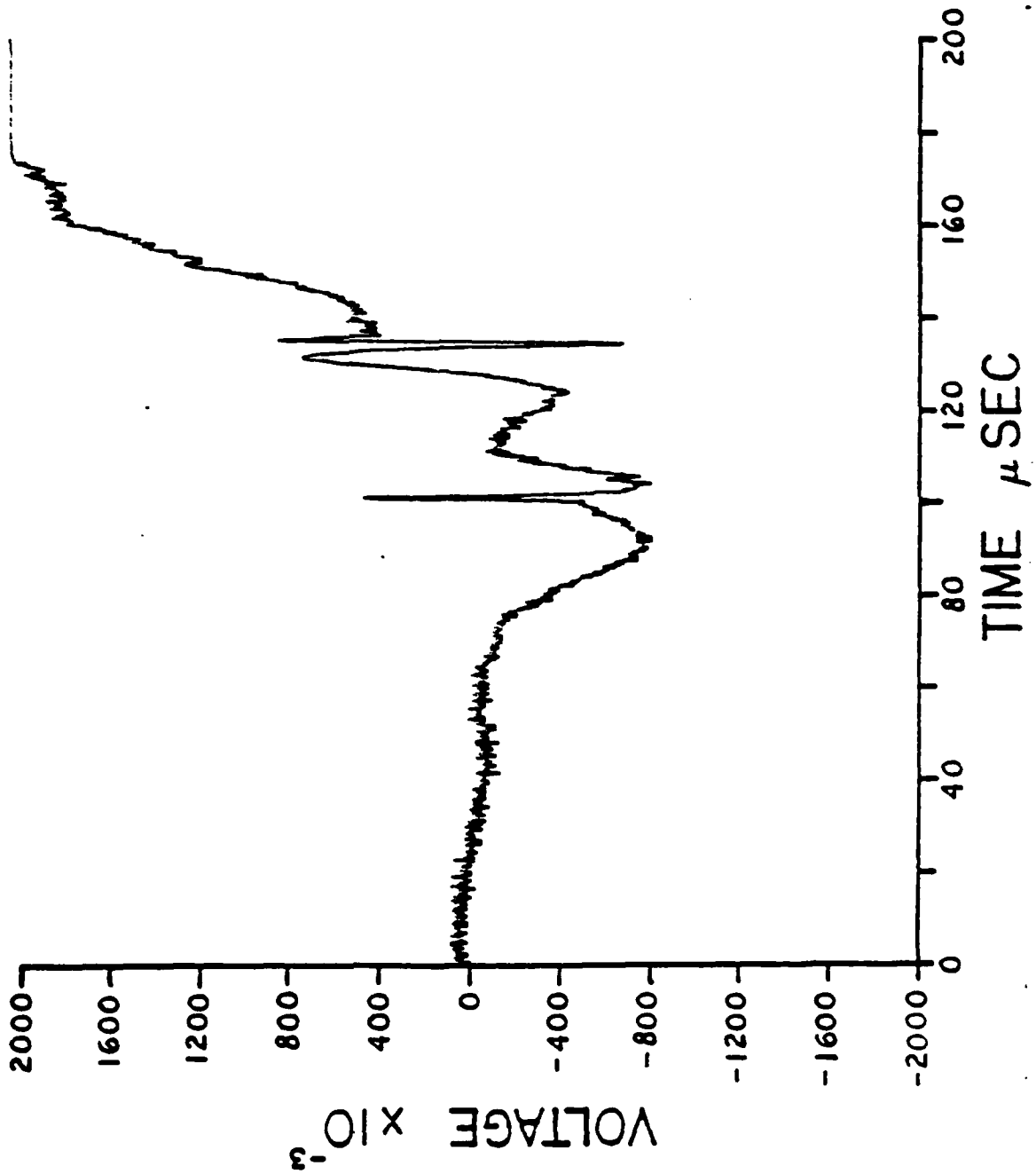
VOLTAGE x10⁻³
2000
1600
1200
800
400
0
-400
-800
-1200
-1600
-2000
0
40
80
120
160
200
TIME μSEC

E30

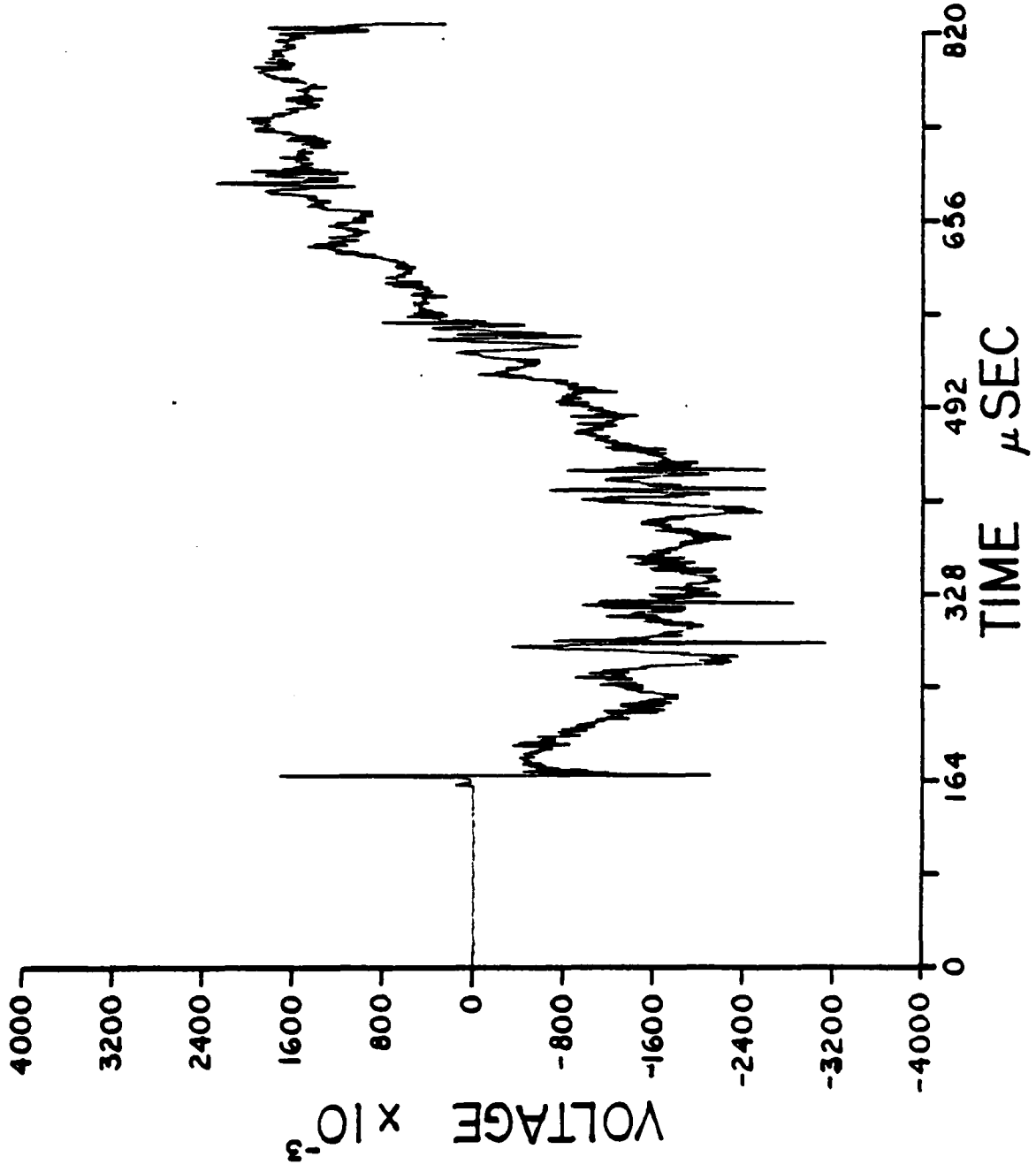
VOLTAGE x 10⁻³
4000
3200
2400
1600
800
0
-800
-1600
-2400
-3200
-4000
0
164
328
492
656
820
TIME μSEC

E31

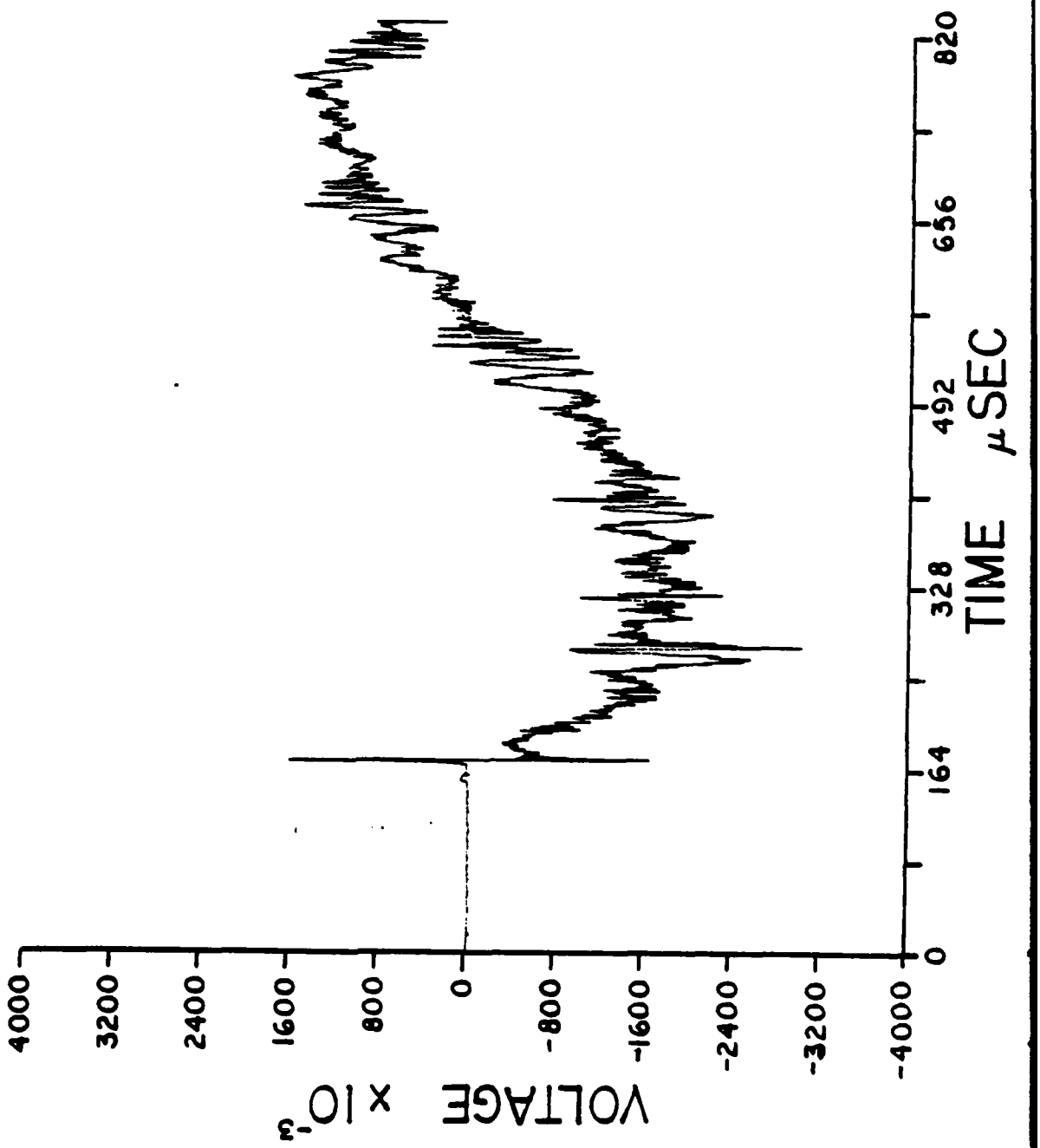
VOLTAGE x 10⁻³
4000
3200
2400
1600
800
0
-800
-1600
-2400
-3200
-4000
0
164
328
492
656
820
TIME μSEC

E32

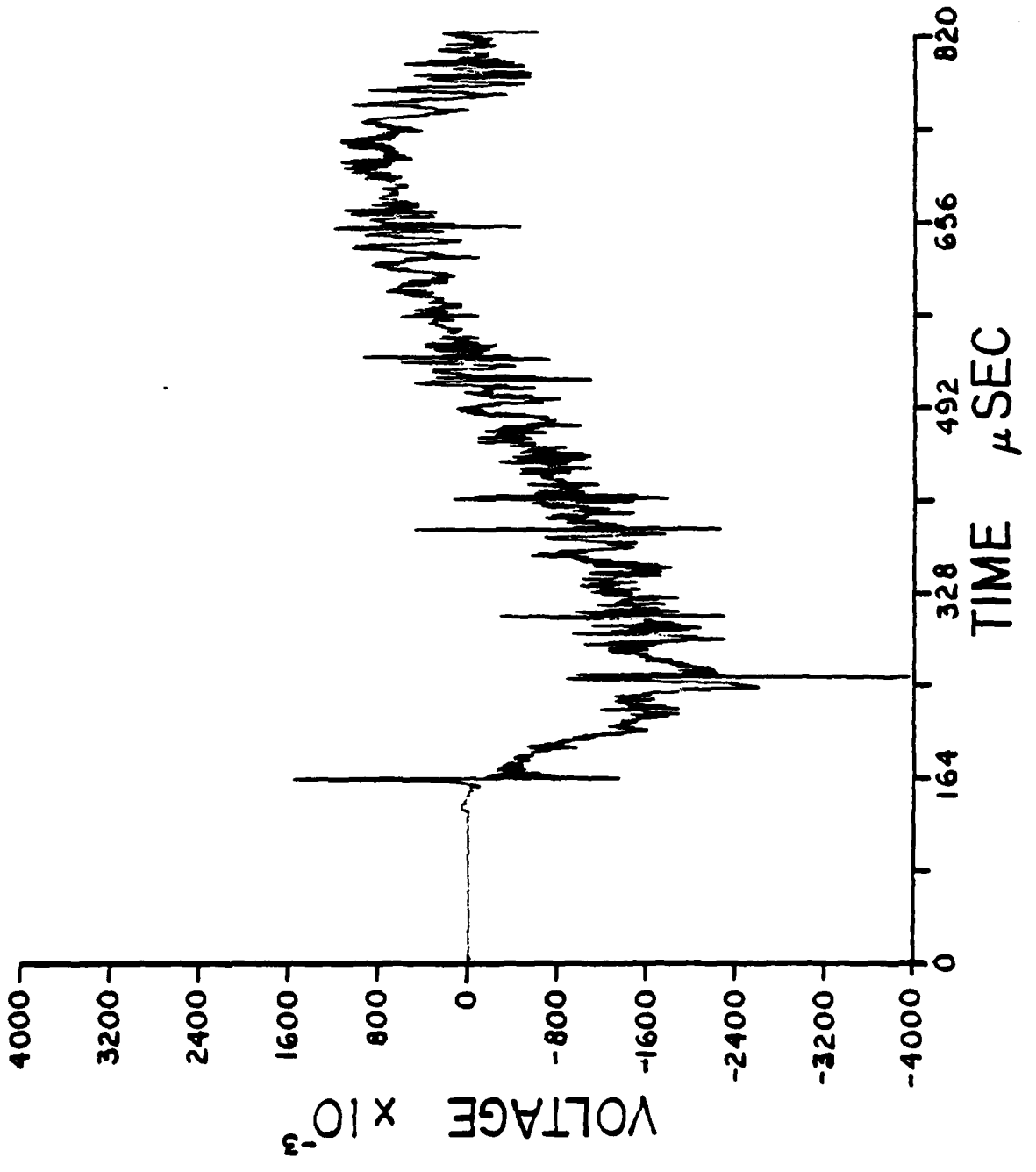
VOLTAGE x 10⁻³
4000
3200
2400
1600
800
0
-800
-1600
-2400
-3200
-4000
0
164
328
492
656
820
TIME μSEC

E33

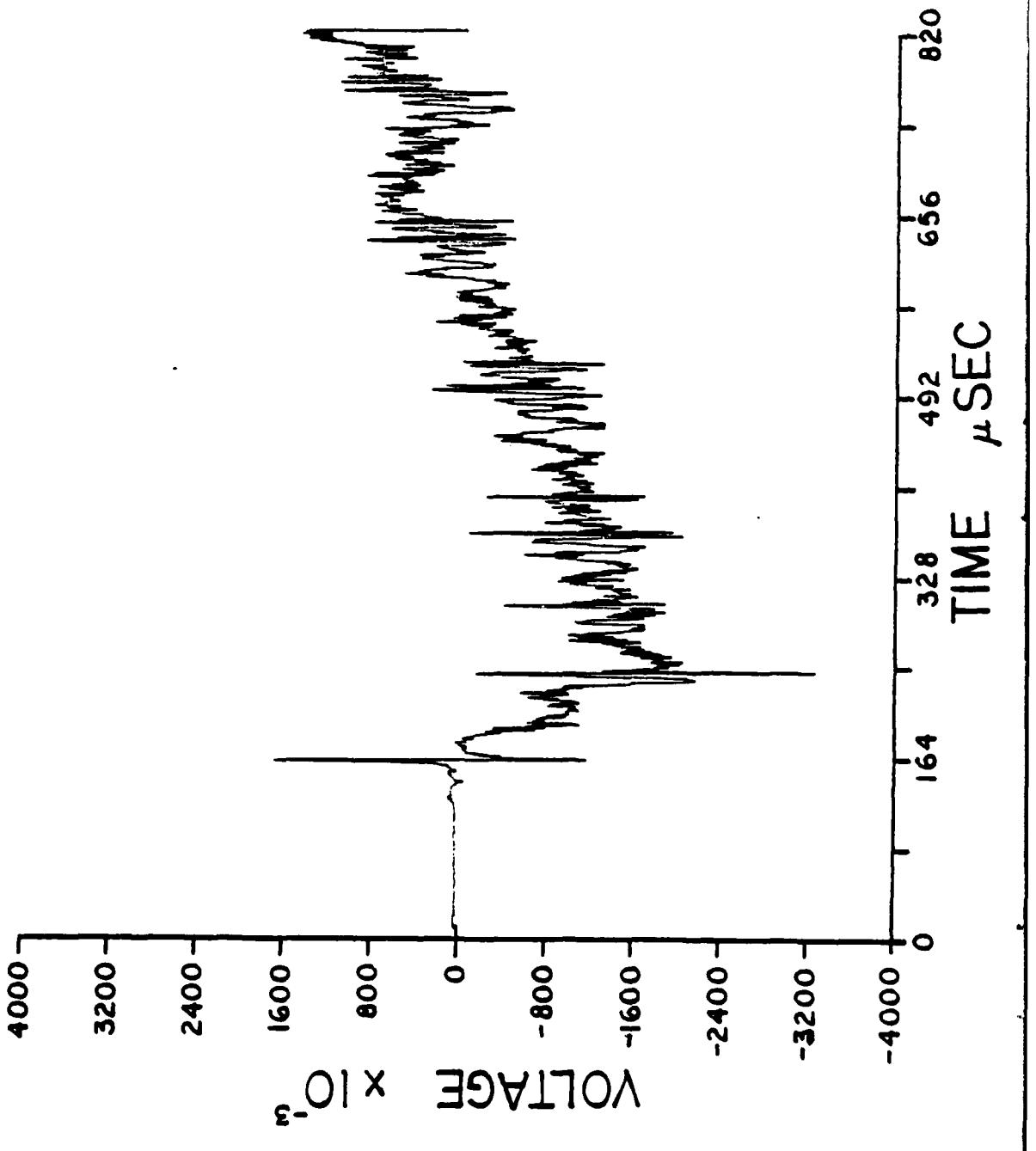
VOLTAGE x 10⁻³
4000
3200
2400
1600
800
0
-800
-1600
-2400
-3200
-4000
0
164
328
492
656
820
TIME μSEC

E34

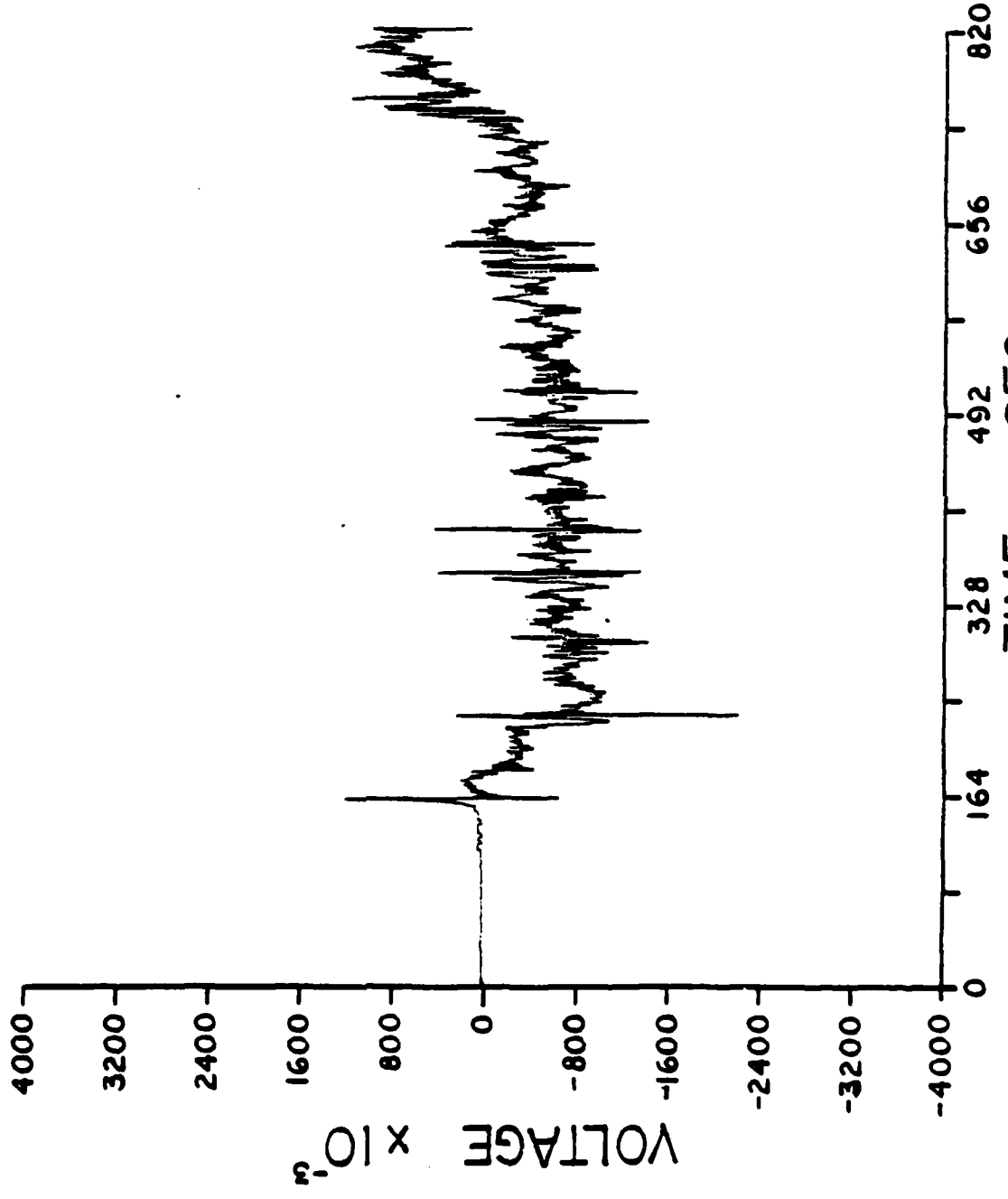
VOLTAGE x 10⁻³
4000
3200
2400
1600
800
0
-800
-1600
-2400
-3200
-4000
0
164
328
492
656
820
TIME μSEC

E35

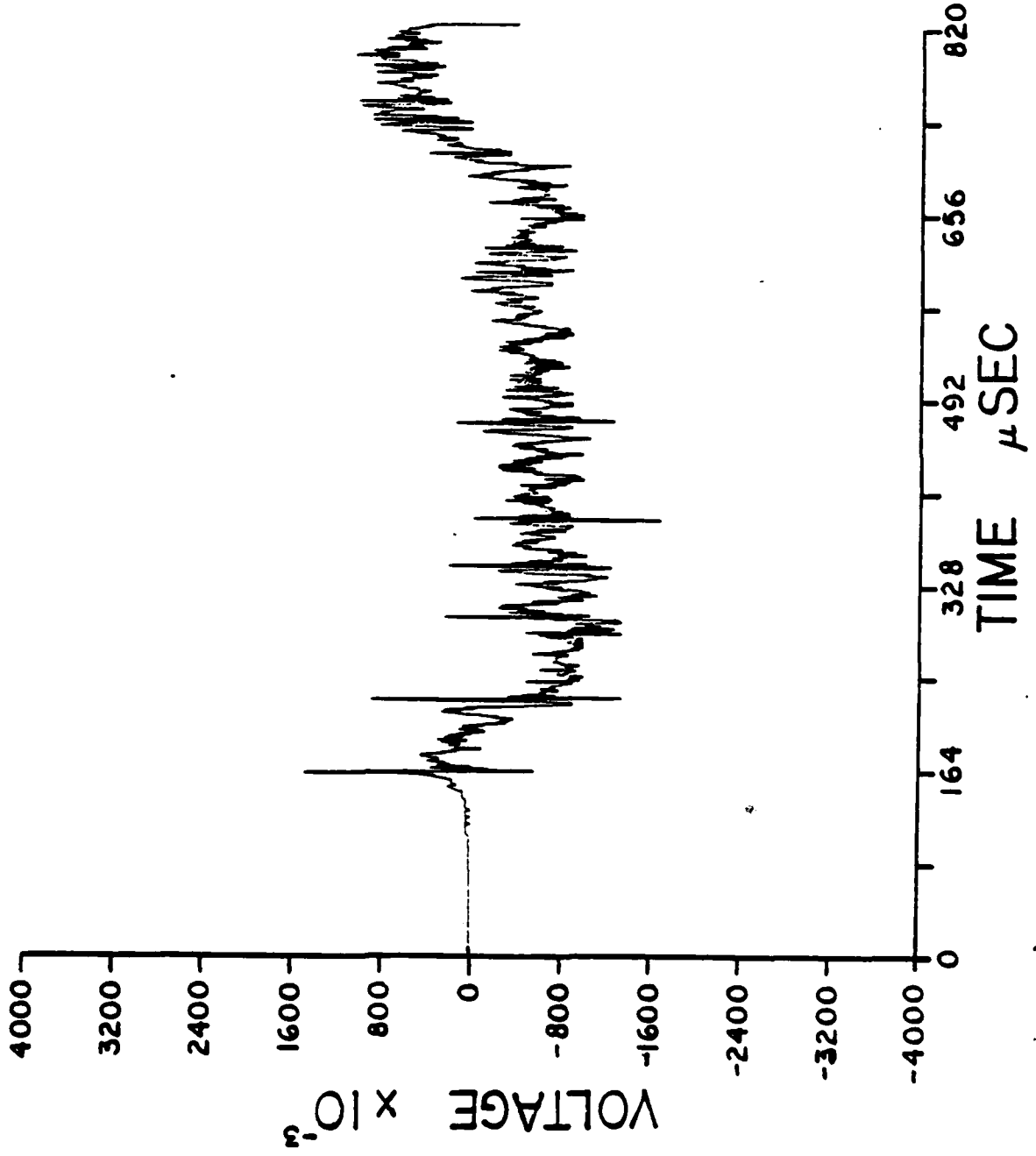
4000
3200
2400
1600
800
0
-800
-1600
-2400
-3200
-4000
VOLTAGE x 10⁻³
0
164
328
492
656
820
TIME μSEC

E36

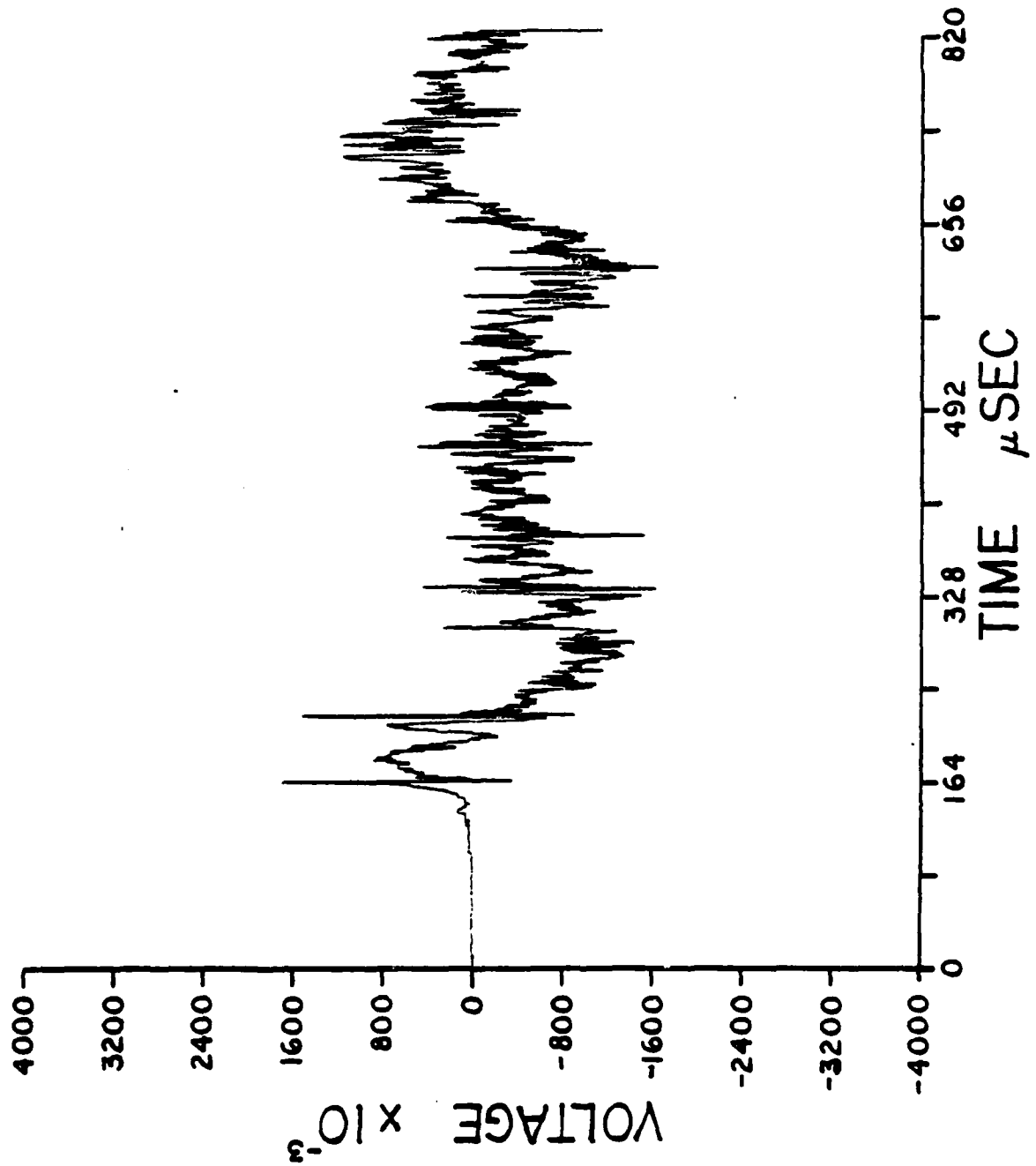
VOLTAGE x 10⁻³
4000
3200
2400
1600
800
0
-800
-1600
-2400
-3200
-4000
0
164
328
492
656
820
TIME μSEC

E37

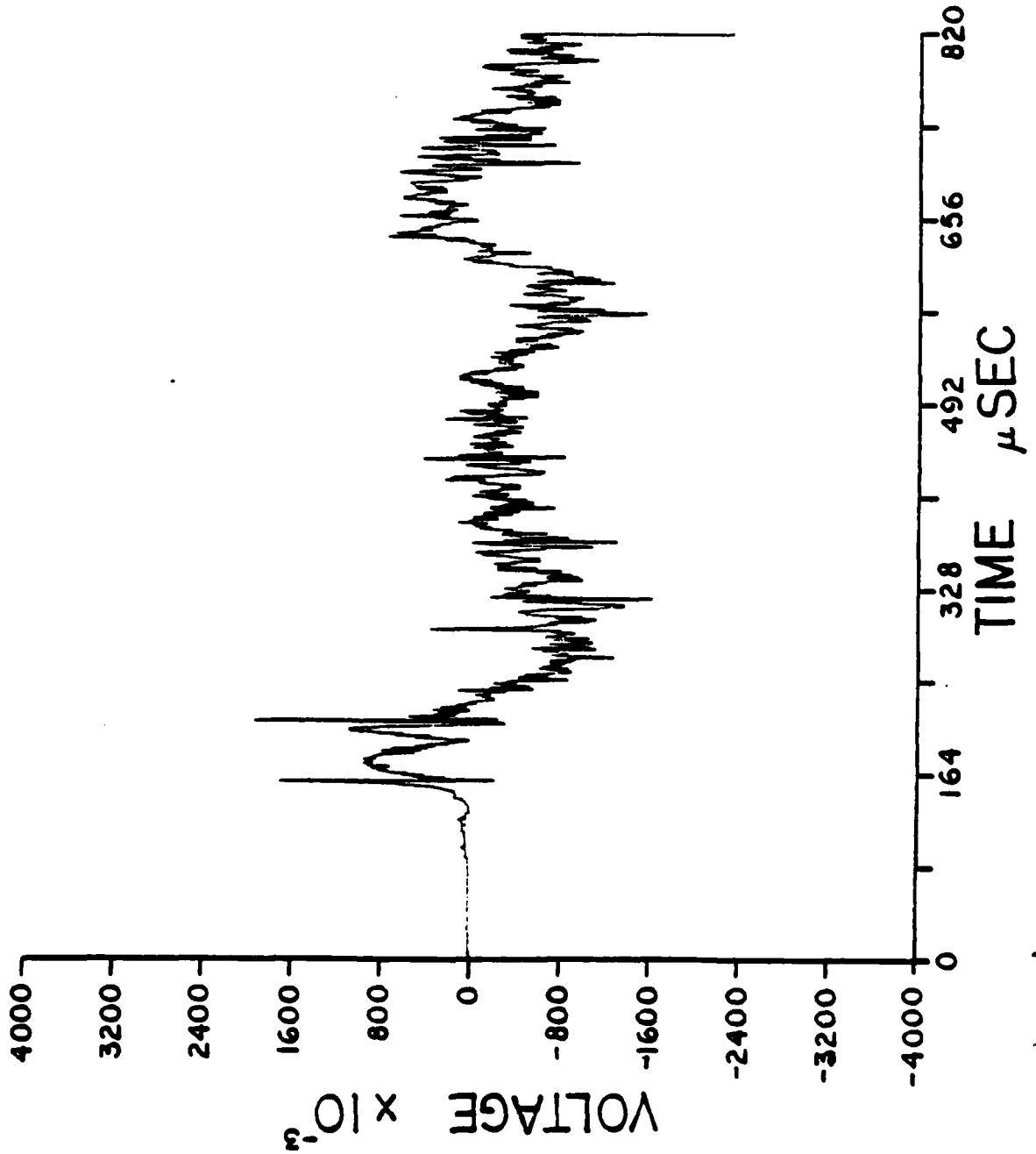
4000
3200
2400
1600
800
0
-800
-1600
-2400
-3200
-4000
VOLTAGE x 10⁻³
0
164
328
492
656
820
TIME μSEC

E38

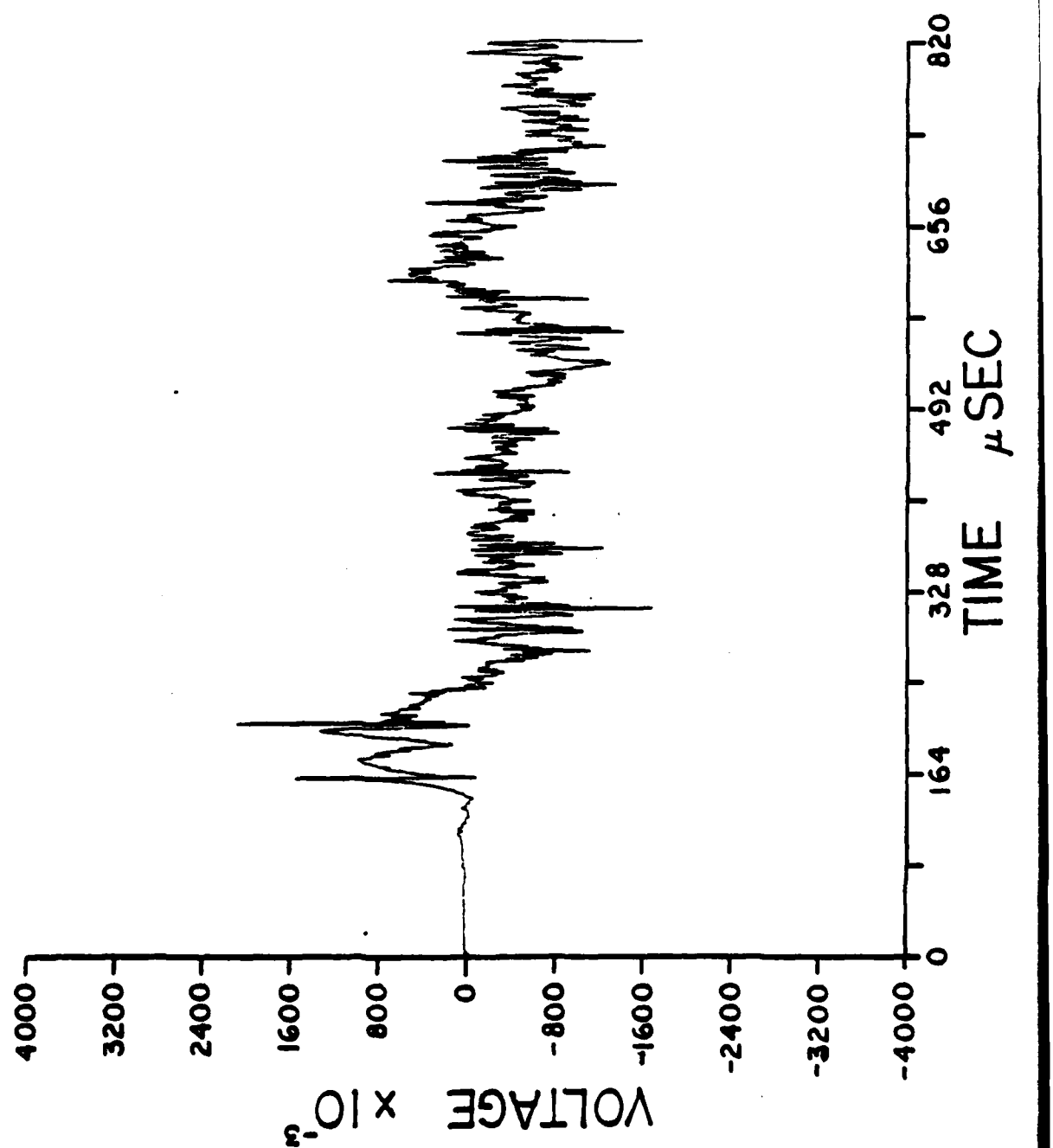
VOLTAGE x 10⁻³
4000
3200
2400
1600
800
0
-800
-1600
-2400
-3200
-4000
0
164
328
492
656
820
TIME μSEC

E39

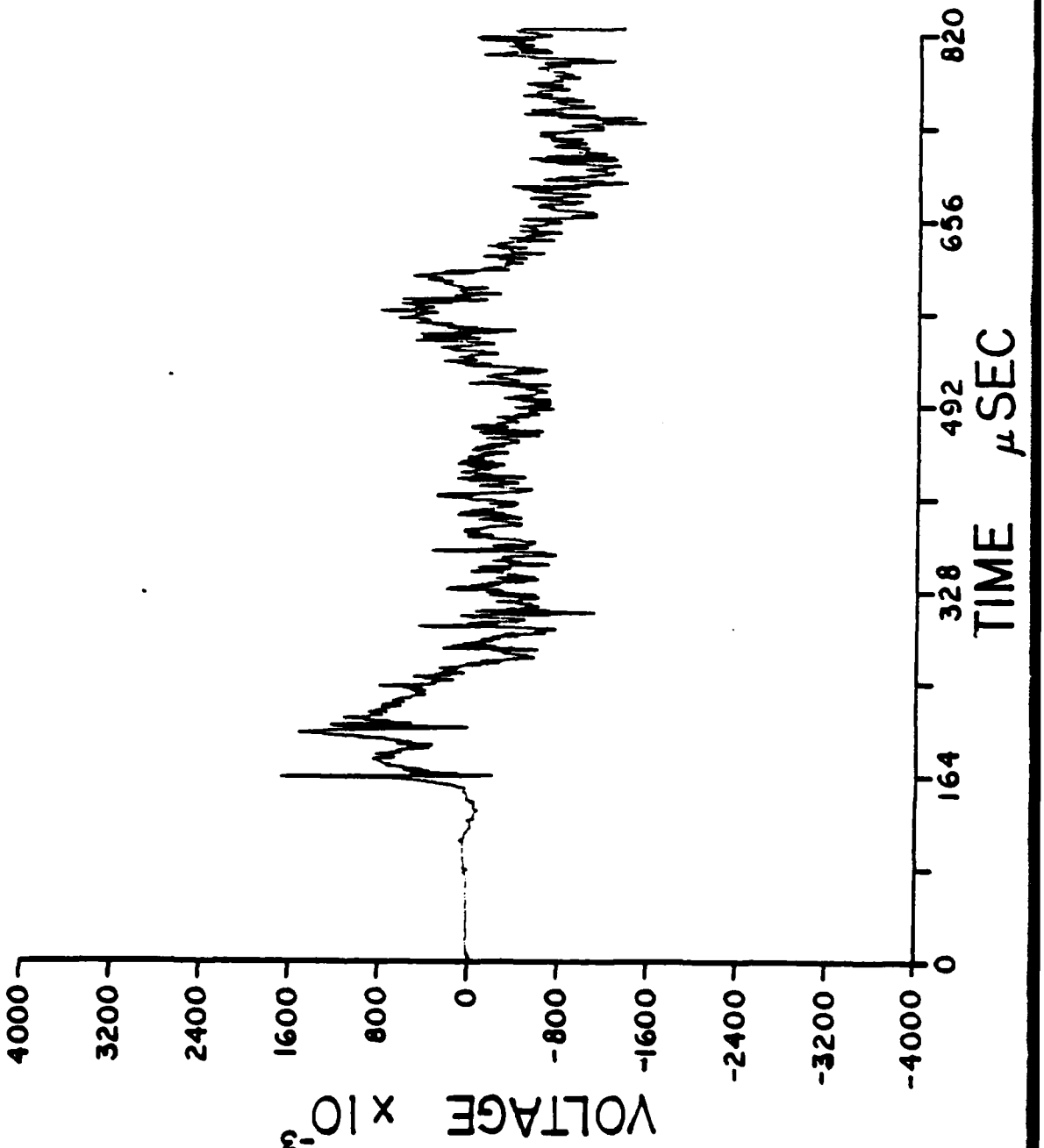
VOLTAGE x 10⁻³
4000
3200
2400
1600
800
0
-800
-1600
-2400
-3200
-4000
0
164
328
492
656
820
TIME μSEC

E40

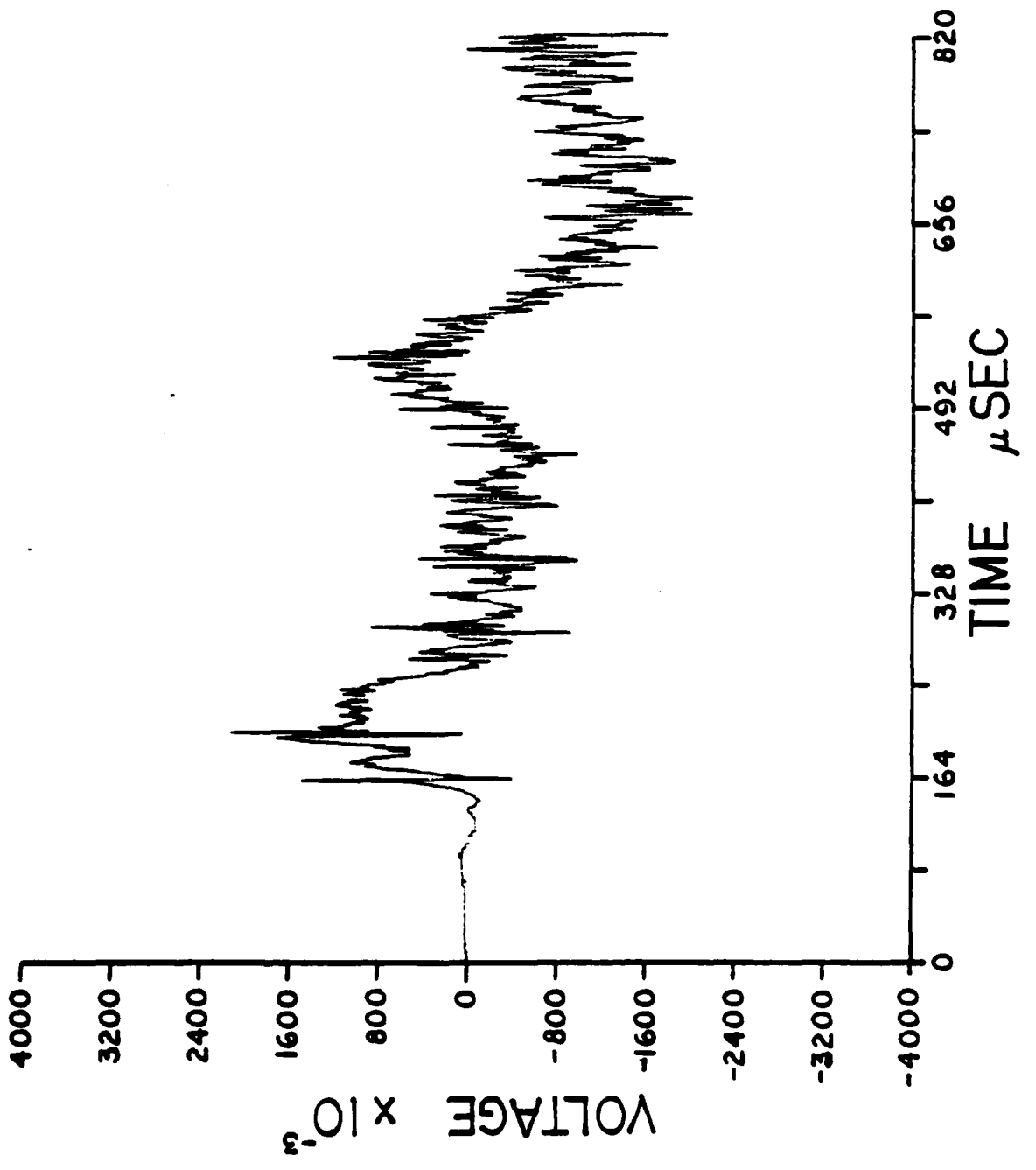
VOLTAGE x 10⁻³
4000
3200
2400
1600
800
0
-800
-1600
-2400
-3200
-4000
0
164
328
492
656
820
TIME μSEC

E41

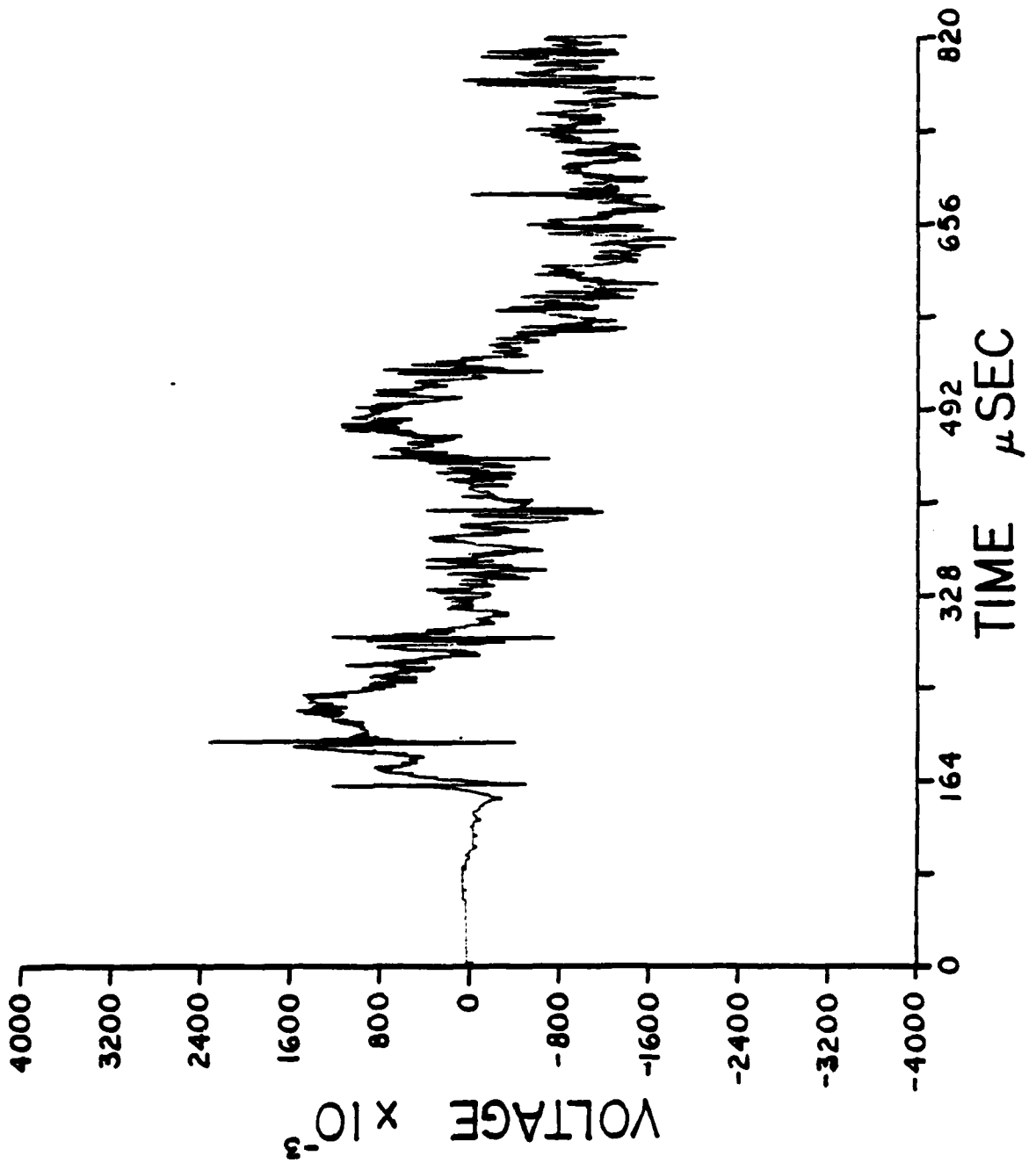
VOLTAGE x 10⁻³
4000
3200
2400
1600
800
0
-800
-1600
-2400
-3200
-4000
0
164
328
492
656
820
TIME μSEC

E42

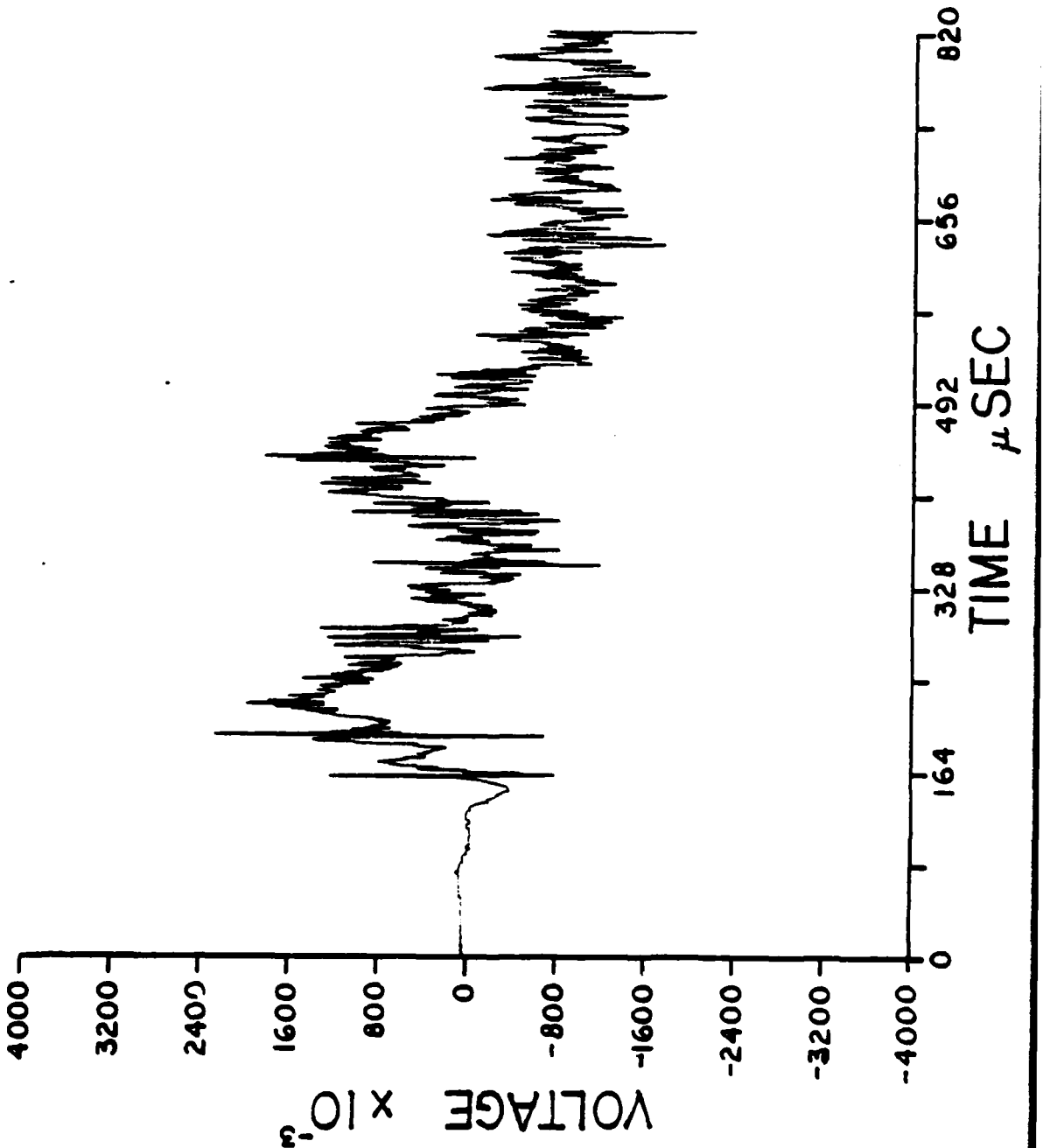
VOLTAGE x 10⁻³
4000
3200
2400
1600
800
0
-800
-1600
-2400
-3200
-4000
0
164
328
492
656
820
TIME μSEC

E43

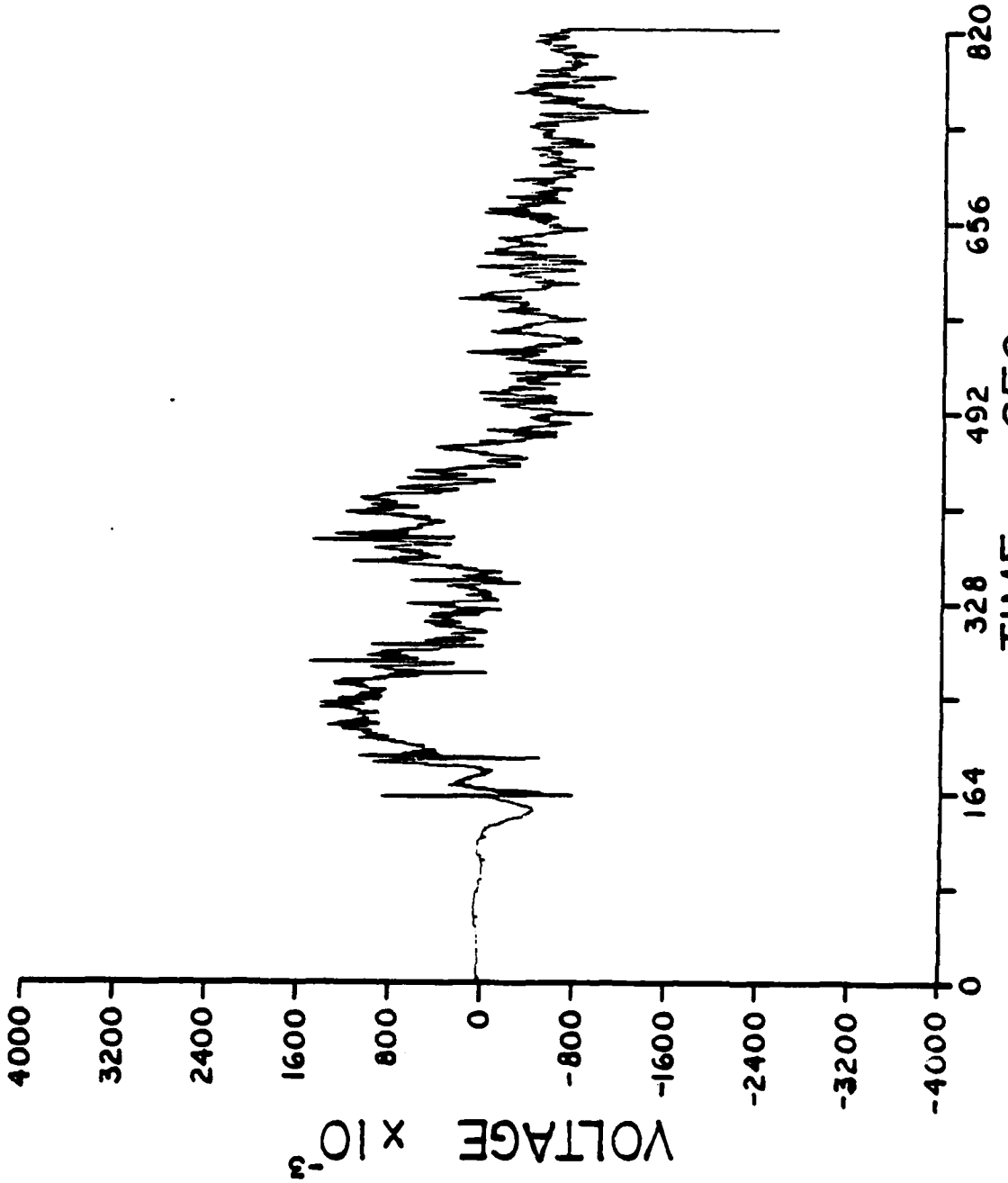
VOLTAGE x 10⁻³
4000
3200
2400
1600
800
0
-800
-1600
-2400
-3200
-4000
0
164
328
492
656
820
TIME μSEC

E44

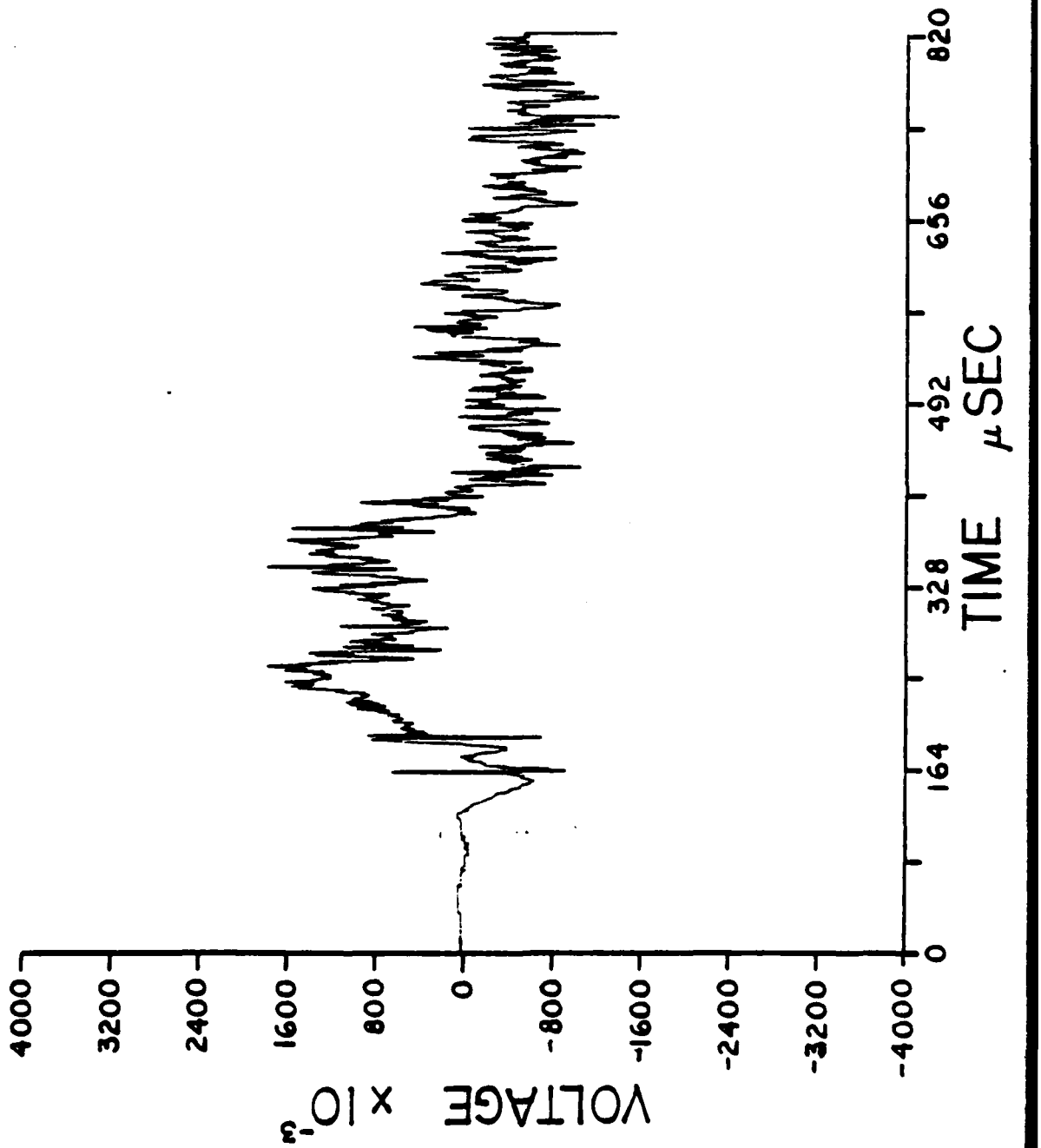
VOLTAGE x 10⁻³
4000
3200
2400
1600
800
0
-800
-1600
-2400
-3200
-4000
0
164
328
492
656
820
TIME μSEC

E45

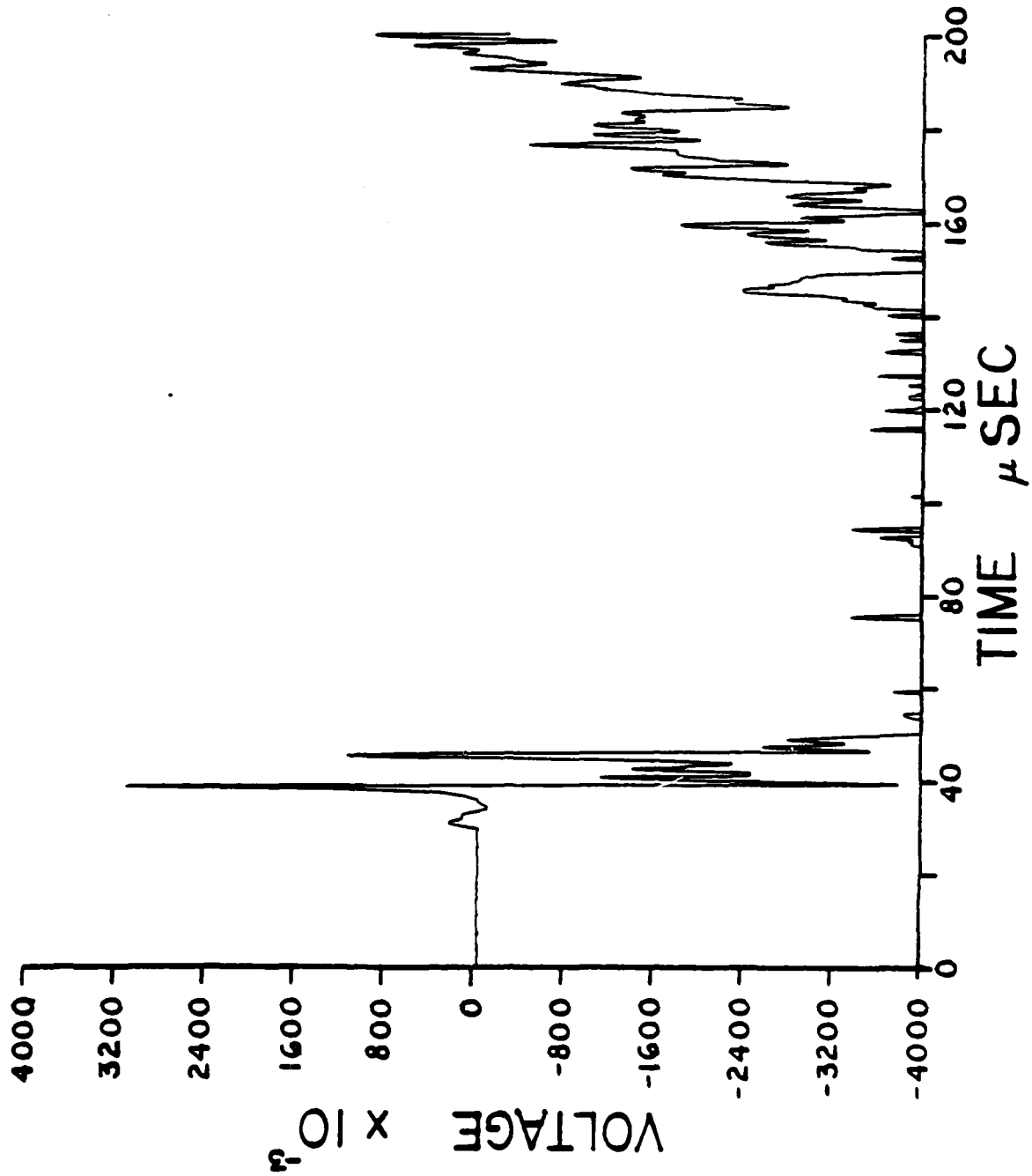
VOLTAGE x 10⁻³
4000
3200
2400
1600
800
0
-800
-1600
-2400
-3200
-4000
0
40
80
120
160
200
TIME μSEC

E46

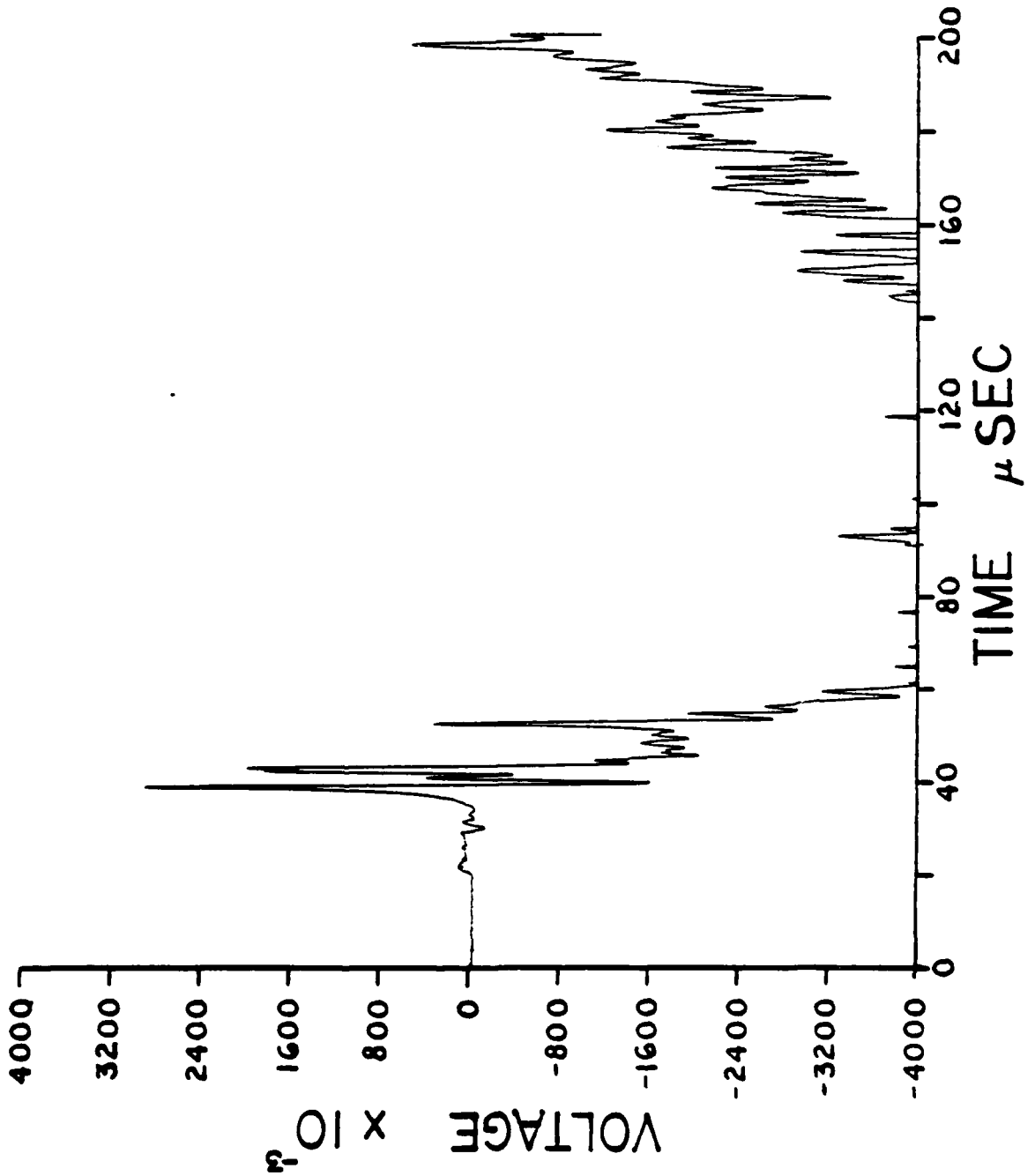
4000
3200
2400
1600
800
0
-800
-1600
-2400
-3200
-4000
VOLTAGE x 10^-3
0
40
80
120
160
200
TIME μSEC

E47

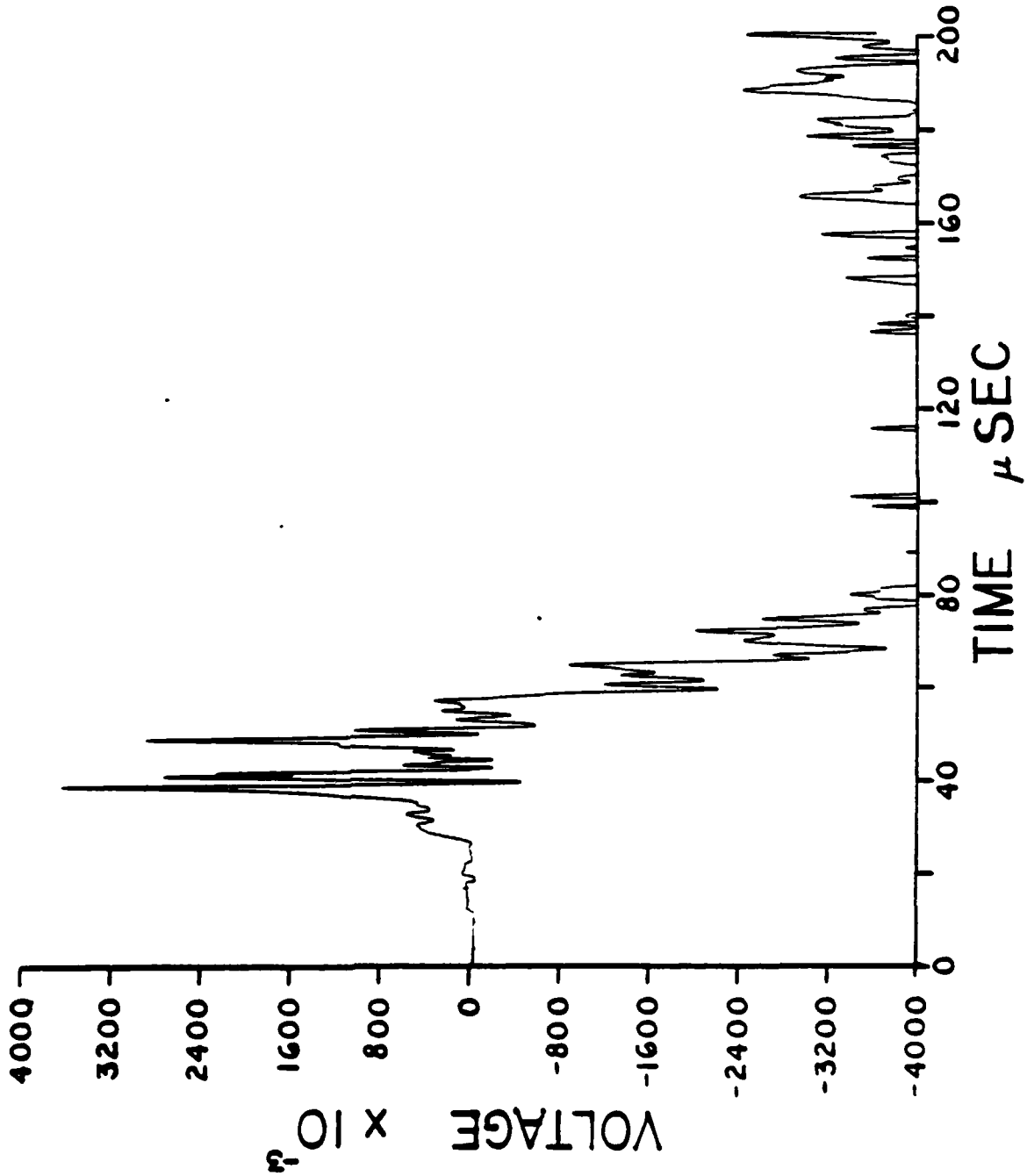
4000
3200
2400
1600
800
0
-800
-1600
-2400
-3200
-4000
VOLTAGE x 10
0
40
80
120
160
200
TIME μSEC

E48

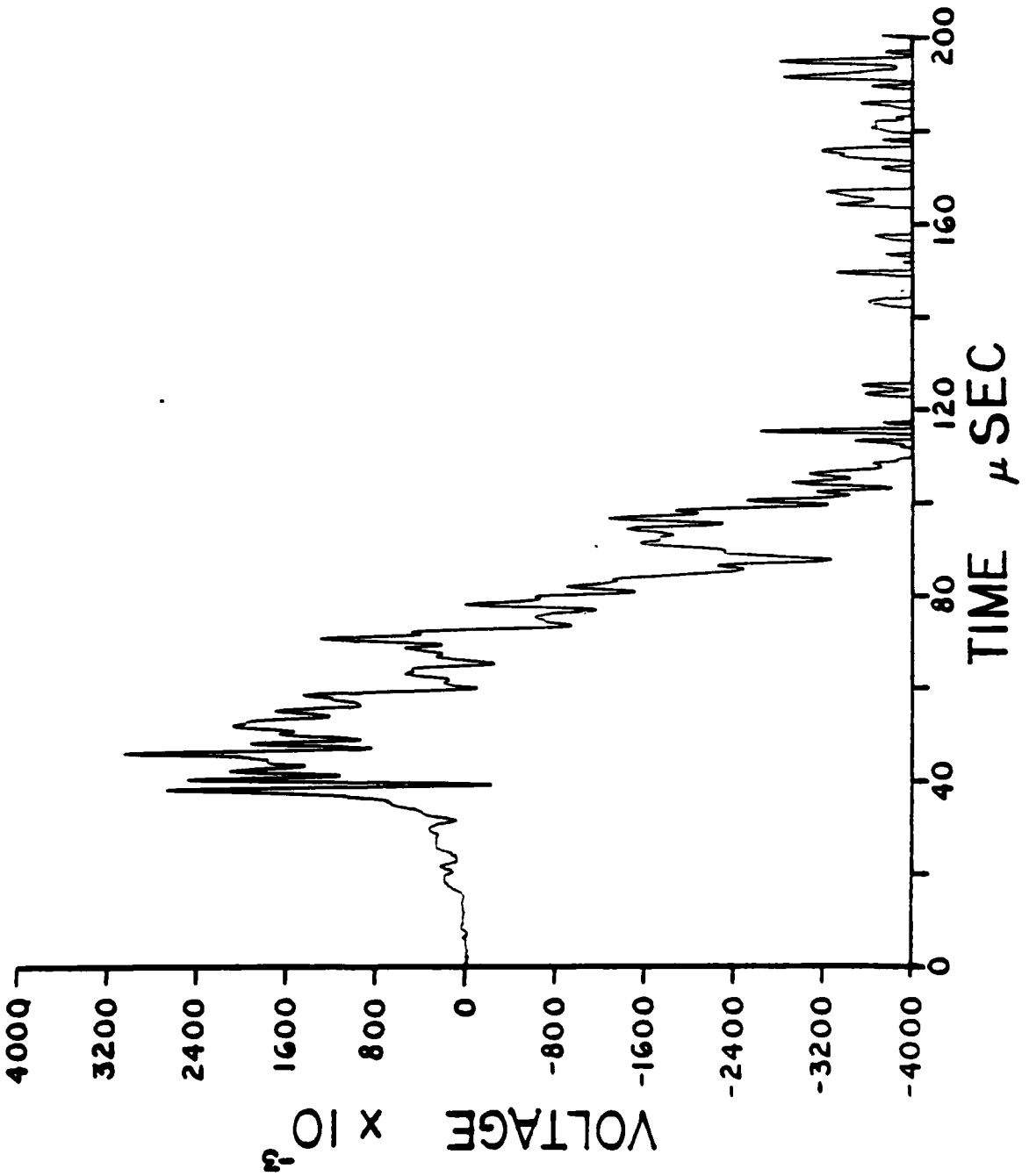
VOLTAGE x 10³
4000
3200
2400
1600
800
0
-800
-1600
-2400
-3200
-4000
0
40
80
120
160
200
TIME μSEC

E49

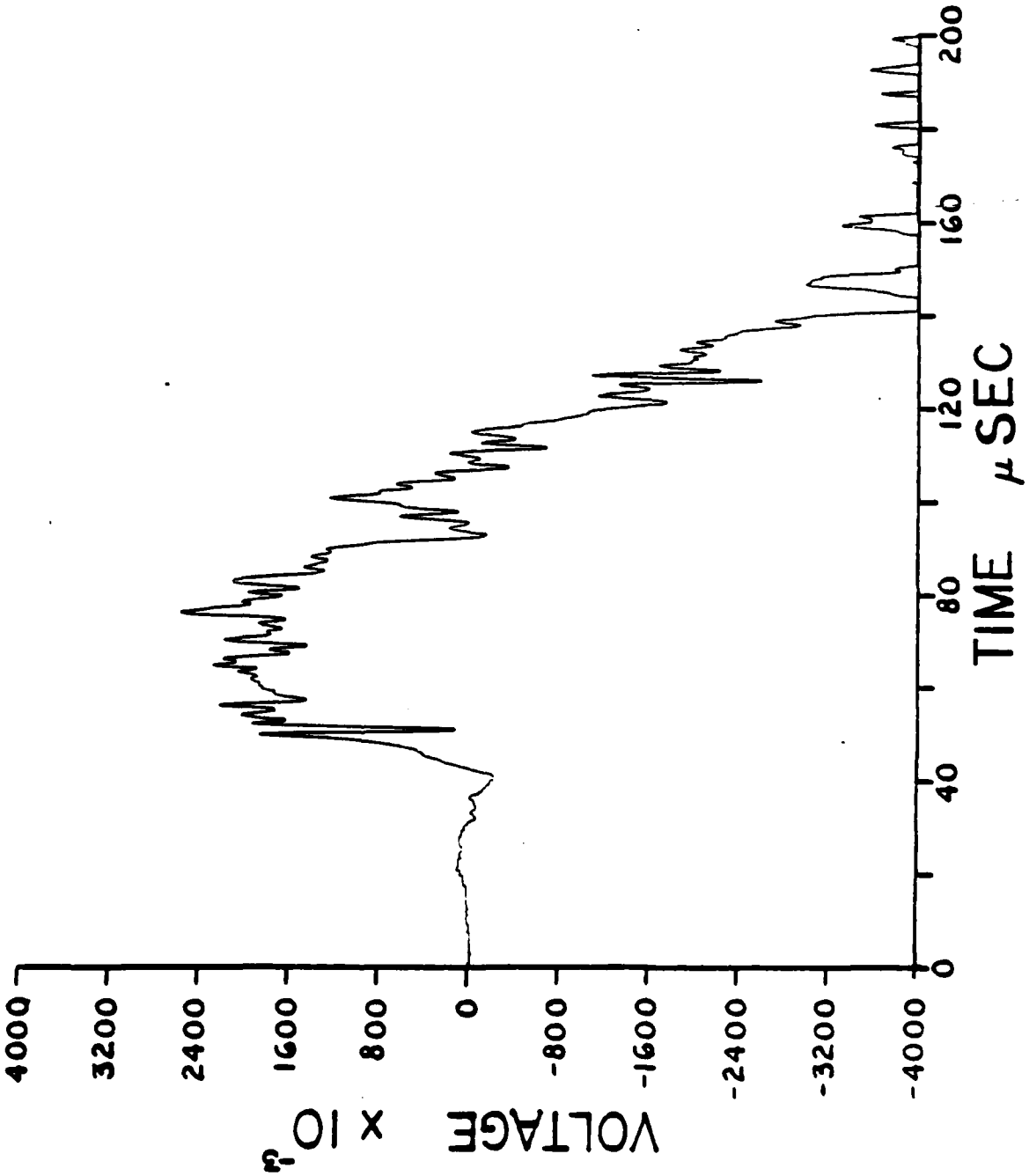
VOLTAGE x 10^{-3}
4000
3200
2400
1600
800
0
-800
-1600
-2400
-3200
-4000
0
40
80
120
160
200
TIME μSEC

E50

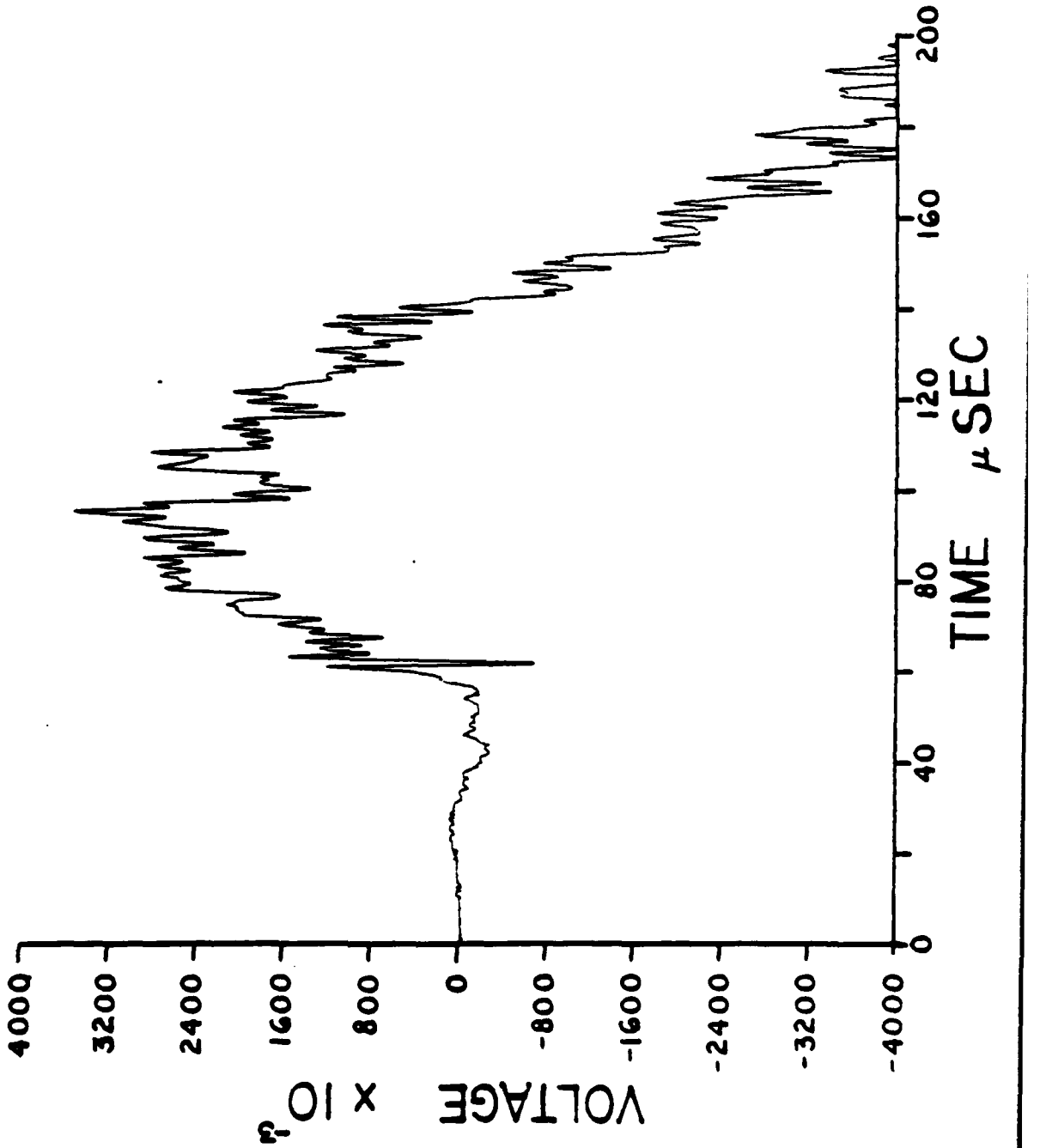
VOLTAGE x 10^3
4000
3200
2400
1600
800
0
-800
-1600
-2400
-3200
-4000
0
40
80
120
160
200
TIME μSEC

E51

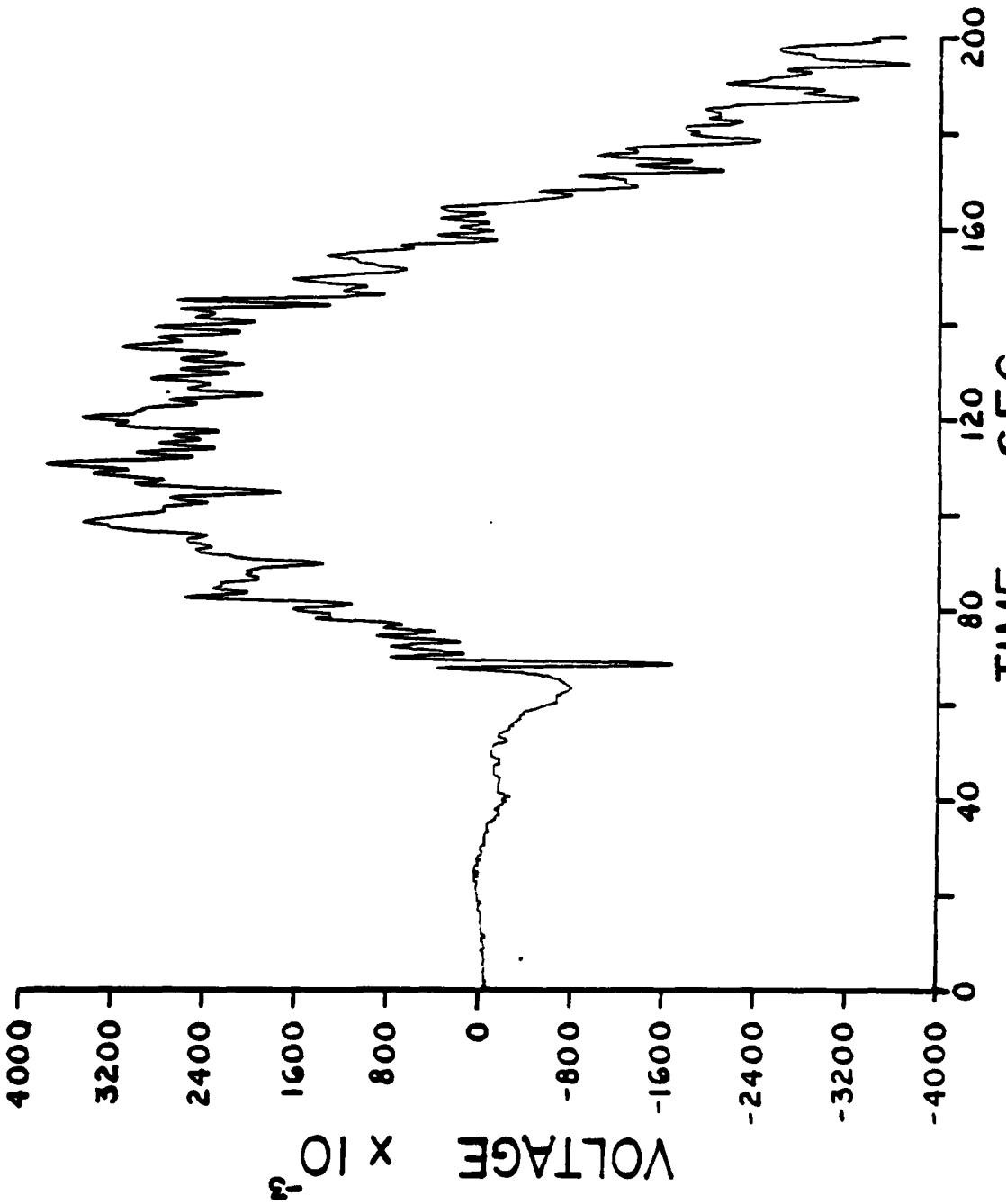
VOLTAGE x 10⁻³
4000
3200
2400
1600
800
0
-800
-1600
-2400
-3200
-4000
0
40
80
120
160
200
TIME μSEC

E52

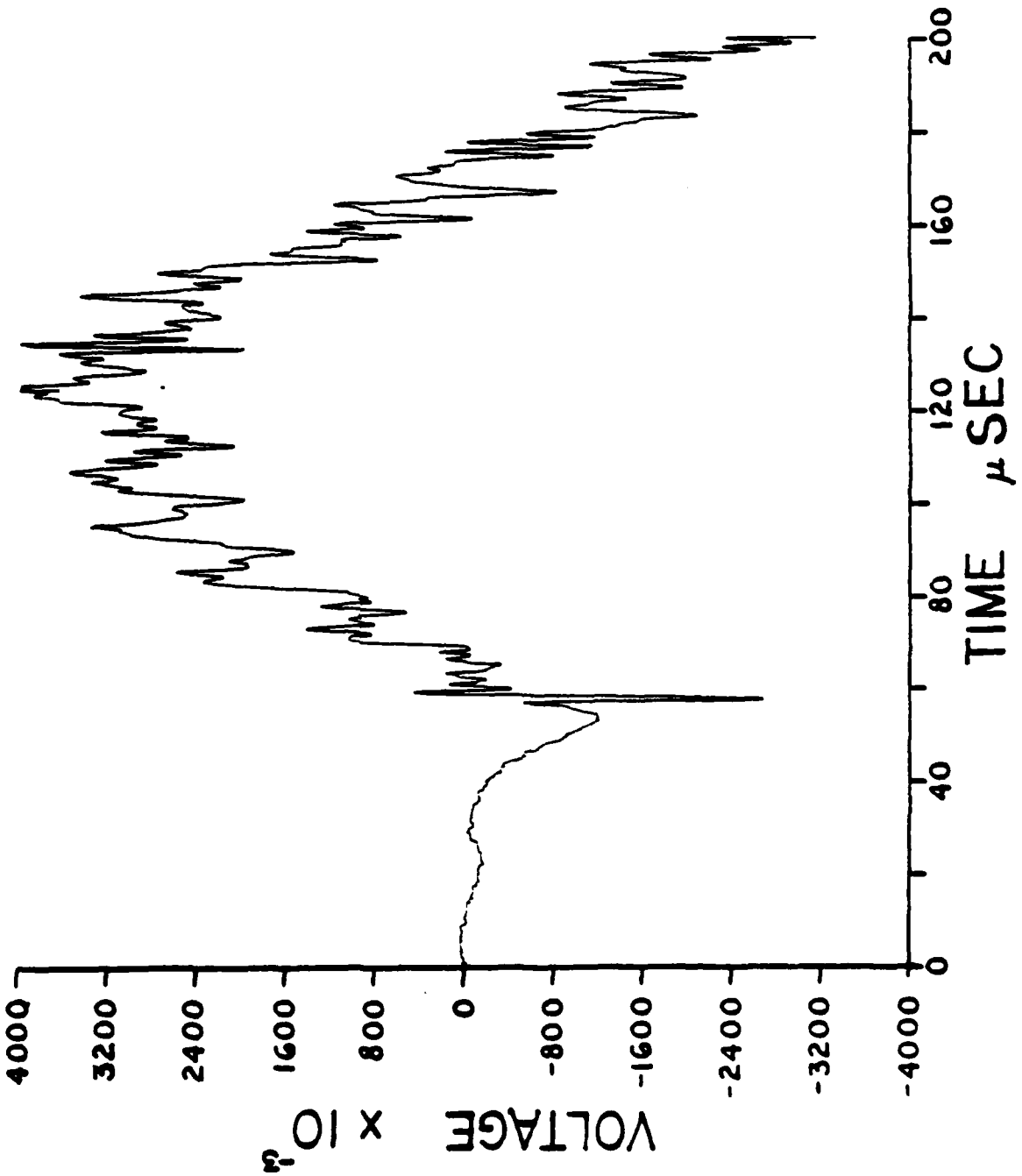
VOLTAGE x 10⁻³
4000
3200
2400
1600
800
0
-800
-1600
-2400
-3200
-4000
0
40
80
120
160
200
TIME μSEC

E53

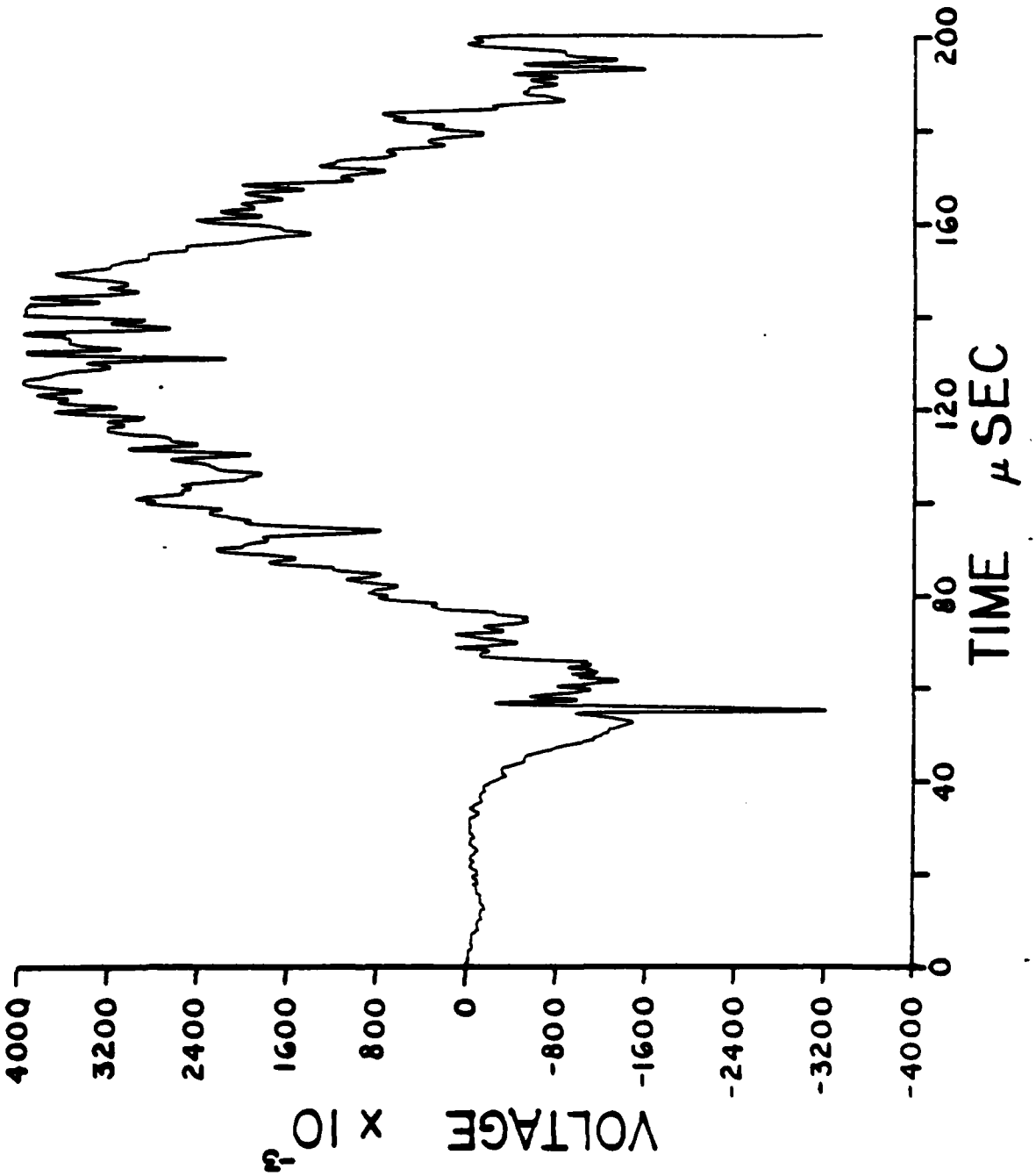
VOLTAGE x 10⁻³
4000
3200
2400
1600
800
0
-800
-1600
-2400
-3200
-4000
0
40
80
120
160
200
TIME μSEC

E54

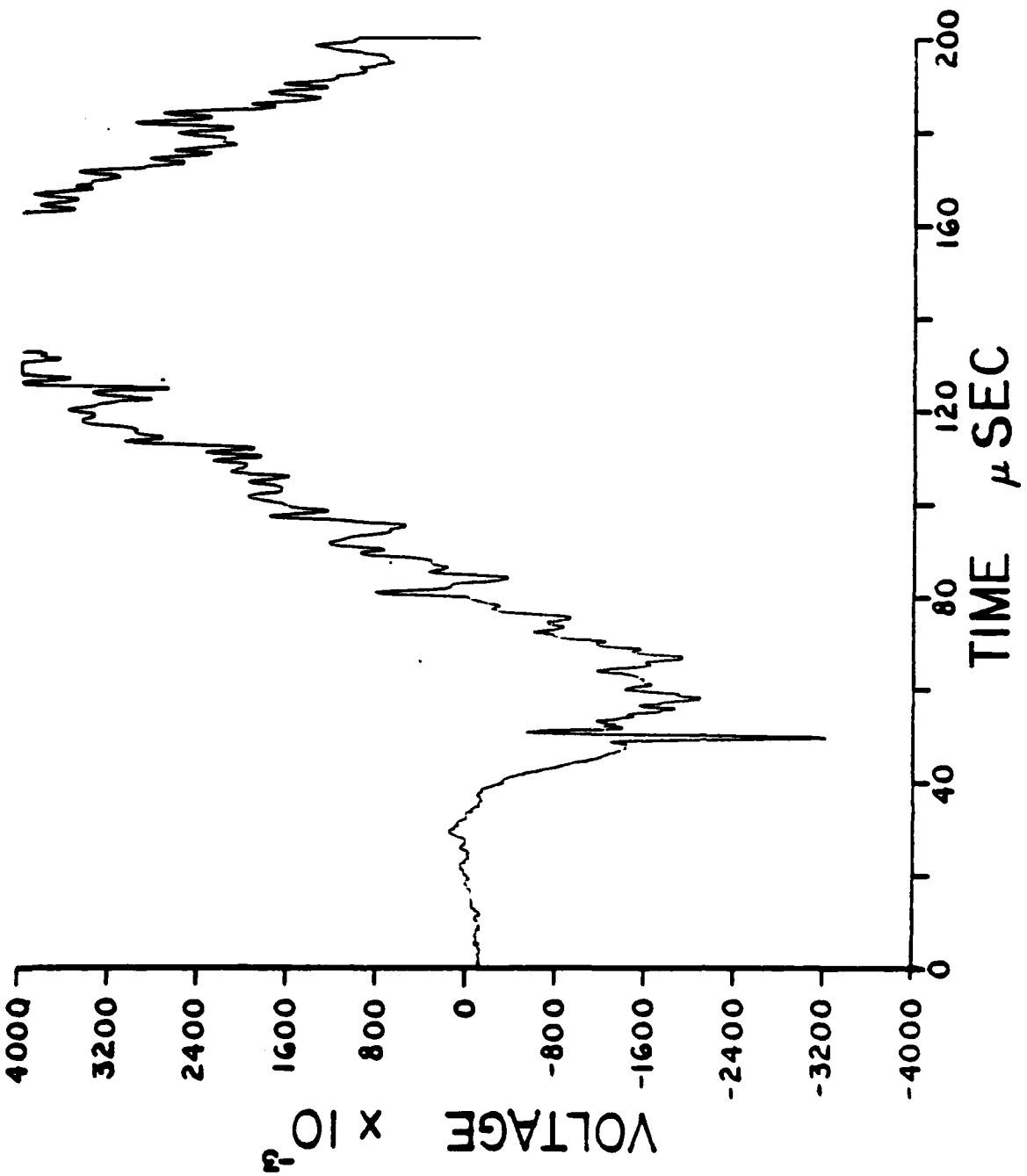
VOLTAGE x 10⁻³
4000
3200
2400
1600
800
0
-800
-1600
-2400
-3200
-4000
0
40
80
120
160
200
TIME μSEC

E55

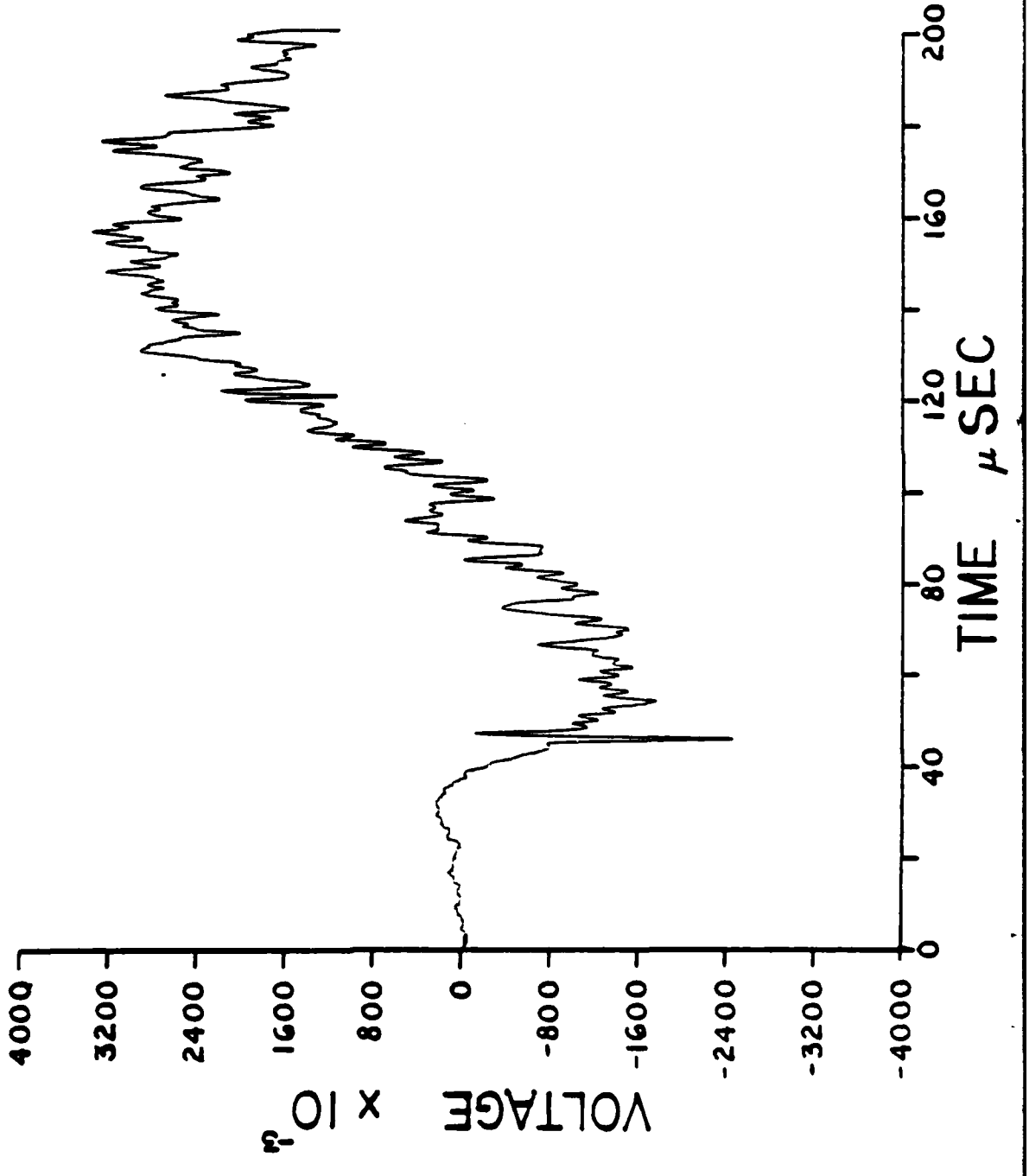
VOLTAGE x 10^{-3}
4000
3200
2400
1600
800
0
-800
-1600
-2400
-3200
-4000
0
40
80
120
160
200
TIME μSEC

E56

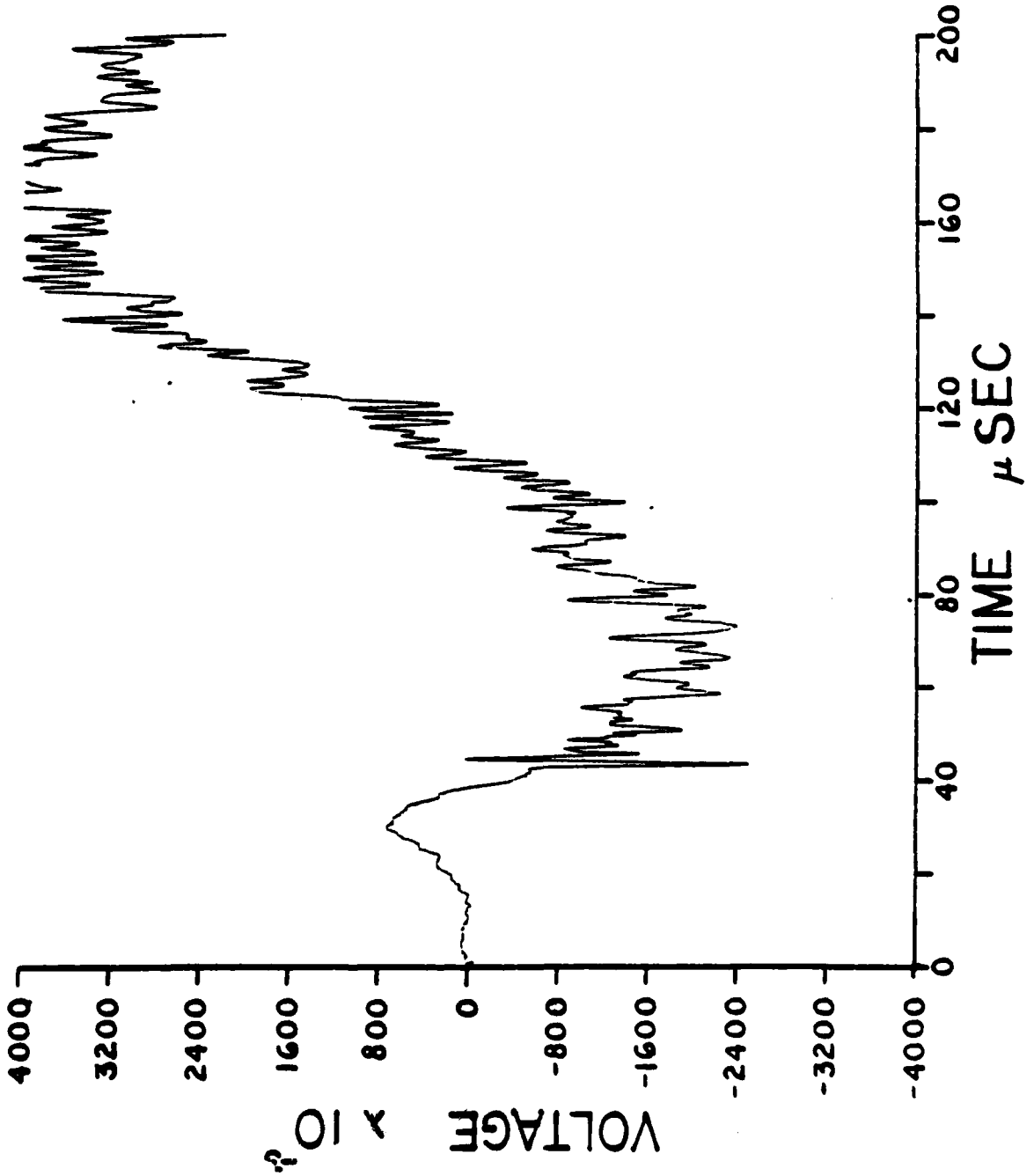
4000
3200
2400
1600
800
0
-800
-1600
-2400
-3200
-4000
VOLTAGE x 10²
0
40
80
120
160
200
TIME μSEC

E57

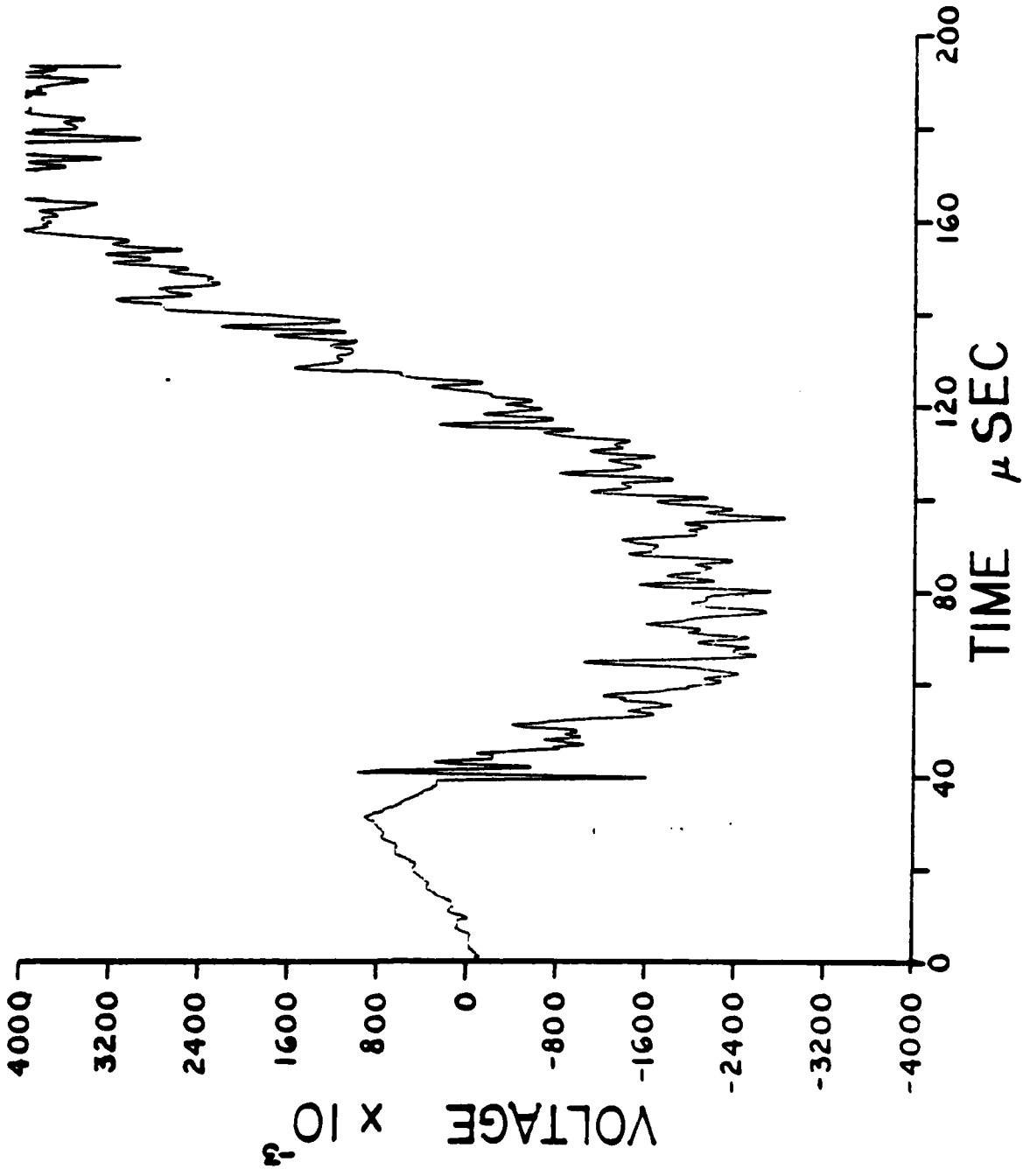
VOLTAGE x 10^3
4000
3200
2400
1600
800
0
-800
-1600
-2400
-3200
-4000
0
40
80
120
160
200
TIME μSEC

E58

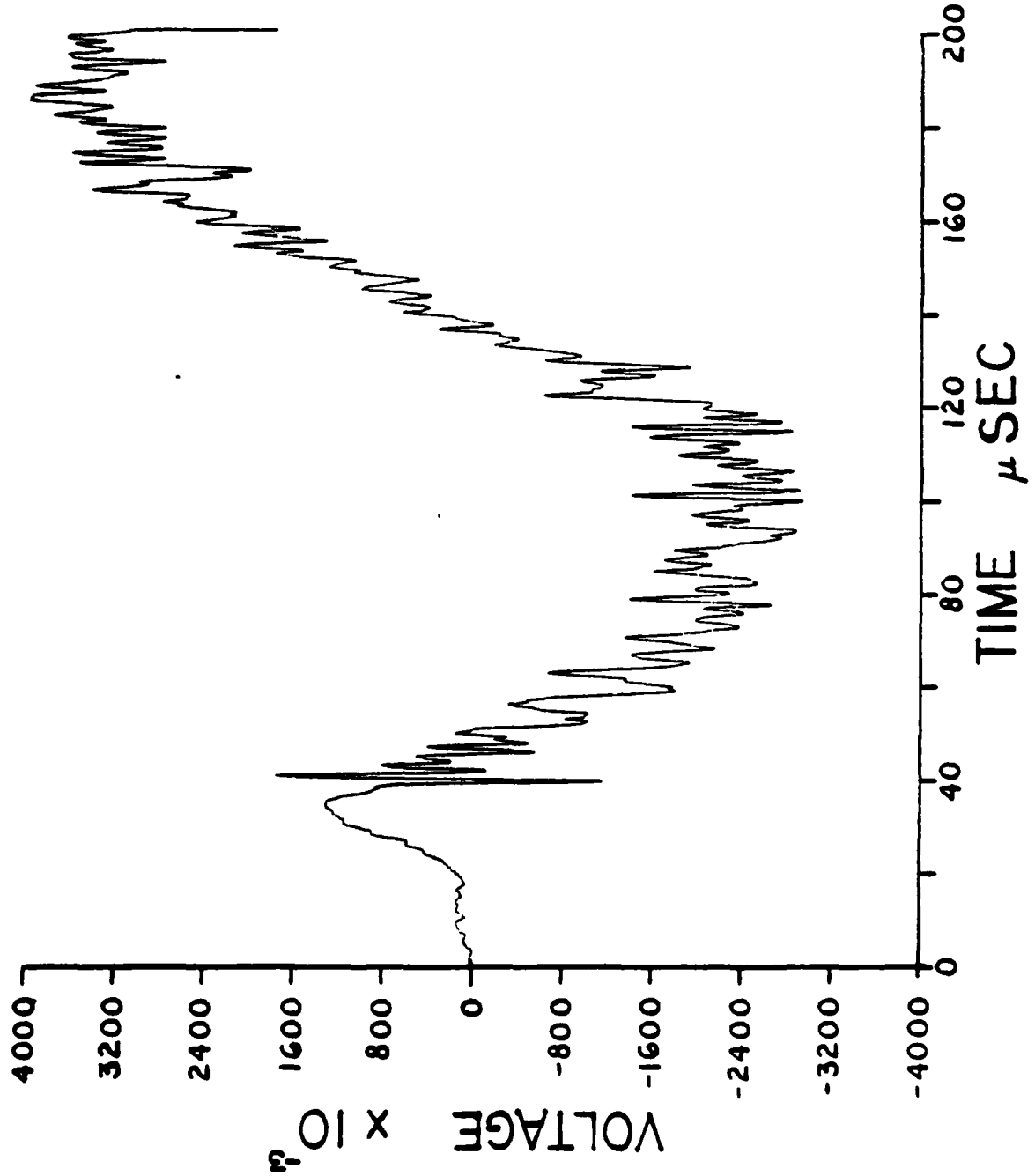
VOLTAGE x 10⁻³
4000
3200
2400
1600
800
0
-800
-1600
-2400
-3200
-4000
0
40
80
120
160
200
TIME μSEC

E59

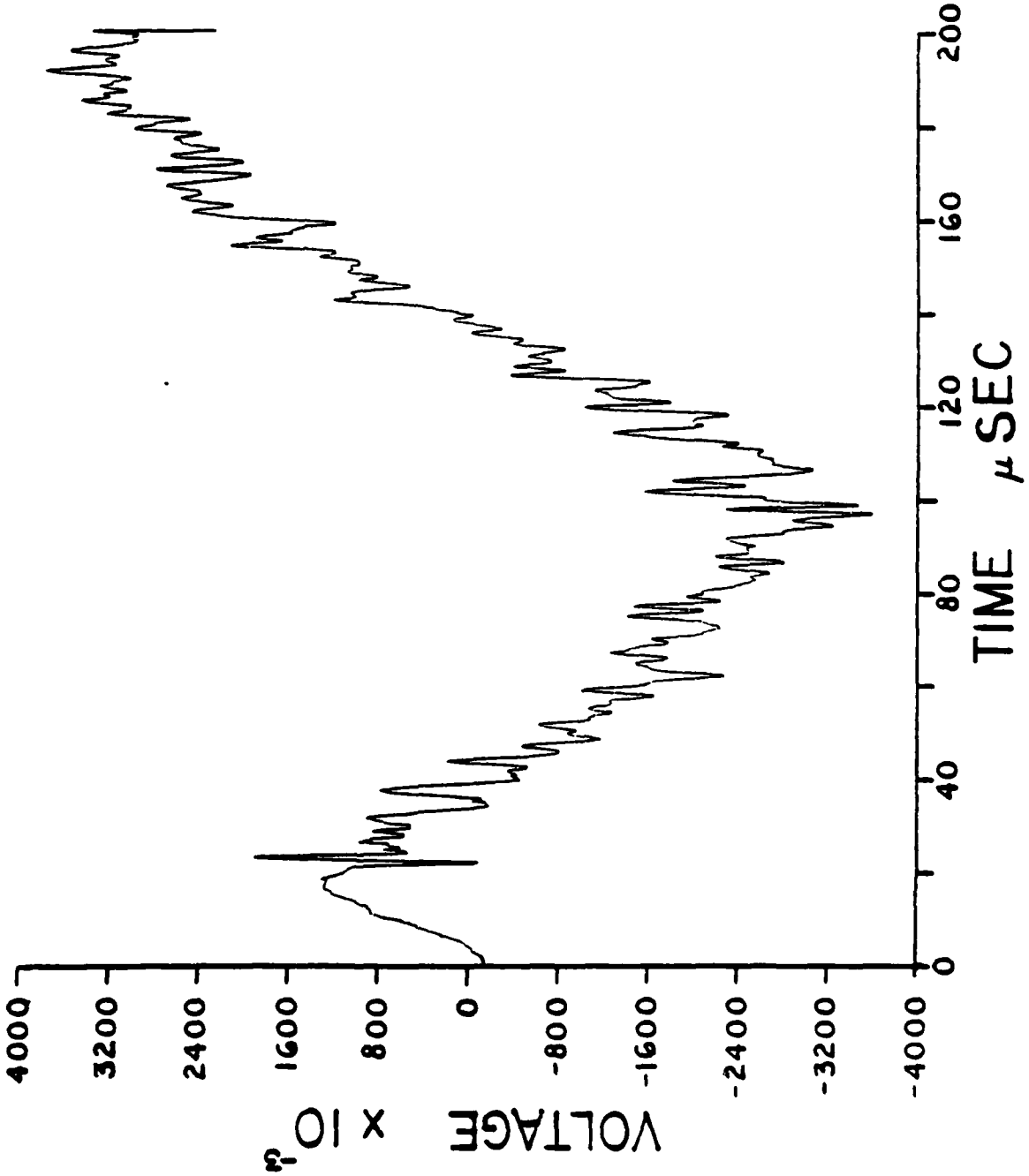
VOLTAGE x 10⁻³
4000
3200
2400
1600
800
0
-800
-1600
-2400
-3200
-4000
0
40
80
120
160
200
TIME μSEC

E60

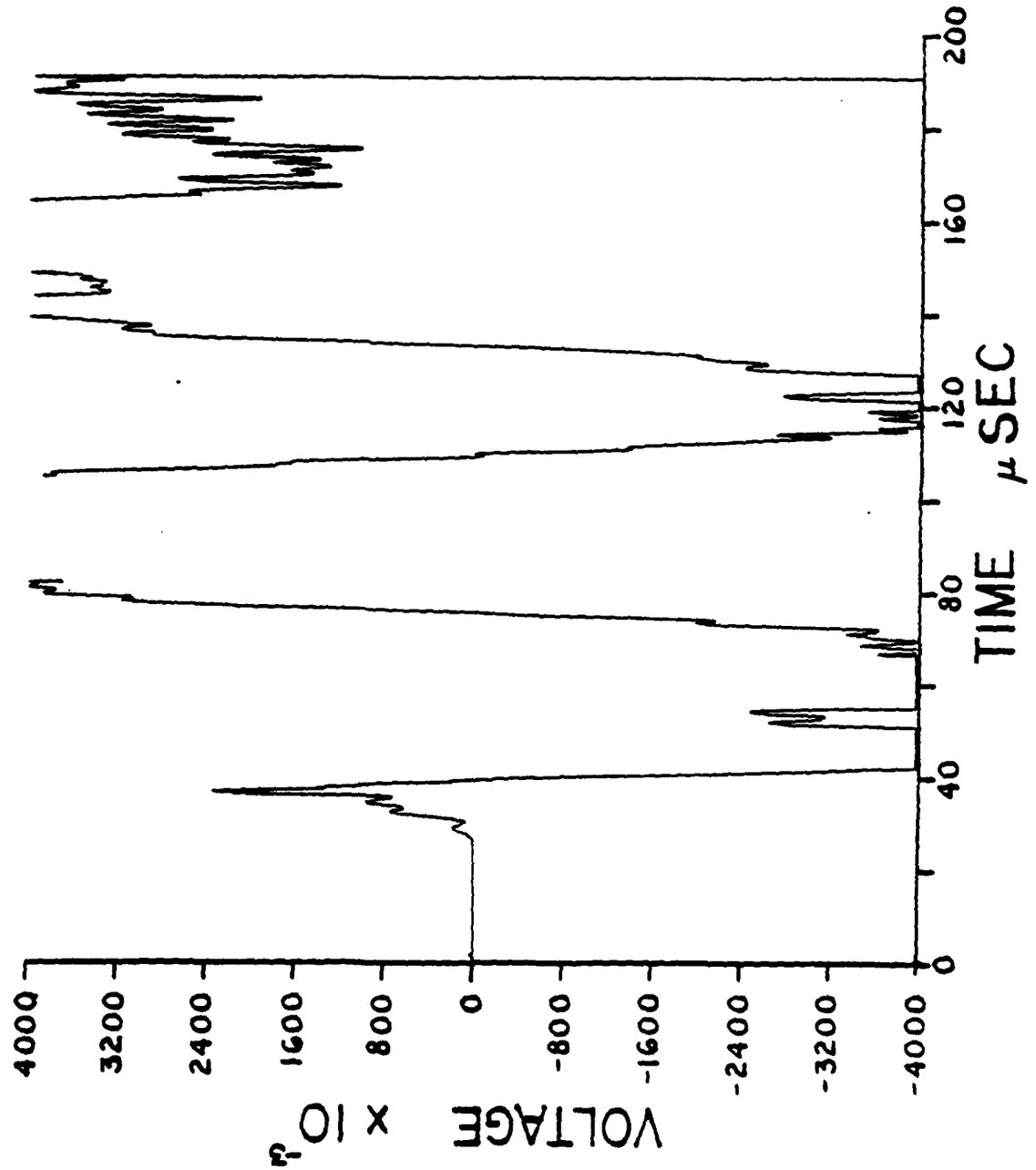
VOLTAGE x 10^{-3}
4000
3200
2400
1600
800
0
-800
-1600
-2400
-3200
-4000
0
40
80
120
160
200
TIME μSEC

E61

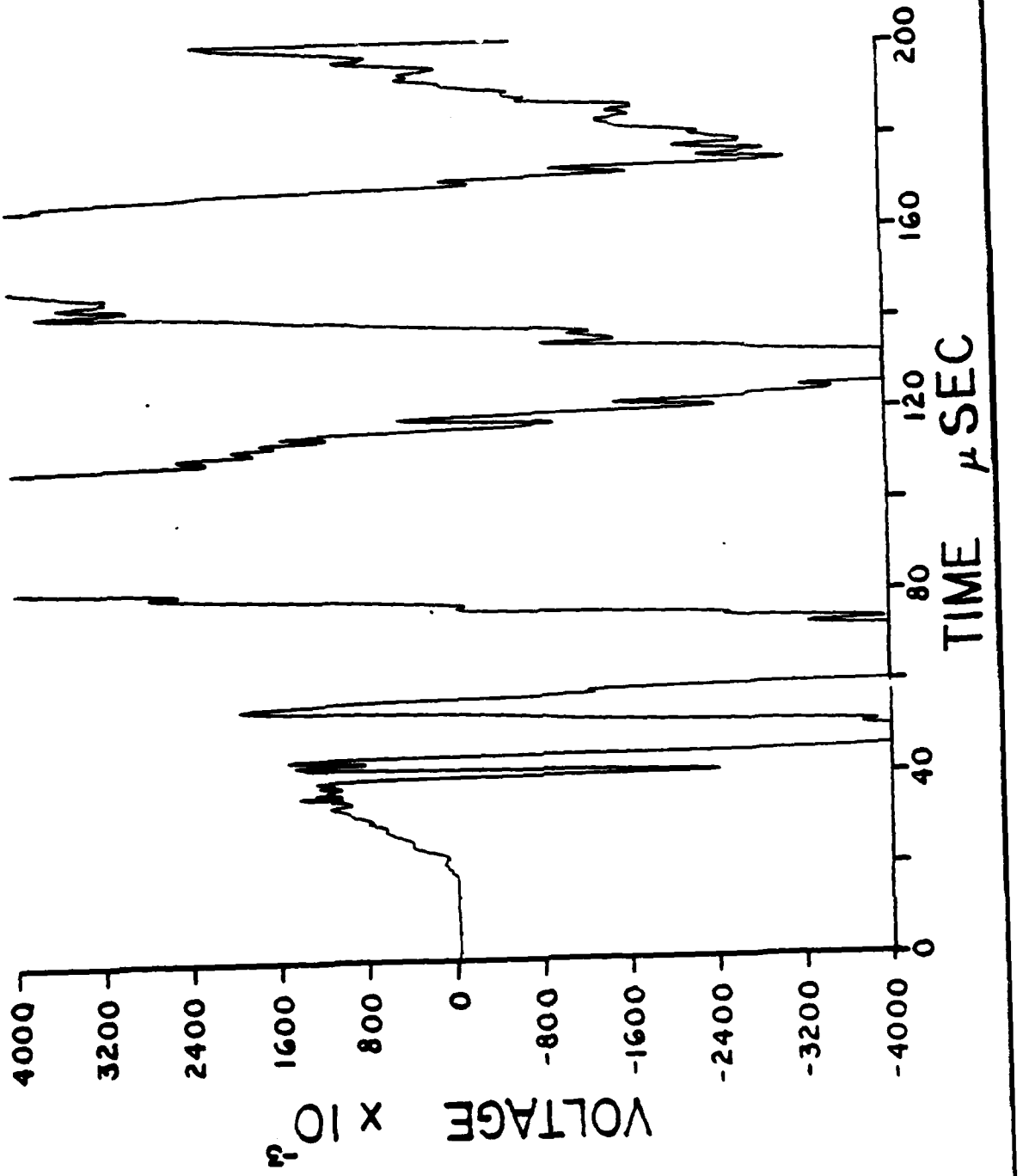
VOLTAGE x 10^3
4000
3200
2400
1600
800
0
-800
-1600
-2400
-3200
-4000
0
40
80
120
160
200
TIME μSEC

E62

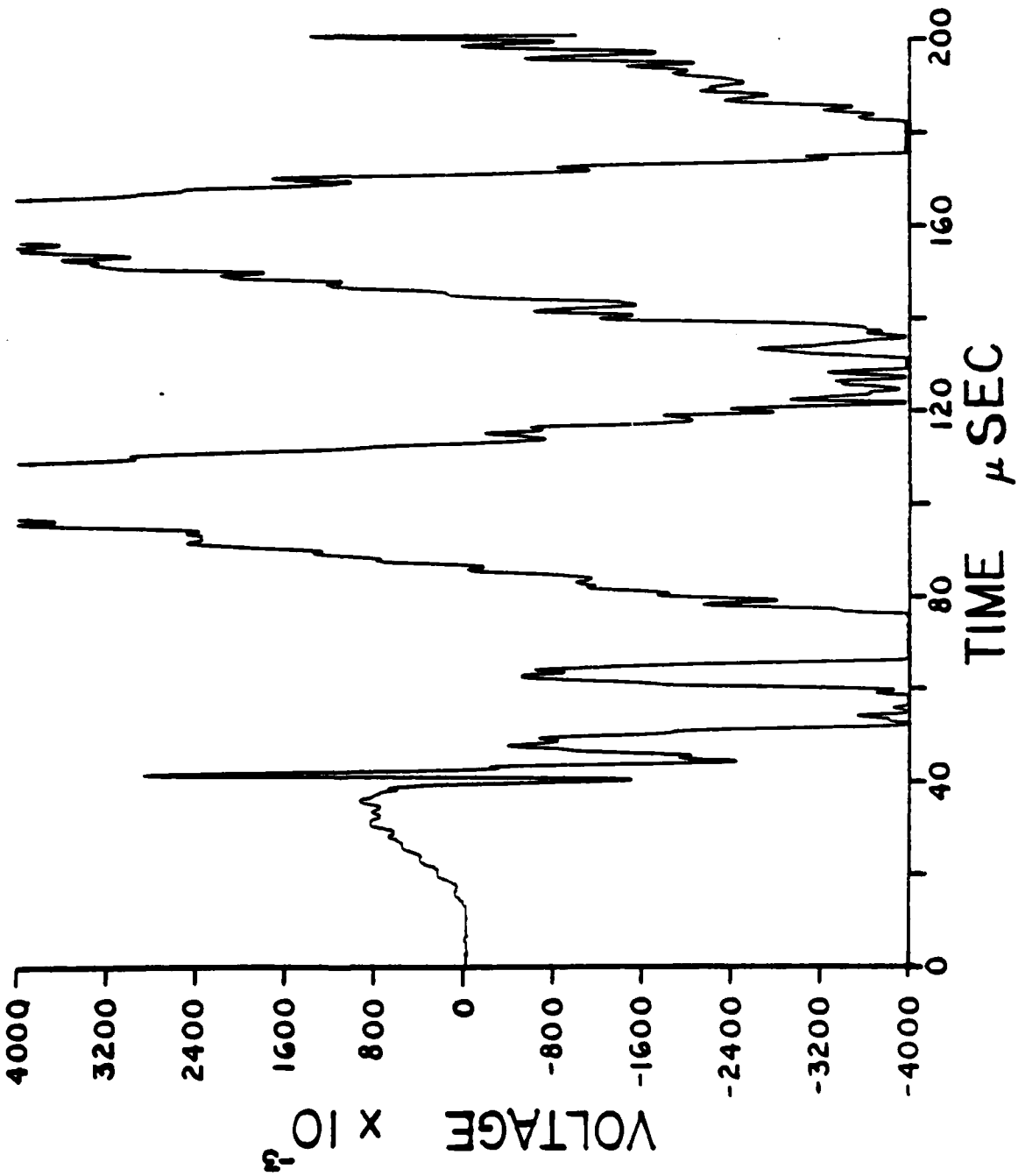
VOLTAGE x 10^-3
4000
3200
2400
1600
800
0
-800
-1600
-2400
-3200
-4000
0
40
80
120
160
200
TIME μSEC

E63

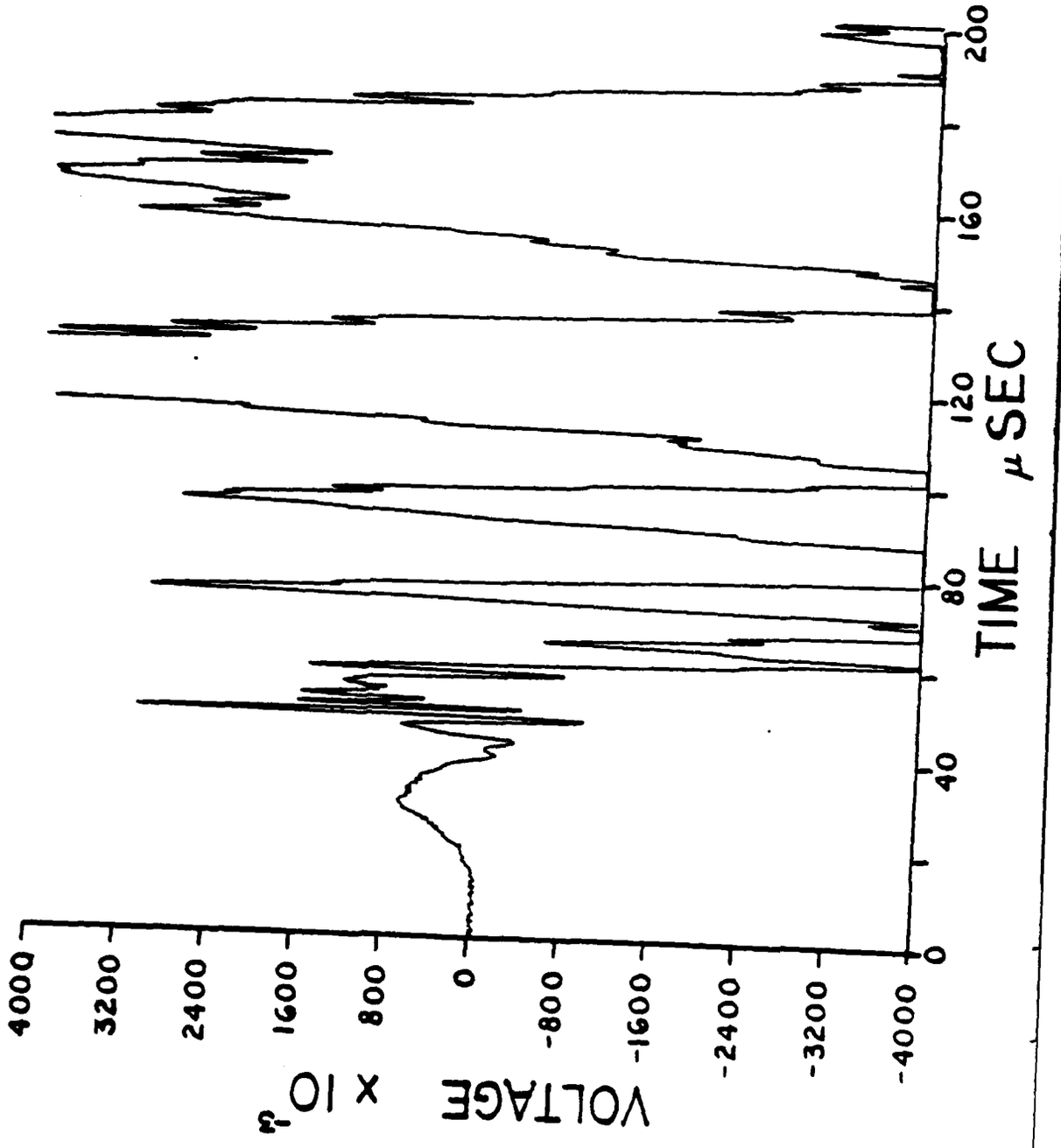
VOLTAGE x 10^{-3}
4000
3200
2400
1600
800
0
-800
-1600
-2400
-3200
-4000
0
40
80
120
160
200
TIME μSEC

E64

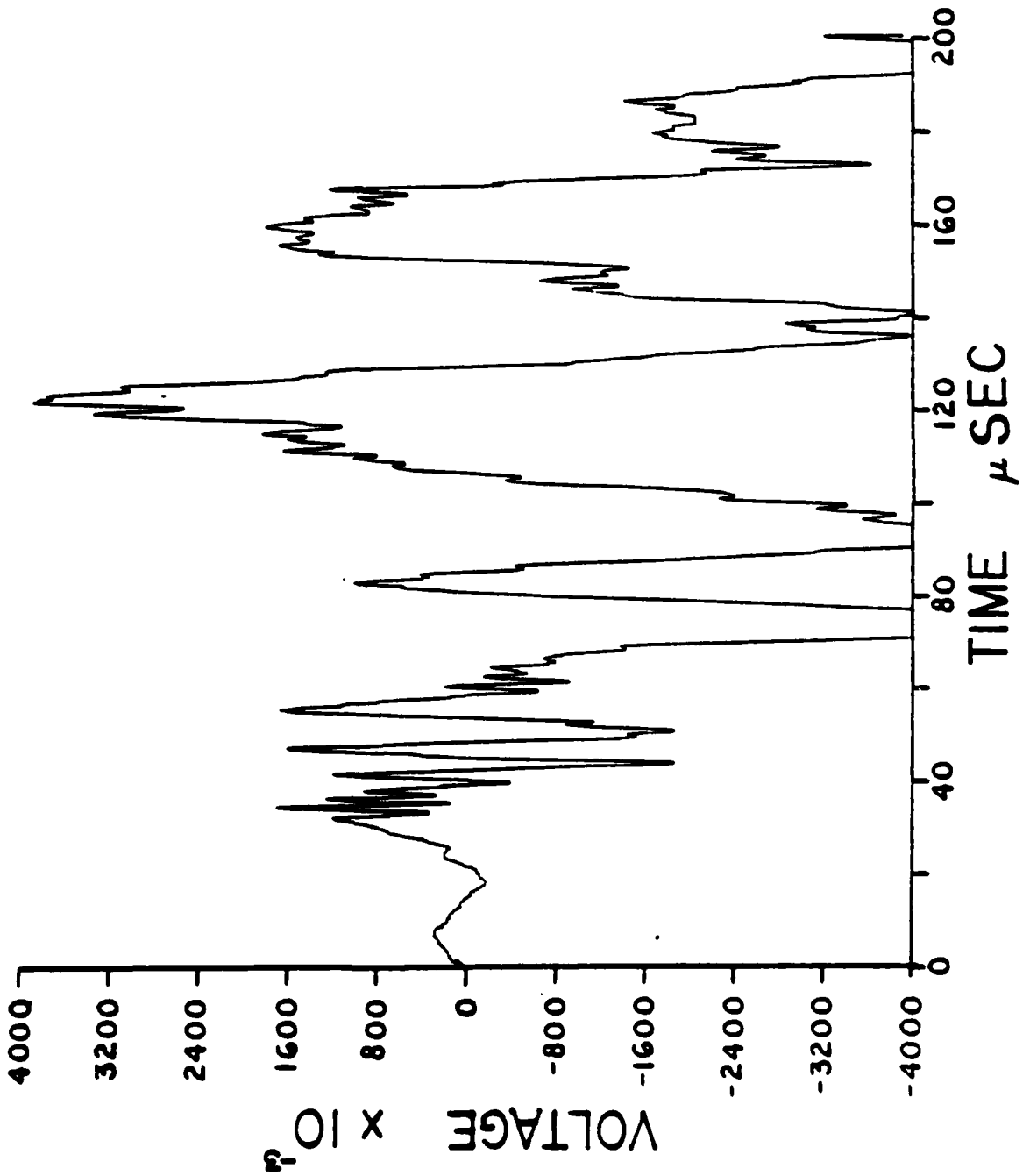
VOLTAGE x 10^-3
4000
3200
2400
1600
800
0
-800
-1600
-2400
-3200
-4000
0
40
80
120
160
200
TIME μSEC

E65

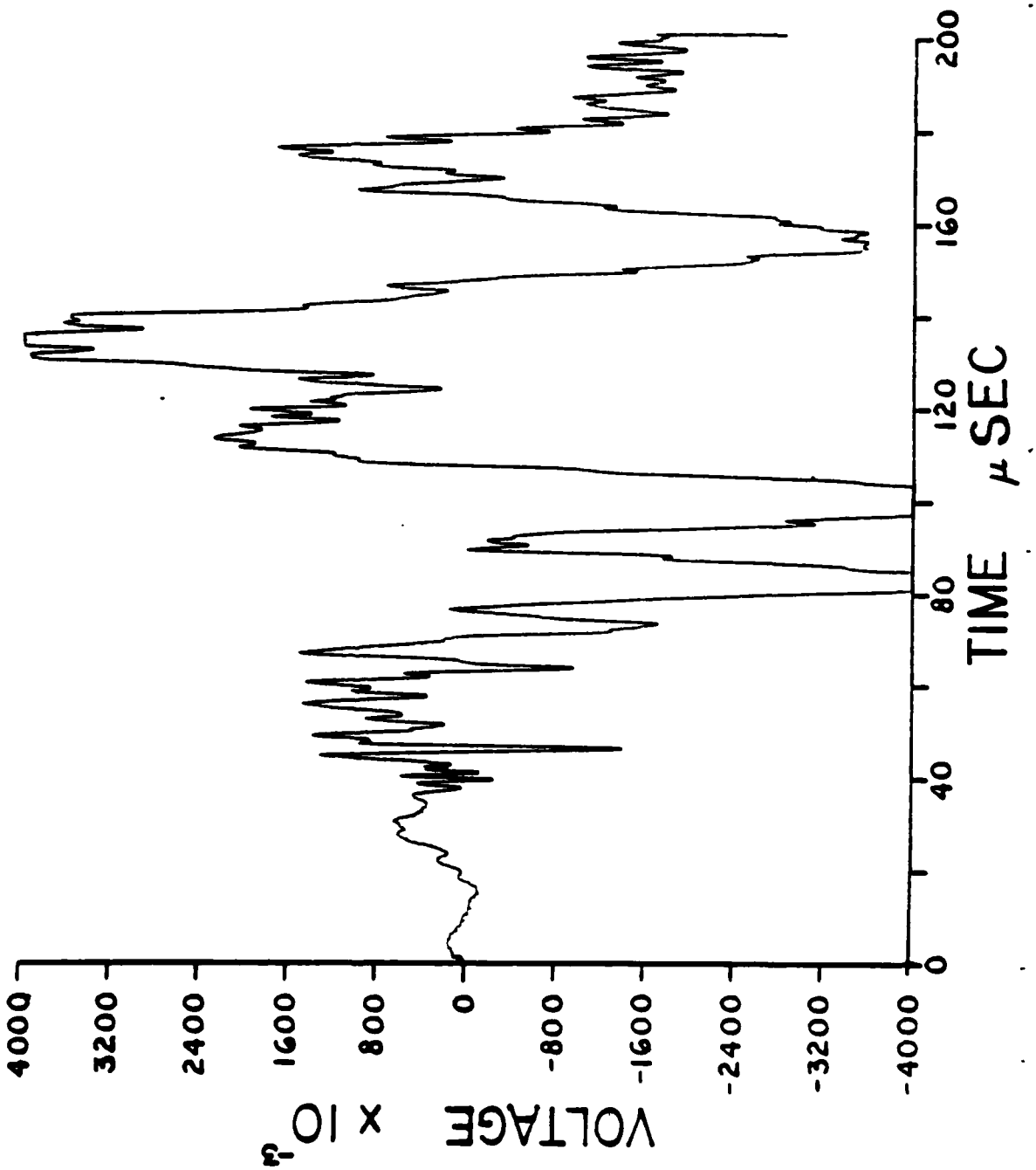
VOLTAGE x 10^-3
4000
3200
2400
1600
800
0
-800
-1600
-2400
-3200
-4000
0
40
80
120
160
200
TIME μSEC

E66

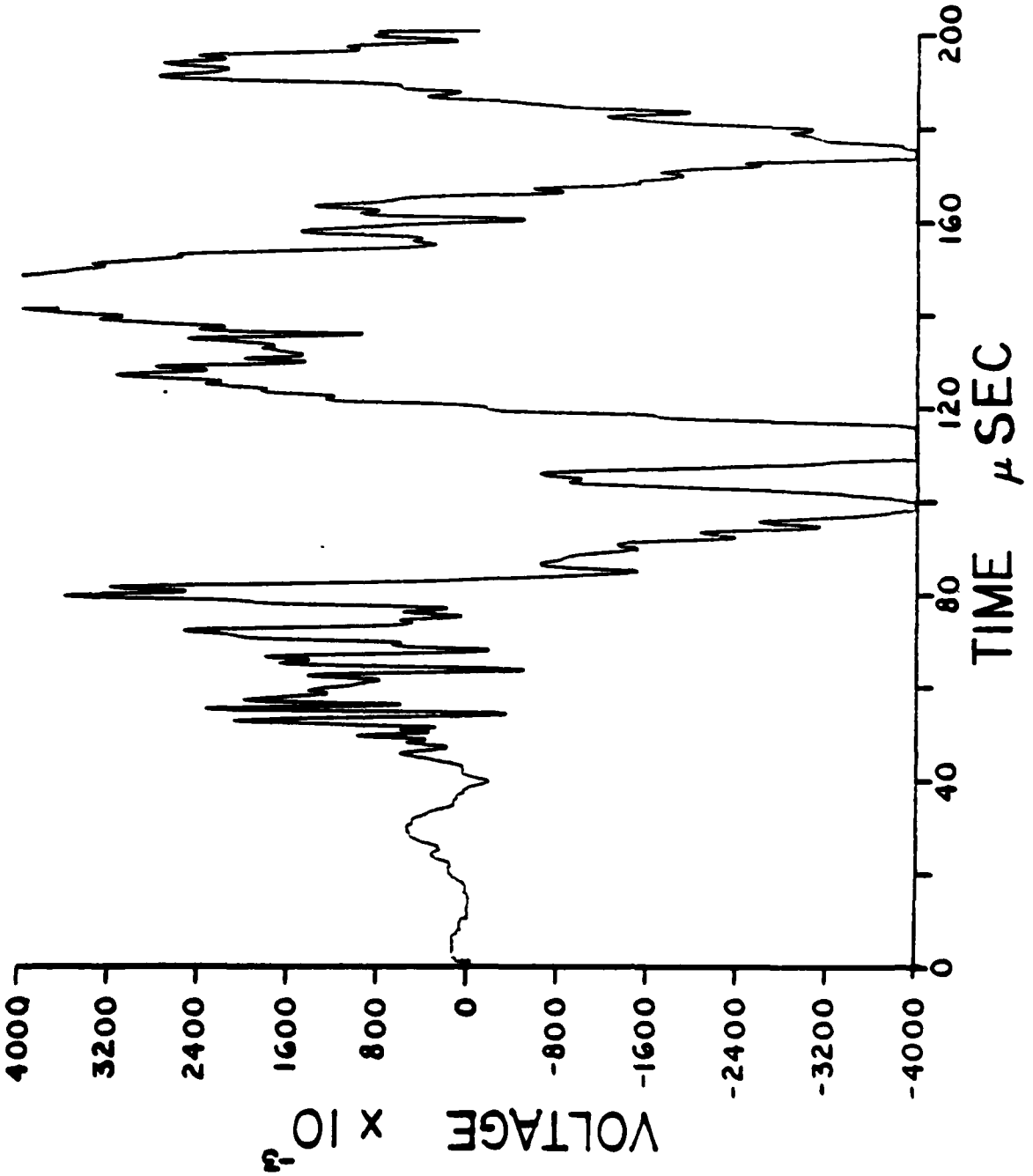
VOLTAGE x 10^3
4000
3200
2400
1600
800
0
-800
-1600
-2400
-3200
-4000
0
40
80
120
160
200
TIME μSEC

E67

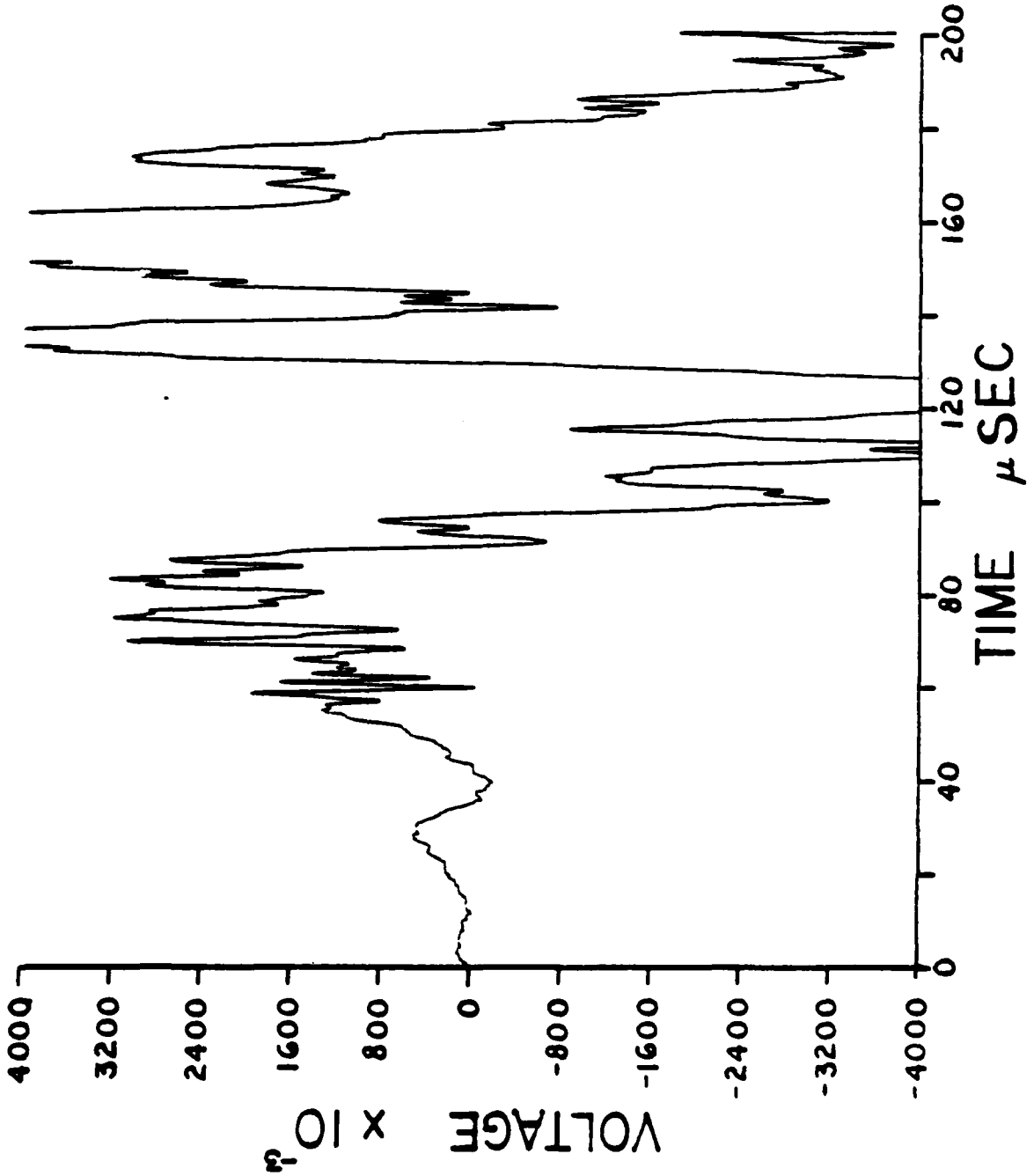
VOLTAGE x 10³
4000
3200
2400
1600
800
0
-800
-1600
-2400
-3200
-4000
0
40
80
120
160
200
TIME μSEC

E68

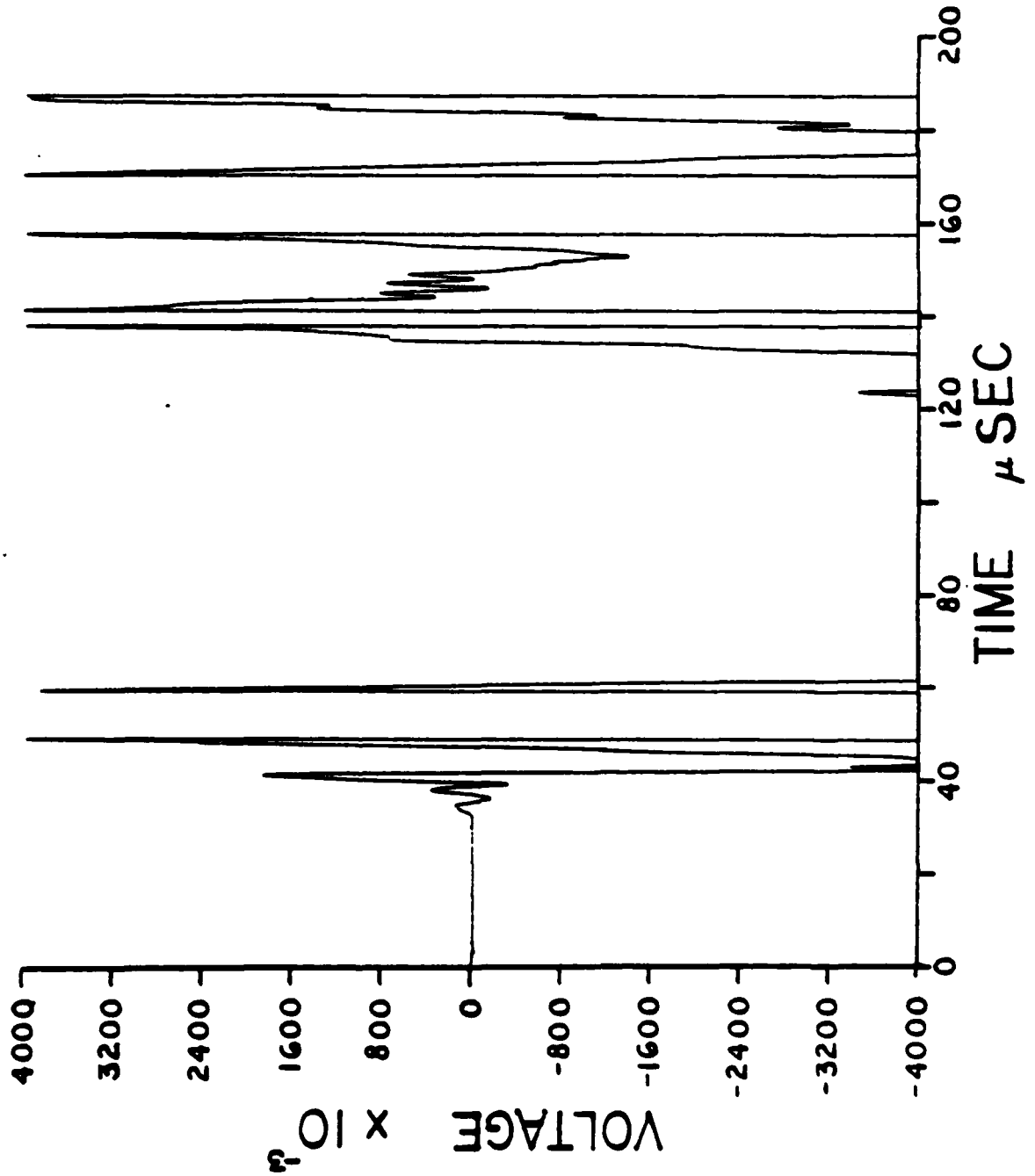
4000
3200
2400
1600
800
0
-800
-1600
-2400
-3200
-4000
VOLTAGE x 10⁻³
0
40
80
120
160
200
TIME μSEC

E69

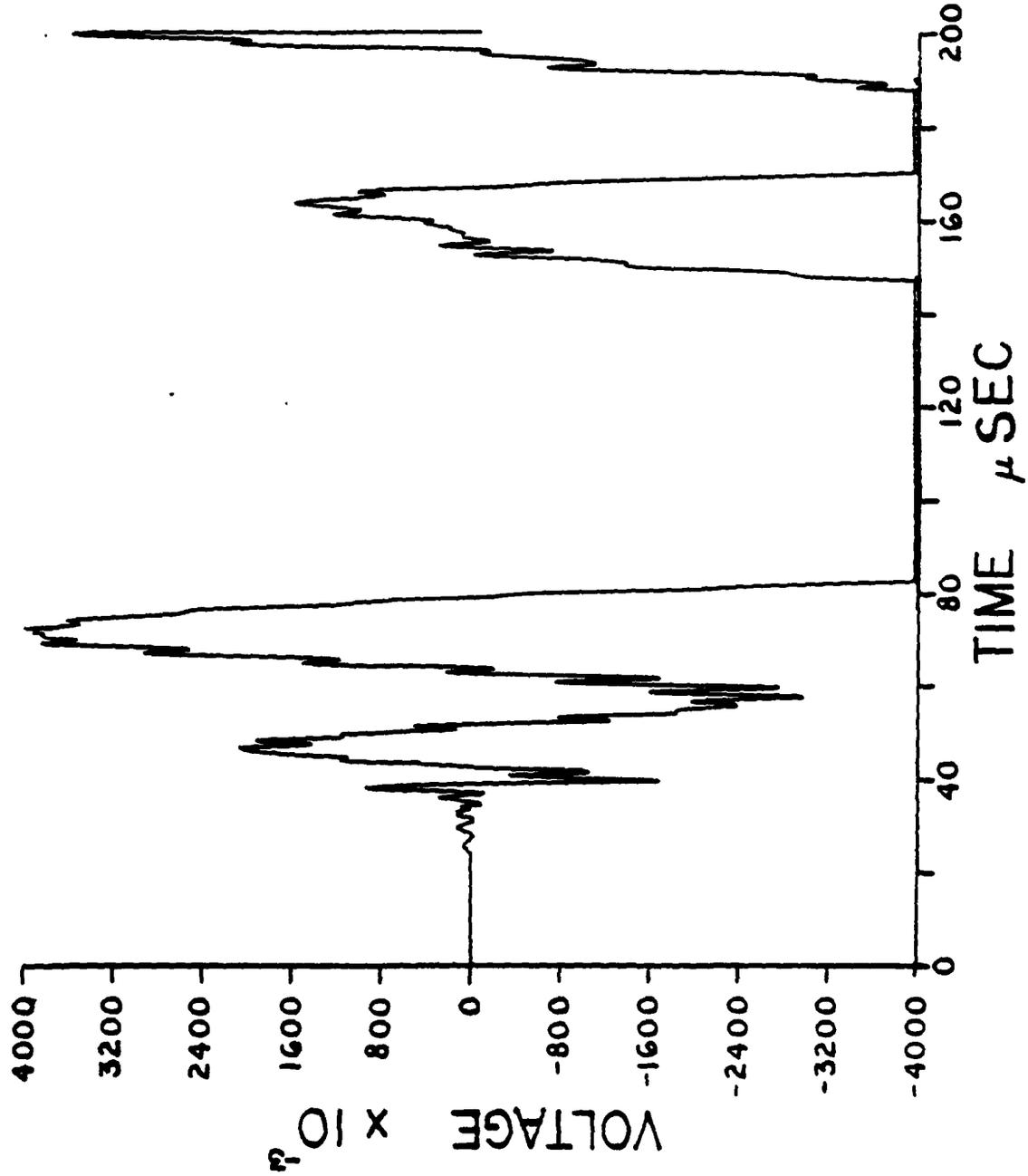
VOLTAGE x 10^3
4000
3200
2400
1600
800
0
-800
-1600
-2400
-3200
-4000
0
40
80
120
160
200
TIME μSEC

E70

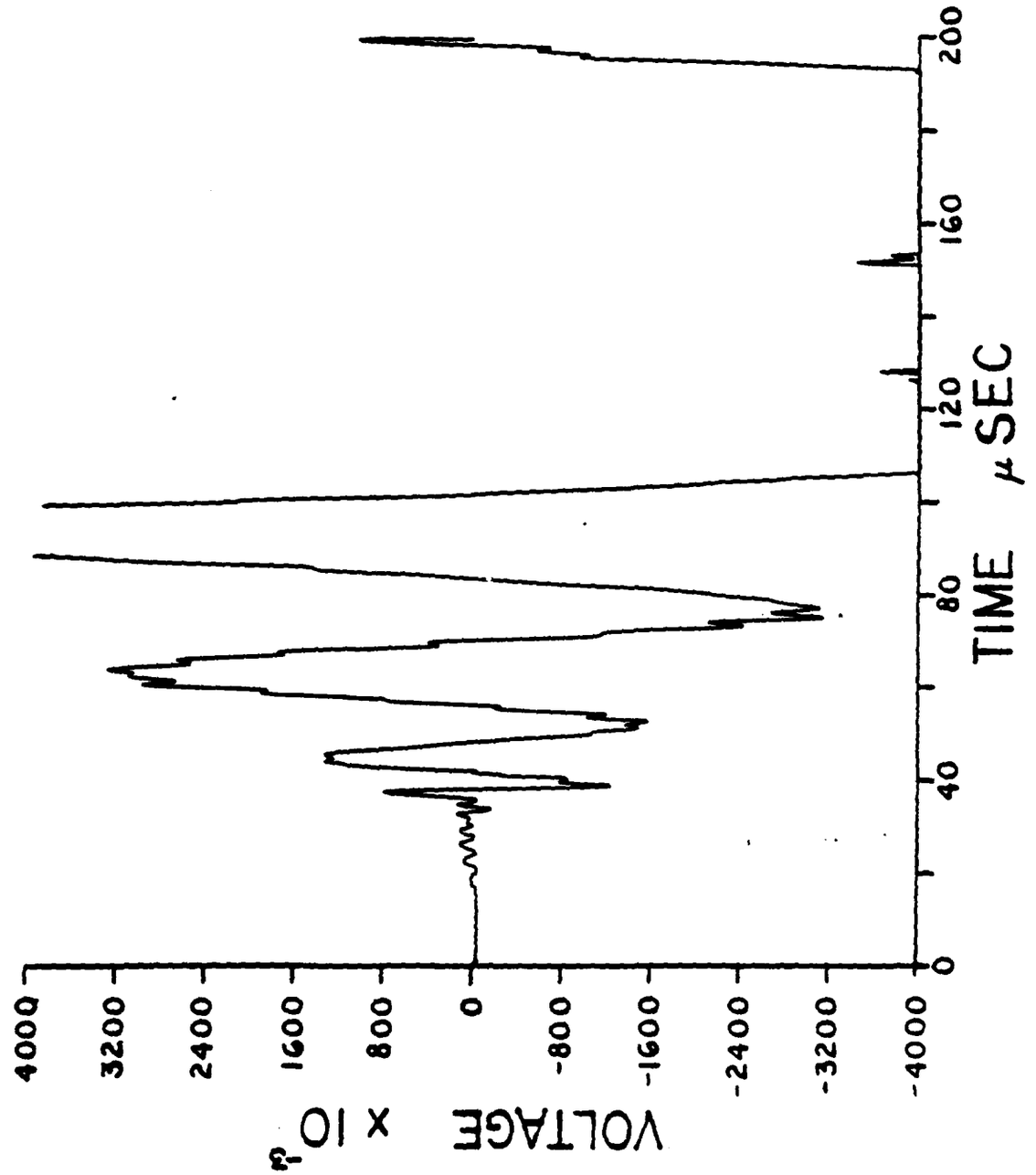
VOLTAGE x 10^3
4000
3200
2400
1600
800
0
-800
-1600
-2400
-3200
-4000
0
40
80
120
160
200
TIME μSEC

E71

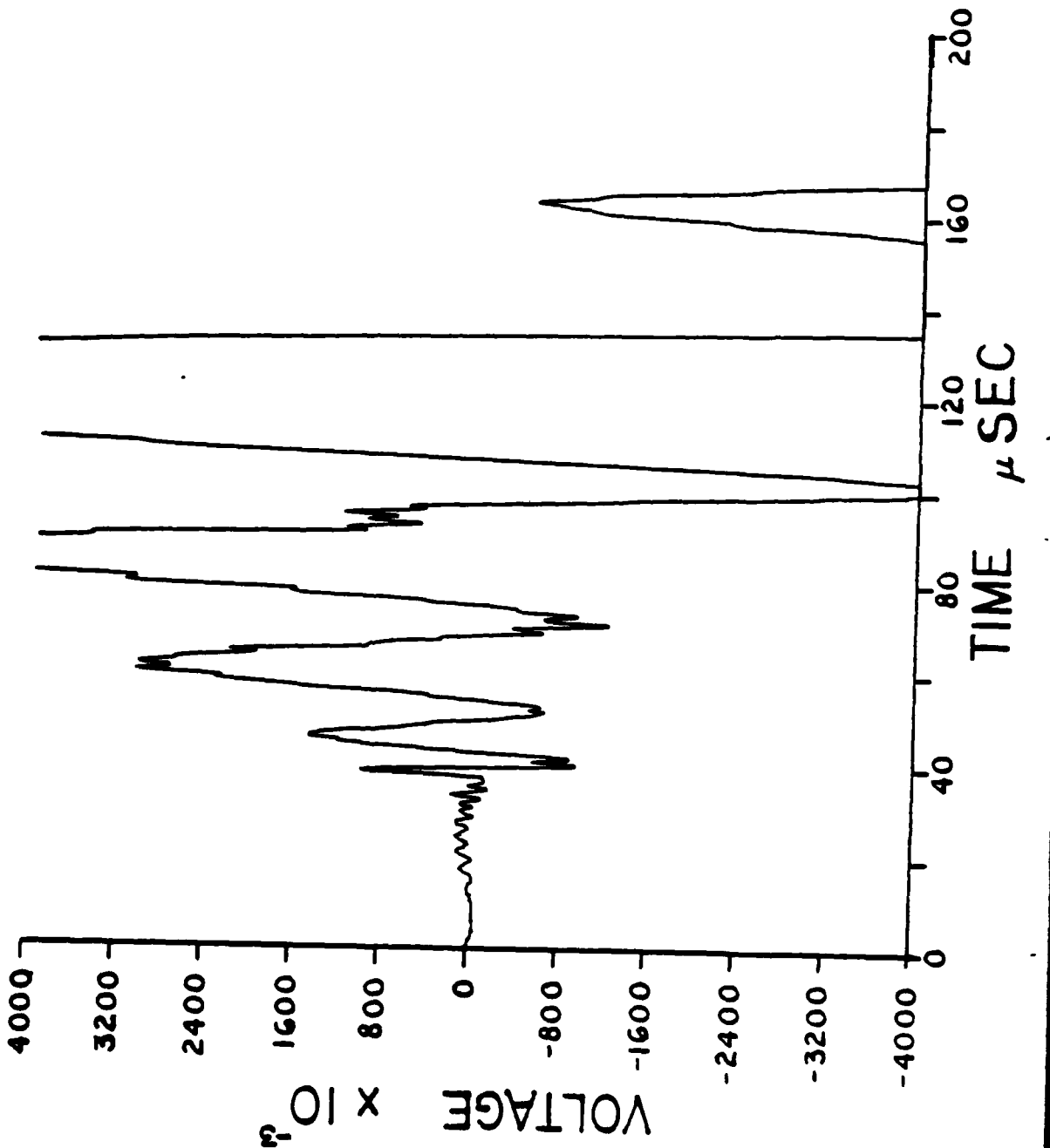
VOLTAGE x 10^{-3}
4000
3200
2400
1600
800
0
-800
-1600
-2400
-3200
-4000
0
40
80
120
160
200
TIME μSEC

E72

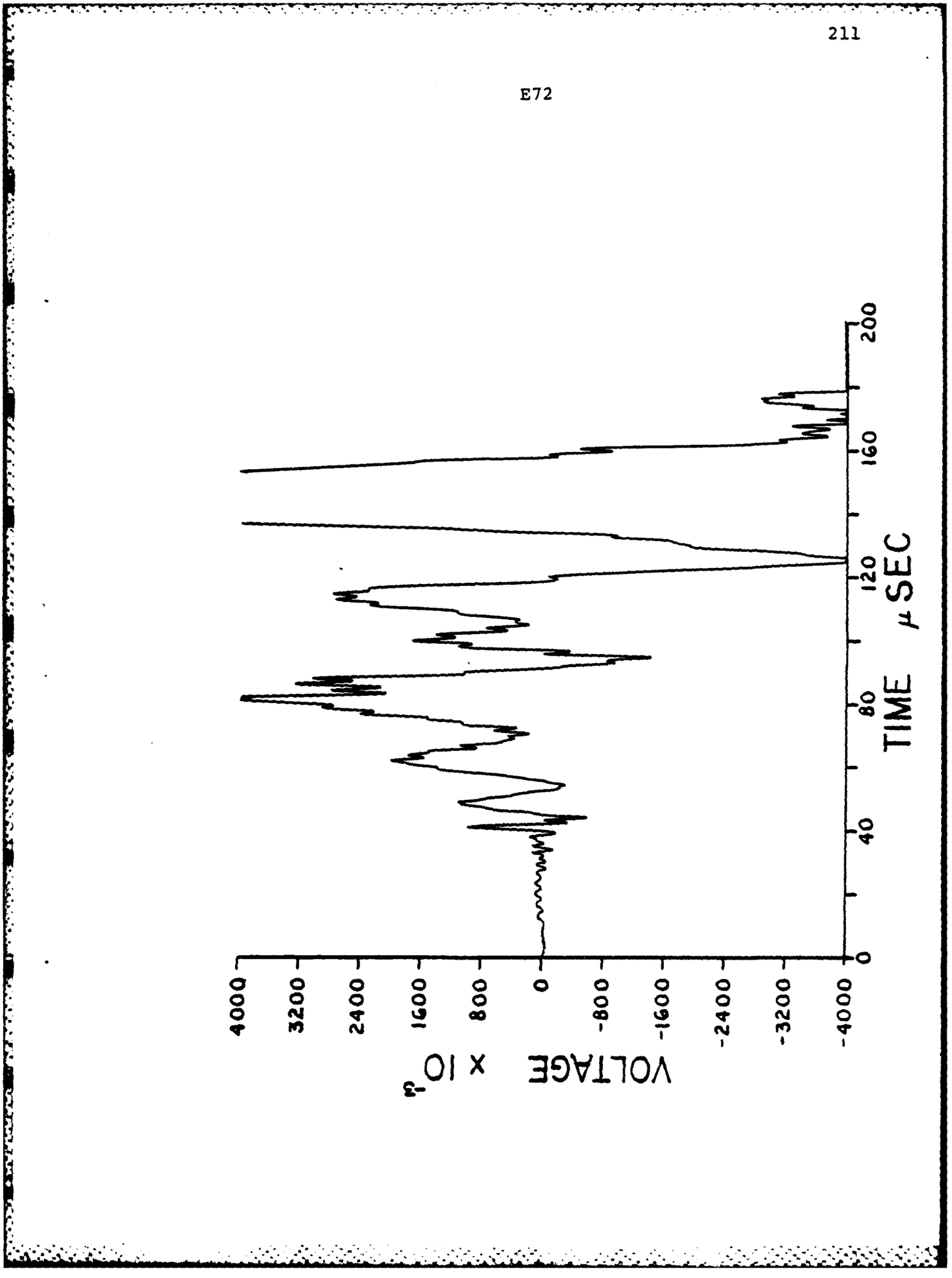
VOLTAGE x 10³
4000
3200
2400
1600
800
0
-800
-1600
-2400
-3200
-4000
0
40
80
120
160
200
TIME μSEC

E73

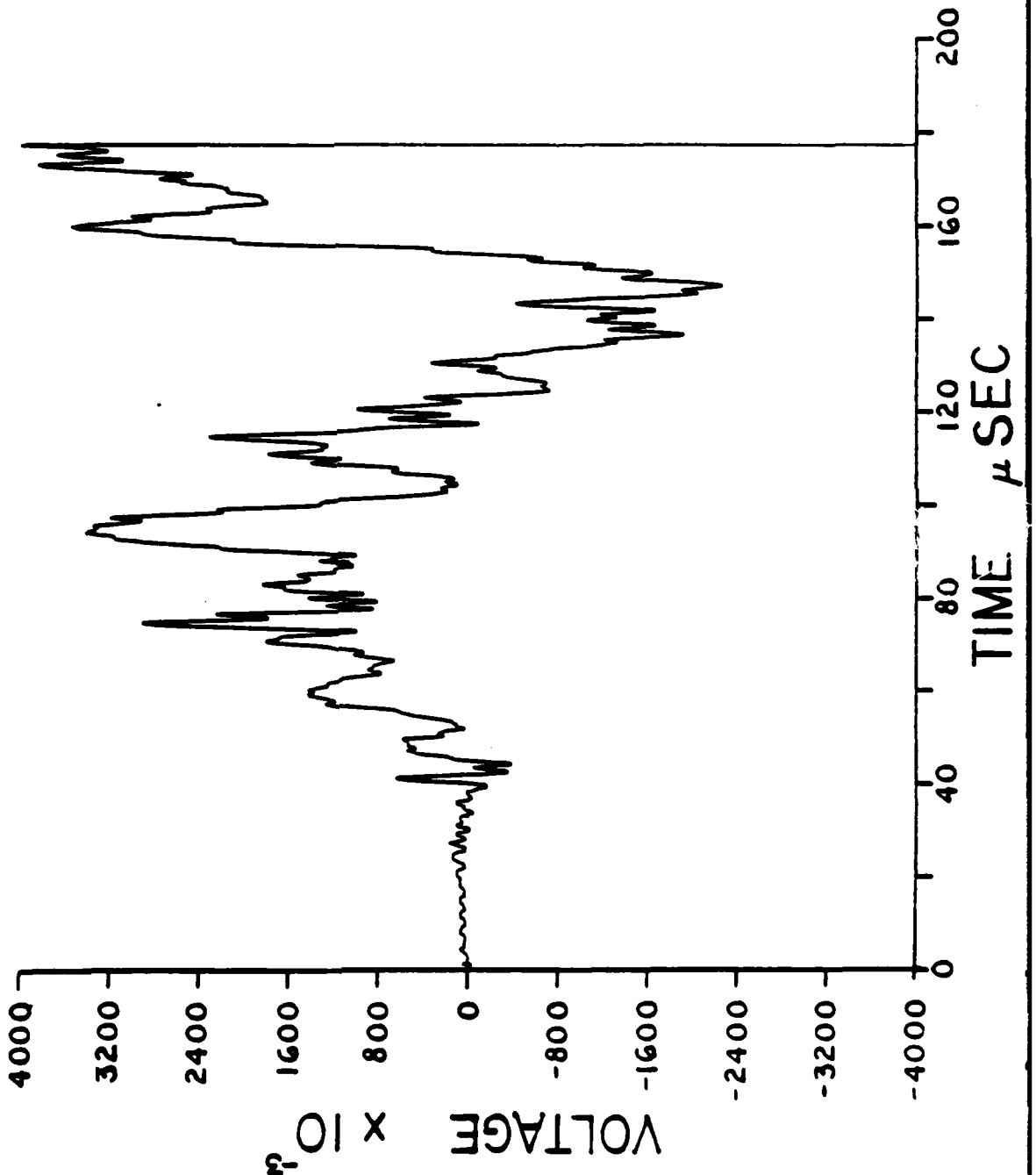
VOLTAGE x 10^3
4000
3200
2400
1600
800
0
-800
-1600
-2400
-3200
-4000
0
40
80
120
160
200
TIME μSEC

E74

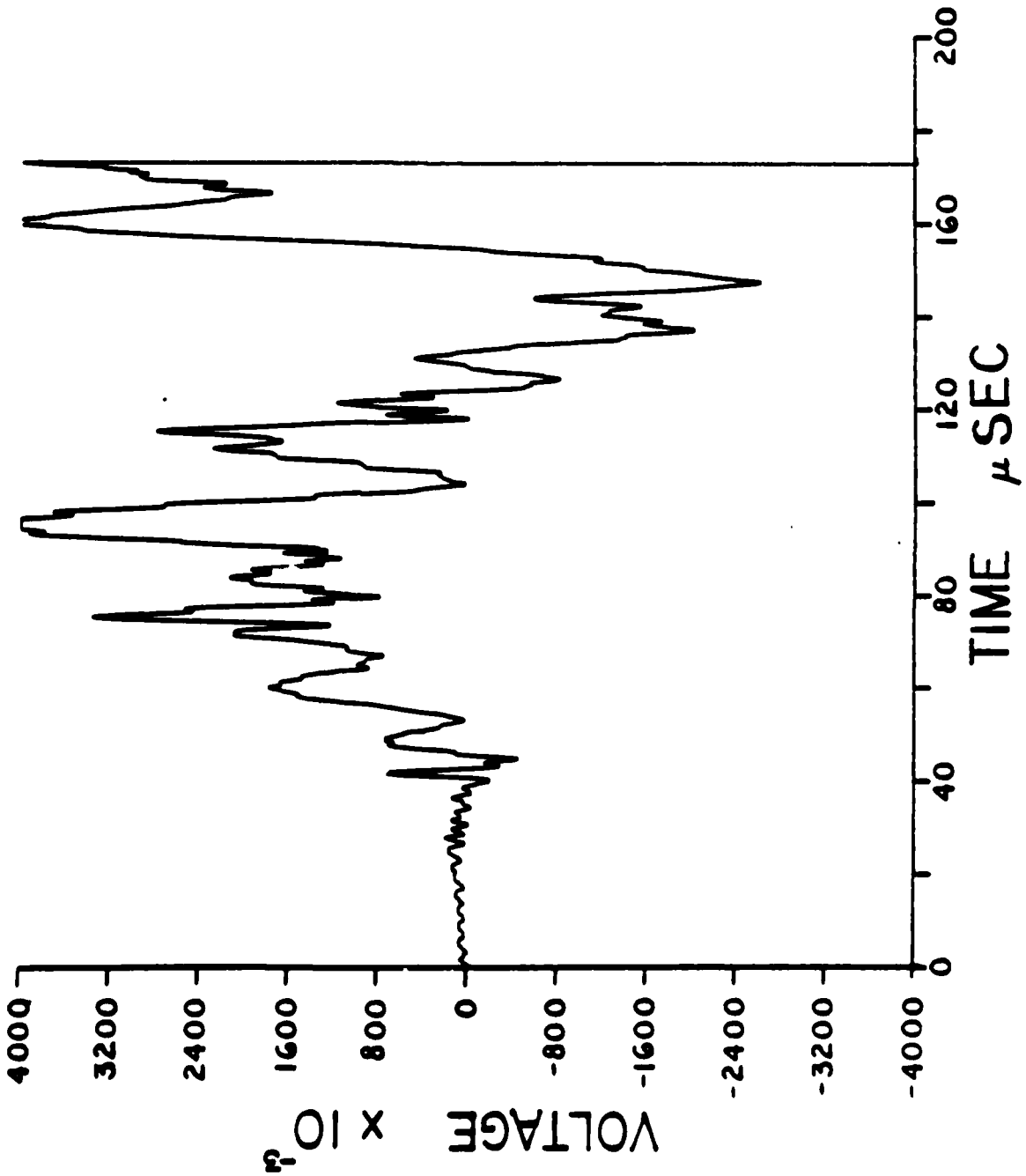
4000
3200
2400
1600
800
0
-800
-1600
-2400
-3200
-4000
VOLTAGE x 10³
0
40
80
120
160
200
TIME μSEC

E75

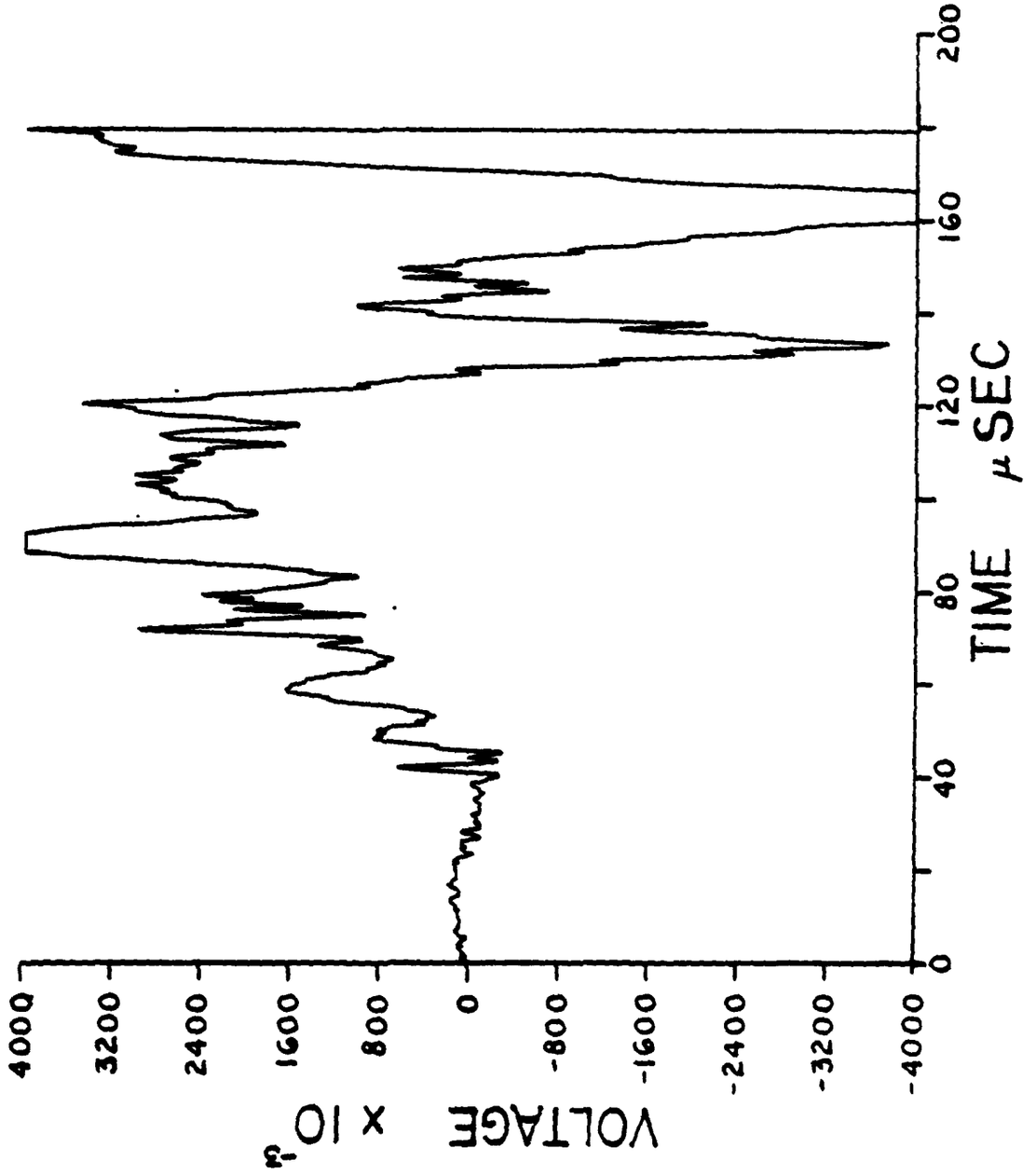
VOLTAGE x 10⁻³
4000
3200
2400
1600
800
0
-800
-1600
-2400
-3200
-4000
0
40
80
120
160
200
TIME μSEC

APPENDIX F

SPECIMEN CHARACTERIZATION FREQUENCY SPECTRA

The following figures are the time domain waveforms from which the frequency spectra were generated. The waveforms were recorded by the APL laser interferometer from the solid cylinder at two inch incremental steps. Figure F1 is the waveform recorded at two inches from the source and Fig. F28 is the waveform recorded twenty inches from the source.

F1

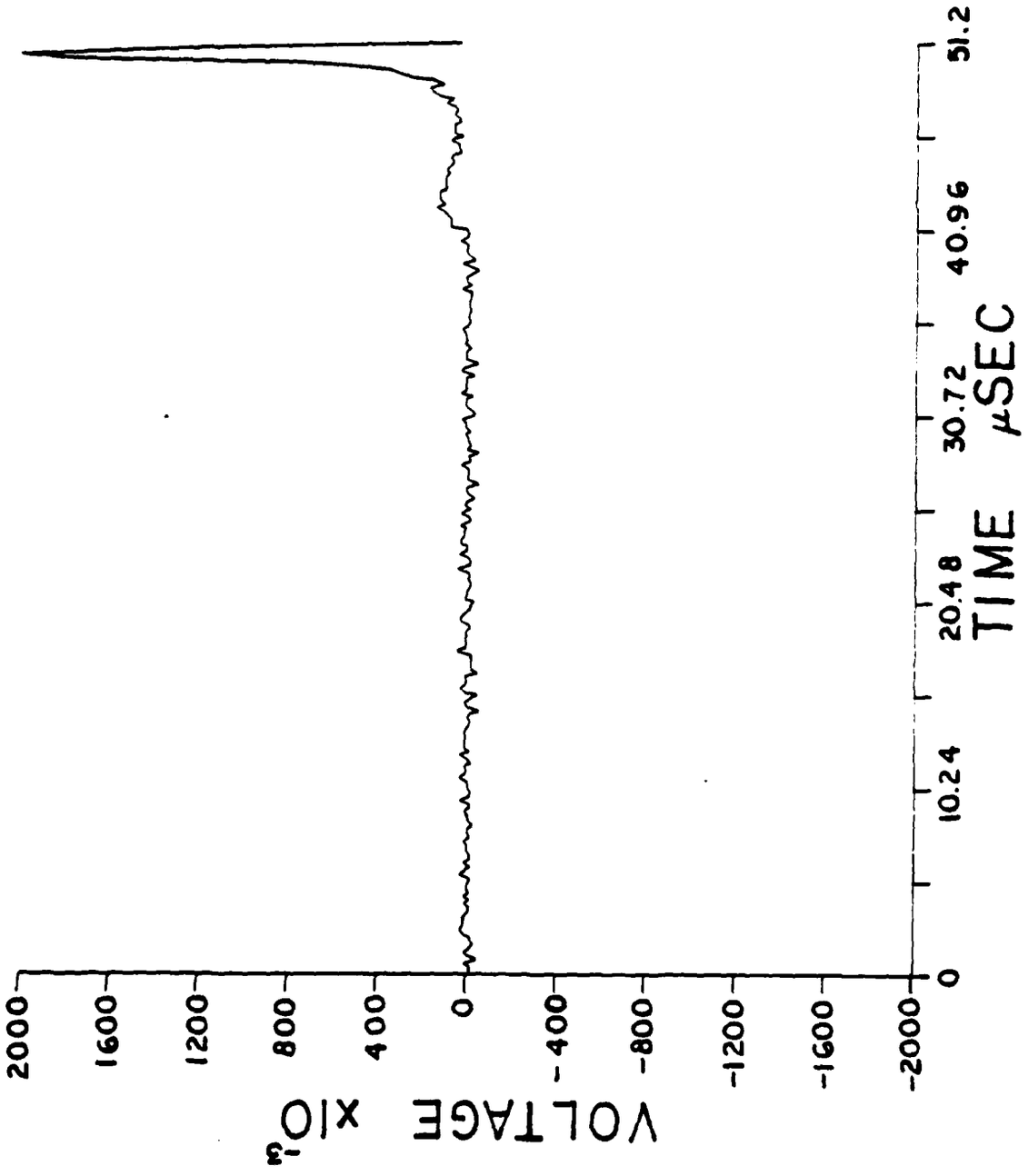
VOLTAGE x10⁻³
2000
1600
1200
800
400
0
-400
-800
-1200
-1600
-2000
0
10.24
20.48
30.72
40.96
51.2
TIME μSEC

F2

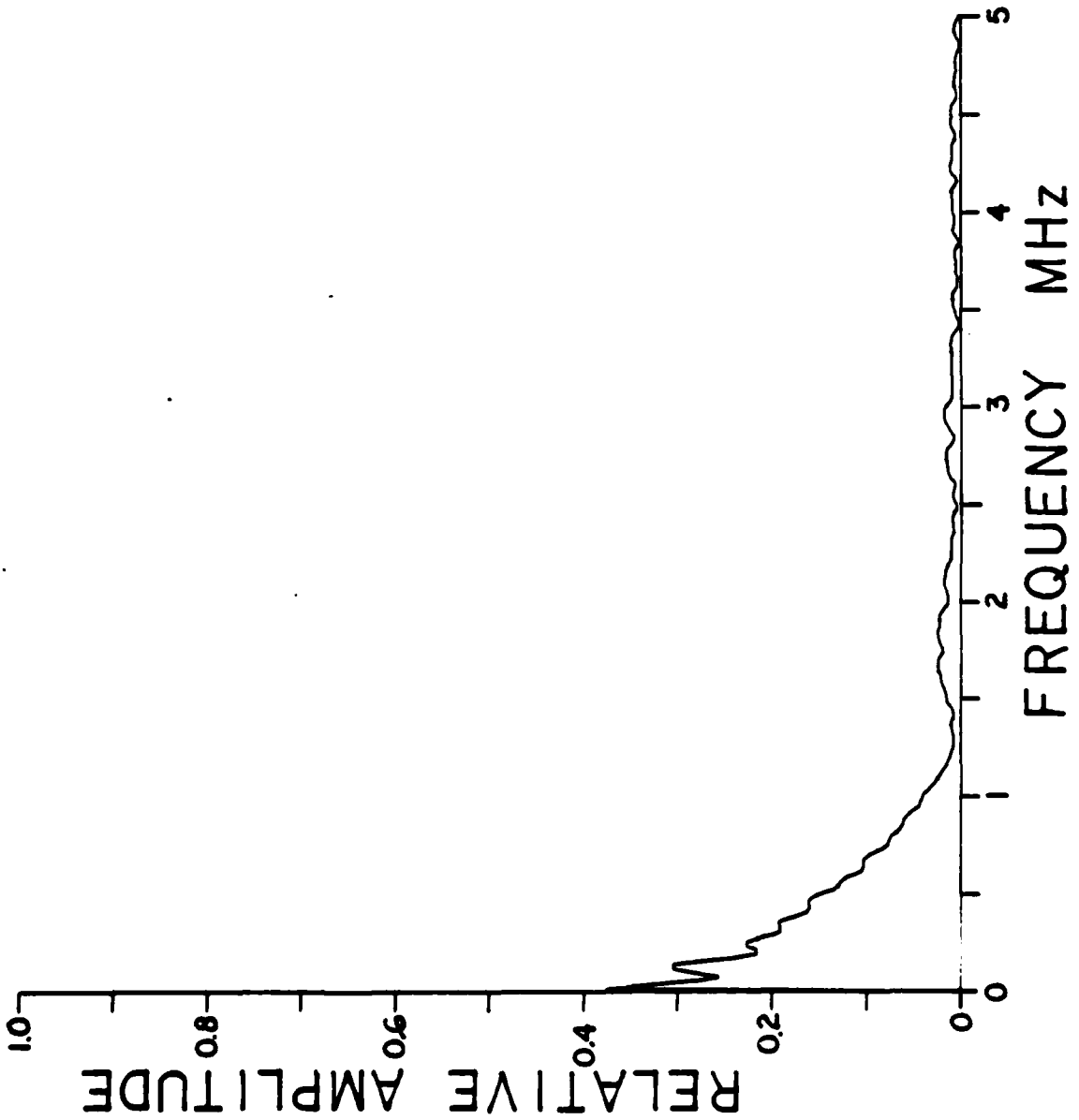

F3

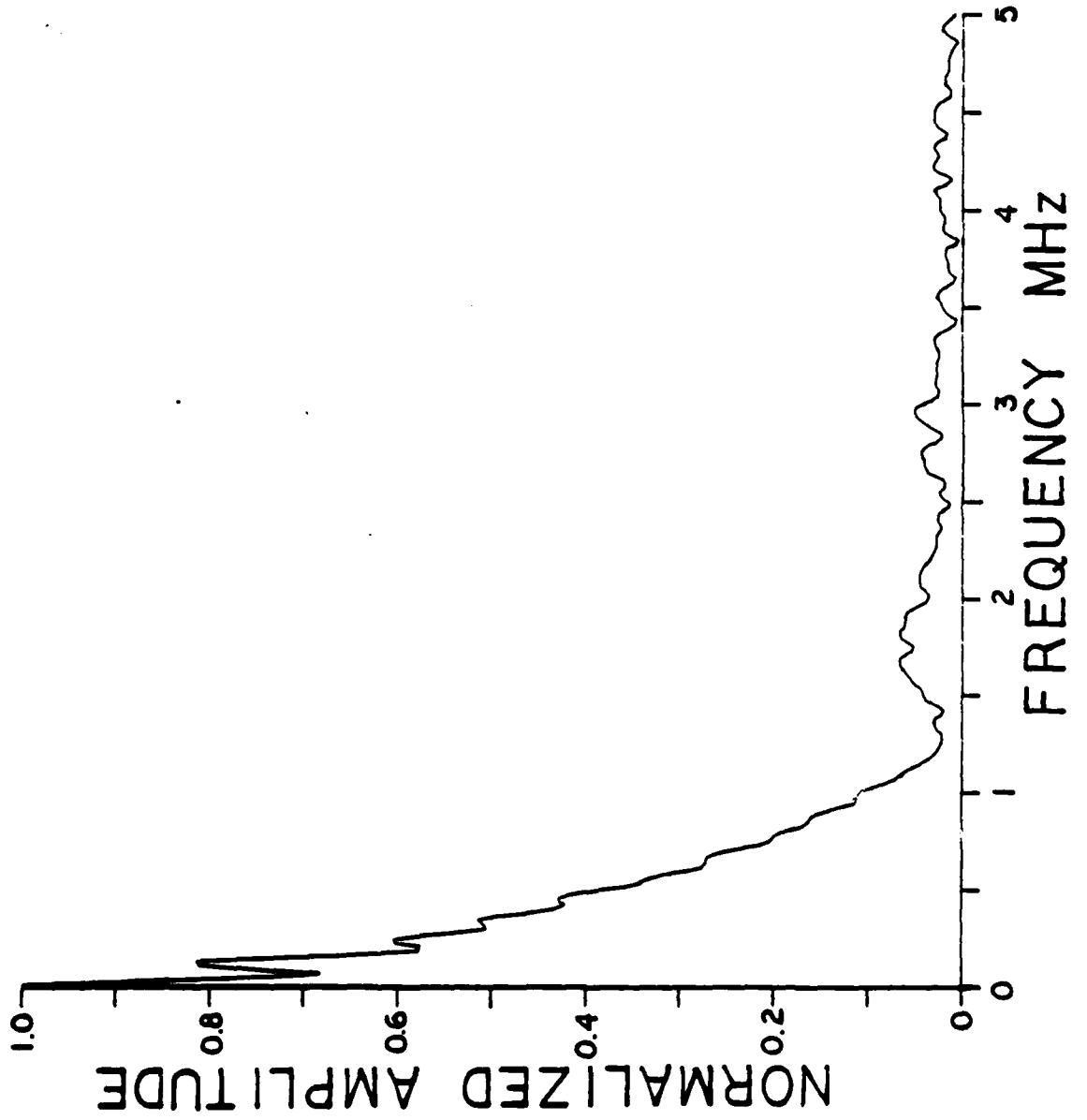

F4

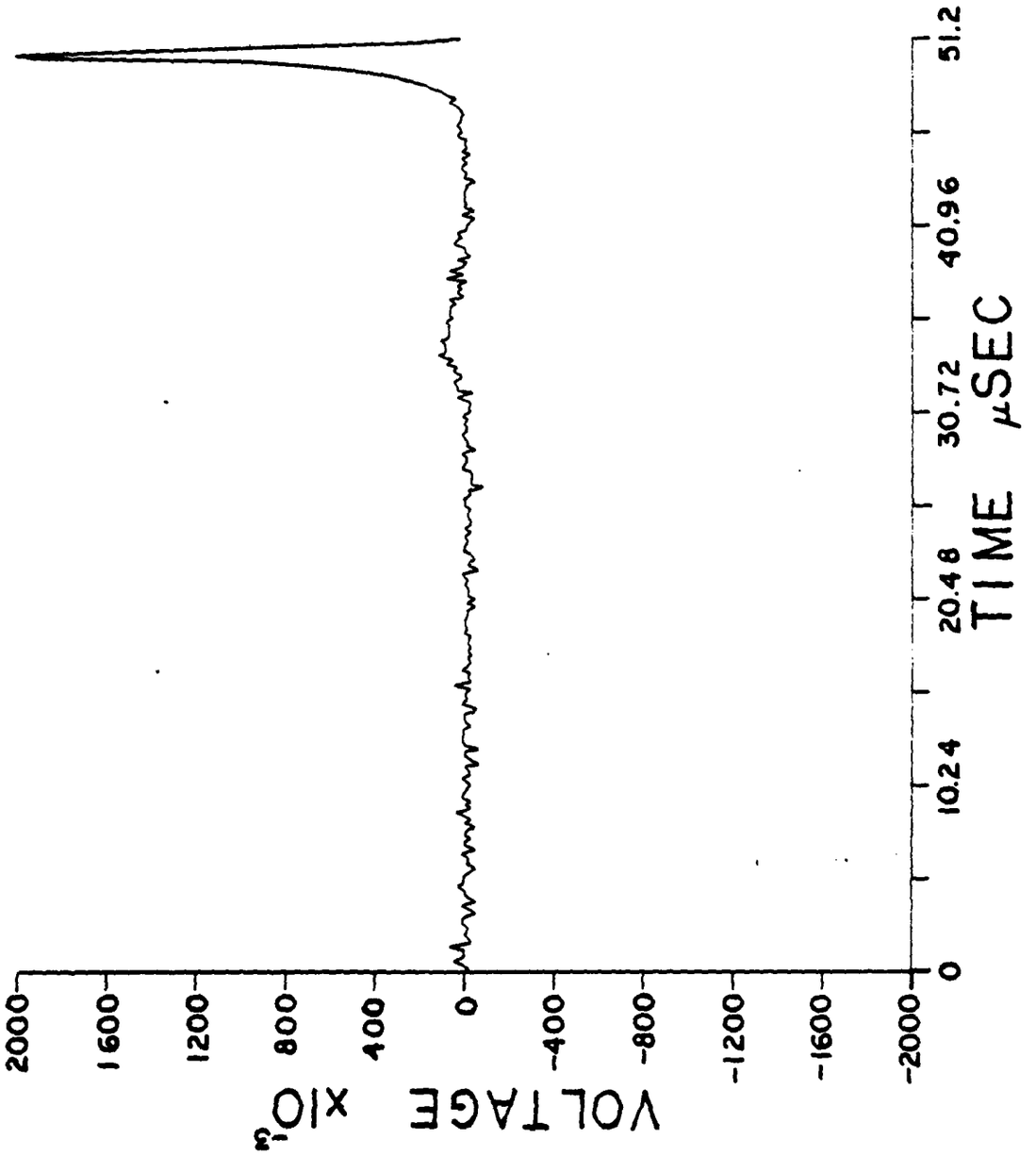
VOLTAGE x10⁻³
2000
1600
1200
800
400
0
-400
-800
-1200
-1600
-2000
0
10.24
20.48
30.72
40.96
51.2
TIME μSEC

F 5

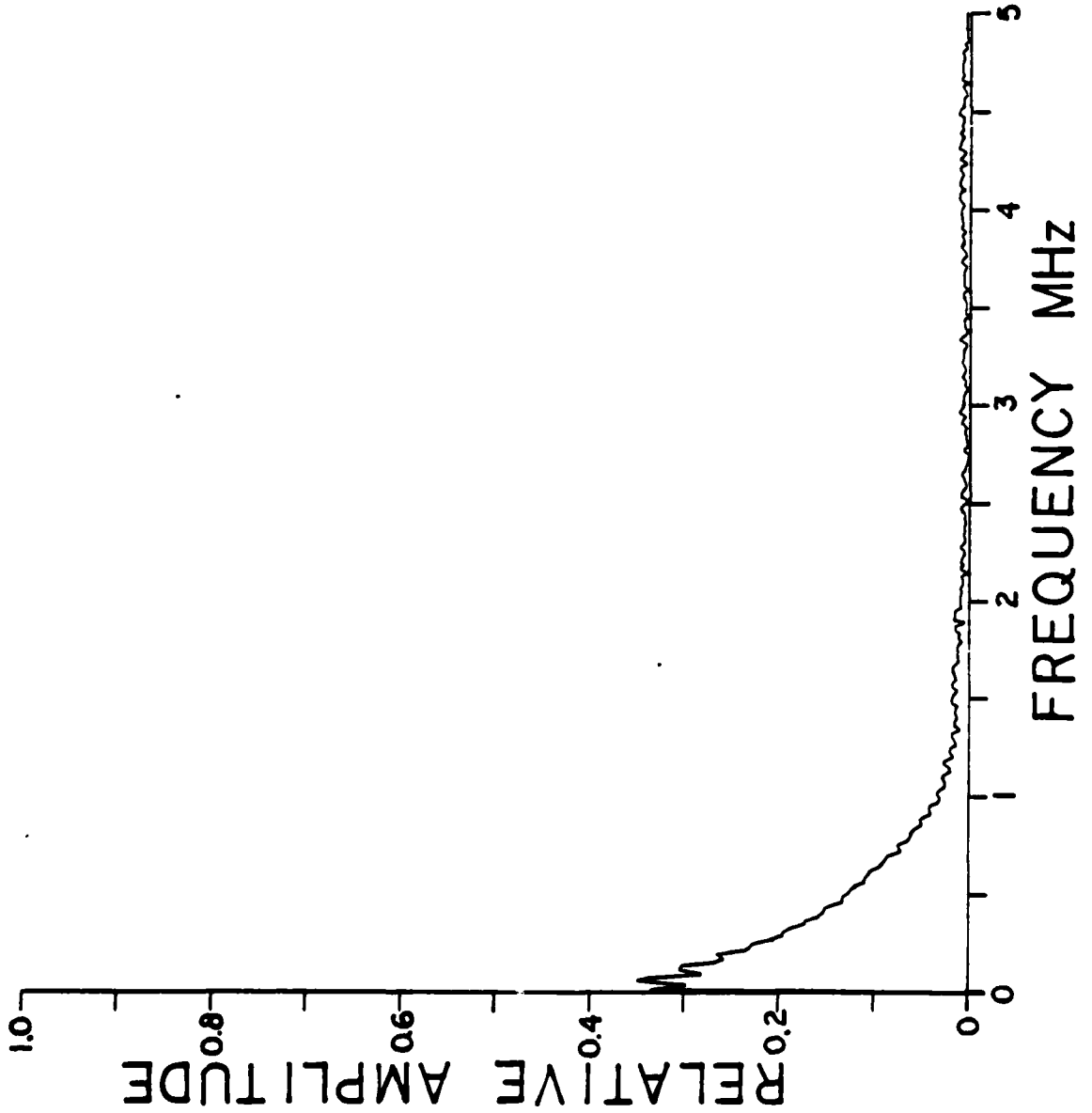

F6

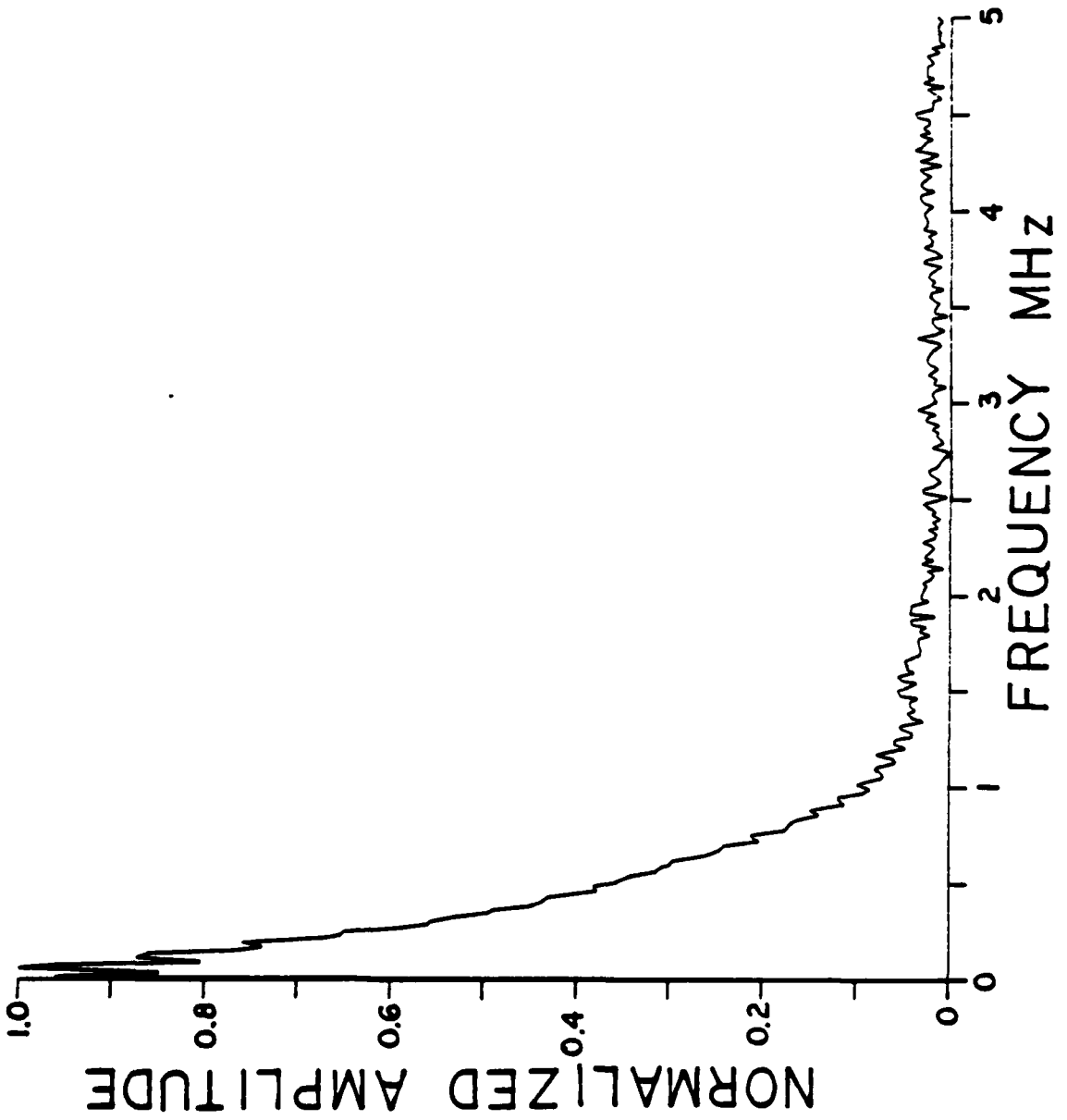

F 7

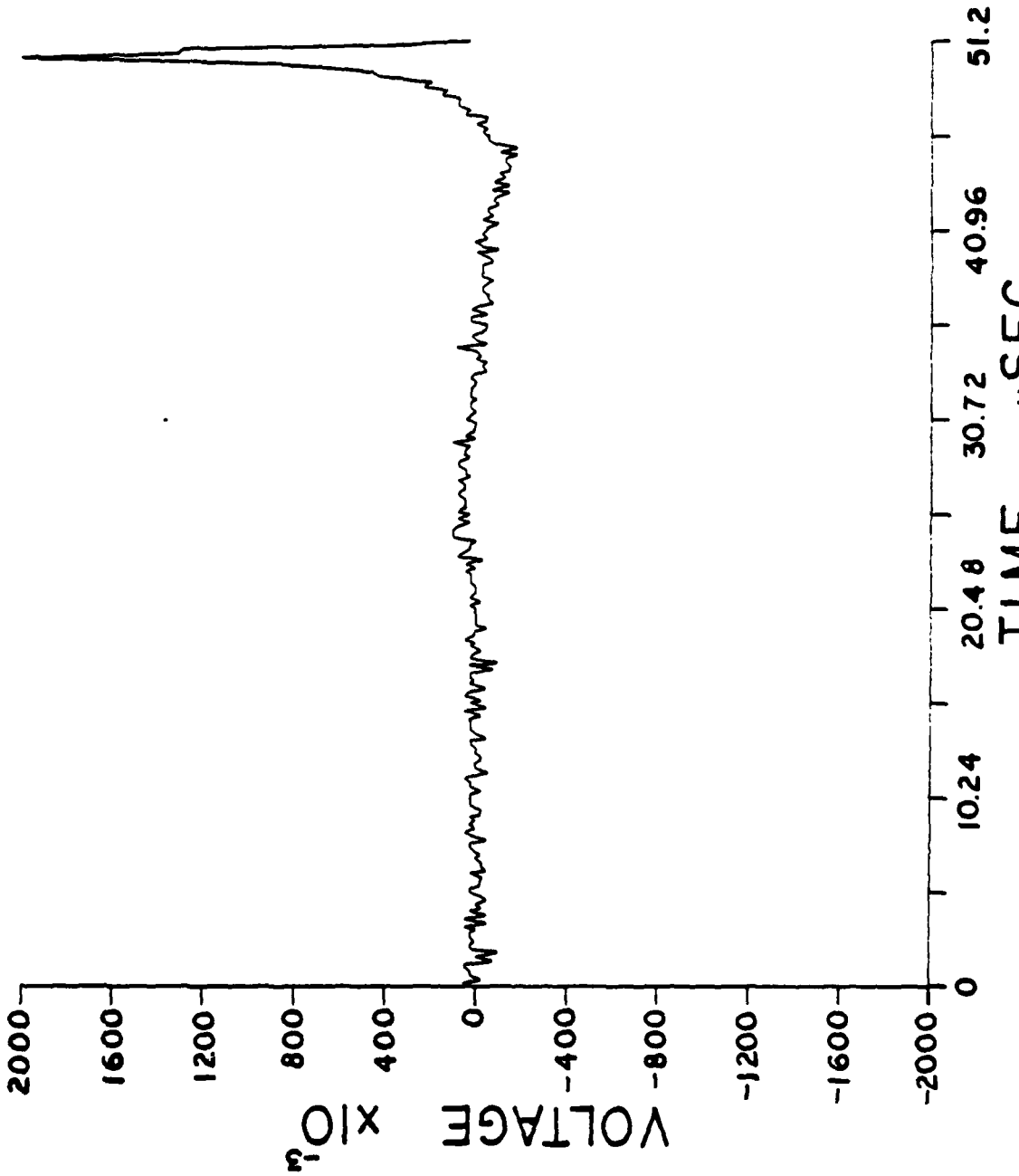
VOLTAGE x10³
2000
1600
1200
800
400
0
-400
-800
-1200
-1600
-2000
0
10.24
20.48
30.72
40.96
51.2
TIME μSEC

F8

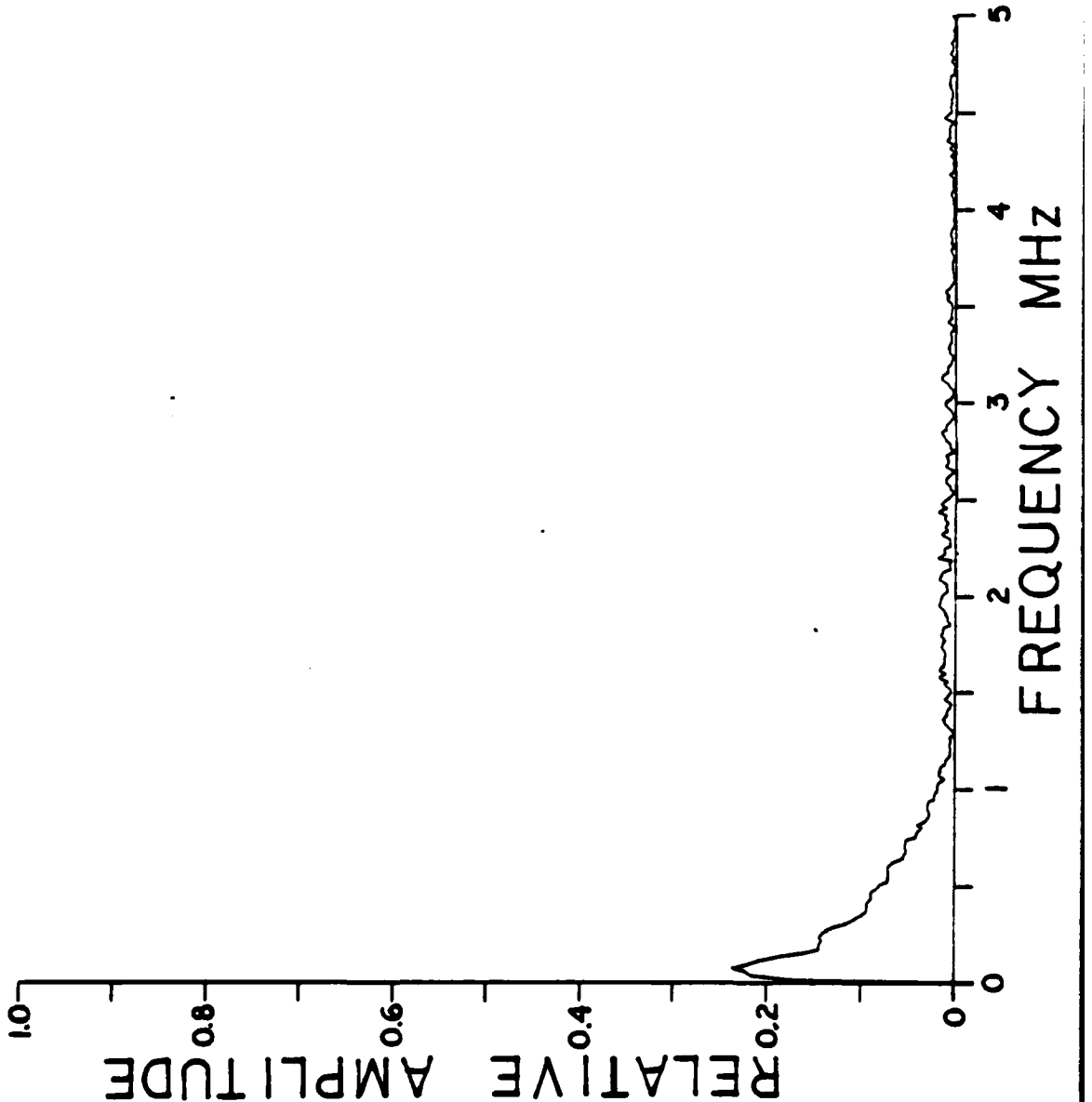

F9

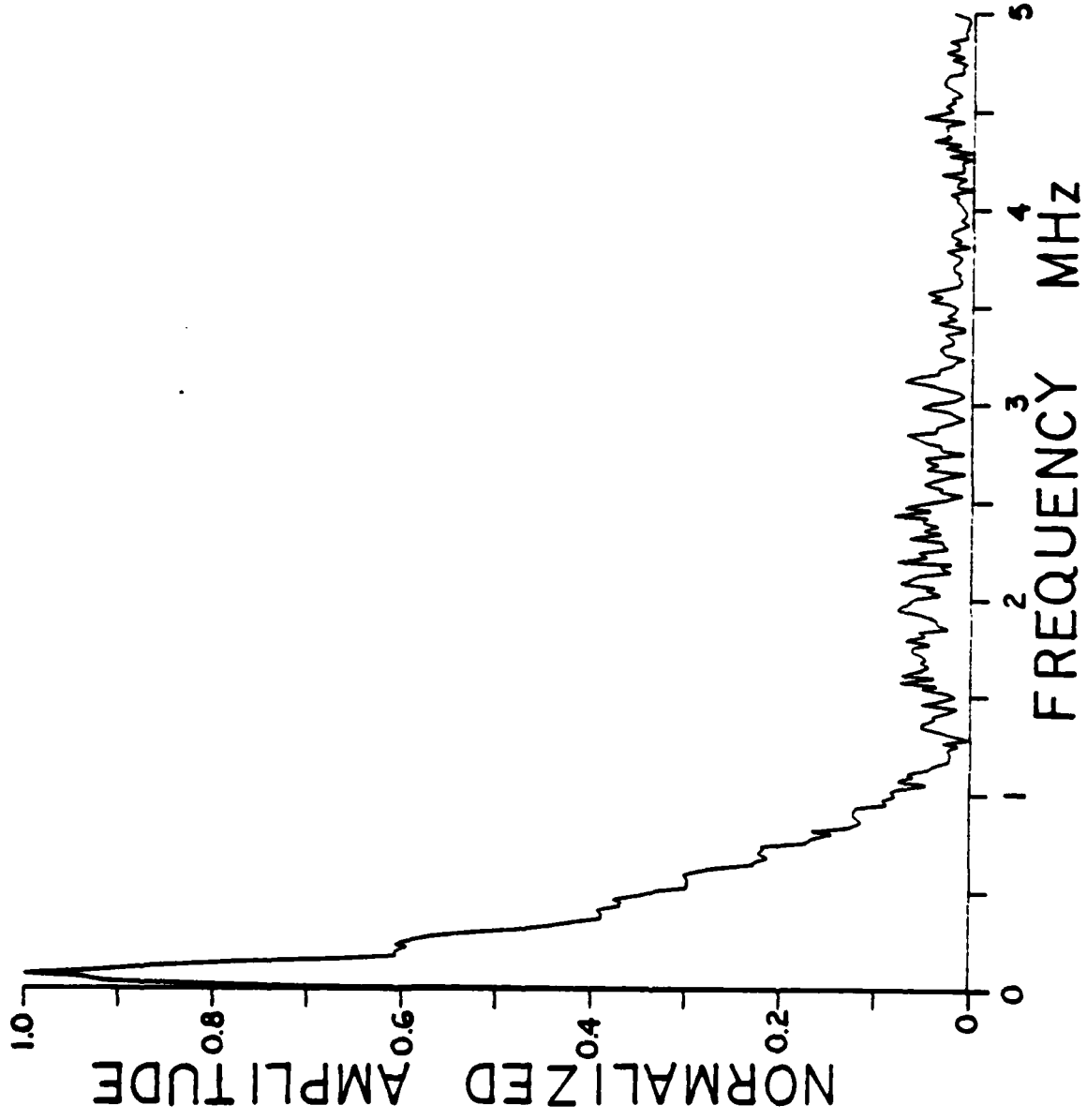

F10

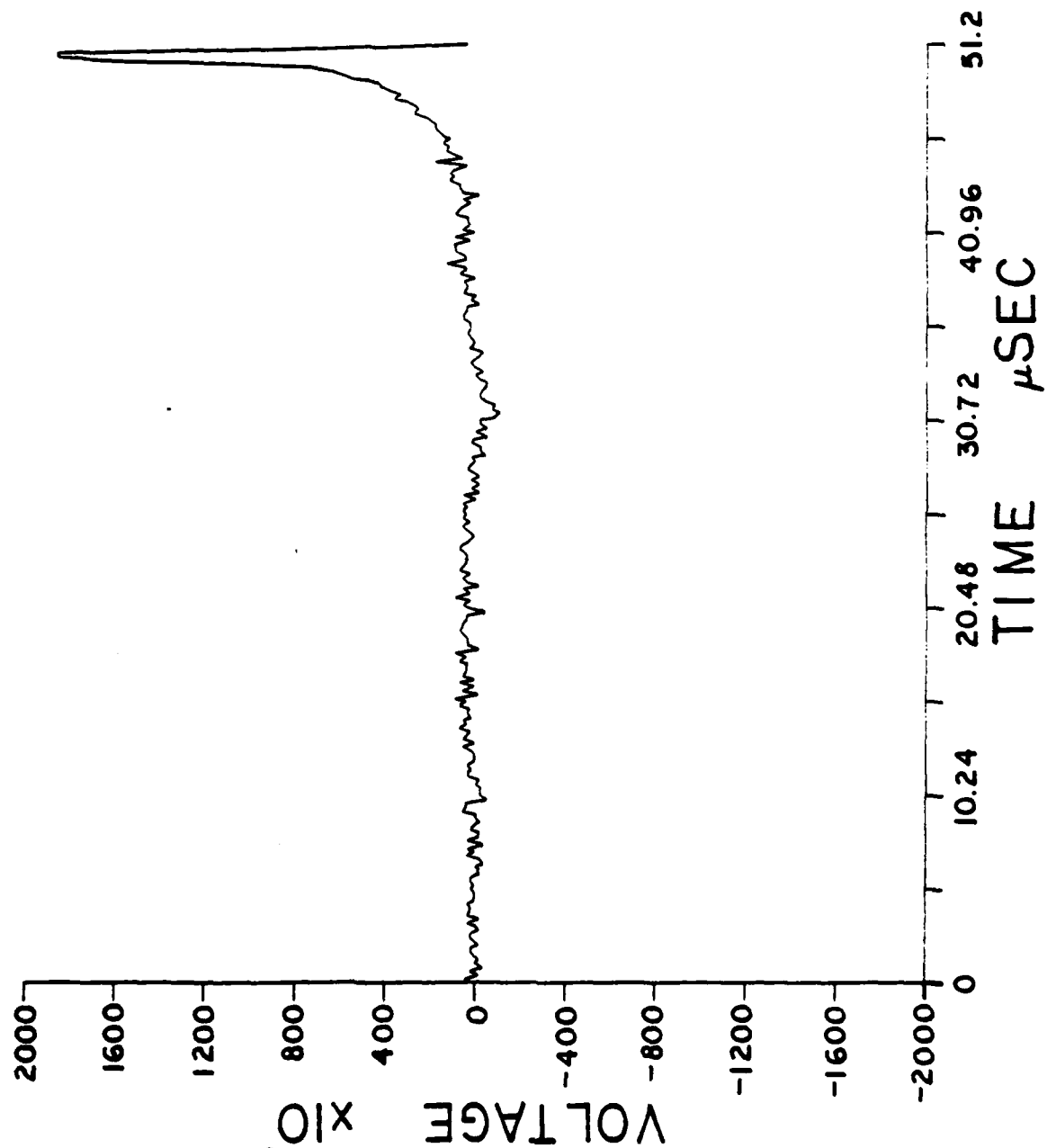
VOLTAGE x10^{-3}
2000
1600
1200
800
400
0
-400
-800
-1200
-1600
-2000
0
10.24
20.48
30.72
40.96
51.2
TIME μSEC

F11

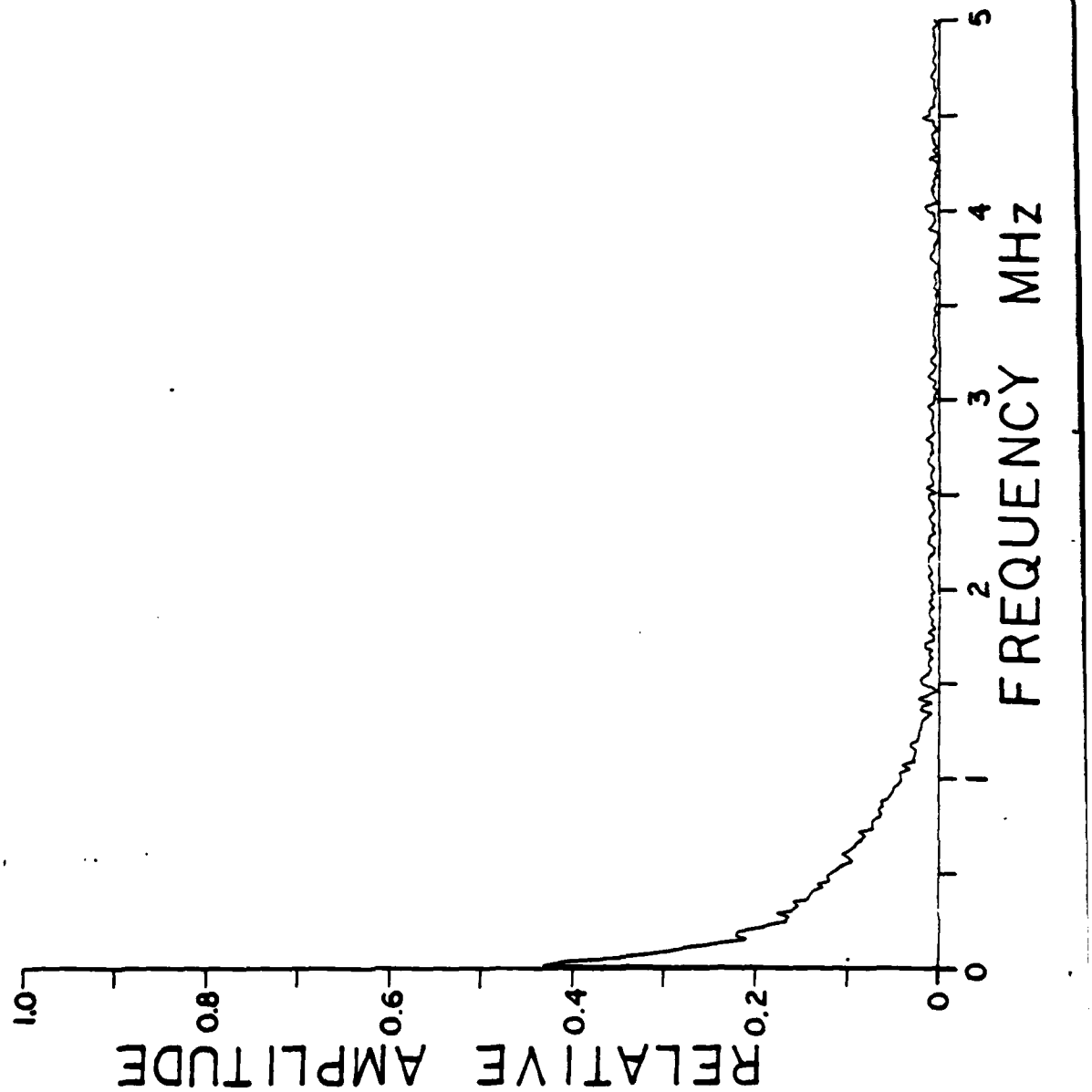

F12

F13

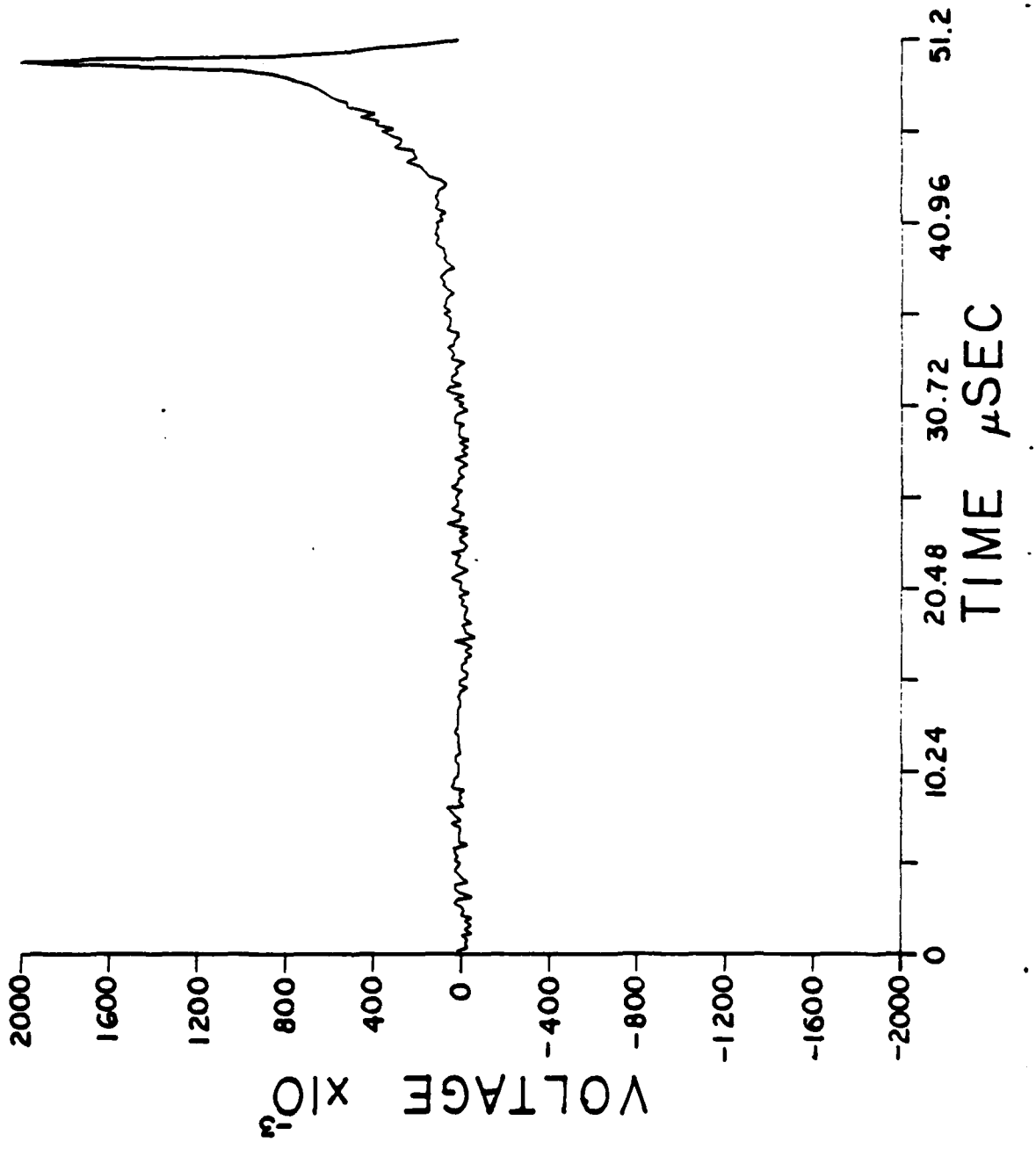
VOLTAGE x10³
2000
1600
1200
800
400
0
-400
-800
-1200
-1600
-2000
0
10.24
20.48
30.72
40.96
51.2
TIME μSEC

F14

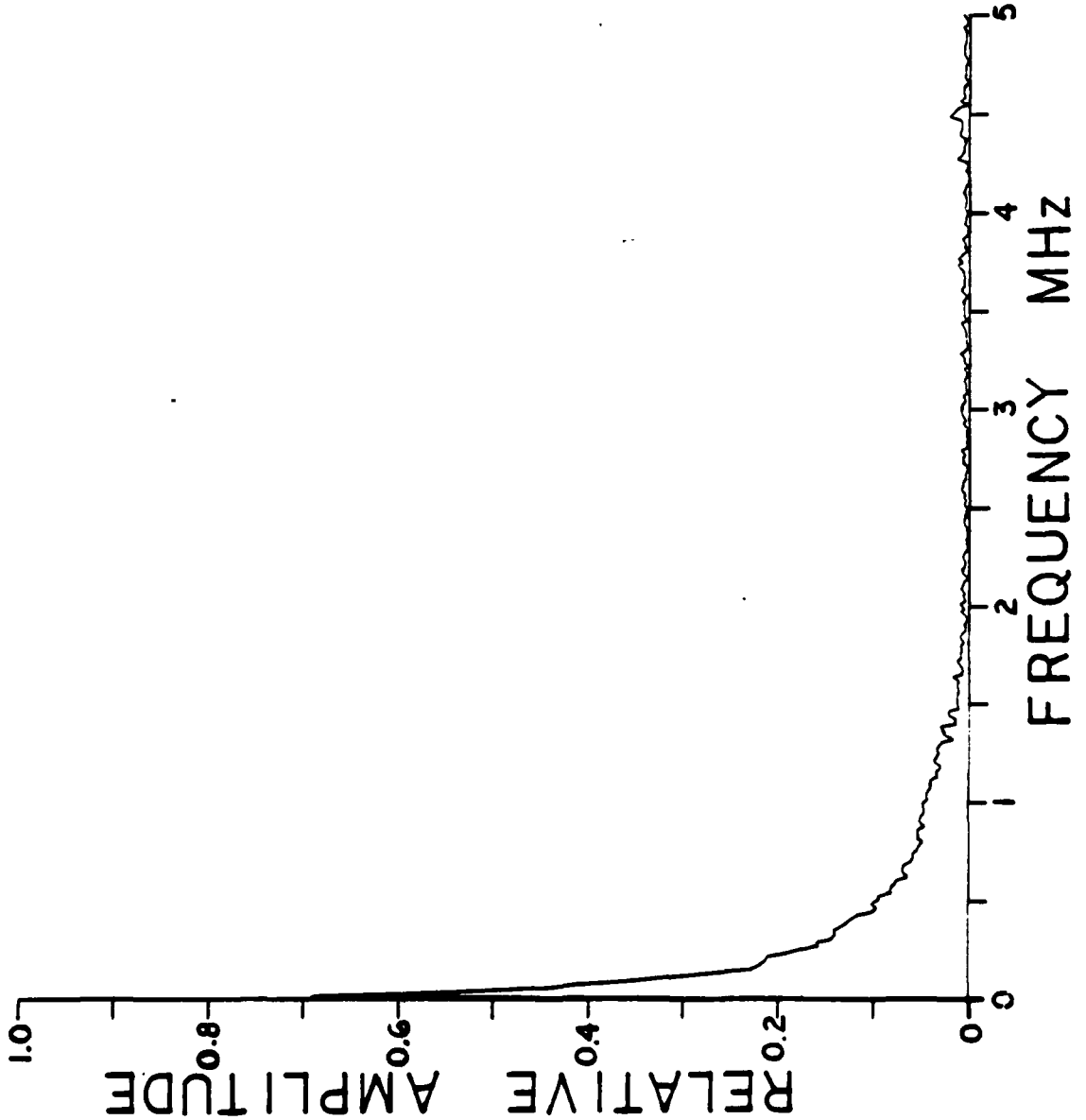

F15

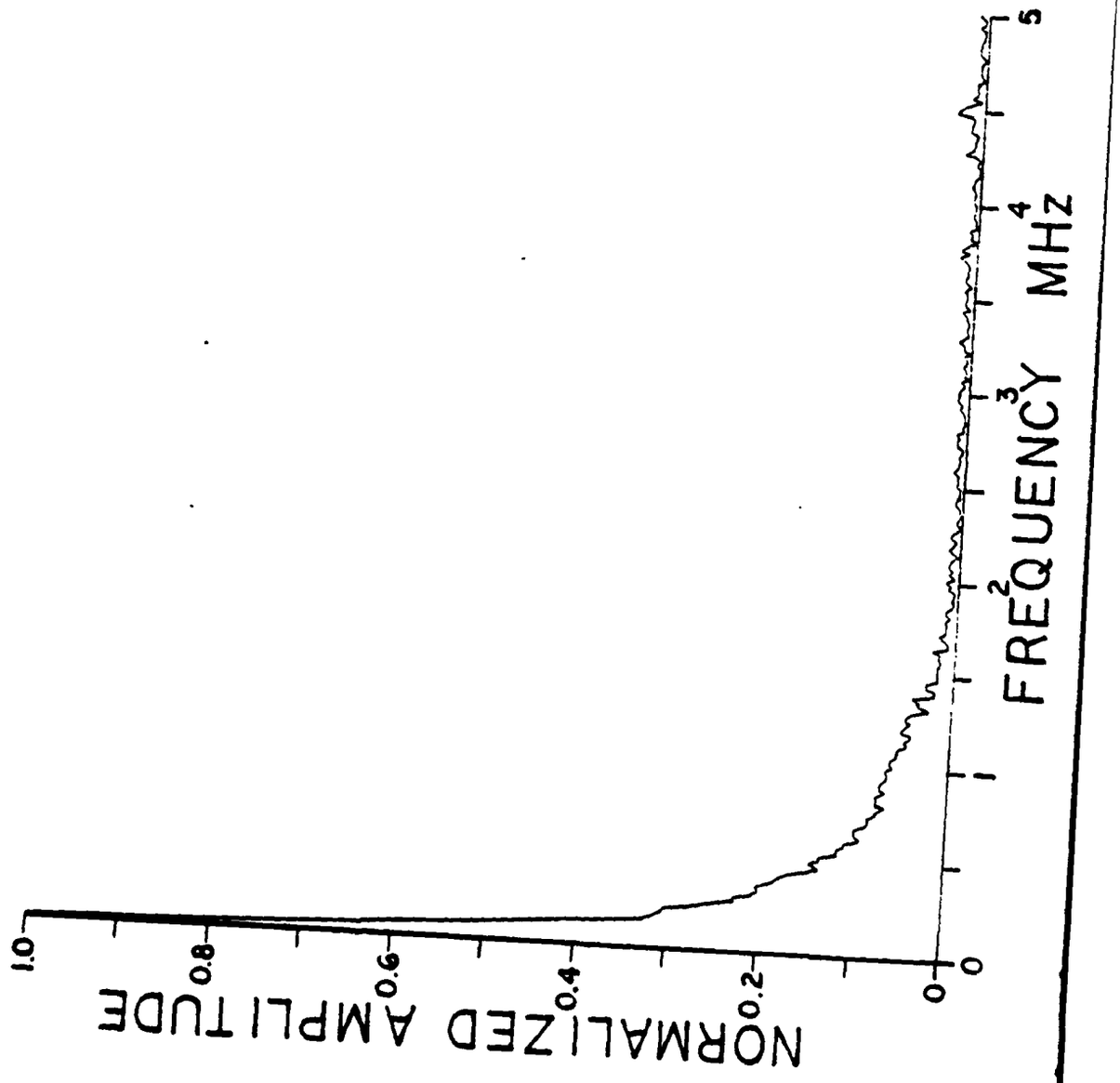

F16

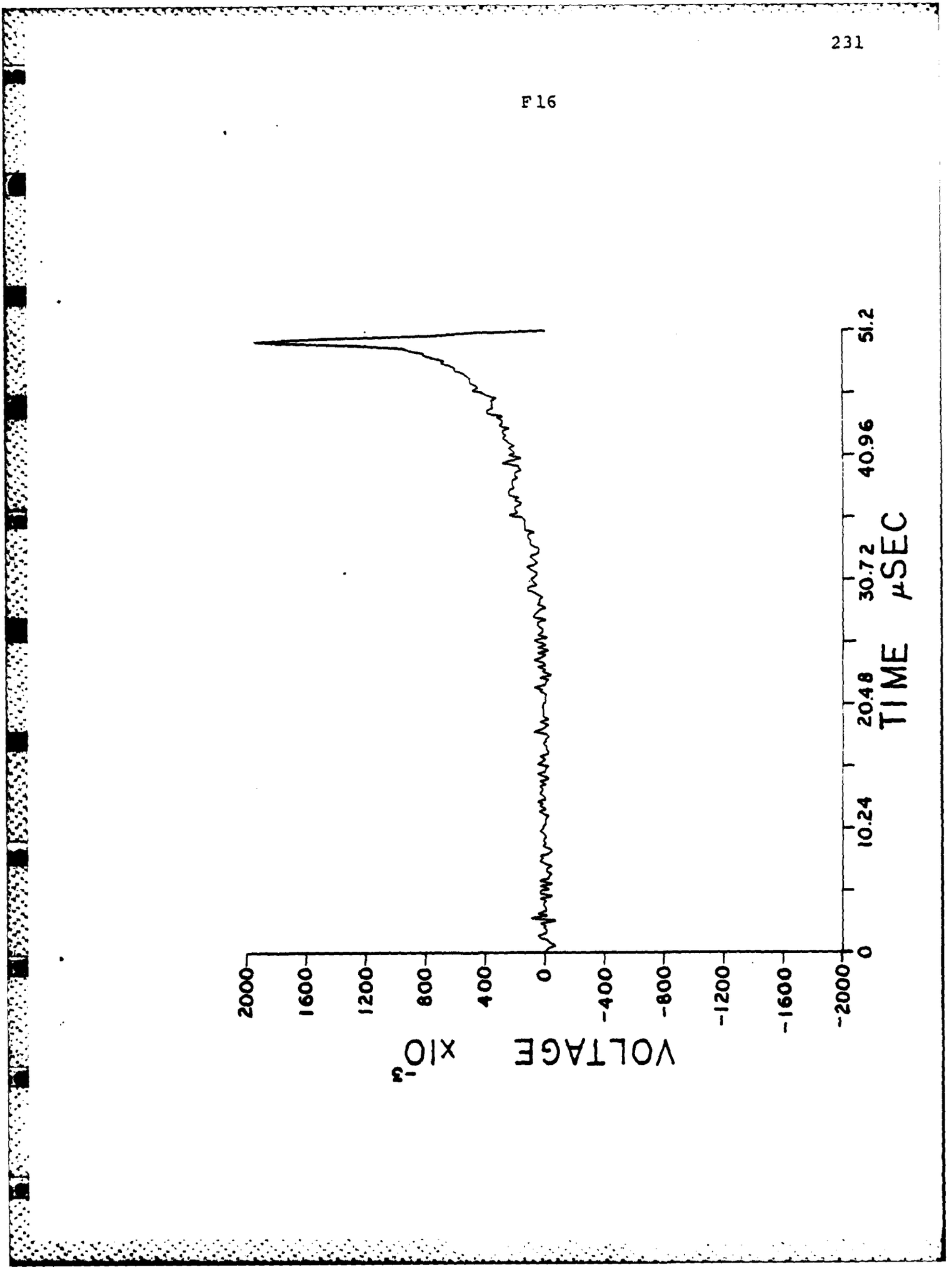
VOLTAGE x10⁻³
2000
1600
1200
800
400
0
-400
-800
-1200
-1600
-2000
0
10.24
20.48
30.72
40.96
51.2
TIME μSEC

F17

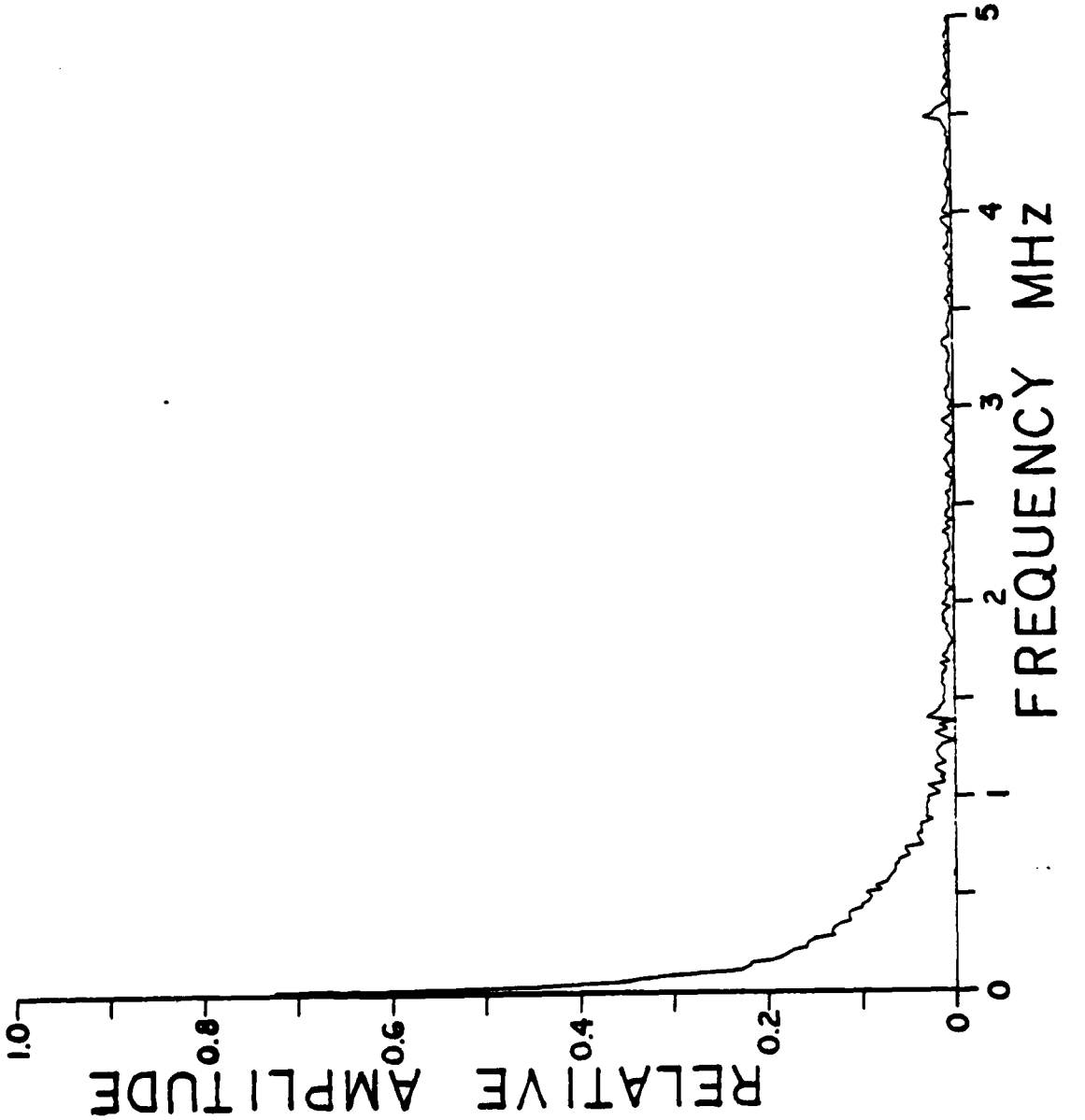

F18

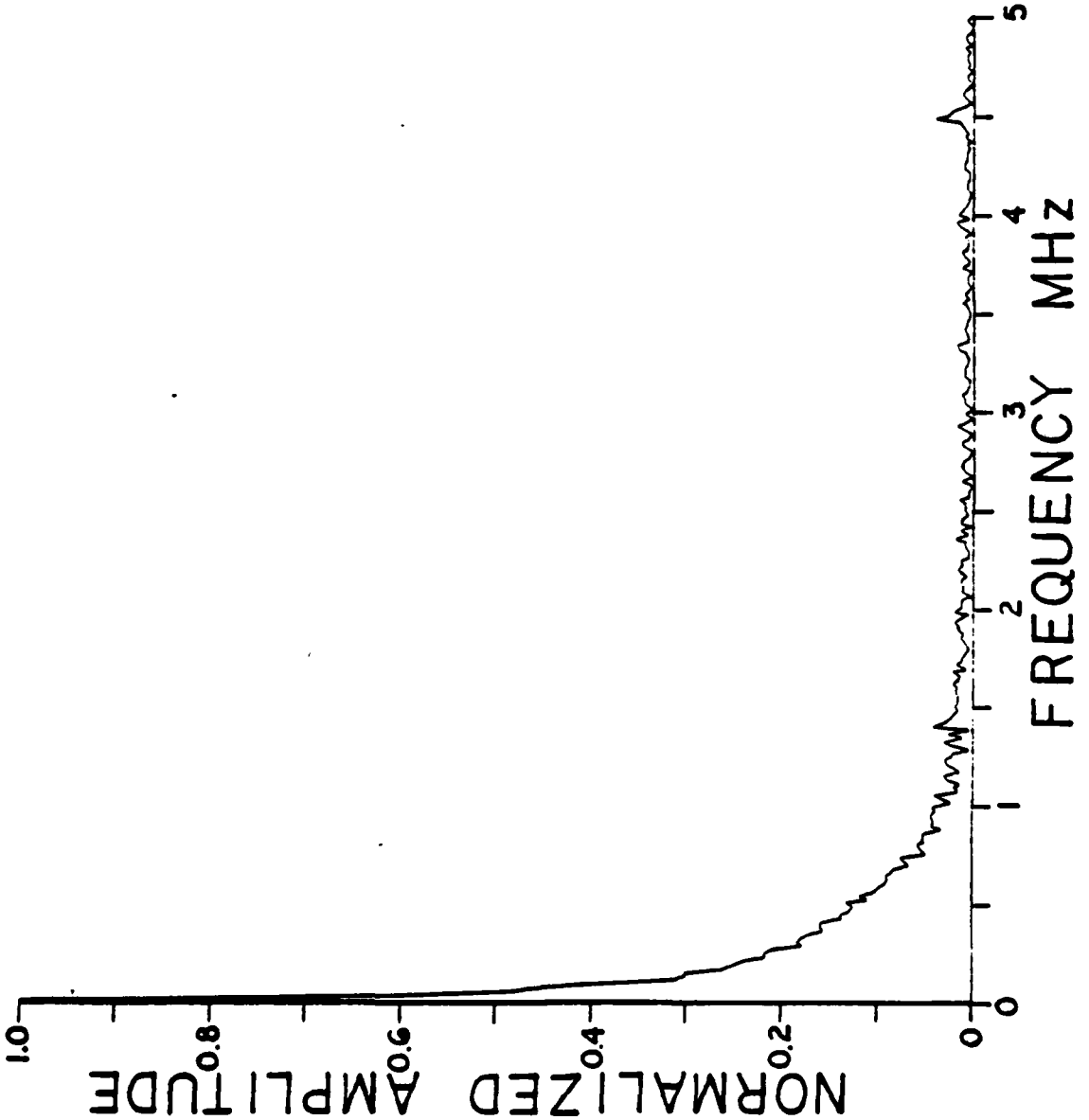

F19

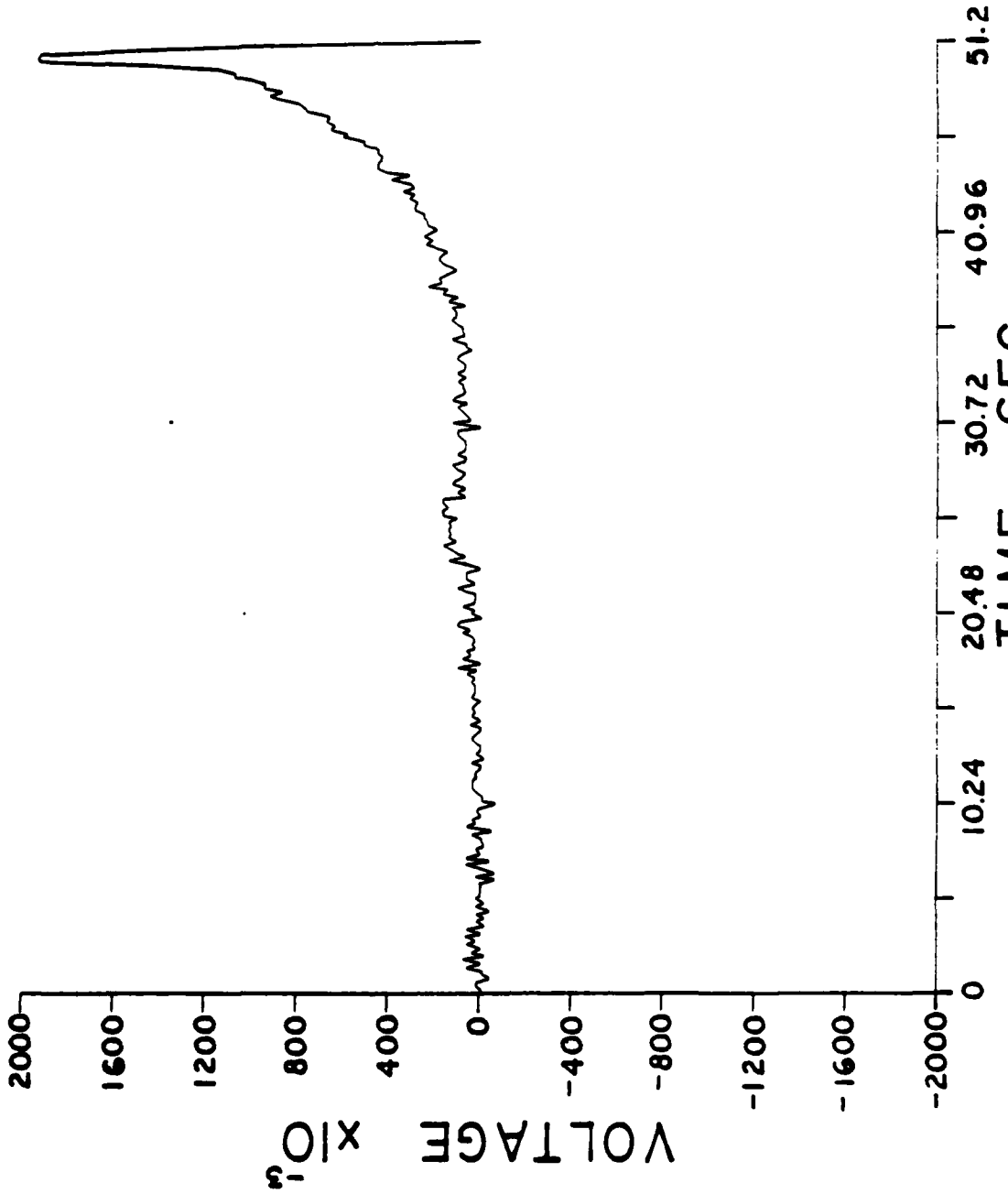
VOLTAGE x10⁻³
2000
1600
1200
800
400
0
-400
-800
-1200
-1600
-2000
0
10.24
20.48
30.72
40.96
51.2
TIME μSEC

F20

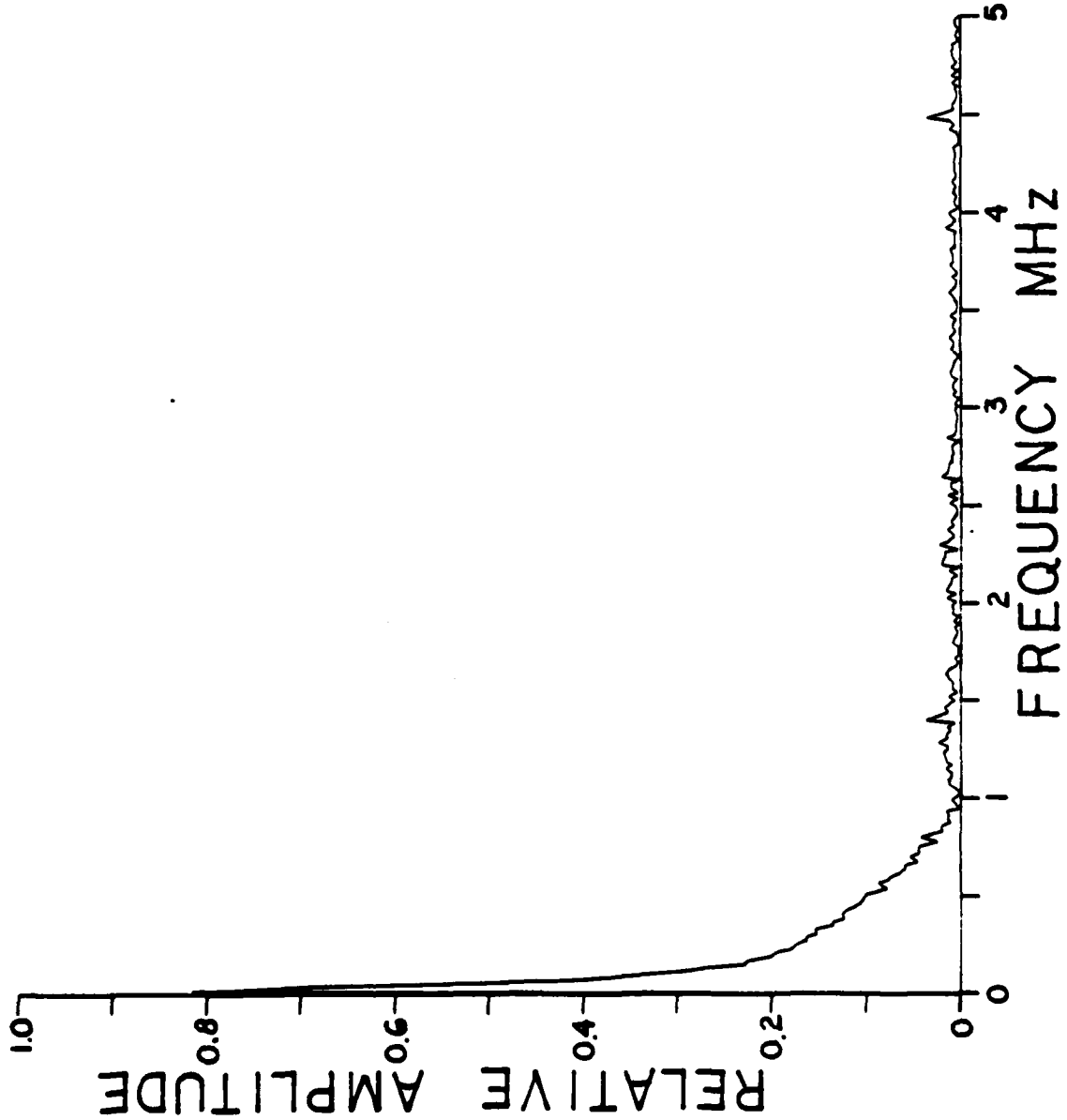

F21

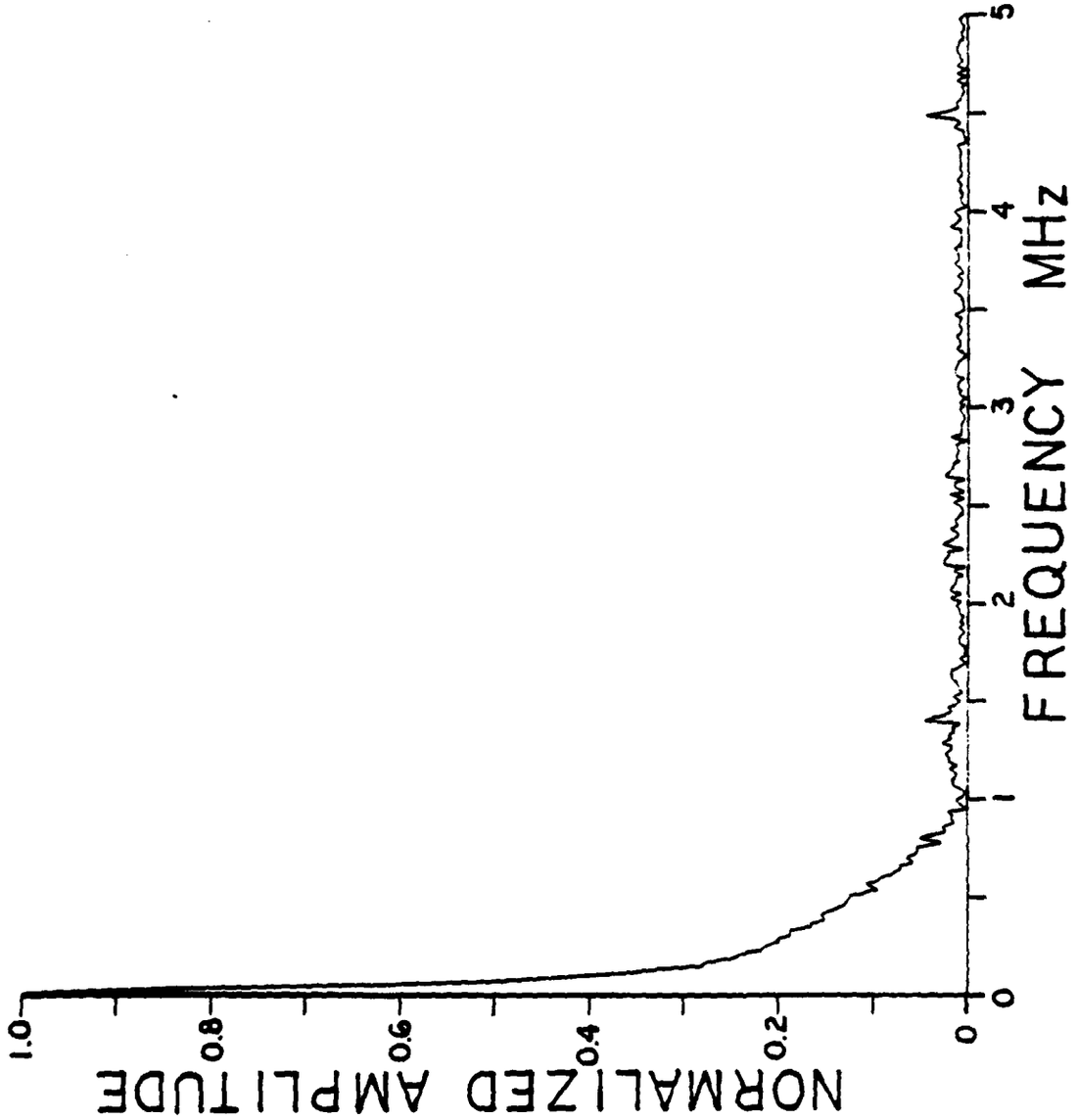

F22

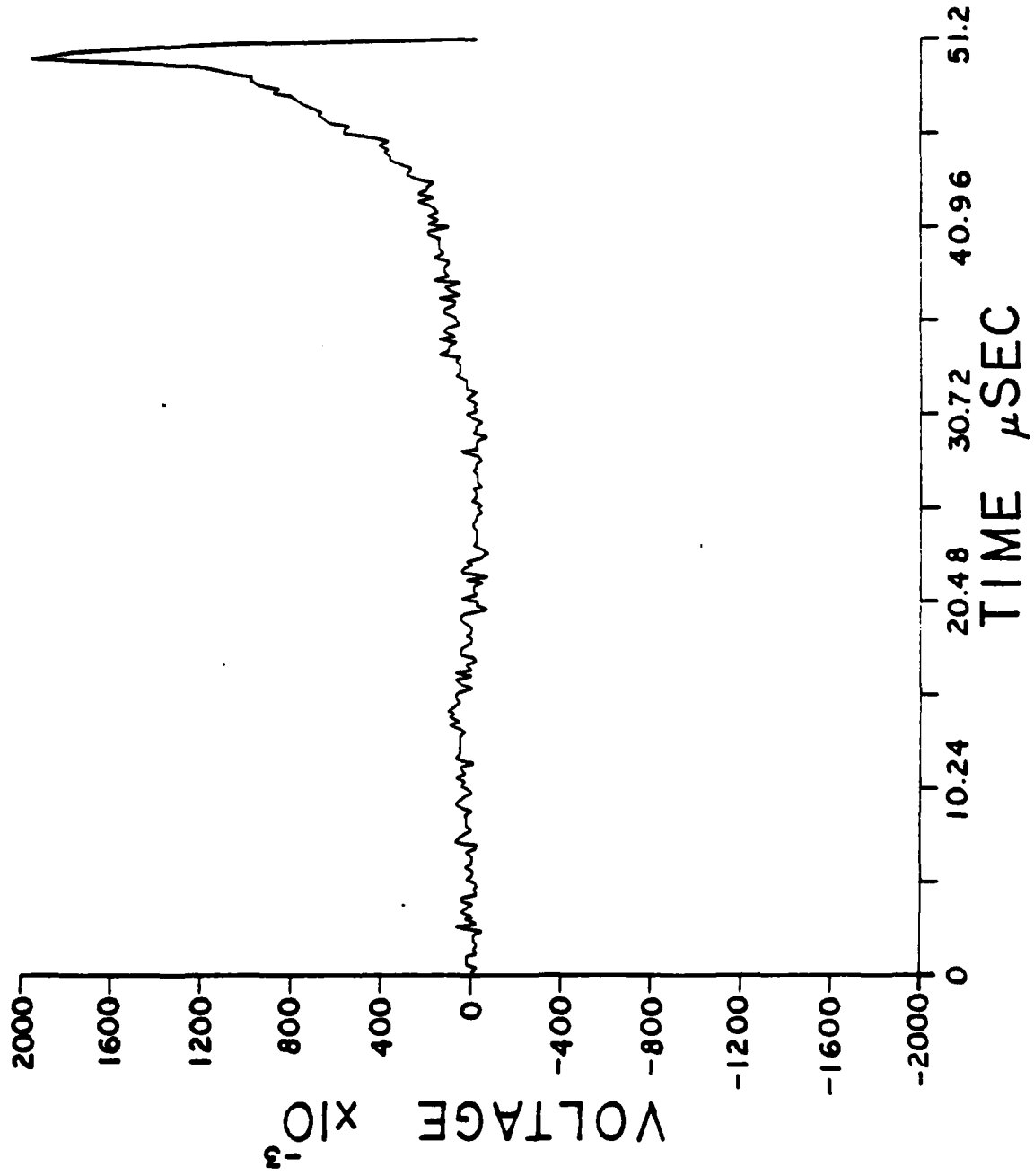
VOLTAGE x10⁻³
2000
1600
1200
800
400
0
-400
-800
-1200
-1600
-2000
0
10.24
20.48
30.72
40.96
51.2
TIME μSEC

F23

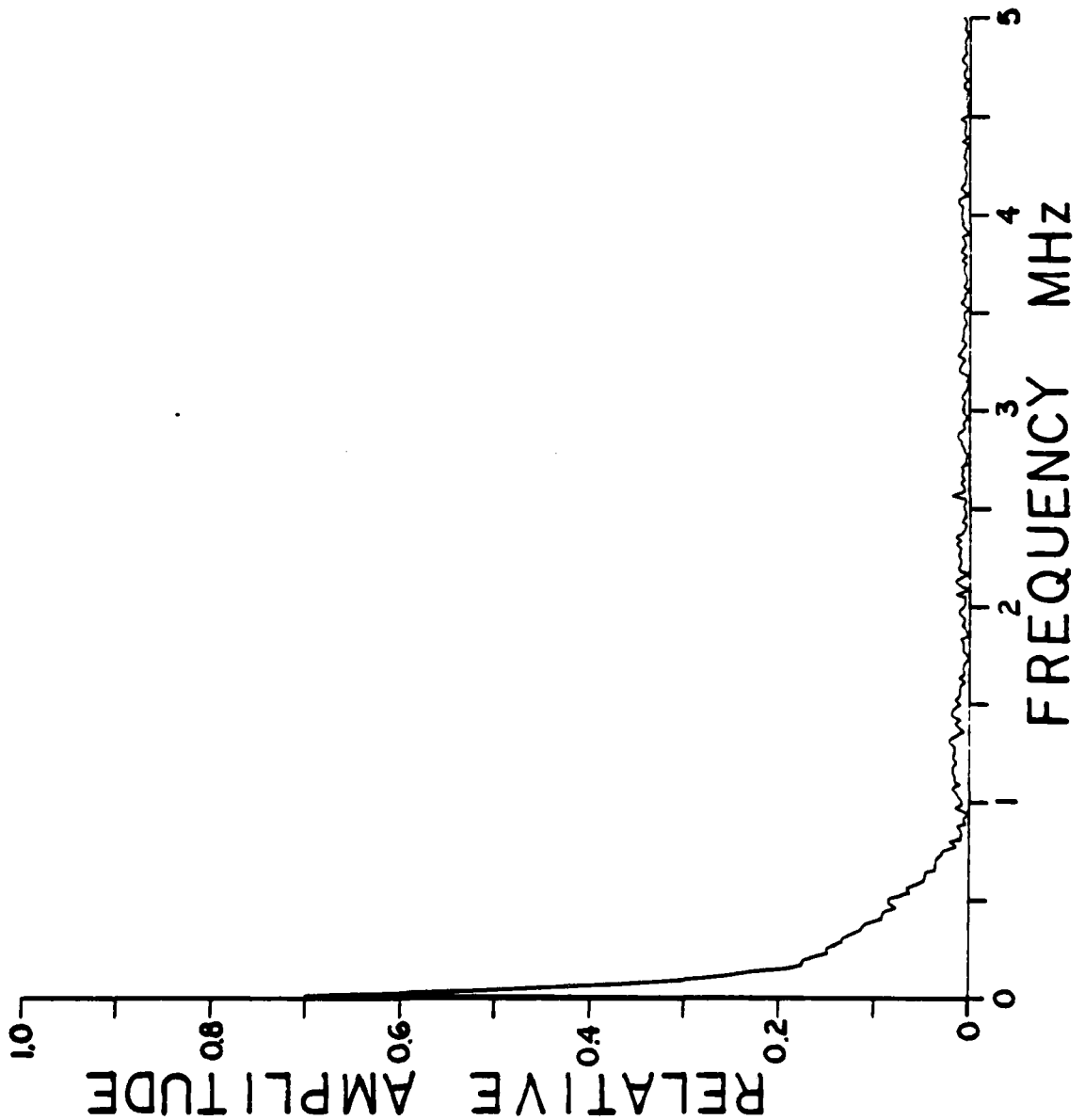

F24

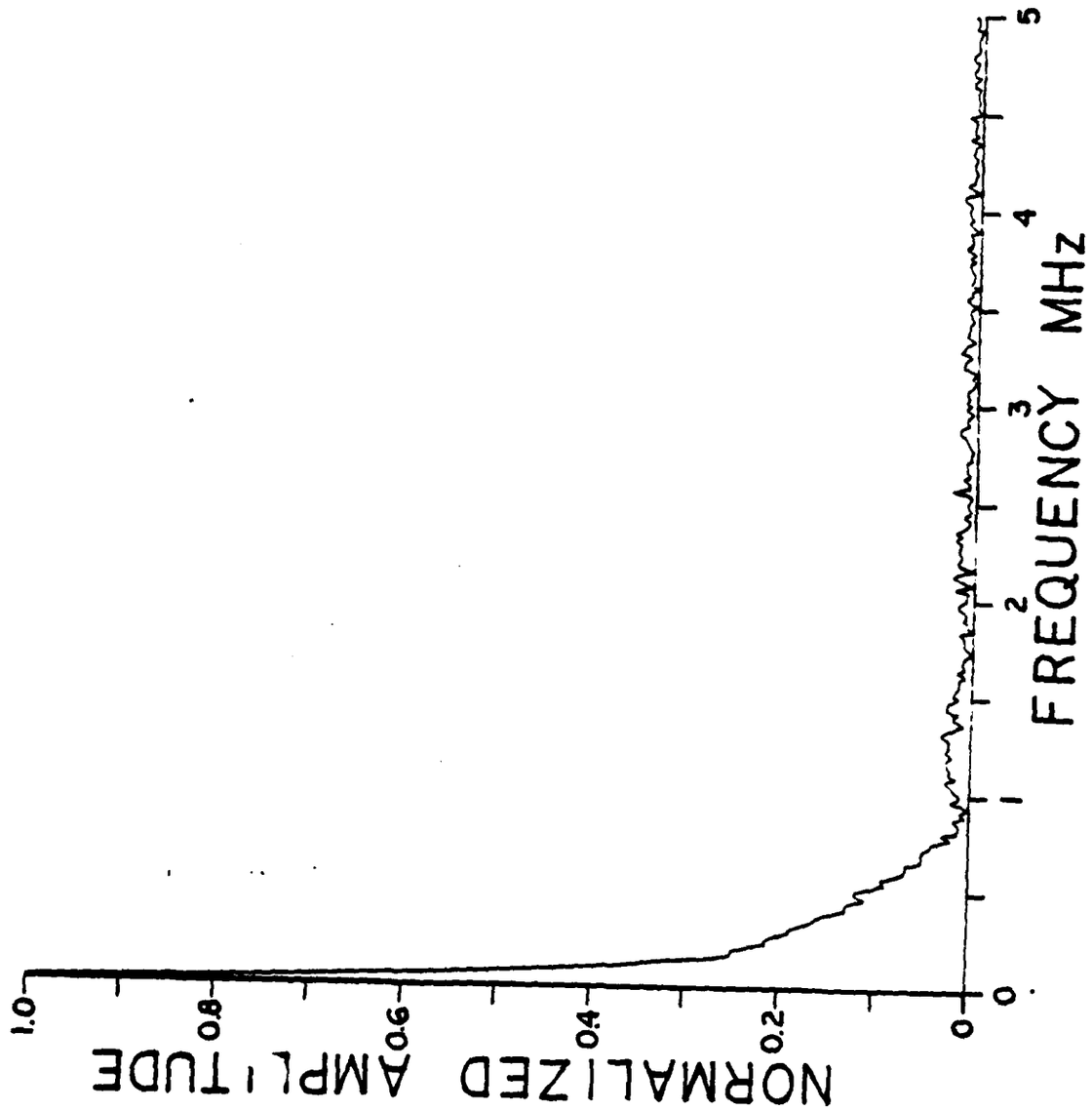

F25

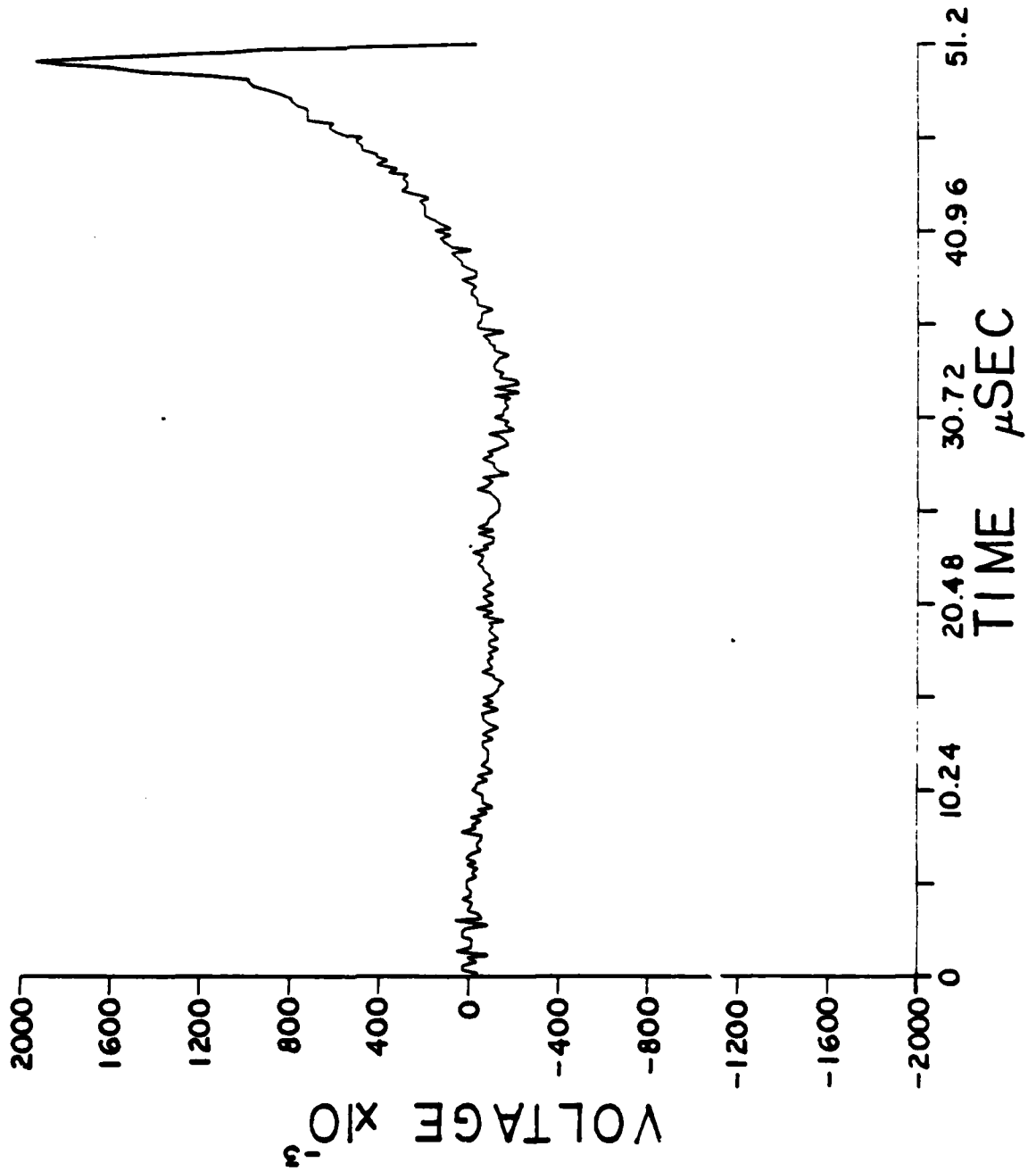
VOLTAGE x10⁻³
2000
1600
1200
800
400
0
-400
-800
-1200
-1600
-2000
0
10.24
20.48
30.72
40.96
51.2
TIME μSEC

F26

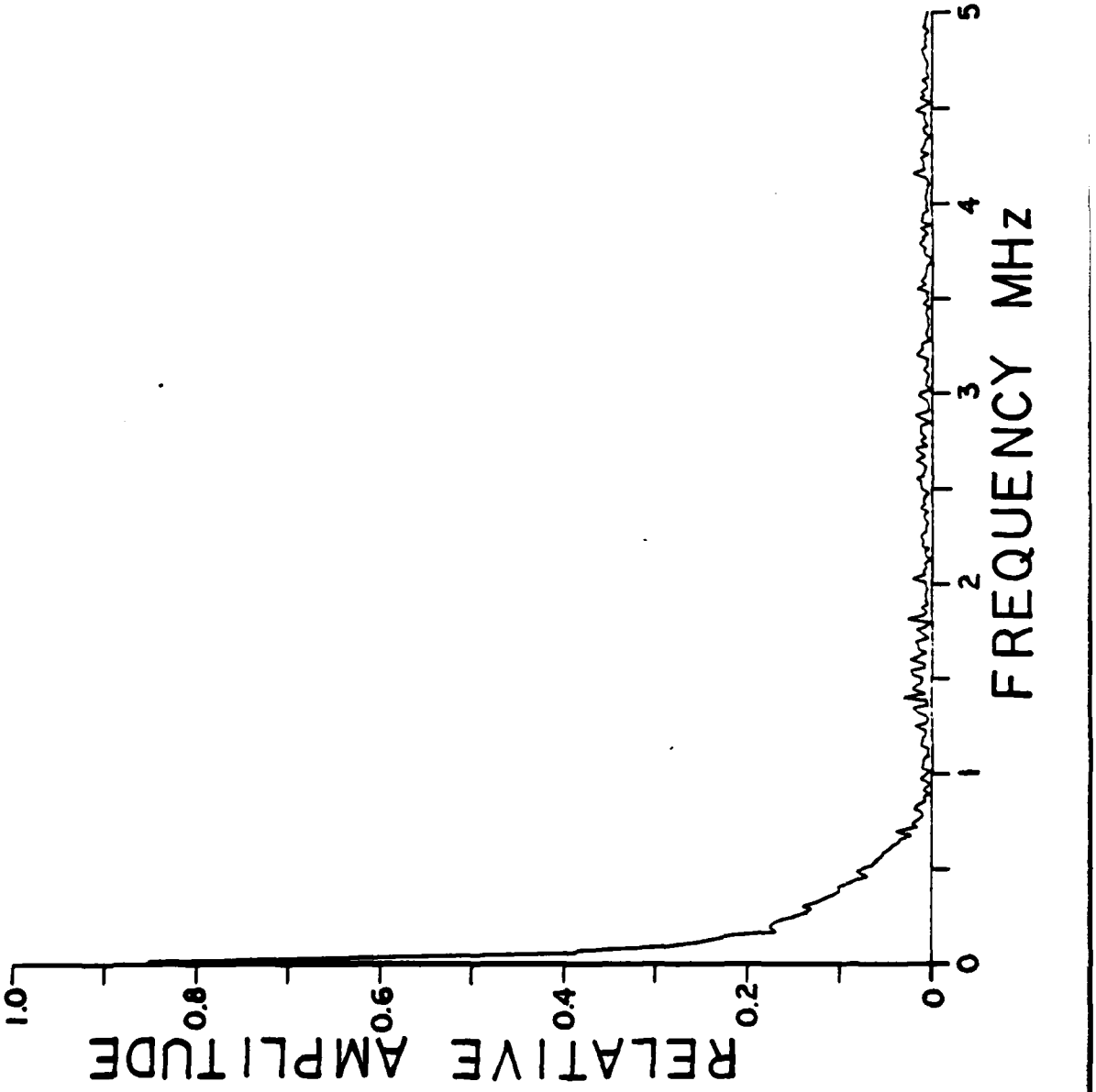

F27

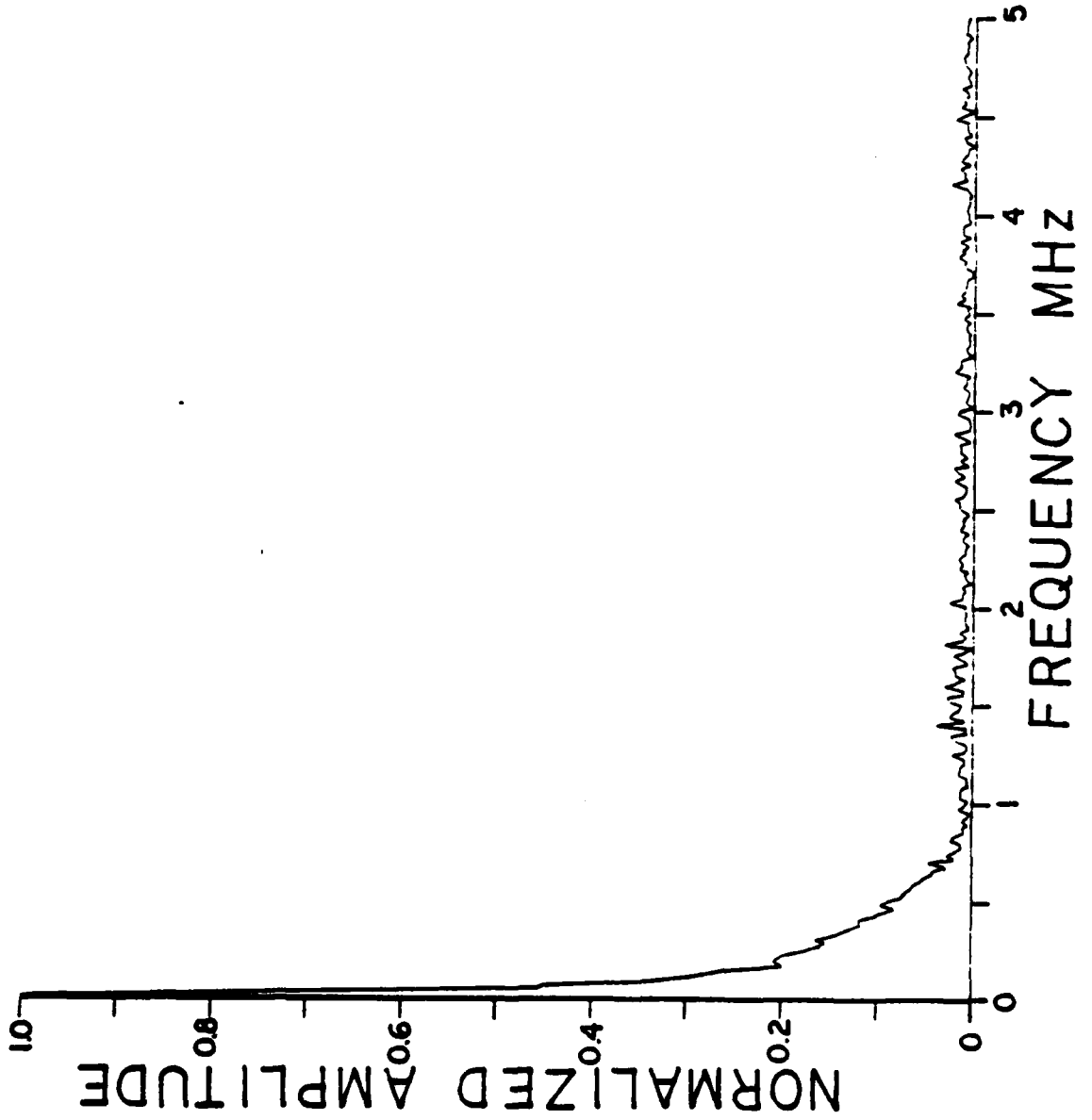

F28

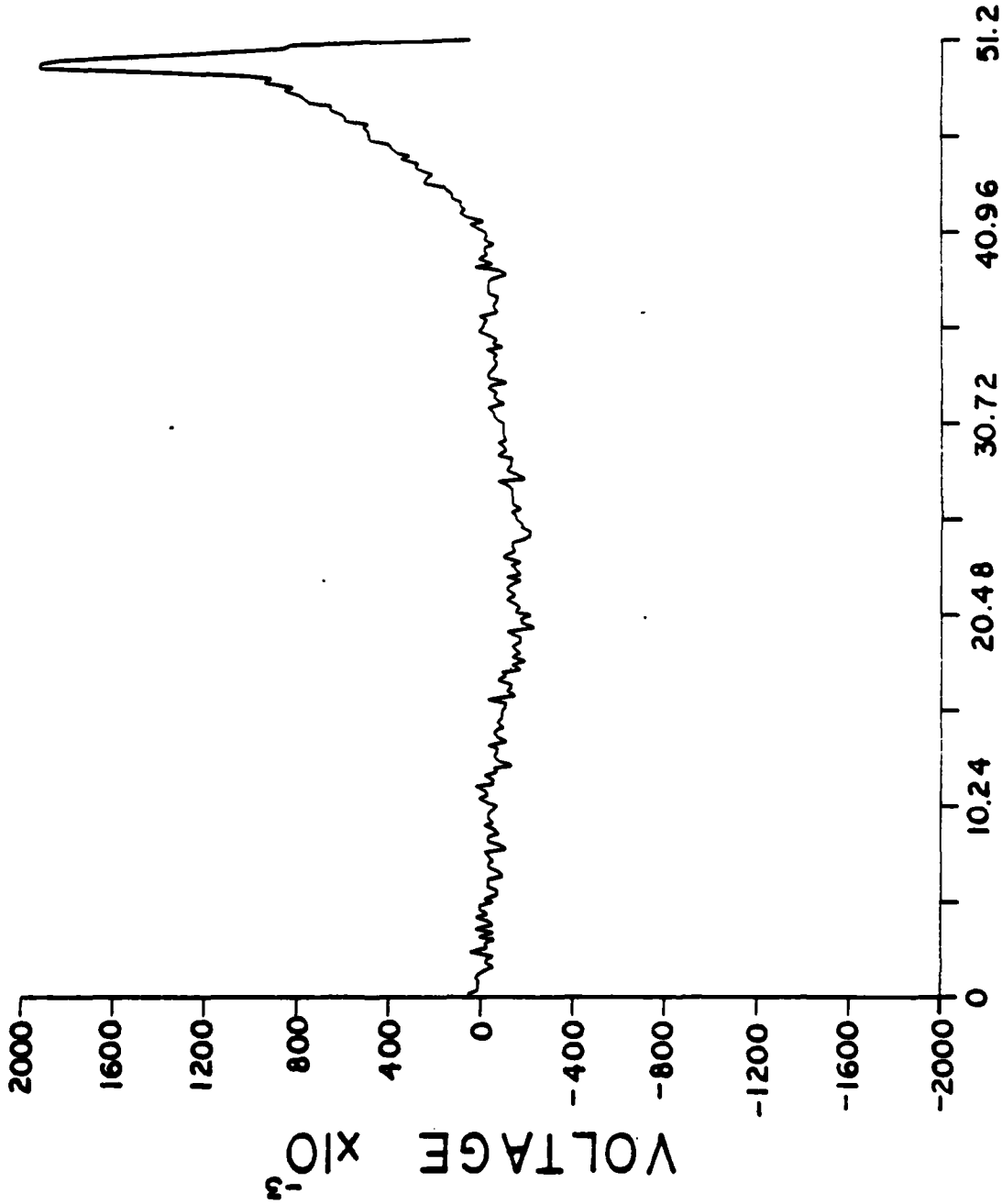
VOLTAGE x10⁻³
2000
1600
1200
800
400
0
-400
-800
-1200
-1600
-2000
0
10.24
20.48
30.72
40.96
51.2
TIME μSEC

F29

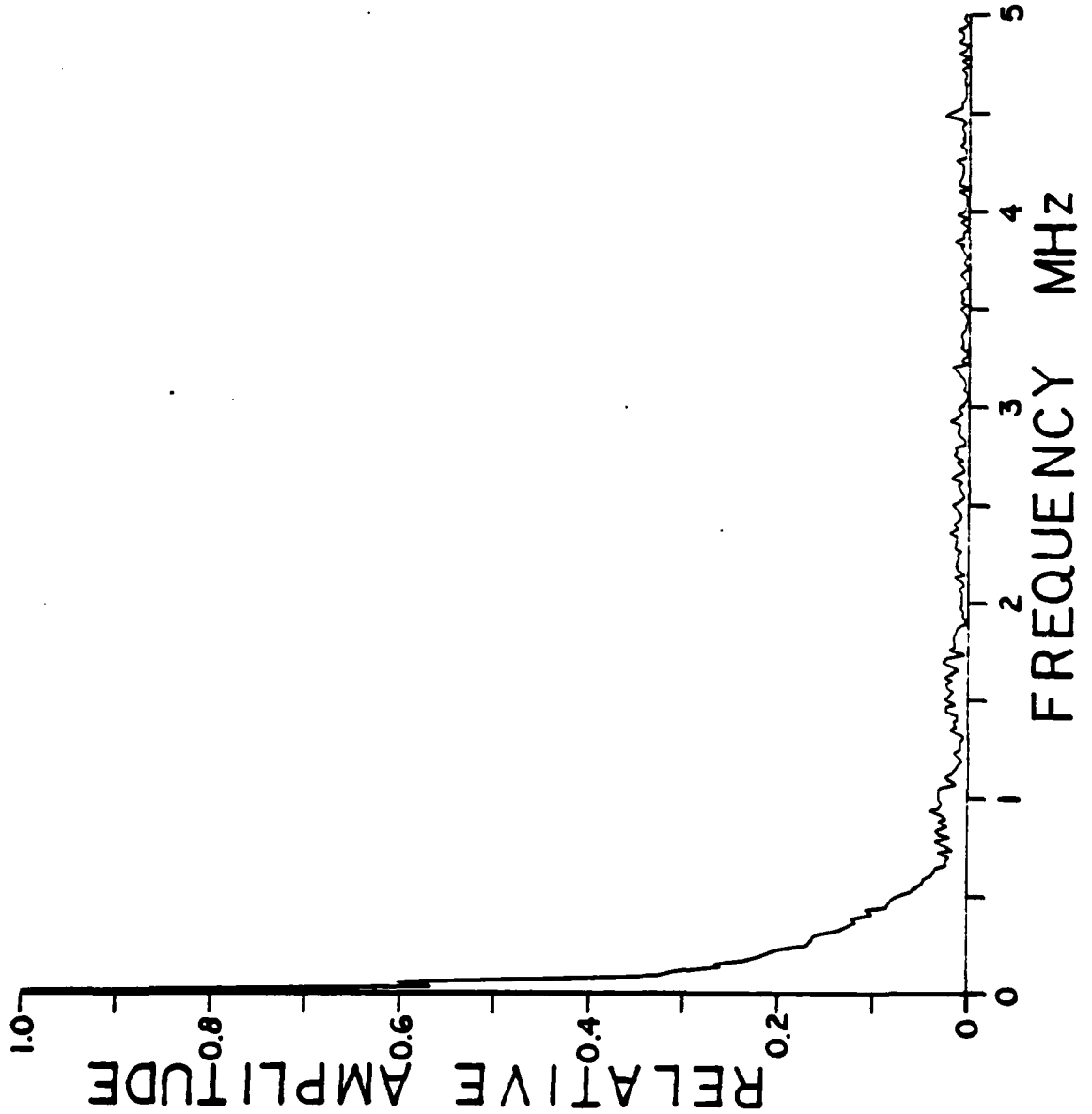

F30

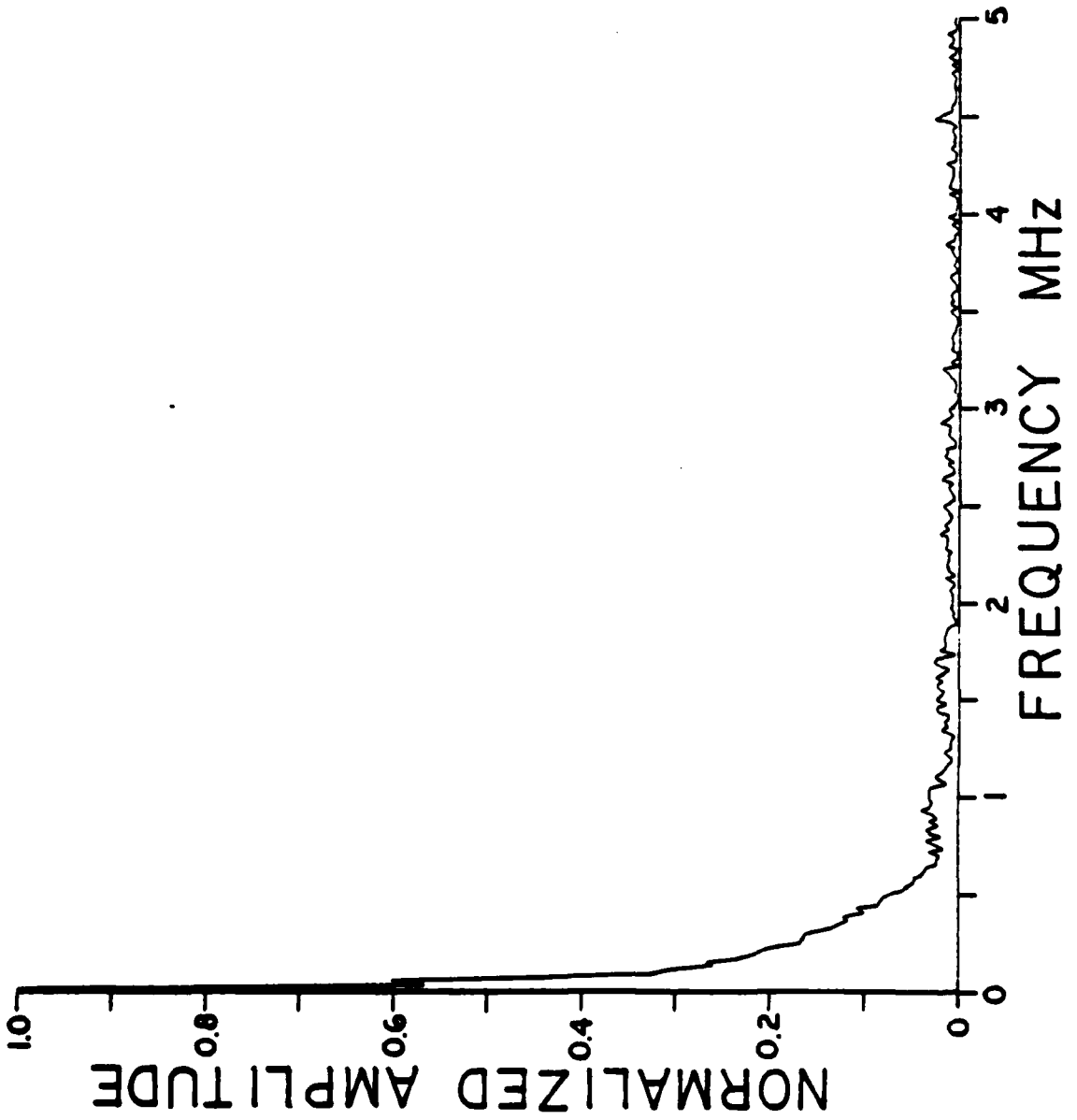

VII. BIBLIOGRAPHY

1. W.J. Bruchey Jr., Optical Probing of Acoustic Emission During Deformation of Micro-Tensile Specimens. Ph.D. Thesis, The Johns Hopkins University, Baltimore, Maryland (1980).

2. H. Kolsky, Stress Waves in Solids, (Dover Publications, N.Y., 1963).

3. R.G. Liptai, D.O. Harris, R.B. Engle, C.A. Tatro, Int. J. of N.D.T., 3, 215-275 (1971).

4. B.B. Djordjevic, Digital Waveform Recording and Computer Analysis of Acoustic Emission and Ultrasonic Transients Detected by Optical and Piezoelectric Probes. Ph.D. Thesis, The Johns Hopkins University, Baltimore, Maryland (1979).

5. H.N.G. Wadley, C.B. Scruby, Acta. Met. 27, 613 (1979).

6. R.A. Kline, Optical and Piezoelectric Detection of Acoustic Emission Signals. Ph.D. Thesis, The Johns Hopkins University, Baltimore, Maryland (1978).

7. S.E. Fick, C.H. Palmer, Applied Optics, 17 (No. 17), 2686 (1978).

8. R.A. Kline, R.E. Green, C.H. Palmer, J. Acoustical Soc. of America, 64 (No. 6), (1978).

9. C.H. Palmer, S.E. Fick, Proc. of Southeastcon '79, 191 (1979).

10. C.H. Palmer, R.E. Green, "Optical Probing of Acoustic Emission Waves". Final Report, U.S. Army Research Office, North Carolina (1979).

11. H. Lamb, "On the Propagation of Tremors Over the Surface of an Elastic Solid", Phil. Trans. Royal Soc. of London, (A) 203, 1-42 (1904).

12. F.R. Breckenridge, C.G. Tschiegg, M. Greenspan, "Acoustic Emission: Some Applications of Lamb's Problem", J. Acoustic Soc. of America, 57 626-631 (1975).

13. R. Weisinger, Acoustic Emission and Lamb's Problem on a Homogeneous Sphere. Master's Thesis, The Johns Hopkins University, Baltimore, Maryland (1979).

14. J.T. Glass, S. Majerowicz, R.E. Green, "Acoustic Emission Determination of Deformation Mechanisms Leading to Failure of Naval Alloys". Research Summary, Naval Sea Systems Command (1981).

15. T. Proctor, "An Improved Piezoelectric Acoustic Emission Transducer". J. Acoust. Soc. Am. 71 (5) May 1982.

16. J. Murphy, D. Culver, The Johns Hopkins University Applied Physics Laboratory, Laurel, Maryland, Private communication.

17. A. Jaffe, L.B. Loeb, Editor, The Physics of Crystals, (McGraw, N.Y., 1928).

18. M. Classen-Nekludowa, Zeitschrift für Physik, 55, 555 (1929).

19. E. Schmid, M. Valouch, Zeitschrift für Physik, 75, 531 (1932).

20. R. Becker, E. Orowan, Zeitschrift für Physik, 79, 566 (1932).

21. W.P. Mason, S. McSkimimi, W. Stockly, "Ultrasonic Observation of Twinning in Tin", Phys. Rev., 73 (No. 10), 1213 (1948).

22. J. Kaiser, Untersuchugen uber das auftreten Gerauschen beim Zugversuch. Ph.D. Thesis, Technische Hochschule, Munich (1950).

23. T.H. Blewitt, R.R. Coltman, J.K. Redman, "How Temperature Deformation of Copper Single Crystals". J. Applied Physics, 28 (No. 6), 651 (1957).

24. C. Crussard, J.B. Leon, J. Plateau, C. Blaket, "Sur la Formation d'ondes Senores, au Cours d'Essai de Traction, Dans des Eproivettes Metalliques". C.R. Acad. Sci., 246, 19 May (1958).

25. B.H. Schofield, R.A. Barress, A.A. Kyrola, "Acoustic Emission Under Applied Stress". ASTIA Document No. AD155674, WADC Technical Report, 58-194 (1958).

26. B.H. Schofield, "Acoustic Emission Under Applied Stress", Aeronautical Research Lab., Office of Technical Services, U.S. Department of Commerce, Washington, D.C. Report ARL-150 (1960).

27. B.H. Schofield, "Acoustic Emission Under Applied Stress, Aeronautical Research Lab., Wright-Patterson A.F.B., Ohio. Contract No. AF33(616)-5640, Project No. 7021, Task No. 70663, Final Report (1964).

28. C.A. Tatro, "Sonic Techniques in the Detection of Crystal Slip in Metals". Division of Engineering Research, College of Engineering, Michigan State University, East Lansing, Michigan. State Report (1959).

29. C.A. Tatro, R.G. Liptai, "Acoustic Emission From Crystalline Substances", in Proc. Symp. Phys. N.D.T., Southwest Research Institute, San Antonio, Texas 145-158 (1962).

30. C.H. Palmer, R.E. Green, "Optical Probing of Acoustic Emission Waves", in Nondestructive Evaluation of Materials, J.J. Burke, V. Weiss Editors, (Plenum, N.Y. 1979).

31. R.E. Green, C.H. Palmer, "Optical Detection of Acoustic Emission Waves", Proceedings of the Ninth International Congress on Acoustics, Madrid, Spain, (July 1977).

32. C.H. Palmer, R.E. Green, "Optical Detection of Acoustic Emission Waves", Applied Optics, 16, 2333-2334 (1977).

33. C.H. Palmer, R.E. Green, "Materials Evaluation by Optical Detection of Acoustic Emissions Signals", Materials Evaluation Research Supplement, 35, 107-112 (1977).

34. C.H. Palmer, R.E. Green, "Optical Detection of Acoustic Emission Signals", Proceedings of ARPA/AFML Review of Progress in Quantitative NDE Meeting. Cornell University, Ithaca, N.Y. (June 1977), AFML-TR-78-55 (May 1978).

35. C.H. Palmer, R.E. Green, "Optical Detection of Ultrasonic Transients", Proceedings of 1978 Conference on Information Sciences and Systems. The Johns Hopkins University, Baltimore, Maryland, 559-563 (1978).

36. C.H. Palmer, "Optical Measurements of Acoustic Emission at High and Low Temperatures", Proceedings of ARPA/AFML Review of Progress in Quantitative NDF Meeting. La Jolla, California (July 1978), AFML-TR-78-205 (January 1979).

37. C.H. Palmer, D.E. Fick, "New Optical Instrument for Acoustic Emission". IEEE Southeastcon, Roanoke, Virginia, 191-192 (April 1979).

38. R.E. Green, B.B. Djordjevic, C.H. Palmer, S.E. Fick, "Laser Beam Detection of Ultrasonic and Acoustic Emission Signals for Nondestructive Testing of Materials". Proceedings of ASM Conference on Applications of Lasers to Materials Processing, Washington, D.C., 161-175 (April 1979), American Society for Metals, Metals Park, Ohio (1979).

39. B.B. Djordjevic, R.E. Green, "High Speed Digital Capture of Acoustic Emission and Ultrasonic Transients as Detected With Optical Laser Beam Probes". Proceedings of Ultrasonic International '79 Conference, Graz, Austria, 82-87 (May 1979).

40. C.H. Palmer, R.E. Green, "Optical Probing of Acoustic Emission Waves". Final Report, U.S. Army Research Office, The Johns Hopkins University (August 1979).

41. R.E. Green, "Acoustic Emission". Encyclopedia of Science and Technology, (McGraw-Hill, N.Y. 1982).

42. R.A. Kline, R.E. Green, C.H. Palmer, "Acoustic Emission Waveforms From Stress-Corrosion Cracking of Steel: Experiment and Theory". (Submitted for publication, J. Applied Phys.).

43. A. Peterlin, B.B. Djordjvic, J.C. Murphy, R.E. Green, "Acoustic Emission During Craze Formation in Polymers". (Submitted for publication, J. Applied Phys. 52, 141-146 (1981).

44. C.D. McGillem, G.R. Cooper, Continuous and Discrete Signal and System Analysis. (Holt, Rinehart and Winston Inc., N.Y., 1974).

INITIAL DISTRIBUTION

Copies

2 ONR
- 1 Code 431
- 1 Code 434

5 NRL
- 1 Code 6307
- 1 Code 6311
- 1 Code 6320
- 1 Code 6380
- 1 Code 6385

2 Naval Air Development Center
Naval Materials Center
Warminster, PA 18974
- 1 Code 6063
- 1 Code 6403

13 NAVSEA
- 1 SEA 05C
- 1 SEA 05M
- 1 SEA 05M/C. Null
- 1 SEA 05R
- 1 SEA 05R24
- 1 SEA 05R25
- 1 SEA 05R26
- 1 SEA 55Y
- 1 SEA 92R
- 2 SEA 996
- 2 SEA 96612

4 Naval Air Systems Command
Washington, DC 20361
- 1 AIR 320B
- 1 AIR 5163
- 1 AIR 5302
- 1 AIR 950D

1 Chief of Naval Material
MAT 0715

1 Naval Surface Weapons
White Oak, MD 20910
Mr. J. Agul

12 DTIC

Copies

1 Naval Ship Systems Engrg. Station
Measurements & Materials Dept.
Philadelphia, PA 19112
T. T. Galie

1 AFWAL
Wright Patterson AFB, OH 45433
Mr. P. A. Parmley

1 Air Force Office of Scientific Research
Bldg 410, Bolling AFB
Washington, DC 20332
Mr. J. Morgan

1 NASA
Langley Research Center
Hampton, VA 23365
Dr. J. Davidson

1 Army Air Mobility R&D Laboratory
Ft. Eustis, VA 23604
SAVDL-EU-SS/Mr. J. Robinson

1 Army Material & Mechanics
Research Center
Watertown, MA 02172
Dr. E. Lenore

1 Army Mobility R&D Laboratory
Ames Research Center
Moffett Field, CA 94035
Dr. Raymond Foye

1 Army Research Office
Research Triangle Park, NC 27709
Dr. F. Schmiedeshoff

50 Johns Hopkins University
Dept. of Civil Eng.
Materials Science & Eng.
Charles & 34th St.
Baltimore, MD 21218
R. E. Green, Jr.

CENTER DISTRIBUTION

Copies	Code	Copies	Code
1	17	1	281
1	172	1	2812
1	1720.1	1	2813
1	173	1	2814
1	2724	1	2815
1	28	1	2816
1	2803	3	522.1
1	2809M	2	5231